Creating Life-like Transience in Synthetic Vesicles

A Thesis Submitted in Partial Fulfilment of the
Requirements for the Degree of

Doctor of Philosophy

in

Chemistry

by

Saurav Das
Roll No.: 176122002

Supervisor

Prof. Debapratim Das

Department of Chemistry
Indian Institute of Technology Guwahati
Guwahati – 781039, Assam (India)

Dedicated to my beloved **mom, dad,** and **sister** for their unwavering support, endless love, and consistent encouragement throughout the years.

Declaration

I hereby declare that the matter embodied in this thesis is result of investigations carried out by me in the Department of Chemistry, Indian Institute of Technology Guwahati, India, under the guidance of Dr. Debapratim Das. In keeping with the general practice of reporting scientific observations, due acknowledgements have been made wherever the work described is based on the findings of other investigators.

(Saurav Das)

भारतीय प्रौद्योगिकी संस्थान गुवाहाटी
INDIAN INSTITUTE OF TECHNOLOGY GUWAHATI

Dr. Debapratim Das
Professor
Department of Chemistry
Ph: + 91 361 258 3301
Fax: + 91 361 258 2349
E-mail: ddas@iitg.ac.in

05th August, 2022

To whom it may concern.

This is to certify that the thesis entitled **"Creating Life-like Transience in Synthetic Vesicles"** submitted by Saurav Das (Roll No. 176122002) for the award of PhD degree to IIT Guwahati, is absolutely based on his own research work and that neither this thesis nor any part of it has been submitted for any degree/diploma or any academic award anywhere before.

(Dr. Debapratim Das)

Contents

Abstract

The thesis "**Creating Life-like Transience in Synthetic Vesicles**" explores several techniques and approaches for imbuing life-like non-equilibrium features in synthetic vesicular systems and their potential biomimetic applications in laboratory settings.

Chapter 1 provides a brief overview of transient out-of-equilibrium systems, the classification of various types of assembly processes based on their energy profiles, and the progress accomplished thus far in the field of non-equilibrium system chemistry.

Chapter 2 presents a novel strategy for constructing transient supramolecular peptide amphiphiles (SPA) based on cucurbit[8]uril and its vesicular assembly under the influence of a pH clock.

Chapter 3 focuses on the development of a cucurbit[8]uril based pH-responsive supramolecular peptide amphiphile (SPA) that transiently assembles into hydrolase mimetic vesicular nanozymes upon the addition of alkaline TRIS buffer (activator) but then instigates its self-destruction due to the catalytic generation of acidic by-products (deactivator).

Chapter 4 describes a chemoenzymatic pH clock mediated transient assembly of a vesicular nanozyme wherein the distinct confinement of two catalytically discrete units, histidine groups on the periphery and hemin in the lipid bilayer, results in an efficient hydrolase-peroxidase tandem catalysis in a temporally controlled fashion.

Chapter 5 discusses the multi-luminescent behaviour of a transiently breathing vesicular light-harvesting system in which variations in the luminescent characteristics of the entrapped FRET donor and acceptor molecules allow broad-spectrum luminescence tuning over the course of the pH regulated breathing cycles.

भारतीय प्रौद्योगिकी संस्थान गुवाहाटी
Indian Institute of Technology Guwahati

Acknowledgements

I am incredibly grateful and humbled to everyone who has helped and supported me in shaping this thesis and translating naive concepts and ideas into something real and tangible. This journey has been quite the roller coaster ride, with ups and downs, triumphs and failures, but overall, it has been a rewarding experience of learning, growing, and flourishing. My deepest admiration goes to my mentor, Prof. Debapratim Das, who not only helped me nurture my scientific skills but occasionally went above and beyond to support and advise me in many different facets of life. I owe Prof. Das a debt of gratitude for his sage advice, inspirational words, and vast knowledge, all delivered with the right amount of humor and wit. He has been an amazing supervisor, and I am happy and grateful to have had the opportunity to work with him. I am extremely thankful to my Doctoral Committee members, Prof. Lal Mohan Kundu, Dr. Kalyan Raidongia, and Dr. Sunanda Chatterjee, for their encouragement, guidance, and suggestions, which have helped me significantly enhance the quality of my research work. I would especially like to thank Dr. Sunanda Chatterjee, whose inspiring and motivating remarks inspired me to strive for excellence and do better each and every time. I'm also grateful to Prof. Oren Scherman (University of Cambridge, UK) for sharing his scientific expertise and perceptive thoughts, which helped to strengthen my study significantly.

I'm indebted to my senior lab mates, Dr. Sahnawaz Ahmed, Dr. Bapan Pramanik, Dr. Nilotpal Singha, Dr. Subhojit Ghosh, Dr. Payel Dowari and Dr. Basab Kanti Das, who helped me find my footing as I started my research career at IIT Guwahati. My heartfelt adorations go to Bapan da, who quickly gained my respect and affection as a brother, and whose love, care, support and guidance helped me escape some of the most trying circumstances at IITG. Also, I'm eternally grateful to Bapan da for guiding me through the intricacies of chemical synthesis during my early days, as it eventually laid the groundwork for my research projects. I'm thankful to Sumit Chowdhuri, Priyam Das, Tanushree Das, Malay Kumar Baroi, and Ritvika Kushwaha for creating a nice and joyful atmosphere in the lab, and for providing their valuable suggestions and endless support towards the fruitful accomplishment of my projects. I genuinely appreciate Priyam for being a kind and supportive brother, for the incessant research related discussions we have had, and for always being there for me. A special thanks to Tanushree for her unprecedented love, care, and selfless support during this endeavor. Tanushree has been a huge part of my ability to stay motivated and push myself to work harder to accomplish my objectives. I'm eternally thankful to Tanushree for her unwavering belief in me and for supporting me through thick and thin.

I gratefully thank everyone at the Department of Chemistry, IIT Guwahati, including my friends, fellow researchers, lecturers, and technical personnel, for their direct or indirect support and assistance throughout this journey. I extend my sincere thanks to Sarupa Roy, Amrita Hazra, Akashdeep Saha and Shreya Debnath for their valuable assistance during project works. I thank the anonymous reviewers who helped in improving the quality of my research articles. I thank the Department of Chemistry and The Central Instruments Facility, IIT Guwahati, for providing instrumental facilities. I'm also thankful to IIT Guwahati for financial assistance.

Last but not the least, I would like to extend my profound gratitude to my loving mother, Mrs. Shipon Rani Das, father, Mr. Sanjay Kumar Das and sister, Ms. Sushmita Das. Their unfathomable love, sacrifices, patience and prayers helped me in enduring this challenging voyage. They encouraged and supported me in all of my life decisions, leaving no stone unturned in their efforts to help me achieve my goals. They gave me hope and strength throughout my life, without which none of my accomplishments would have been possible. I consider myself exceedingly fortunate to have been born into this family, and words will never be adequate to describe my gratitude and thankfulness. In closing, I thank God for giving me enough strength and blessings to successfully complete this challenging yet remarkable journey, and achieve one of the most alluring milestones of my life.

List of Abbreviations

Abbreviations

NMR	Nuclear Magnetic Resonance
ESI-MS	Electrospray Ionization
MALDI	Matrix Assisted Laser Desorption/Ionization
FESEM	Field Emission Scanning Electron Microscopy
FETEM	Field Emission Transmission Electron Microscopy
EDX	Energy Dispersive X-ray
CLSM	Confocal Laser Scanning Microscopy
AFM	Atomic Force Microscopy
FTIR	Fourier-Transform Infrared Spectroscopy
DLS	Dynamic Light Scattering
HPLC	High-Performance Liquid Chromatography
CIE	Commission Internationale de l'Elcairage
UV-Vis	Ultraviolet–Visible Spectroscopy
FL	Fluorescence
λ_{max}	The wavelength in the absorption spectrum where the absorbance is maximum
λ_{em}	The wavelength in the emission spectrum where the emission is maximum
ζ	Zeta Potential
Φ	Quantum Yield
Φ_{ET}	Energy Transfer Efficiency
AE	Antenna Effect
TLC	Thin Layer Chromatography
ITC	Isothermal Titration Calorimetry
K_a	Binding Constant
K_d	Dissociation Constant
ΔH	Change in Enthalpy
ΔS	Change in Entropy
ΔG	Change in Gibbs Free Energy
MeOH	Methanol
EtOH	Ethanol
ACN	Acetonitrile

DMSO	Dimethyl Sulfoxide
DMF	N,N-Dimethylformamide
DIPEA	N,N-Diisopropylethylamine
TFA	Trifluoroacetic Acid
TES	Triethylsilane
TEA	Triethylamine
DMAP	4-Dimethylaminopyridine
HBTU	Hexafluorophosphate Benzotriazole Tetramethyl Uronium
DPH	1,6-Diphenyl-1,3,5-hexatriene
NR	Nile Red
ANS	8-Anilinonaphthalene-1-sulfonic acid
DBT	4,7-dithien-2-yl-2,1,3-benzothiadiazole
CF	5(6)-Carboxyfluorescein
CTAB	Cetyltrimethylammonium bromide
SDS	Sodium dodecyl sulphate
TRIS	Tris(hydroxymethyl) aminomethane
ADP	Adenosine diphosphate
ATP	Adenosine triphosphate
GDP	Guanosine diphosphate
GTP	Guanosine triphosphate
HK	Hexokinase
CPK	Creatine phosphokinase
CytC	Cytochrome C
GOx	Glucose oxidase
HRP	Horseradish peroxidase
CGTase	Cyclodextrin glucanotransferase
DD	Dormant Deactivator
δ-GL, GdL	Glucono delta-lactone
MF	Methyl formate
ε-CL	ε-caprolactone
DMS	Dimethyl sulphate
DBC	N,N'-dibenzoyl-l-cystine
TCEP	Tris(2-carboxyethyl)phosphine
DTT	Dithiothreitol

EDC	1-Ethyl-3-(3-dimethylaminopropyl)carbodiimide
NHS	N-hydroxy succinimide
BTB	Bromothymol blue
SDT	Sodium dithionite
Au-NP	Gold Nanoparticle
RNA	Ribonucleic acid
DNA	Deoxyribonucleic acid
CAC	Critical Aggregation Concentration
SPA	Supramolecular Peptide Amphiphile
CB[n]	Cucurbit[n]uril (n = 5, 6, 7, 8, 10)
FRET	Förster Resonance Energy Transfer
CT	Charge Transfer
PDI	Perylenediimide
cNDI	Core-Substituted Naphthalene Diimide
pNP	p-Nitrophenol
pNPA	p-Nitrophenylacetate
pNPCAA	p-Nitrophenylchloroacetate
DNP	2,4-Dinitrophenol
DNPA	2,4-Dinitrophenylacetate
MPA	2-Methoxyphenylacetate
MP-Im	3-(3-(2-methoxyphenoxy)-3-oxopropyl)-1-methyl-1H-imidazol-3-ium bromide

भारतीय प्रौद्योगिकी संस्थान गुवाहाटी
Indian Institute of Technology Guwahati

Chapter 1

Introduction

भारतीय प्रौद्योगिकी संस्थान गुवाहाटी
Indian Institute of Technology Guwahati

1.1. Transient Out-of-Equilibrium Processes – An Introduction

The self-organization of simple molecular building blocks into highly complex assemblies through self-assembly process is paramount for the development and formation of a wide array of functional structures in nature. Biological systems make extensive use of self-assembly, and in fact, the extremely intricate and ordered arrangement of proteins, nucleic acids, etc., is responsible for the origin of primitive life forms and their evolution. From the formation of micelles in detergent to the alignment of liquid crystals in LCDs, mankind too has effectively used molecular self-assembly to develop innovations and make life simpler in countless ways. Self-assembly processes, be it natural or artificial, relies on non-covalent interactions such as hydrogen bonding, π-π stacking, hydrophobic interactions, van der Waals forces, electrostatic interactions, etc. Self-assembly processes are generally energetically downhill processes and tend towards a low energy equilibrium state. The self-assembled states are highly dynamic, but are in a stable chemical equilibrium as long as the physiological conditions are conducive. However, many self-assembly processes occurring in nature, such as the reversible formation of actin filaments,[1] formation of microtubules,[2] cell division,[2] motility,[3] and signal transduction[4] are energetically demanding processes and require a steady inflow of energy to retain the functional self-assembled state. The thermodynamic pathway of assembly is inadequate to maintain the functional efficacy of these systems, and therefore such systems are kinetically driven where the assembly process is governed by the assembly pathway rather than the stability of the assembled state.[5] Such out of equilibrium self-assembly processes which are self-regulatory in nature and generate supramolecular assemblies of short finite lifetimes are referred to as transient self-assembly processes.

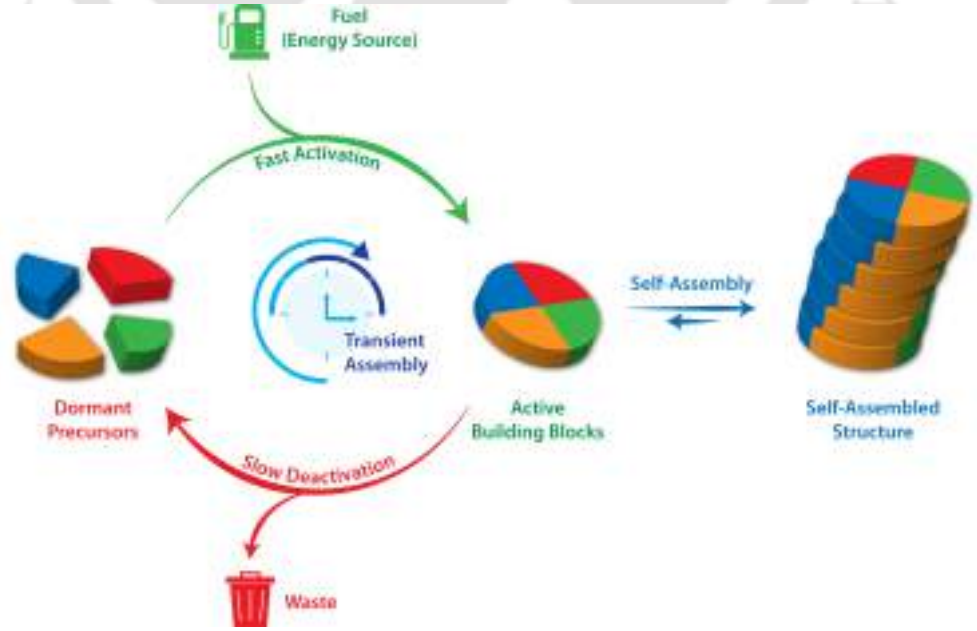

Figure 1.1. Schematic representation of transient self-assembly process.

Chemists have long prioritised the design and development of stable and durable self-assembled systems. However, in the last several decades, constructing molecular building blocks that demonstrate an energy-driven autonomous self-assembly process has been a major scientific objective for system's chemists in order to produce life-like dynamic systems that are self-sustaining, adaptable, and capable of exhibiting smart properties like replication, reproduction, and catalysis. In transient self-assembly, the chemical building blocks are essentially dormant and solubilised in the media (Figure 1.1). Upon activation by an energy source (fuel), these building blocks undergo assembly in a highly spatiotemporal order. However, these activated blocks and their assemblies are extremely unstable, and their fate is determined by the supply of energy. When the energy supply is depleted, they revert to a low-energy inactive state, and the assembly dissipates. The notion of transient self-assembly allows one to obtain control over the assembly/disassembly kinetics and lifespan of the self-assemblies. Furthermore, it enables for the time-gated regulation of various functions and characteristics of the system in a repetitive and self-regulatory manner.

1.2. Thermodynamic Regimes of Self-Assembly Processes

On the basis of thermodynamic and kinetic stability of the molecular building blocks as well as the self-assembled structures, and the pathway adopted for the self-assembly process, three different thermodynamic regimes have been identified (Figure 1.2).[5] The most researched and commonly seen self-assembly process is equilibrium self-assembly, in which the assembly process is primarily thermodynamically driven. In equilibrium self-assembly, the precursor molecules are energetically unstable and occupy a slightly higher energy state in the energy landscape. As the precursor molecules interact with each other through various non-covalent interactions, energy is lost and the self-assembled structures come down to a low energy equilibrium state. These thermodynamically favoured ensembles are highly dynamic, but allow exchange of molecules and energy between the assembled and disassembled states. However, the exchange takes place in an equilibrated manner and a stable chemical equilibrium is maintained within the system. Thus, there is no net influx or efflux of energy and matter, and overall the assembly process is in equilibrium.

Occasionally, during self-assembly, the ensembles may fall into a state of local energy minima, which is substantially higher than the global minimum of the given thermodynamic energy landscape. There are two conceivable outcomes in such a scenario, depending on the amount of activation energy needed to break out of the local energy minima. If the activation energy required is relatively low, the self-assembled state can cross the energy barrier and escape to the global minima of the energy landscape. In this situation, the self-assembly in the high energy trapped state has a finite lifespan and is hence referred to as metastable. However, if the available energy is insufficient to transcend the energy barrier, or if the self-assembled state is incapable of exchanging

matter or energy with the surrounding environment, the self-assembled state becomes "kinetically trapped" in the local minima for an endless duration. In either situation, these self-assemblies are not in equilibrium.

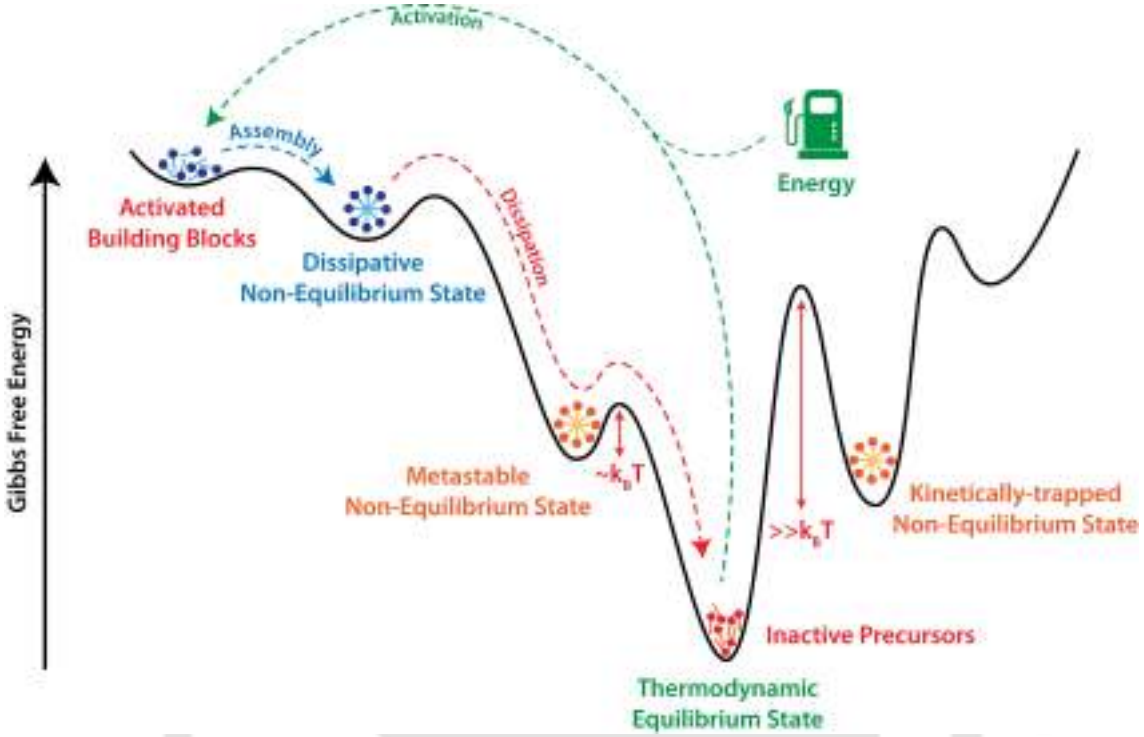

Figure 1.2. Thermodynamic regimes of equilibrium and non-equilibrium self-assembly processes. Adapted with permission from Ref. 5, 6.

In the third scenario, the self-assembled state occupies a higher energy state than the precursors and hence are out-of-equilibrium. This assembly process is also referred to as “dissipative or transient self-assembly”. In this case, the low energy monomers stay dormant and do not self-assemble, however when excited to a higher energy state, they spontaneously form self-assembled structures. These inactive building blocks can be assembled transiently under the influence of two orthogonally coupled chemical reactions. The activation reaction, exhibiting faster reaction kinetics, activates the precursor molecules by pushing them out-of-equilibrium into a high energy active building block state. The population of activated building blocks increases as the activation stage advances, and they eventually assemble into high energy and transient self-assembled structures. These transient structures, however, are thermodynamically labile and may be kept out-of-equilibrium by constant influx of energy. Once the energy source is depleted or as the activation reaction culminates, the deactivation reaction sets in and destabilizes the system. It is worth mentioning here that the non-equilibrium assemblies may disintegrate either because of their inherent thermodynamic instability or as a result of the deactivating reaction. The former is regarded as "dissipative," whilst the latter is referred to as "transient." Nonetheless, following deactivation, the activated building blocks revert back to their initial inactive state. The amount of energy (fuel)

supplied into the system, as well as the kinetics of the activation/deactivation phases, control the longevity of transient assemblies and allow for the time-gated modulation of emergent properties of the system.

1.3. Non-Equilibrium Processes in Nature

Life is a manifestation of out-of-equilibrium processes that are maintained at the expense of energy. Nature primarily employs chemical energy to trigger the thermodynamic actuation of inert cellular components into kinetically stable ensembles that carry out essential life-sustaining processes. The smallest organised unit of life, the cell, exploits out-of-equilibrium chemistry to perform vital tasks such as reproduction, metabolism, motility and communication with the external environment. The non-equilibrium nature of biological machinery endows them with excellent dynamicity and adaptivity. The continuous flow of energy in the form of nutrition keeps these systems functioning, and once the energy reserves are exhausted, the cells starve to death.

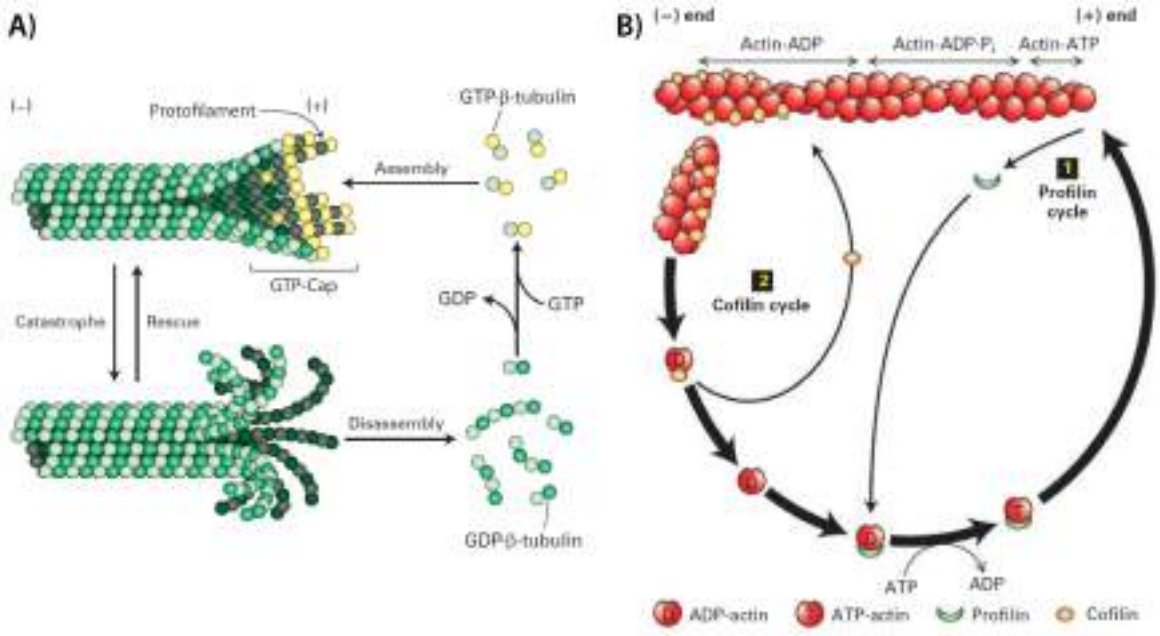

Figure 1.3. A) Tubulin GTPase cycle: GTP fuelled dissipative polymerization of microtubules. **B)** Monomer treadmilling: ATP fuelled dissipative growth of Actin filaments. Reproduced from Ref. 7.

From breathing to division, numerous non-equilibrium processes have been observed in nature. A well-known example of non-equilibrium assembly process in biological systems is the GTP fuelled dissipative polymerization of microtubules.[8] The rigid cores of organelles like axonemes and mitotic spindles are formed by microtubules, which are polymers of the tubulin protein.[9] Besides, they also act as tracks for motor proteins and provide structural integrity to the cells. Microtubules are nanotubular structures that grow by incorporating heterodimers of α- and ß-tubulin into their growing end. Above a certain threshold concentration of tubulin, microtubules spontaneously incorporate tubulin units in the polymeric structure (Figure 1.3A). However, below the threshold

concentration, they display an intriguing switch-like behaviour known as “dynamic instability”, where they abruptly switch between phases of growth and shrinking.[10] Head-to-tail interactions between αß-tubulin heterodimers generate elongated structures known as protofilaments. Microtubules are formed by lateral associations of these protofilaments. The longitudinal arrangement of tubulin heterodimers in the protofilaments causes the microtubules to have one end (-) with the α-subunits exposed, and the other end (+) with the ß-subunits exposed.

The assembly and disassembly of microtubules are controlled by guanosine triphosphate (GTP). Both the α and ß-tubulin monomers can bind with GTP but their binding sites have stark differences. The α-tubulin binding site (N-site) is buried at the juncture of α- and ß-tubulin, where the bound GTP is neither exchangeable nor hydrolysable. In contrast, the binding site (E-site) in ß-tubulin is exposed. Again, the E-site of free and polymerized tubulin show different properties. GDP bound free tubulin effectively exchanges GDP with GTP, which in fact, initiates the microtubule formation. GTP-tubulin adds to the (+) - end of developing microtubules through a thermodynamically favourable route. Following binding, kinked GTP-tubulin dimers are forced into the straight form, and GTP-tubulin dimers are spontaneously hydrolysed to GDP-tubulin dimers. The conversion of GTP to GDP increases strain in the microtubule lattice, but the tubular shape remains stable as long as the stabilising GTP cap is present at the (+)-end of the microtubule. As the amount of stabilising GTP-tubulin in the cap declines, the microtubule enters the "catastrophe" phase and eventually collapses.

Likewise, the ATP-driven self-assembly of the actin filaments presents another noteworthy example of non-equilibrium self-assembly in nature.[11] The actin filaments constitute the cytoskeletal networks that offer structural support to the cell wall and aid in cell movements. The formation of actin filaments (F-actin) begins with the activation of globular actin subunits (G-actin) by ATP, which results in the formation of small oligomers, which then organize into elongated filaments (Figure 1.3B). ATP-activated actin subunits are spontaneously added to the (+)-end of the filament and, at a slower rate, to the (-)-end. However, following self-assembly, the ATP bound to actin hydrolyses spontaneously into ADP and the resultant inactive actin subunits disassemble. The net effect is the spontaneous insertion of the active actin subunits to the (+)-end and the dissociation of the inactive subunits from the (-)-end. This is termed as monomer treadmilling.[12] As the concentration of active G-actin units decline, the dissipation phase predominates and the actin filament collapses.

In addition to these, many other processes, including the templated self-assembly of viral capsids,[13-15] enzyme-regulated reversible activation and deactivation of motor proteins during muscle contractions,[16] unidirectional motion of kinesin for cargo transport,[17] and numerous signal

transduction pathways,[18, 19] invariably follow non-equilibrium thermodynamics to accomplish their tasks.

1.4. Designing Transient Reaction Networks

Over the last decade or so, supramolecular chemists throughout the world have been inspired by both covalent and non-covalent modification strategies found in nature to construct artificial reaction cycles for regulating assembly and disassembly processes. Several studies have been published that use biological components such as enzymes[20-24], living cells[25, 26], and DNA[27, 28], as well as abiotic triggers such as redox reactions,[29, 30] and temporary pH changes[31] to generate non-equilibrium states. These investigations have revealed unique phenomena, wherein transient gels, vesicles, nanoreactors, etc.,[21, 30, 32-39] which defy the thermodynamic rules followed by conventional supramolecular systems, are produced by the use of supramolecular oscillations between activated and deactivated states.

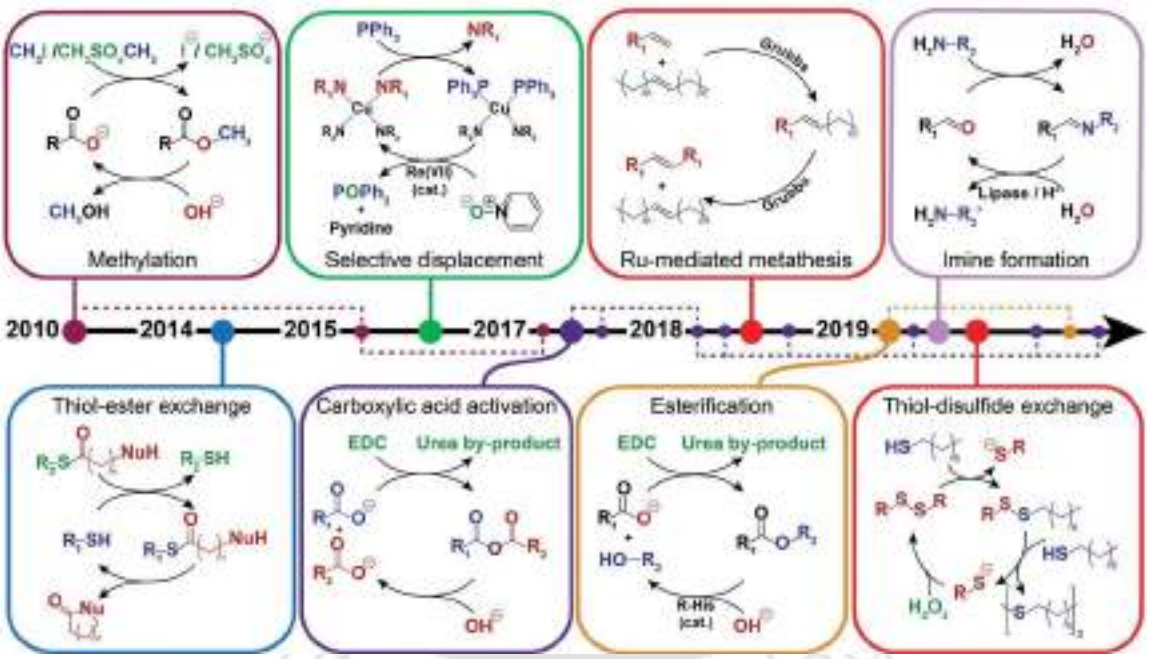

Figure 1.4. Timeline of chemical reaction cycles developed so far that have been used to control the assembly and disassembly of supramolecular structures. Reproduced with permission from Ref. 40.

A wide range of chemical reaction networks developed over the years for designing transient self-assembling systems are summarised in Figure 1.4.[40] The chemical reactions outlined above serve to thermodynamically activate the precursor molecules and propagate the otherwise thermodynamically unfavourable self-assembly process via a high energy kinetic pathway. Energy dissipation may occur via two separate paths following the formation of self-assembled structures. In the first case, the high energy self-assembled structure may breakdown to their original form due to the intrinsic instability of the activated state under the given environmental conditions. In such cases, the solvent molecules mostly drive the degradation of active building blocks to inactive

precursors. These transitory processes are referred to as "dissipative self-assembly" because they dissipate energy and return to a low energy state on their own and without any external intervention. In the second case, a competitive and particularly slow backward deactivation reaction is necessary to trigger the breakdown of the formed structure. These systems tend to retain their self-assembled structure in the absence of the backward reaction. As the disassembly process is directed by reaction conditions rather than intrinsic molecular instability, these processes are referred to as "transient self-assembly under non-equilibrium conditions." The following section provide a comprehensive assessment of the progress made thus far in the design and development of out-of-equilibrium systems employing the aforementioned strategies.

1.4.1. Dissipative Assembly

As the name suggests, the self-assembled structures in this case are composed of metastable building blocks which autonomously dissipate in the absence of the fuel and without the need of a deactivating agent. These metastable species are thermodynamically unstable and are maintained out-of-equilibrium at the expense of persistent energy supply. In most cases, the solvent initially promotes the self-assembly of the active self-assembling species, but eventually causes their deactivation, endowing them with metastable attributes. A variety of chemical agents have been identified which transiently generate activated building blocks from inactive precursors in water and allow the creation of self-dissipating self-assemblies. The following sections provide a succinct description of the advances made in this direction.

1.4.1.1. Self-Hydrolysing Chemical Bonds

A distinct class of dissipative self-assembly processes make use of transient chemical bonds that are generated upon the addition of a chemical fuel and subsequently hydrolysed under the same reaction conditions, regenerating the precursors. This approach gave rise to the notion of dissipative self-assembly in 2010, when van Esch et al. employed methyl iodide (MeI) in the presence of hydroxide ions under alkaline conditions to produce transient, metastable ester linkages.[41] By employing MeI as the fuel for the methylation reaction, they were able to shield the negative charges of the dianionic DBC (N,N'-dibenzoyl-l-cystine) molecule, and create a supramolecular hydrogel (Figure 1.5A). The hydrogel, however, dissolved shortly after due to hydrolysis of the ester bonds under alkaline conditions. In a subsequent investigation, they obtained similar results using dimethyl sulphate (DMS) as the alkylating agent, but with substantially faster reaction kinetics.[38] Boekhoven et al. used carbodiimides, especially EDC (1-ethyl-3-(3-dimethylaminopropyl)-carbodiimide), as the chemical fuel to produce similar shielding and charge-neutralization response (Figure 1.5B). The precursors used in this scenario are non-assembling dicarboxylates that are activated for assembly upon the formation of relatively hydrophobic and metastable anhydrides.[42]

When the EDC in the system is depleted, the anhydrides hydrolyse back to their inactive diacid state. The carbodiimide chemistry has been extensively utilised to stimulate the assembly of a range of C-terminal aspartic/glutamic acid containing non-assembling peptide precursors into a variety of autonomously forming and degrading supramolecular ensembles.[43] The self-assembly pathway and the kinetics of activation/deactivation reaction in these systems is predominantly determined by the molecular design of the precursors[44] and degree of organisation of the self-assembled structures.[45] The charge-neutralization feature of EDC-powered systems has been used on many occasions to reversibly modulate the overall charge of multivalent peptide sequences, prompting the transient formation of active droplets and coacervates.[46-48] Hartley et al. revealed that EDC can also be utilised as a transient cross-linking agent and can cyclize oligo(ethylene glycol) diacids into transient crown ether analogues (Figure 1.5C).[49] Later this strategy was used to transiently cross-link carboxylic acid containing polymeric as well as monomeric building blocks in order to induce transient hydrogelation.[50-52]

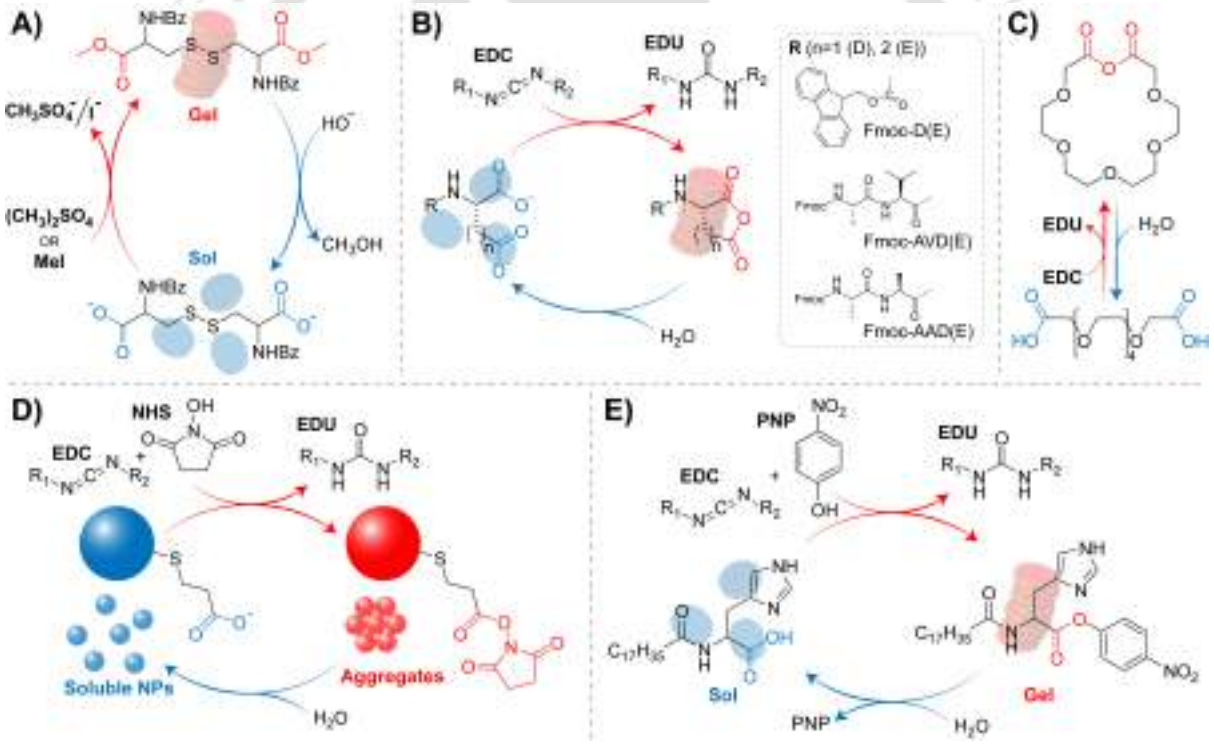

Figure 1.5. **A)** DMS/MeI fuelled transient hydrogelation of N,N'-dibenzoyl-l-cystine, **B)** EDC fuelled dissipative assembly of peptides, **C)** EDC fuelled dissipative formation of crown ether, **D)** Dissipative assembly of nanoparticles (NPs) triggered by EDC fuelled formation of transient NHS esters, **E)** EDC fuelled transient p-nitrophenolate ester hydrogel that dissipates following a cooperative ester hydrolysis reaction.

In addition to producing unstable anhydrides, the carbodiimide hydration reaction has also been investigated for producing unstable ester derivatives. Using N-hydroxysuccinimide (NHS) in combination with EDC, Boekhoven et al. transiently capped the negatively charged carboxylate units on the surface of gold and silica nanoparticles through the formation of corresponding NHS-

esters (Figure 1.5D).[53] The charge shielding resulted in the aggregation of the otherwise soluble nanoparticles, but as the NHS-esters are only feebly stable, they were slowly hydrolysed and the assembly dispersed. It is worth mentioning that NHS-esters are more stable than anhydrides and allow easy manipulation of reaction kinetics and lifetime of self-assembled state. Das et al. employed p-nitrophenol to produce esters via EDC coupling (Figure 1.5E).[35] In this study, they used an amphiphilic histidine containing carboxylic acid in which the histidine moiety initially acts as an internal base to help in the synthesis of p-nitrophenol ester derivatives. The resultant ester derivatives co-assemble to produce a supramolecular gel. Later, as the EDC is consumed, histidine assumes its hydrolase mimicking activity and breaks down the ester linkages, causing the hydrogel to dissolve. This action is reminiscent to the disintegration of tubulin microtubules in biology. All these studies substantiate the fact that simple molecules like MeI, DMS and EDC have the ability to drive the dissipative assembly of a diverse set of precursor molecules. Furthermore, combining these reagents with other chemical reactions may open up a world of possibilities for building transient structures with advanced functional attributes.

1.4.1.2. Autonomous Decarboxylation of Carboxylic Acids

Chemical agents that produce predictable alterations in the pH of a solution provide an elegant method for manipulating the pH sensitive characteristics of molecular assemblies. Some activated carboxylic acids have been found to serve this job extremely efficiently, allowing a cyclic basic-acidic-basic pH shift to be produced with a single chemical fuel. In general, when these acids (RCOOH) are added to a basic solution, the pH of the solution drops rapidly. The unstable carboxylate ions ($RCOO^-$) produced in this process are decarboxylated to produce a very strong carbanion base (R^-). These carbanions then absorb protons from the solution, shifting the pH back to the alkaline range.[54] The first example of an activated carboxylic acid is 2-cyano-2-phenylpropanoic acid. Di Stefano et al. were the first to exploit this to autonomously switch a phenanthroline-based [2]catenane between an "ON" and "OFF" state via transient protonation-deprotonation of the system (Figure 1.6A).[55] In brief, when 2-cyano-2-phenylpropanoic acid is added to the system, the neutral catenand (the "OFF" state) is protonated and transformed to the catenate (the "ON" state). Following decarboxylation, reverse proton transfer from the catenate to the carbanion restores the catenane's "OFF" state. They also demonstrated that para-substituting 2-cyano-2-arylpropanoic acid with different electron donating and electron withdrawing substituents allow the lifetime of the protonation-deprotonations cycles to be varied from minutes to days.[56] They further availed the variable kinetics of differently substituted 2-cyano-2-arylpropanoic acids to control the shuttling kinetics of a crown-ether based wheel along the axel of a pH-sensitive bistable rotaxane.[57] Schmittel et al. also employed 2-cyano-2-arylpropanoic acid as a chemical fuel to

transiently establish logic circuits and tune emissive properties of interlocked and metal coordinated molecular devices.[58, 59]

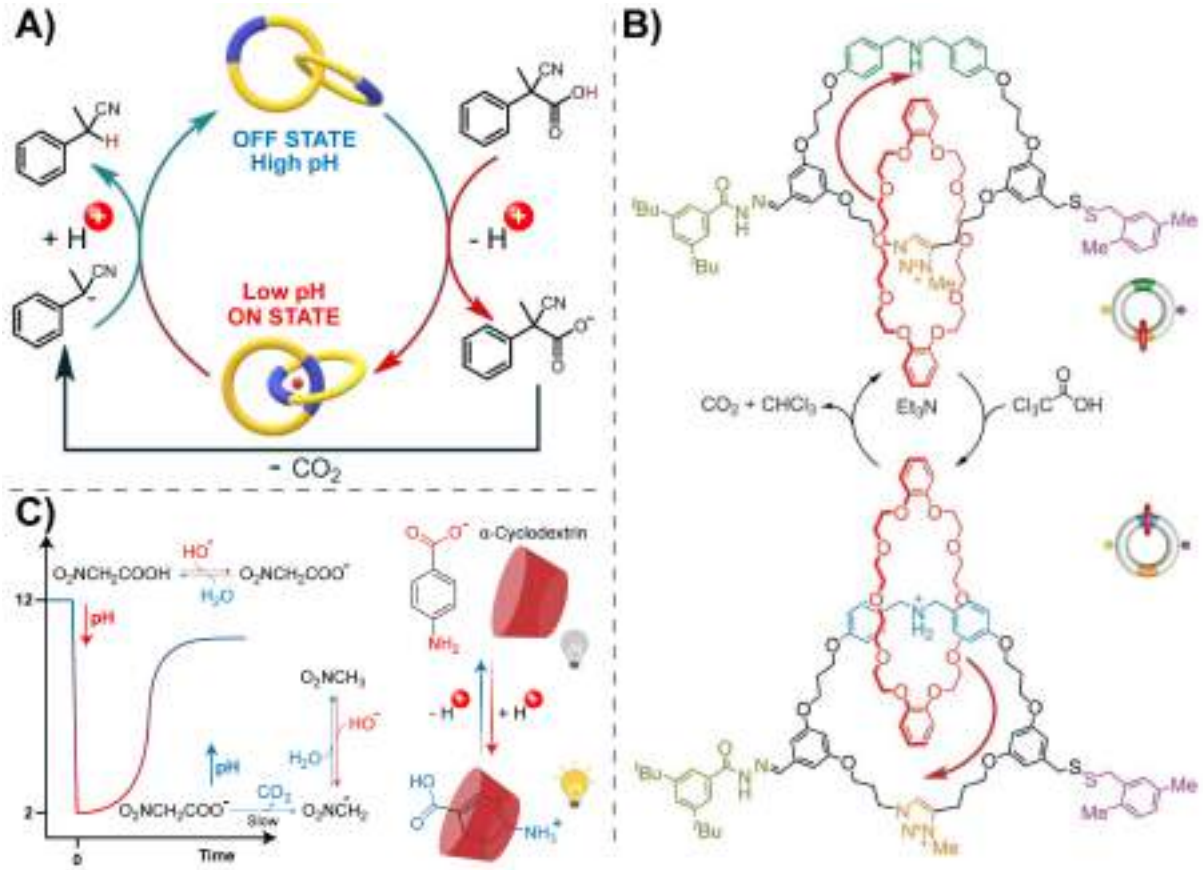

Figure 1.6. **A)** 2-cyano-2-phenylpropanoic acid fuelled transient back and forth motion of a phenanthroline-based [2]catenane, **B)** Trichloroacetic acid fuelled transient operation of a catenane-based molecular rotor, **C)** pH dependent host-guest interaction between α-cyclodextrin and p-aminobenzoic acid. Reproduced with permission from Ref. 54, 60.

Trichloroacetic acid is another activated carboxylic acid that was first utilised by Leigh et al. to demonstrate unidirectional motion in a catenane-based molecular rotor (Figure 1.6B).[60] They constructed a molecular rotor with a pH sensitive dibenzylammonium station and a triazolium station, both guarded by an acid-labile hydrazone-based blocker and a base-labile disulphide-based blocker. When trichloroacetic acid is added as a fuel, the crown-ether based wheel shuttles to the dibenzylammonium station due to scission of the hydrazone blocker and protonation of the dibenzylammonium site. Thereafter, as the pH of the system returns to the alkaline range, the hydrazone blockers are fixed in place while the disulphide blocker is cleaved. Concurrently, the dibenzylammonium group is deprotonated, causing the wheel to return to its initial triazolium position. In another report, using the same principle, they showed fuel-induced transient shuttling and catalysis using a rotaxane based molecular machine.[61] The fact that trichloroacetic acid generates volatile by-products like CO_2 and $CHCl_3$, it significantly helps with waste management. As trichloroacetic acid is easily cleared out of the system, Kim et al. were able to produce transient

single crystals of a cucurbituril-based host-guest complex with minimum poisoning and excellent repeatability across several cycles.[62] Tribromoacetic acid has recently been discovered to be an alternative to trichloroacetic acid and has been employed for the transient assembly of covalent cages capable of transiently hosting guest molecules.[63] Nitroacetic acid is another activated carboxylic acid that permits the pH of a solution to be shifted from high to low and back to pH ~9.[64] The starting pH and duration of the pH cycle may be readily modulated depending on the concentration of NaOH in the system and the amount of fuel (i.e., Nitroacetic acid) injected. As a proof of concept, this new pH clock was used to control the transient pH dependent host-guest interaction between α-cyclodextrin and p-aminobenzoic acid (Figure 1.6C). All of these studies suggest that, due to their autonomous mode of proton donation and reabsorption, activated carboxylic acids offer a simple technique for imbuing transitory properties in pH sensitive systems.

1.4.1.3. Light/Sound Driven Structural Remodelling

Light has numerous benefits as a fuel for dissipative self-assembly since it is a clean and abundant source of energy, it provides great spatiotemporal resolution, it can be provided in many wavelengths, and, most significantly, it generates minimal waste in the system.[65] There are two fundamental approaches to utilise light as a fuel. First, light energy is used to elicit a chemical response in the system, which indirectly drives the self-assembly process in photo-irresponsive materials. A notable example of light energy to chemical energy transformation is presented by the photoacid, protonated merocyanine (MCH^+). When exposed to blue light, MCH^+ undergoes ring-closing isomerization to generate spiropyran, releasing a proton.[66] The spiropyran form, however, is short lived and it spontaneously reverts to the MCH^+ state, reabsorbing the proton. Klajn et al. utilised this unique behaviour of spiropyran to trigger transient self-assembly of carboxylic acid functionalized gold nanoparticles (AuNPs). In methanol, strong hydrogen bonding interactions between the terminal COOH groups causes the AuNPs to stay in aggregated form (Figure 1.7A).[67] In presence of MCH^+, irradiation with blue light causes acidification of the medium and consequently disengages the hydrogen-bonded bridges between the AuNPs, causing dissolution of the AuNPs into a stable suspension. In the absence of blue light, thermal relaxation of spiropyran to MCH^+ induces reabsorption of protons from the medium and reassembly of the AuNPs. Later, they validated the applicability of this concept in aqueous media as well, wherein, using a water-soluble spiropyran derivative as the photoacid, they demonstrated AuNP aggregation upon irradiation and subsequent disassembly in the dark.[68] Many other research groups employed spiropyran's photoacidic feature to demonstrate photo-controlled transient shuttling in a molecular shuttle,[69] assembly of cyclic peptides into supramolecular tubules,[70] and light-triggered transient photo-deformation of emissive self-assemblies.[71]

In the second approach to using light as a fuel, light is used to trigger a transient structural change in the molecular building blocks. In this context, Parquette et al. employed spiropyran not as a photoacid generator but as a component of their gelator molecules (Figure 1.7B).[72] They developed a peptide-spiropyran conjugate wherein the positively charged merocyanine form inhibits hydrogel formation in the dark. When exposed to visible light, the conversion to neutral spiropyran form causes the formation of transient nanofiber gel. In absence of light, as spiropyran reverts to the merocyanine state, the gel disintegrates. Azobenzene is another well-known photo-responsive molecule that undergoes reversible cis-trans isomerization when exposed to light. Huck et al. employed azobenzene to create a variety of photo-switchable enzyme inhibitors (PIs). They inserted enzyme inhibitory modules (denoted as W, meaning enzyme inhibiting Warhead) at the terminals of several azobenzene derivatives and showed that the trans-azobenzene PI competitively binds to the active site of the enzyme and inhibits its activity under visible light (Figure 1.7C). When exposed to UV light, the cis-azobenzene PIs are drawn out of the active site due to a lack of conformational parity with the enzyme site, and the enzymes become active. A microfluidic flow arrangement was employed to induce out-of-equilibrium conditions, with chemicals and enzymes continually supplied and withdrawn from the system. Using this method, they successfully controlled the catalytic activity of α-chymotrypsin and trypsin.[73, 74]

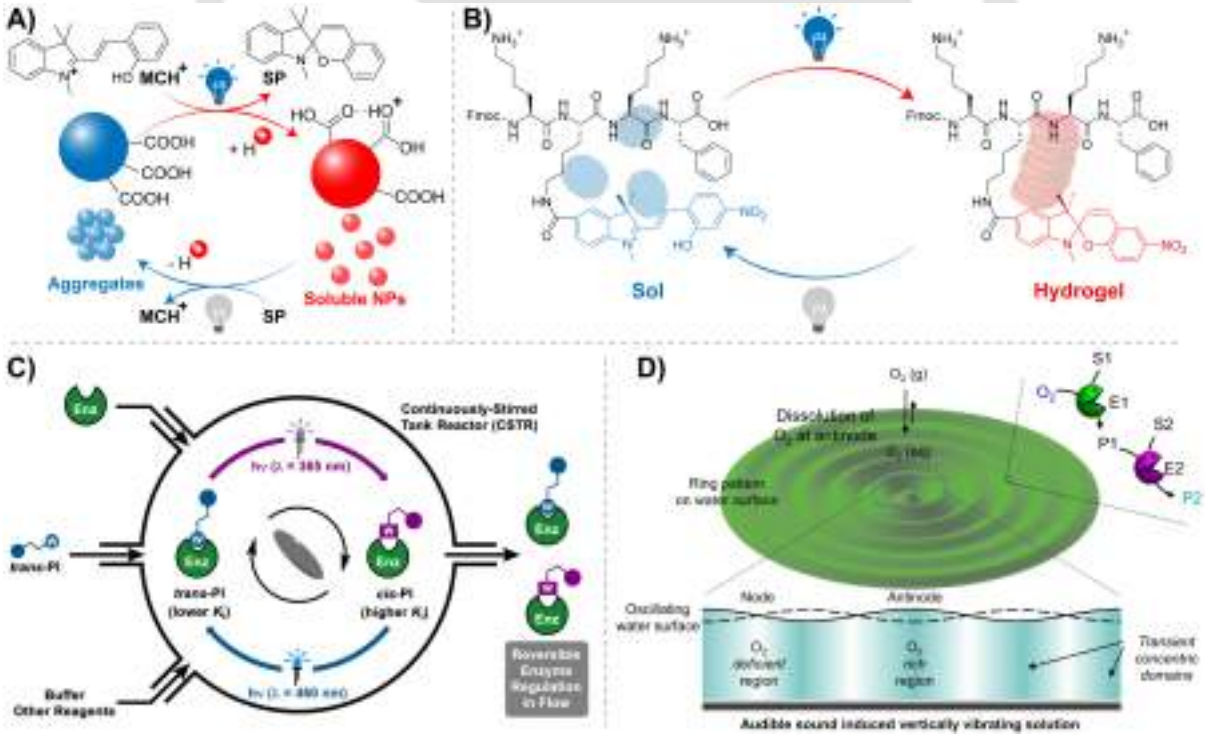

Figure 1.7. **A)** Light controlled transient assembly of non-photoresponsive NPs, **B)** Light triggered dissipative assembly of a peptide hydrogel, **C)** Light controlled transient regulation of enzyme activity, **D)** Sound controlled generation of transient O_2 rich domains and spatiotemporal regulation of a GOx-HRP bienzymatic cascade. Reproduced with permission from Ref. 73, 75.

Among other stimuli, Hwang, Mukhopadhyay, and Kim et al. chose audible sound as a trigger to produce out-of-equilibrium self-assembly. They created standing waves of predictable and controllable patterns on the surface of water using low-frequency audible sound.[76] In these standing waves, the regions with the lowest vibrations (nodes) have low gas dissolution, while the regions with the highest vibrations (antinodes) have relatively high gas dissolution (Figure 1.7D). Thus, by regulating the dissolution of gases such as O_2 and CO_2 at the nodes and antinodes, transient spatiotemporal zones with discrete redox and pH-specific features were formed in the bulk solution. These transient domains maintained their boundary features for a set period of time, allowing pH and redox chemical reactions to be carried out with excellent spatiotemporal control. In the first example, they demonstrated varied rates of oxidation of methyl viologen radical cation (produced via reduction of methyl viologen using sodium dithionite) at discrete spatiotemporal zones of the solution using O_2 as the diffusing gas. They also demonstrated formation of spatially distinct pH zones utilising CO_2 as the diffusing gas and bromothymol blue (BTB) as the pH sensitive probe. Later, utilising aerial O_2 as a substrate, they established a GOx-HRP bienzymatic cascade in the spatiotemporal domains.[75] In another study, they demonstrated complex mechanical functions such as maze solving and cargo movement utilising a combination of light and sound as stimulus.[77] Thus, in comparison to chemical fuelling agents, physical stimuli like light and sound often offer several advantages. They are extremely benign, give excellent spatiotemporal control, and produce no waste. As a result, they are a superior alternative for developing future out-of-equilibrium systems.

1.4.2. Transient Assembly Under Non-Equilibrium Conditions

A well-established approach for imbuing transient features in synthetic precursor molecules is to strategically integrate stimuli responsive functionalities in the system that may aid in inducing sequential assembly and then disassembly under the simultaneous action of two orthogonally related chemical stimuli. The following sections provide a concise overview of the various activator-deactivator pairings that produce transient alterations in the assembly process.

1.4.2.1. pH Controlled Transient Assembly

The pH of the medium plays a decisive role in guiding the assembly of pH responsive building blocks in solution. To control the lifetime of assemblies generated as a function of pH, Walther et al. developed a generic concept of using an alkaline buffer (TRIS) as a fast promoter and different types of lactones/ester as the dormant deactivator (DD) (Figure 1.8A).[31] They strategically chose three distinct self-assembling systems, all of which assemble in the alkaline regime: a polymeric micelle (Figure 1.8B),[78] a peptide gelator (Figure 1,8C)[79] and, Au-NPs functionalized with a phenol ligand (Figure 1.8D).[80] and Upon addition of a combination of the promoter and the DD,

the rapid jump in pH triggers the self-assembly process. Concurrently, the DDs undergo hydrolysis at alkaline pH and produce acids that function as the active deactivator. As dormant deactivators, three distinct lactones/ester were used: gluconic acid δ-lactone (δ-GL), methyl formate (MF), and ε-caprolactone (ε-CL). It is worth mentioning that lactones with strained rings show higher rate of hydrolysis in order to get rid of the strain. Thus, the lactones/ester displayed varying rates of hydrolysis and allowed the lifespan of the self-assemblies to be tuned from minutes (δ-GL) to hours (MF), and even days (ε-CL).

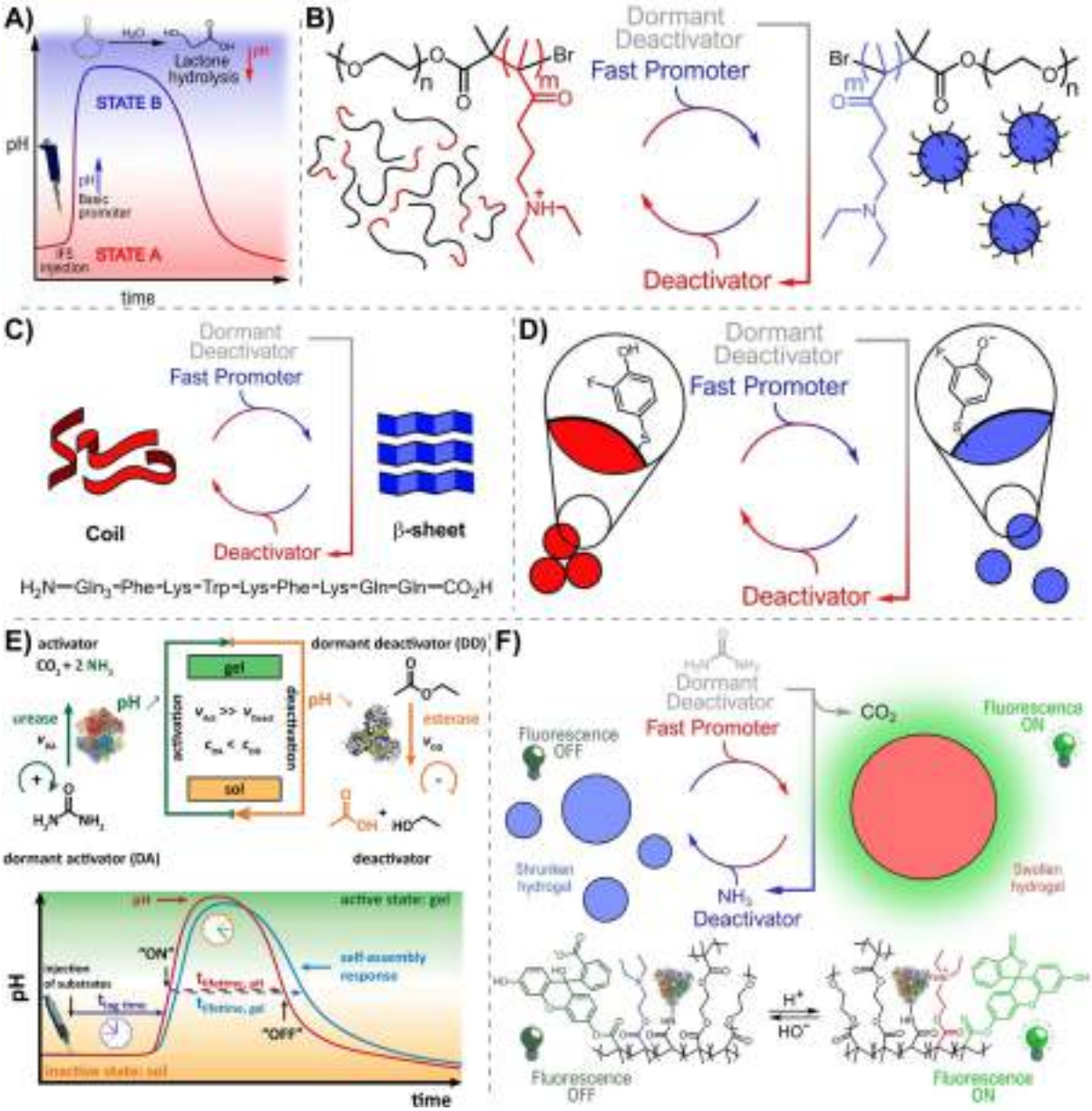

Figure 1.8. A) Transient pH variations using alkaline buffer as a promoter and lactones as the dormant deactivator, and application of this pH cycle for transient assembly of **B)** Block copolymer micelles, **C)** Peptide hydrogel, and **D)** AuNPs, in the alkaline region. **E)** Programming transient pH changes using a bienzymatic reaction network, **F)** Acidic buffer/Urea-Urease pH cycle controlled transient breathing and luminescence of a polymersome. Reproduced with permission from Ref. 23, 54.

In an alternative approach, they designed enzymatic logic gates utilising invertase-glucose oxidase and ß-galactosidase-glucose oxidase enzyme couples which mediate an enzymatic disaccharide-to-monosaccharide-to-sugar acid reaction cascade.[81] By combining a sequential TRIS buffer powered YES gate and the enzymatic cascade powered NAND gate, they effectively modulated the lifespan of the transient pH regime from minutes to days. Apart from sucrose or glucose as chemical fuels, they also used everyday items such as soda and baking soda as promoters, and sucrose from sugar beet syrup and lactose from milk as fuelling agents. To gain finer control over the pH modulations, in another study, they employed an antagonistic enzyme couple, urease and esterase, for generating ammonia and acetic acid from urea and ethyl acetate, respectively (Figure 1.8E).[23] They started the pH cycle at an acidic pH, which keeps both the chemical fuels dormant. Initially, slow generation of ammonia takes place (lag phase) owing to the low activity of urease at acidic pH. After that, when the pH becomes slightly acidic/neutral, the activity of urease increases and a rapid jump in pH (ON phase) is observed. Thereafter, at alkaline pH, the activity of esterase increases and it lowers the pH back to the acidic regime, completing the pH cycle. By varying the buffer strength and the ratio of the enzymes and the substrates, they precisely regulated the lag time and lifespan of the pH cycles and also showed highly programmable transient assembly of a DNA based hydrogel.

Later, to generate transient assemblies in the acidic regime, Walther's group coupled a fast promoter (acidic buffer) with the slow biocatalytic transformation of urea (DD) to ammonia (active deactivator) using urease.[82] By varying the ratio of the activator and the deactivator, they effectively programmed the lifetime of a transiently formed peptide hydrogel (Fmoc-Leu-Gly-OH dipeptide)[83] across orders of magnitude of time. In a following report, they coupled a pH-responsive block copolymer photonic gel with this urease-based enzymatic switch and demonstrated advanced autonomous features such as transient memories, photonic patterning, and remotely controlled signal propagation.[84] van Hest et al. employed the same pH cycle to demonstrate transient breathing behaviour with concurrent change of fluorescence intensity in a fluorescein tethered hybrid microgel (Figure 1.8F).[85] At the transient acidic pH, protonation of the polymer and ring-opening of the lactone moiety of fluorescein resulted in swollen microgels with strong fluorescence intensity. However, as the pH dropped to the alkaline range, deprotonation of the polymer and lactone ring-closing produced shrunken microgels with quenched fluorescence intensity.

Adams et al. described the transient hydrogelation of a minimalistic cationic amphiphile, mono-Fmoc ethylene diamine hydrochloride, using a combination of Urea-Urease mediated fast pH rise and the slow generation of formic acid through hydrolysis of methyl formate.[86] The initial lag time, longevity, and mechanical characteristics of the transient hydrogels could all be easily

regulated by varying the urease concentration in the system and the activator/deactivator ratio. In a subsequent work, they showed that, in addition to generating transient assemblies, the slow pH variations during the pH cycle also aid in accessing certain kinetically stable states that would otherwise be inaccessible via thermodynamic routes. They demonstrated that when urea is added to a solution containing a peptide hydrogelator, Nap-FF-OH, urease and Ca^{2+} ions, initially a hydrogel is generated at an acidic pH due to protonation of terminal acid groups of the peptide gelator.[87] The acidic groups begin to deprotonate as the pH gradually rises, which causes the hydrogel to disintegrate. Interestingly, as the pH rises further, the Ca^{2+} ions present in the solution bind two peptide building units together, resulting in a refined and mechanically stronger hydrogel. Such a gel-sol-gel transition is extremely unusual and cannot be obtained by directly adding a base such as NaOH. All these studies support the idea that by carefully selecting acid and base producing chemical/enzymatic processes, one may simply install a feedback mechanism into a pH responsive self-assembling system and build kinetically stable assemblies with tuneable lifespan and emergent features.

1.4.2.2. Redox Triggered Transient Assembly

Amongst the various approaches adopted for generating transient self-assembly, redox fuelled approaches are particularly appealing because they reversibly alter the building blocks at the molecular level and help in controlled association/dissociation of various disulphide linked molecules, charge-transfer complexes, and chromophoric substrates.[88, 89] In this regard, Hermans et al. designed perylenediimide (PDI) based supramolecular fibres which show redox responsive collapse and growth cycles under the influence of a redox cycle driven by sodium dithionite ($Na_2S_2O_4$, reducing agent) and aerial oxygen (oxidising agent) (Figure 1.9A).[29] The neutral PDI derivative (PDI-1), under thermodynamic control, form extended supramolecular fibres which gradually precipitate out of the solution. However, when $Na_2S_2O_4$ is added, the PDI derivatives are reduced to their dianionic form ($PDI\text{-}1^{2-}$), which destabilises the fibres due to their strong repulsive interactions. Since the anionic species are unstable and have short lifetime, they eventually return to their neutral state by aerial oxidation, restoring the fibrillar structure. Later, George et al. described transient reconfiguration of supramolecular organisation with an accompanying shift in fluorescence colour using the same redox cycle.[90] They used a core-substituted naphthalene diimide (cNDIs) derivative that forms green emitting vesicles. Upon reduction with $Na_2S_2O_4$, the resulting dianionic species are reconfigured into sheet-like structures. Simultaneously, the fluorescence colour shifts from green to red. After $Na_2S_2O_4$ is consumed, the sheets reconfigure back to their vesicular state and the fluorescence colour changes back to green. The lifetimes and decay rates of these assemblies may be efficiently controlled by altering the dose of $Na_2S_2O_4$. In another work, to

gain control over the dissipation step, they coupled glucose oxidase catalysed H_2O_2 generation (oxidation) with the $Na_2S_2O_4$ facilitated reduction process.[91] They designed an amphiphilic foldamer, PN–VN, consisting of an electron-rich pyranine unit and an electron deficient viologen unit (Figure 1.9B). As a result of charge-transfer (CT) interaction between the pyranine and viologen units, the molecule assumes a folded state and assembles into vesicles. When subjected to the redox cycle, reduction of viologen by $Na_2S_2O_4$ (SDT) disrupts CT interactions in the molecule and the transiently generated unfolded conformation reconfigures into sheet-like morphology. The transient existence of the sheets could be effectively regulated by controlling the ratio of $Na_2S_2O_4$, glucose and glucose oxidase. Aerial oxidation also produced similar results but with a slower decay kinetics.

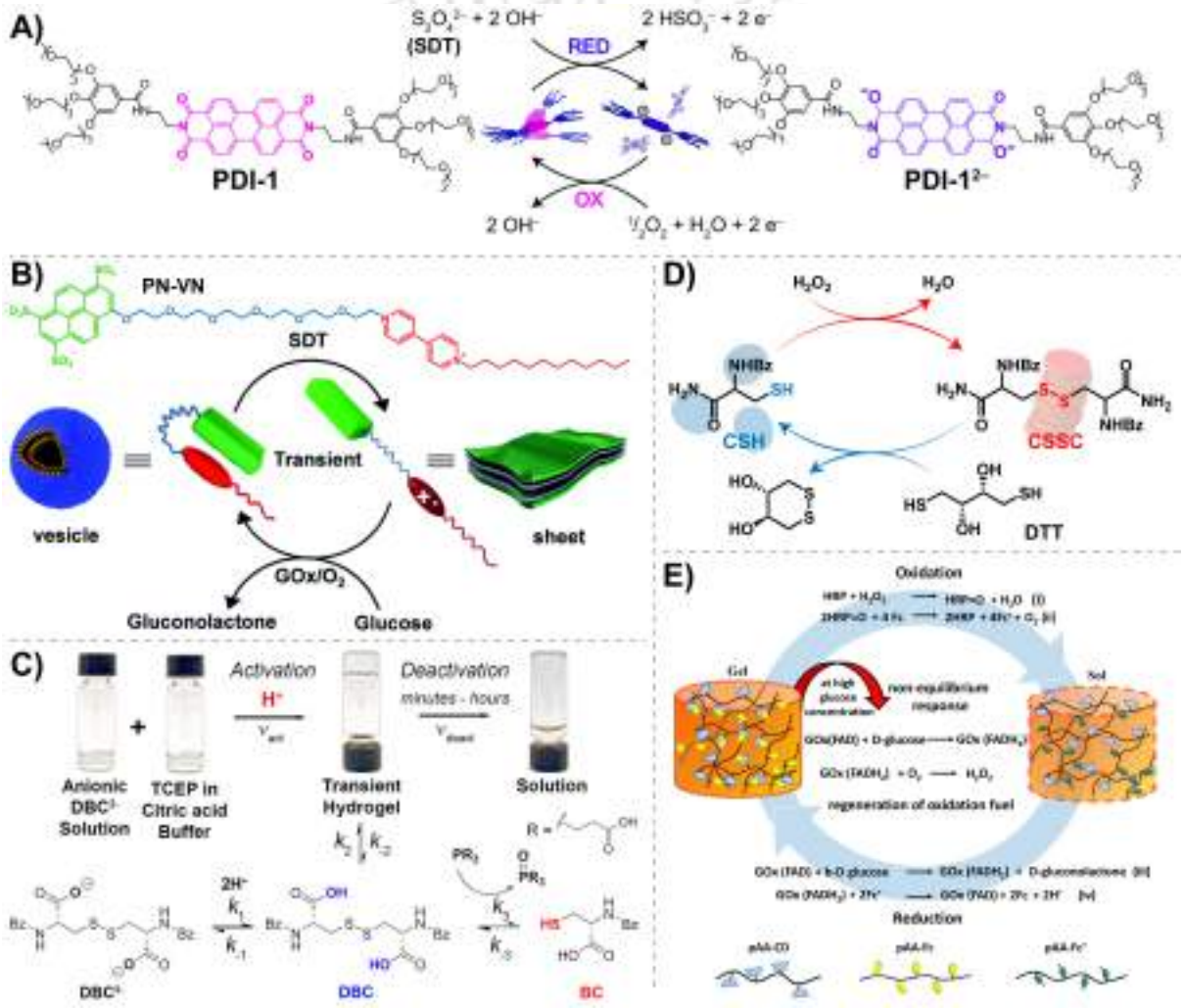

Figure 1.9. A) Redox controlled transient disassembly-assembly of PDI based supramolecular fibers, **B)** Redox responsive transient conformational switching of PN-VN foldamer, **C)** Citric acid buffer/TCEP guided transient hydrogelation of DBC, **D)** Generic concept for transient assembly of disulphide containing hydrogelators, **E)** Glucose regulated transient assembly/disassembly of a polymeric hydrogel. Reproduced with permission from Ref. 29, 30, 91, 92.

Disulphide bonds are dynamic covalent bonds that form spontaneously in an oxidising environment and cleave in a reducing environment.[93-95] Thordarson et al. used disulphide chemistry

for the first time to achieve transient hydrogelation of a well-known gelator, N,N'-dibenzoyl-l-cystine (DBC).[30] DBC in anionic form (DBC^{2-}) is soluble and shows no gelation (Figure 1.9C). To induce transient gelation of anionic DBC, TCEP dissolved in citric acid buffer was used as a fuel. Protonation of the carboxylic acid units by the acidic buffer resulted in immediate hydrogelation. However, TCEP, a disulphide breaking agent, gradually hydrolysed the disulphide bonds, eventually dissipating the hydrogel. Guan et al. proposed a generic kinetically controlled reaction network for controlling the transient assembly of disulphide-based hydrogelators (Figure 1.9D).[96] They used a dilute solution of H_2O_2 as the oxidant and a relatively concentrated solution of dithiothreitol (DTT) as the reductant. Both H_2O_2 and DTT activity were found to be pH sensitive, with the latter being more active at higher pH and less active at lower pH. Thus, a slightly acidic pH (5.5-6.0) was chosen to achieve operable lifetimes. By varying the concentrations of the redox-active fuels, the H_2O_2-DTT couple generated redox gradients of tuneable lifetimes and facilitated the transient hydrogelation of a rather simple cysteine disulphide based hydrogelator (CSSC). Ferrocene is another redox sensitive molecule that exhibits redox responsive switching of oxidation states and has been widely used in the development of a variety of smart materials.[97, 98] Das et al. exploited ferrocene's unique redox sensitive property to create a fatty acid-based hydrogel that is triggered for gelation when a ferrocenylated-base (Fc-NMe_2) is added as a counteraction.[99] Under an oxidising environment, ferrocene progressively oxidised, and the loss of ion pair interactions between Fc-NMe_2 and the fatty acid caused the gel network to disintegrate. Meanwhile, the transiently generated gel network entrapped hemin in its hydrophobic domains, permitting time-gated upregulation and downregulation of peroxidase-mimetic catalytic activity across multiple cycles. Ravoo et al. utilised the host-guest chemistry of ferrocene (Fc) and ß-cyclodextrin (ß-CD) to design a redox responsive hydrogel (Figure 1.9E).[92] When Fc is oxidized by HRP/H_2O_2, the positively charged oxidized ferrocene (Fc^+) dislodges out of the ß-CD cavity, disintegrating the hydrogel. However, when reduced by GOx/Glucose, Fc^+ reverts back to its neutral form (Fc) and the gel structure is restored. The biocatalytic intermediate, GOx[$FADH_2$], formed during the oxidation of glucose, interestingly plays a dual role here. It catalyses the conversion of Fc^+ to Fc at low glucose concentrations, causing a sol to gel transition. However, at higher glucose concentration, the excess GOx[$FADH_2$] generated converts aerial oxygen to H_2O_2, generating a non-equilibrium response and triggering autonomous gel to sol transition. As a result of the negative feedback response at high glucose concentrations, the redox responsive system was able to transition to a non-equilibrium system, and display autonomous assembly and disassembly of the hydrogel. In nutshell, as redox sensitive molecules show stringently different properties in their oxidised and reduced state, they offer a wide range of opportunities for the design and development of out-of-equilibrium autonomous self-assembly processes.

1.4.2.3. Enzyme Assisted Transient Assembly

Enzymes are known for their high substrate specificity and have been profusely employed to direct the assembly as well as disassembly of supramolecular structures in both physiological and abiotic environments. Ulijn et al. described the first example of enzyme-regulated transient assembly, in which both the transient assembly and subsequent disassembly stages were propagated by a single enzyme, α-chymotrypsin (Figure 1.10A).[20] It is a serine protease that preferentially cleaves peptide bonds containing hydrophobic residues such as tyrosine, tryptophan, and phenylalanine at the N-terminus. It can also catalyse the formation of amide bonds between a free amine group and an activated acyl donor via a kinetically favoured pathway. Thus, in the presence of α-chymotrypsin, a naphthalene-functionalized amino acid acyl donor (Nap-Y-OMe) underwent trans-acetylation reaction with an amino acid amide (X-NH_2; where X=L-tyrosine, L-phenylalanine, or L-leucine) to generate a self-assembling dipeptide amide Nap-YX-NH_2. After a short while, the peptide bonds were slowly hydrolysed by α-chymotrypsin itself, disintegrating the gel and regenerating the starting amino acid amide and the corresponding acid, Nap-Y-OH. It is worth mentioning that the peptide Nap-YF-NH_2, which has a comparatively low critical gelation concentration (CGC), formed thermodynamically stable gel. However, the peptides Nap-YY-NH_2 and Nap-YL-NH_2, exhibiting comparatively higher CGC, displayed non-equilibrium hydrogelation. This methodology was further extended by employing the methyl ester of aspartame (DF-OMe) as the acyl donor, and it was shown that the peptide sequence used intimately controls the kinetics and hence the lifespan of transient nanostructures.[100] Also, using fluorogenic 1,8-naphthalimide amino acid methyl esters as the acyl donating substrates allowed for in situ imaging of the transient assembly process.[101]

Adenosine triphosphate (ATP) is a fascinating biomolecule that has been employed as both a template and a fuel to control transitory self-assembly processes.[102] George et al. discovered that a zinc(II) dipicolylethylenediamine appended naphthalene diimide derivative (NDPA) attaches to the phosphate groups of ATP to form assemblies with P-helicity ((P)-NDPA-ADP), whereas binding to ADP results in M-helices ((M)-NDPA-ADP).[103] Using the complementarity of the two phosphoryl transferase enzymes, hexokinase (HK) and creatine phosphokinase (CPK), which consume and create ATP, respectively, they obtained temporal control over the transient interconversion of ATP to ADP and demonstrated transient switching of conformational helicity with modular control over lifespan and stereomutation rates (Figure 1.10B).[104] Later, using ATP in combination with an ATP hydrolysing enzyme, potato apyrase, they demonstrated fuel-mediated controlled nucleation, growth and subsequent decay of a chiral supramolecular polymer in a highly programmed manner.[24] The same approach was adopted by Schanze et al. to trigger the transient assembly of a

cationic water-soluble porphyrin derivative into chiral double-helical supramolecular fibers.[105] Das et al. also employed ATP as a fuel to promote the condensation of small polycationic peptides into coacervate droplets.[106] When an ATP-ase enzyme was present, these condensates also only lasted for a brief duration. Moreover, these coacervates could temporally entrap and boost the catalytic activity of cytochrome c (CytC), mimicking membraneless condensates of enzymatic proteins in biology.

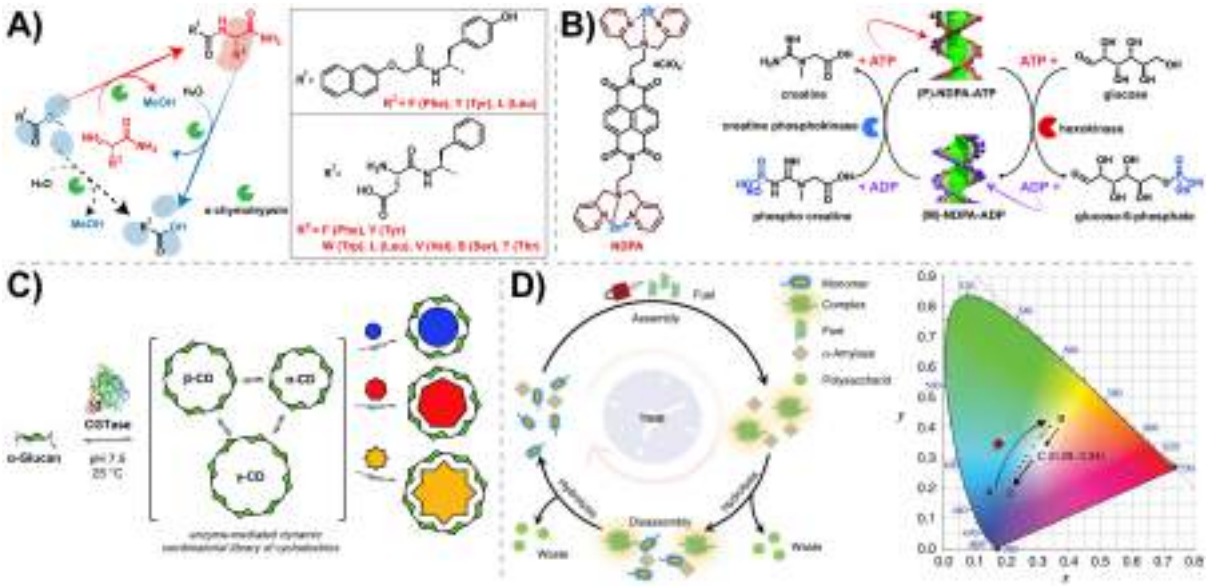

Figure 1.10. **A)** α-chymotrypsin catalysed non-equilibrium self-assembly, **B)** Bienzymatic cascade driven transient switching of supramolecular helicity, **C)** CGTase mediated transient formation/degradation of cyclodextrins, **D)** γ-CD/amylase driven transient assembly and the resultant multicolour fluorescence emission. Reproduced with permission from Ref. 107-109.

Cyclodextrins (CD), one of the most widely employed hosts, have been utilized extensively to create a range of self-assembled structures. Beeren et al. described for the first time an out-of-equilibrium technique for producing different types of CDs utilising cyclodextrin glucanotransferase (CGTase), a glycosyltransferase enzyme (Figure 1.10C).[108] It first catalyses the cyclization of linear-1,4-glucans into various types of CDs via a reversible pseudo-thermodynamic mechanism, and then causes irreversible hydrolysis of CDs, resulting in transitory behaviour. Furthermore, using different types of stimuli-responsive (pH[110] and light[111]) as well as non-responsive templates, they exquisitely tweaked the distribution of the various types of cyclodextrins and exclusively created either α, ß, or γ-CD with fine control and selectivity. Qu et al. created a pyrene-containing single fluorophore system in which the assembly state and resulting luminescence characteristics may be tuned by varying the concentration of γ-CD.[109] Thus, employing γ-CD as a fuel and α-amylase, a carbohydrate digesting enzyme, as a slow deactivator, they demonstrated dynamic changes of the assembly state and multicolour photoluminescence in a transitory manner (Figure 1.10D). Similarly, using α-CD as a hydrolysable host cum fuel and α-amylase as an enzymatic scavenger, Wang et al.

showed host-guest interactions mediated transient cross-linking and subsequent hydrogelation of Pluronic F127 micelles.[112] Furthermore, by varying the temperature and composition of the hydrogel, the lifespan of the sol-gel-sol transitions could be precisely tuned. All of these examples demonstrate that enzymes are exceptionally capable of changing the energy landscape of self-assembly processes, making them an attractive choice for the design of transient self-assembling systems.

1.5. Non-Equilibrium Assembly of Vesicles

Vesicles have extensively been employed in the creation of synthetic cells and protocell models to explore and imitate the biological functions of cells. Developing techniques and approaches to create transient vesicles may therefore get us closer to the notion of achieving life-like qualities in synthetic systems. Prins et al. described transient generation of vesicles using ATP as a chemical fuel.[21] Here, ATP acts as a multivalent anionic counterion which complexes with multiple cationic amphiphiles, C_{16}TACN·Zn^{2+}, through electrostatic interactions and results in the formation of the vesicles (Figure 1.11A). The lifespan of these vesicles is regulated by an ATP hydrolysing enzyme, potato apyrase, which slowly hydrolyses ATP, disrupting the multivalent interaction between ATP and the surfactants and causing the vesicles to disassemble. The apolar lipid compartments of the vesicles were used to catalyse a nucleophilic aromatic substitution reaction between two hydrophobic precursor molecules. The kinetics of this reaction and the amount of product formed is determined by the lifespan of the out-of-equilibrium state, which in turn depends on the concentrations of ATP and potato apyrase in the system. The cationic amphiphile, C_{16}TACN·Zn^{2+}, also possesses the ability to cleave phosphodiester bonds. To exploit this catalytic activity of C_{16}TACN·Zn^{2+} for transient assembly, in another study, 2-hydroxypropyl p-nitrophenyl phosphate (HPNPP), a model substrate for phosphodiester hydrolysis, was used as the counterion to trigger the assembly of C_{16}TACN·Zn^{2+} into vesicles.[113] Following the formation of the vesicles, the HPNPP counterions were slowly hydrolysed by C_{16}TACN·Zn^{2+} through a cooperative mechanism and the assembly was disrupted owing to loss of favourable ion-pair interactions. This presented a unique example of substrate induced self-assembly and subsequent disassembly through cooperative catalysis. Lee et al. also used hydrophobic substrates to induce self-assembly of otherwise soluble pyridine-based amphiphiles into vesicles (Figure 1.11B).[36] The hydrophobic substrates underwent aromatic nucleophilic substitution reaction in the hydrophobic lipid bilayer of the vesicles and generated acid as the by-product. This acid in turn protonated the pyridine groups of the amphiphiles, solubilising the vesicles and introducing the out-of-equilibrium nature. The precipitated product could be easily removed from the system and following neutralization of

protonated pyridine groups (using K_2CO_3), the cycles could be repeated by simple addition of fresh batches of substrate.

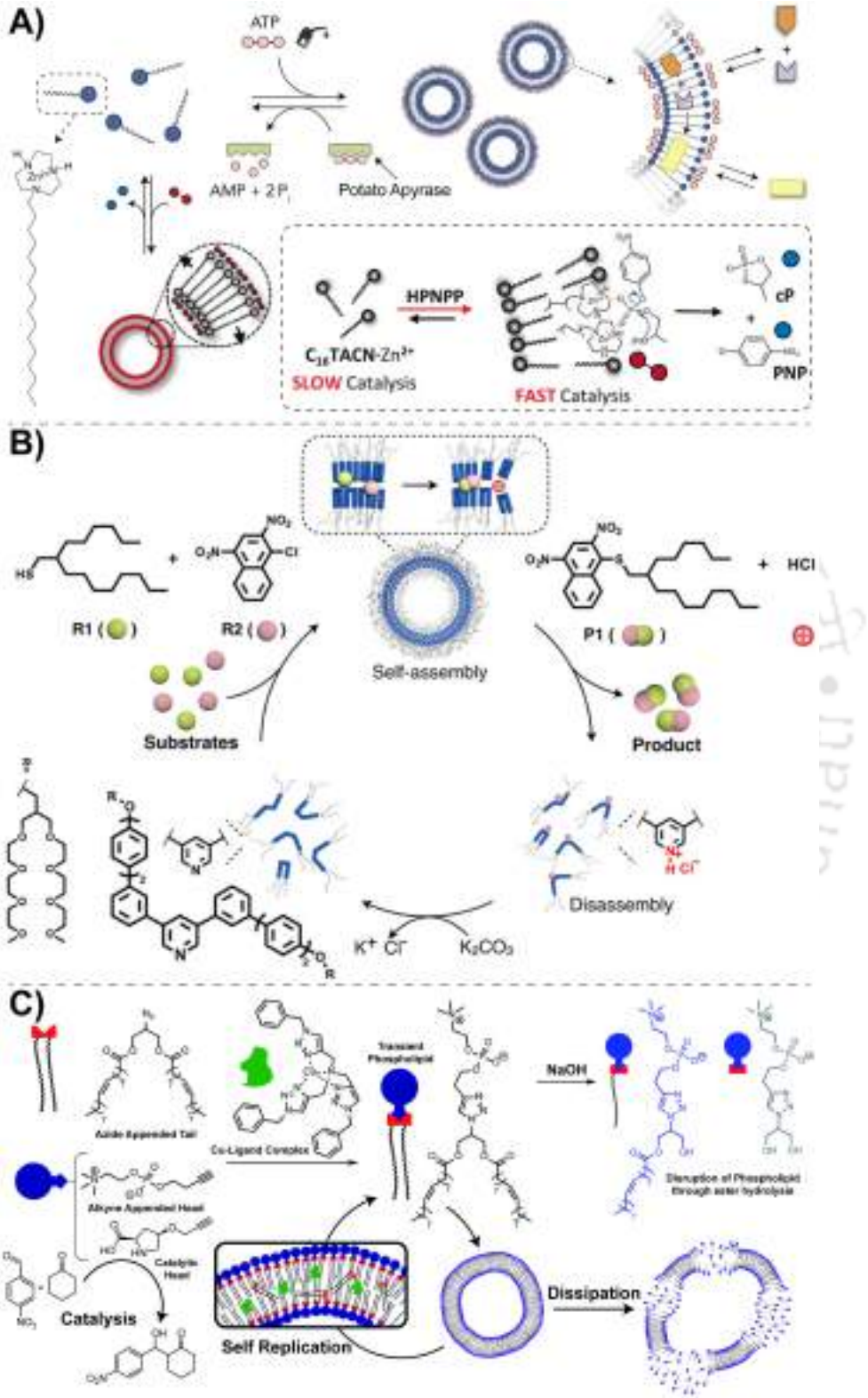

Figure 1.11. **A)** Transient vesicular aggregation triggered by addition of ATP/Potato Apyrase (Top) and HPNPP (Bottom), **B)** Substrate induced transient assembly of vesicles, **C)** Transient assembly of self-replicating vesicles. Reproduced with permission from Ref. 21, 36, 113, 114.

In addition to exhibiting dissipative self-assembly, natural systems also show features like reproduction and metabolism. To incorporate these life-like features in vesicular assemblies, Fletcher et al. exploited the well-known Cu-catalysed alkyne–azide cycloaddition (CuAAC) reaction to create transiently forming and self-replicating catalytic protocells (Figure 1.11C).[114] Briefly, in a phase separated solution of a hydrophobic azide (tail) and a hydrophilic phosphocholine (head), slow CuAAC reaction using a hydrophobic copper-ligand complex leads to the formation of surfactants capable of assembling into vesicles. The produced vesicles engage in a process known as self-replication whereby they draw in and sequester increasing amounts of hydrophobic tails from the organic phase into the aqueous phase, speeding up the production of the surfactants. In order to add transient properties, ester linkages were deliberately placed in the tail group. Thus, in alkaline conditions, vesicles are generated by an autocatalytic process, and then the vesicles are destroyed via base-promoted ester bond hydrolysis. Furthermore, employing a proline-containing alkyne derivative as the head group, they exhibited enantioselective aldol reaction at the interface of the resulting organocatalytic vesicles. In another report, Boekhoven et al. demonstrated the dissipative formation of peptide-based vesicles at the expense of carbodiimide fuel.[115] They used two peptides, Fmoc-GGD-OH and Fmoc-GGE-OH, both of which remain solubilized in their di-anionic form. Following EDC-induced anhydride formation, these peptides assemble into vesicles that undergo continuous membrane remodelling as they progress through the various phases of growth and decay. Despite the fact that vesicles can replicate life-like properties far more effectively than other types of self-assembled structures, little progress has been achieved in their utilisation as dissipative assemblies. Developing novel methodologies and techniques for producing non-equilibrium vesicles holds enormous potential and thus, there is a pressing need for further advancement in this direction for the creation of life-like systems.

1.6. Emergent Features of Transient Systems

Nature chose out-of-equilibrium dynamics because it permits biological systems to work flexibly based on the demands of the cell. A constant influx of energy-rich feed molecules into the system and an outflow of undesirable effluents from the system permits certain metabolic processes to be accomplished in a time-regulated manner with minimum systemic toxicity in the interior cellular compartments. This gives critical biological processes self-regulatory, self-responsive, self-adaptive characteristics and enables the system to maintain a homeostatic environment. System's chemists share this common goal of generating transient functions, but in closed abiotic reaction systems. In an effort to create systems with life-like properties, transient systems with certain distinctive qualities such as modular lifetimes, adaptivity, reproducibility, signal generation and

catalysis have been developed over the years, and a summary of these transient functions is given in the following sections.

1.6.1. Tuneable Lifespan

The generation of dynamic assemblies with tuneable lifetimes is central to the idea of transitory self-assembly and has been extensively covered in the preceding sections. There are two general approaches to tuning the lifespan of transient assemblies depending on the stability of the intermediate active building blocks. If the activated building blocks are unstable in the given reaction media, the lifespan of the transiently assembled state is dictated by the kinetic imbalance between the rate of chemically-fuelled formation and self-dissociation of the building blocks. The continuous supply of energy maintains the high-energy state populated and permits the creation of transient assemblies. At some point, when there is no more fuel to produce new building blocks, the equilibrium swings towards the dissipation phase, causing the assembly to disintegrate. This is the case of dissipative self-assembly. Here, the lifetime of the assembly solely depends on the concentration of the chemical fuel and the molecular properties of the building blocks.

In certain situations, the generated building blocks are stable and require the intervention of a deactivator to disassemble. In these cases, a combination of activator and deactivator indirectly create a kinetic imbalance for the transient formation of active assemblies. To achieve the transitory nature, low dosages of fast activators are typically delivered in combination with relatively high doses of slow deactivators. The activator's fast reaction kinetics rapidly actuates the building blocks for assembly. Following that, the slow and orthogonal coupled deactivator gradually dissolves the assembly. In these instances, the assembly's lifespan is determined by an intricate balance of the activator and deactivator concentrations, as well as the kinetics of the activation and deactivation events. These systems offer a far greater degree of control over the kinetics of the dissipative assembly process.

1.6.2. Adaptivity and Reproducibility

One of the most crucial stages in the evolution of complex living forms is learning to adapt to unfavourable environmental conditions. Adaptability is represented in a system's ability to store energy rather than its proclivity to dissipate energy.[116] Small changes in the molecular structure of building blocks can significantly modify their self-assembling properties, opening up new energy routes for self-assembly with new emergent properties. Ulijn et al. demonstrated, using a series of tripeptides, that the molecular structure of the peptide dictates the kinetics pathway of a transitory biocatalytic self-assembly process.[100] Using a common fuel, aspartyl-phenylalanine-methyl ester (DF-OMe), and the enzyme α-chymotrypsin, they proved that the amino acid amides F-NH_2 and Y-NH_2 produce transient hydrogels, but W, L, V, S, and T do not (Figure 1.10A). Moreover, as compared

to Y-NH_2, F-NH_2 formed stronger and more persistent hydrogels. Interestingly, when F-NH_2 and Y-NH_2 are mixed together for transient assembly, they compete for the common fuel, and it was discovered that the dominant F-NH_2 populated the corresponding high energy tripeptide state to a much greater extent than Y-NH_2. This kinetics selection is because of the ability of the more hydrophobic DFF-NH_2 to store energy more efficiently and adapt to the changes presented by the bienzymatic reaction cycle more effectively, as compared to DFY-NH_2. Although the tripeptides, DFX-NH_2 (X = W, L, V, S, and T), have the ability to generate hydrogels, they were either not generated or extremely short lived during the transient cycle owing to their inability to store energy and adapt to the transient changes. Boekhoven et al. reported similar findings, stating that when peptides are exposed to the EDC-fuelled reaction cycle, they can adapt to a dissipative, equilibrium, or non-assembling pathway depending on the molecular design of the precursors.[44] Both studies concluded that the peptides exhibited sequence-dependent pathway selection and adaptation in a non-equilibrium self-assembly process, analogous to natural selection in biology.

The ability to generate reproducible functions is another key aspect of natural systems, and to some extent, artificial transient systems also exhibit this trait. Natural systems pump out the effluents out of the cells and organelles, and maintain the conditions conducive to the biochemical processes. Artificial transient systems, on the contrary, mostly operate in a closed setup and suffer dampening owing to accumulation of waste in the system. Though light and sound energy and chemical fuels such as trichloroacetic acid, provide a waste-free route to transient self-assembly, the majority of chemically fuelled reaction cycles generate waste, which affects the system's repeatability. Nonetheless, with careful optimizations, nearly all transient systems documented thus far present repeatability across multiple cycles with fresh addition of fuel after each cycle. A convenient approach to mitigate the issue of waste accumulation may be to perform transient chemical reactions in a continuous flow reactor such that fresh fuel is continuously refuelled and waste is simultaneously removed from the system. This will significantly improve the reproducibility and adaptability of the transient systems across multiple reaction cycles.

1.6.3. Transient Signal Generation

The numerous cellular microcompartments communicate with one another and transduce signals through mechanisms that are invariably non-equilibrium in nature. Processes like transient membrane permeabilization and transient opening/closing of ion-channels allow for the exchange of matter and signal transduction, respectively. Researchers have made significant efforts to recreate these processes using synthetic analogues. Flyes et al. described the dissipative formation of an ion-transport channel through a thiol-thioester exchange process (Figure 1.12A).[117] In brief, they began with an amphiphilic thiol that is not long enough to span the membrane and hence is

incapable of transporting ions. When a high energy amine terminated thioester (fuel) was introduced into the system, a fast thiol-thioester exchange resulted in the formation of elongated thioester, which was capable of forming ion-channels in the membrane. Following that, the amine group's intramolecular nucleophilic attack on the thioester group progressively hydrolysed the thioester linkages, releasing the starting inactive thiol and disrupting the ion channel. Fresh pulses of thioester fuel could reactivate the channels for ion transport.

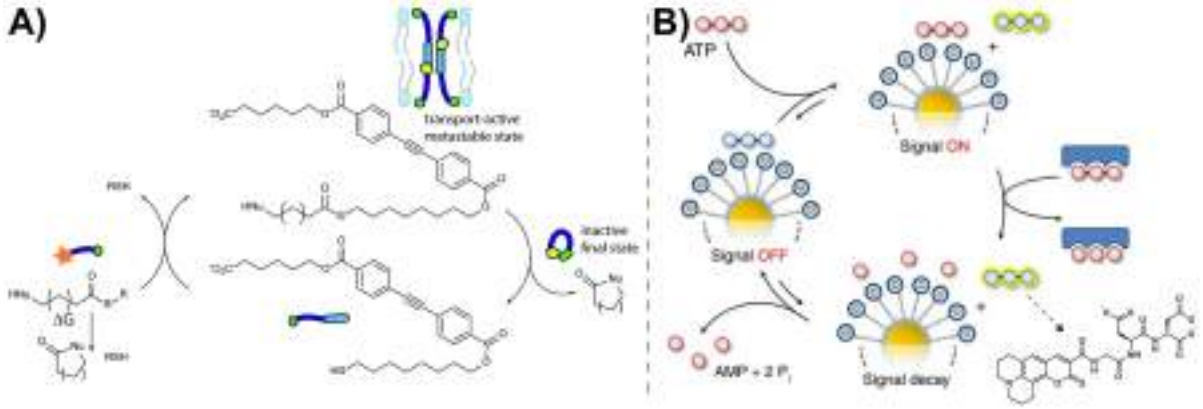

Figure 1.12. **A)** Dissipative assembly of a membrane transport channel, **B)** ATP fuelled transient signal generation. Reproduced with permission from Ref. 117, 118.

Living systems transduce and perceive signals using various sensory mechanisms. In abiotic systems, signal generation is typically reciprocated by luminescence and colour changes. To demonstrate transient signal generation using ATP, Prins et al. developed gold nanoparticles (AuNPs) with their surface functionalised with cationic ligands (Figure 1.12B).[118] They employed an anionic fluorophore that could adhere to the positively charged surface of the AuNPs and experience fluorescence quenching. When ATP is added to the system, it competitively binds to the surface of AuNPs, dislodging the fluorophores. The liberated fluorophores regain their fluorescence in the free state. Under dissipative conditions, the ATP molecules are slowly hydrolysed by potato apyrase already present in the system. The generated ADP and AMP monomers have a low binding affinity for the AuNP surface, and thus, the free fluorophores again bind to the AuNP surface, suppressing the fluorescence. In this way, each fuel pulse transiently produces a fluorescence signal, whose lifespan may be tuned by adjusting the fuel and enzyme concentrations. In another study, they demonstrated that ATP may also be utilised as a template to transiently produce vesicles that can accommodate and enhance the fluorescence properties of a hydrophobic named Laurdan dye.[119] After addition of ATP, time dependent transient gradients of ATP concentration in the system allows the assembly state to transition from a non-fluorescent aggregated state (high ATP) to a metastable fluorescent vesicular state (intermediate ATP) and then back to the initial non-assembled state (low ATP). Thus, the time-gated sequential activation of the different assembly state allowed the fluorescent properties of the entrapped dye to be controlled in the time-domain. These

signal generation features not only add to the appeal of transient systems but also provide a quantifiable output that can be utilised to gauge the progress of the transient assembly process.

1.6.4. Confinement and Catalysis

Compartmentalization and metabolism are two essential criteria for the creation, propagation, and evolution of life. A multitude of metabolic processes keep natural systems out-of-equilibrium. Advances in non-equilibrium system chemistry have resulted in the emergence of artificial systems that excel in biomimetic catalytic activities. Transiently formed self-assemblies have distinct microdomains with characteristics that differ from the bulk solution. These microdomains can accumulate catalyst and substrate in a transitory manner and orchestrate chemical reactions in a time-controlled fashion. For example, Das et al. showed that the peroxidase activity of cytochrome c is transiently boosted when it is trapped in the hydrophobic domains of transient peptide-based coacervates.[106] Likewise, they also showed that hemin, which is inherently inactive in aqueous medium, becomes catalytically active when compartmentalized in the hydrophobic spaces of a transiently formed hydrogel.[99] Prins et al. revealed that ATP templated transient vesicles may selectively harbour hydrophobic precursors in their lipid bilayer and speed up the formation of hydrazone bonds in a time-dependent manner.[120] Also, Boekhoven et al. reported the transient assembly of a polymeric micellar nanoreactor capable of sequestering substrates in its hydrophobic core and increasing the rate of a Diels-Alder reaction.[121]

Some catalytic groups have been shown to exhibit catalytic activity exclusively through a cooperative mechanism in which a number of catalytic units located in close proximity work together to accomplish a catalytic reaction. This synergistic catalysis is conceivable when the catalytic entities are aligned in a well-ordered self-assembled structure. Making use of this property, Prins et al. demonstrated hydrolysis of phosphodiester bonds through a cooperative mechanism in a transient system (Figure 1.11A).[113, 122] Similarly, Das et al. exploited the cooperative effect of closely aligned histidine units in a supramolecular gel to catalyse ester hydrolysis in a transient fashion.[35] In each of these examples, when the transient structures are disassembled, the cooperativity is lost and the catalysis stops. Fresh fuel injection may again restore the assembled structure and restart the catalytic process.

Transient systems have shown great promise for the development of dynamic, intelligent and responsive materials. Non-equilibrium features endow them with unique autonomous, self-sustaining and reproducible features that are not attainable under equilibrium conditions. However, this discipline is still in an evolutionary phase and there is enormous scope for further growth and development in this sector.

1.7. Objectives of the Present Thesis

Intrigued by the exceptional life-like features of transient systems, we envisioned the use of synthetic vesicles as our platform of choice for the development of transient systems. Vesicles are highly dynamic yet far more stable than other amphiphilic assemblies such as micelles. Vesicles feature a hydrophilic corona with easily customizable structural and functional characteristics. They also have hydrophobic bilayer and a hydrophilic aqueous lumen, allowing them to host both hydrophobic and hydrophilic guest molecules. The assembly properties of vesicles can be easily controlled in the time domain by transient changes in their hydrophilic to lipophilic balance.

Vesicles are typically constituted by amphiphilic species that bear two or more aliphatic chains. However, macrocyclic host molecules such as cyclodextrins, calixarenes, pillararenes, and cucurbiturils have been found to form vesicular aggregates when bound to single tail guest molecules.[123] Cucurbiturils are a class of pumpkin shaped macrocyclic hosts composed of cyclic methylene-bridged glycoluril oligomers.[124] Depending on the number of glycoluril units, cucurbiturils have varying cavity sizes and thus can accommodate a wide range of guest molecules of different sizes and shapes. Cucurbit[8]uril is unique in that it can form a ternary complex by clamping together two different guest molecules, one electron-rich and one electron-deficient, in its hydrophobic cavity. Scherman et al. and our group have used this ternary complexation to create supramolecular peptide amphiphiles (SPA) that readily assemble into vesicles.[125-127] The hydrophilic peptide segments lined along the corona of these vesicles can be easily tweaked to instil different functional attributes in these vesicles. As the SPA mentioned herein place no restrictions on the nature or charge of the hydrophilic peptide segment, using catalytic peptides containing histidine, lysine, proline, and/or arginine residues may allow the creation of enzyme mimetic vesicular nanozymes.[128] These distinguishing characteristics enabled us to design vesicle-based transient systems with distinct feedback mechanisms and advanced functions such as tandem catalysis and self-inhibition.

Furthermore, in response to certain stimuli, vesicles have the ability to selectively and reversibly trap and release various fluorophores from both their charged hydrophilic corona and hydrophobic bilayer. The rational selection of fluorophores that can fluoresce and communicate with each other through a FRET mechanism, only when colocalized in the vesicular domains, may thus open up the possibility of realising stimuli-responsive multi-colour luminescence. This concept has been explored in the current thesis to create jellyfish-like breathing vesicles with broad-spectrum multi-luminescence in a temporally controlled manner. The complete thesis work is organised into four chapters, with a brief summary of each part provided below.

Chapter 2: pH Clock Instructed Transient Supramolecular Peptide Amphiphile and Its Vesicular Assembly

This chapter demonstrates a new method for creating a transient supramolecular peptide amphiphile (SPA) and its vesicular aggregates. The ternary complexation of cucurbit[8]uril and the creation of pH sensitive imine bonds aid in the construction of the amphiphile. The transient assembly corresponds to a pH clock established by urea/urease and glucono delta-lactone hydrolysis (GdL). By feeding the system with fresh fuel pulses, the transient assembly may be performed several times.

Chapter 3: Controlling the Lifetime of Cucurbit[8]uril based Self-Abolishing Nanozymes

In this chapter, we report a cucurbit[8]uril-based pH sensitive supramolecular peptide amphiphile (SPA) that assembles into hydrolase mimetic vesicular nanozymes upon addition of alkaline TRIS buffer (activator) but eventually disintegrates due to the catalytic formation of acidic by-products (deactivator). The lifespan of these nanozymes may be controlled in a variety of ways, including varying the number of catalytic groups on the surface of the vesicles, the acid producing substrate, or the activator/substrate ratio. The self-inhibitory nanozymes demonstrated highly customizable lifetimes spanning from minutes to hours, controlled and in situ production of deactivating agents, and excellent repeatability over multiple pH cycles.

Chapter 4: Bi-directional Feedback-Controlled Transience in Cucurbituril based Tandem Nanozyme

In this chapter, we present a chemoenzymatic pH clock mediated transient assembly of a vesicular nanozyme in an attempt to mimic natural catalytic systems. An effective hydrolase-peroxidase tandem catalysis is demonstrated in a time-controlled manner by the distinct confinement of two catalytically separate components, Histidine groups on the periphery and hemin in the lipid bilayer. The pH clock, constituted by alkaline TRIS buffer (promoter) and glucose oxidase (GOx) catalysed oxidation of glucose, guides the transience in an asymmetric manner. The addition of alkaline TRIS buffer raises the pH of the solution, causing the creation and subsequent assembly of imine-linked Supramolecular Peptide Amphiphiles (SPAs) into vesicles. The oxidation of glucose, on the other hand, creates gluconolactone and H_2O_2. Gluconolactone hydrolyses to gluconic acid (deactivator), which dissipates the nanozyme, whilst H_2O_2 is utilised in peroxidase catalysis. Thus, the bi-directional feedback from the fuel not only governs the existence of the transient state but also controls the activity of the assembly. The transiently constructed nanozyme preserved the activity of the catalytic units, demonstrated substrate selectivity, and demonstrated catalytic repeatability through several fuelling cycles.

Chapter 5: Transiently Breathing Multi-Luminescent Vesicles with Broad-Spectrum Tunability

To replicate the complex non-equilibrium dynamics of cell membranes, in this chapter, we present a pH responsive vesicular assembly that exhibits jellyfish-like breathing behaviour and broad-spectrum transient fluorescence oscillations under the influence of a chemically induced pH cycle. The vesicular architecture serves as a versatile platform for entrapping and displaying FRET interactions between multiple donor and acceptor fluorophores. The breathing effect was produced by the vesicle's spontaneously fluctuating interfacial charge during the pH cycle. It also altered the donor fluorophore's emission intensity, affecting the efficacy of FRET interactions between donor-acceptor couples. This allowed the vesicles to glow in several colours during the breathing cycles. Furthermore, the vesicles displayed remarkable adaptability in terms of the lifespan of the breathing cycles and the tunability of the luminescence colour transitions.

Chapter 2

pH Clock Instructed Transient Supramolecular Peptide Amphiphile And Its Vesicular Assembly

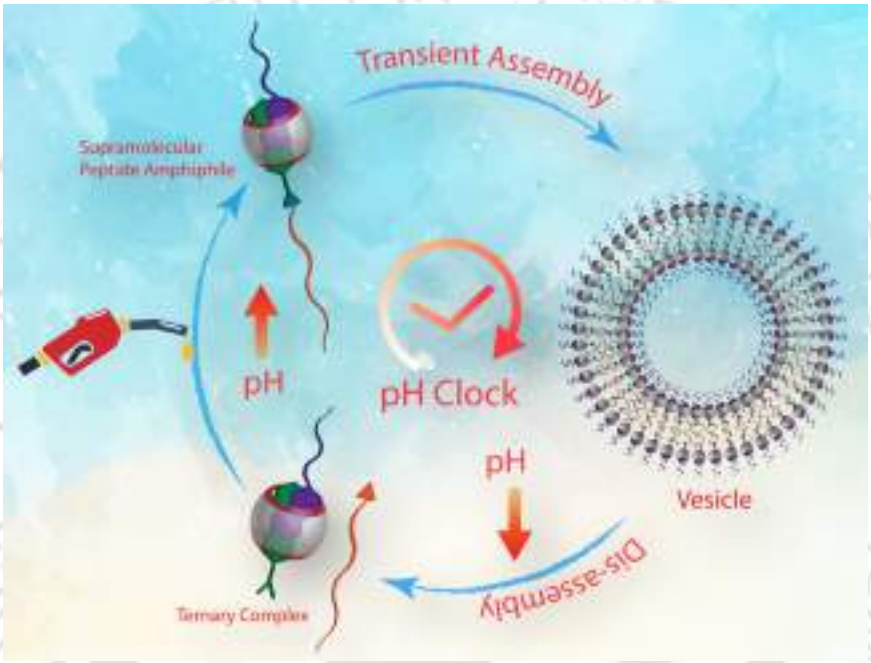

भारतीय प्रौद्योगिकी संस्थान गुवाहाटी
Indian Institute of Technology Guwahati

2.1. Introduction

One of the primary instruments employed by nature for the development and sustenance of life is the self-assembly of simple molecules into complex and highly organised systems that execute vital biological processes.[129] As previously stated, the assembly of synthetically designed supramolecular structures follow a thermodynamic pathway, and the assembled form typically occupies a low-energy equilibrium state.[5, 116] However, the majority of self-assembly processes that occur in nature are energetically demanding processes that require a steady inflow of energy to keep the self-assembled systems functional.[8] In natural systems, a constant flow of energy kinetically and transiently pushes the system out of equilibrium, endowing it with energy-dependent self-responsive, self-regulatory, and self-adaptive qualities.

Recently, substantial efforts have been made to mimic the out of equilibrium processes in nature and to unravel the mysteries regarding the origin of life. The concept of transient assembly has been exploited to develop temporally controlled and short lived gels, vesicles, nanoreactors and nano-assemblies.[21, 30, 32-38] An elegant approach towards developing transient systems is to temporally control various factors such as temperature, pressure, light, pH etc. [67, 86] which mediate the formation of the self-assembled state. Using a combination of two competing triggers that induce a change in pH from acidic to basic reaching a transient state before coming back to the acidic range can be established.[31] Combining this pH clock efficiently with any self-assembling system whose assembly/disassembly is governed by the pH of the medium can lead to a transient self-assembled system.[32]

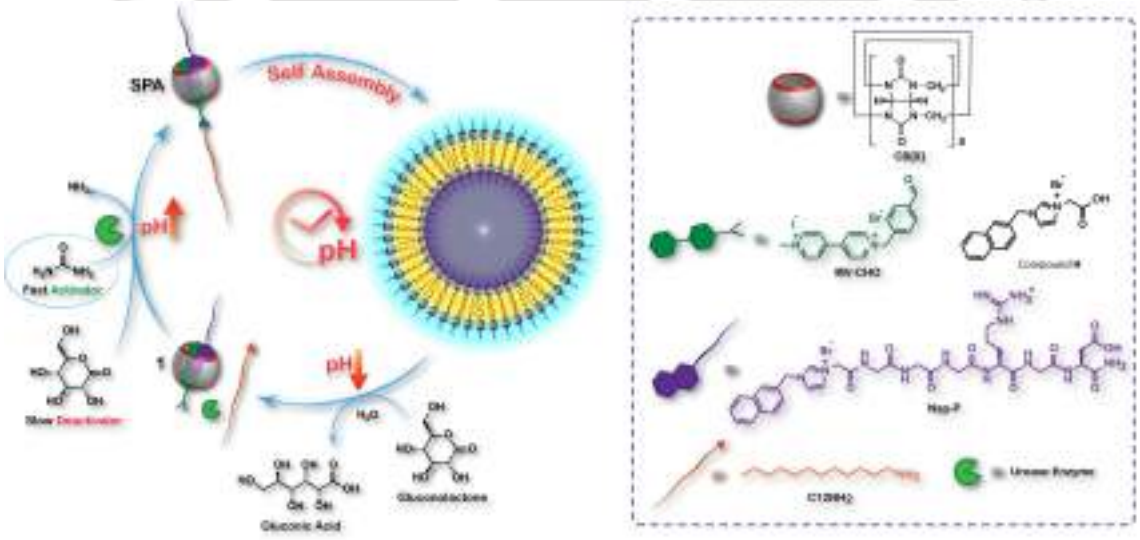

Scheme 2.1. Chemical structures of different components and graphical presentation of the fuel driven temporal formation of CB[8] assisted supramolecular peptide amphiphile and its vesicles.

We anticipated that such a fuel-driven pH clock can be utilized to temporally form supramolecular peptide amphiphiles and also their self-assembly. In this regard, cucurbit[8]uril

(CB[8], Scheme 2.1)[124, 130, 131] assisted ternary complexation driven formation of supramolecular amphiphiles and their self-assembly into robust and stimuli responsive vesicles have been reported on several occassions.[125-127, 132] Inspired by our previous experience with CB[8] based vesicles, herein we report pH regulated transient formation of a supramolecular peptide amphiphile (SPA) which self assembles to form transient vesicles.

2.2. Results and Discussion

2.2.1. Formation of Supramolecular Peptide Amphiphile through Ternary Complexation

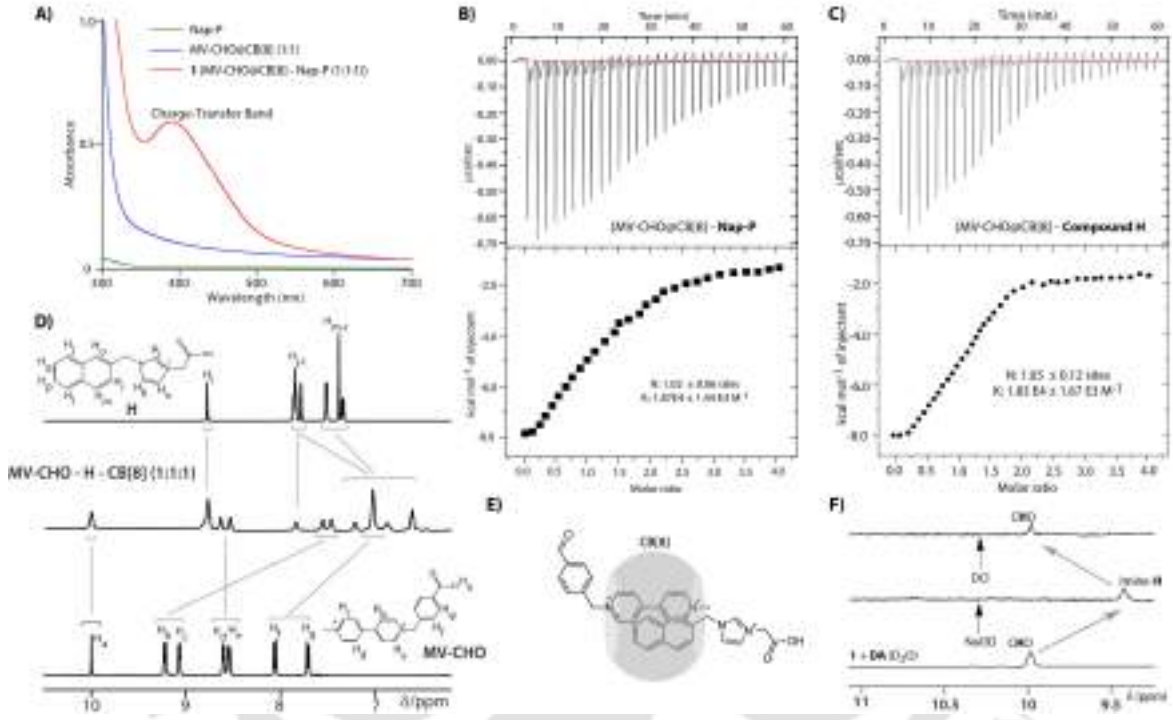

Figure 2.1. A) UV-Visible spectra of 0.75mM aqueous solutions of different components of **1** showing the appearance of the charge transfer band upon ternary complexation in case of 1; Thermogram (top) and binding isotherm (bottom) of **B)** MV-CHO@CB[8] with Nap-P, and **C)** MV-CHO@CB[8] with Compound-H at 298 K, **D)** ^{1}H NMR of different combinations of MV-CHO, compound H and CB[8] showing the ternary complexation between them, **E)** Slipped packed arrangement of MV-CHO and Compound-H in the ternary complex, **F)** ^{1}H NMR of **1** and DA under different conditions showing formation and disappearance of the SPA as a function of pH of the medium.

Prior to the construction of the pH clock and the transient system, the ternary complex (**1**) formation by the viologen unit (MV-CHO) and naphthalene functionalized peptide (Nap-P) with CB[8] was confirmed through the appearance of the characteristic broad charge transfer (CT) band at 396 nm in absorption spectra (Figure 2.1A).[133] The isothermal titration calorimetric (ITC) titration experiment also showed a 1:1 complexation between Nap-P and MV-CHO@CB[8] (Figure 2.1B).[134] Since a ^{1}H NMR experiment with Nap-P resulted in a complex spectrum, a shorter analogue, compound **H**, (Scheme 2.1) was used to understand the situation. An ITC experiment using compound **H** and MV-CHO@CB[8] also showed 1 : 1 : 1 ternary complexation (Figure 2.1C). The NMR

spectra of different compositions of MV-CHO, **H** and CB[8] were recorded (Figure 2.1D). In the presence of CB[8], the MV and naphthalene-protons of **H** showed an up-field shift[135] but no change in position was observed for the imidazolium-protons. This indicated a slipped parallel stacking of the viologen and naphthalene units inside the CB[8] cavity (Figure 2.1E). A similar slipped-stacking between donor acceptor groups has also been reported earlier.[136, 137] In presence of dodecylamine (DA), the ternary complex **1** formed the desired SPA under basic condition (pH ~8). The formation of the SPA was confirmed by the disappearance of the aldehyde signal and appearance of the imine peaks in ^{1}H NMR spectra as shown in Figure 2.1F.

2.2.2. pH Clock Directed Transient Assembly

Imine bonds are dynamic covalent bonds (DCB) which are stable at basic pH but are highly labile under acidic conditions.[138] The SPA breaks down to the parent amine and **1** upon acidification which is confirmed by the disappearance of the imine signals and reappearance of the aldehyde proton. The formation-deformation of the SPA thus can be controlled using a pH switch. To verify the proposed temporal aggregated system using this SPA, the pH clock was established. The pH clock (Scheme 2.1) has been realised by using a combination of two triggers: (i) the autocatalytic reaction of urea with the enzyme, urease, which releases NH_3 and leads to an increase in pH of the system, and (ii) the base-catalysed saponification reaction of the dormant deactivator Glucono delta-lactone (GdL) as a counter trigger which furnishes gluconic acid and thereby decreases the pH.

Upon addition of a mixture of urea and GdL in a definite ratio to an aqueous solution of urease enzyme, initially a swift increase in pH was observed. After the activation kinetics of urease reaches its peak, no further rise in pH takes place. Under alkaline conditions, the hydrolysis of GdL is aggravated and initially, there is a rapid fall in pH until the pH reaches around 7.5 when the decrease in pH becomes slow and steady (Figure 2.2A). A probable reason for this is that as the optimum pH for urease is 7.4[139], the rate of formation of ammonia abruptly increases at this pH range and slows down the drop in pH. An increase in the concentration of urea and/or urease not only elates the rate of activation but also causes an increment in the maximum overall pH. A high concentration of GdL restricts the rise in pH and escalates the rate of fall in pH. By fine tuning the rates of the activation and deactivation steps, the lifetime of the transient supramolecular assemblies can be easily modulated. An aqueous solution containing 0.2 mg/ml of urease showed an initial pH in the range of 6.5-6.8. The pH of the solution was adjusted to ~5 before initiating the pH cycle. A very slow deactivation kinetics was observed when the amount of GdL was ≤ 2 equivalents of urea (Figure 2.2A). This may be ascribed to the fact that one molecule of urea releases two molecules of NH_3 which neutralize the acid generated by GdL and thereby slow down the decay in pH. In order to

accelerate the deactivation step, the amount of GdL used should be sufficient to counter the neutralization caused by urea. Upon adding a mixture of Urea and GdL in the ratio 1:3, an initial pH jump to 9.2 - 9.3 followed by a steady decay to 6.8 - 6.9 was observed in 120 minutes (Figure 2.2A).

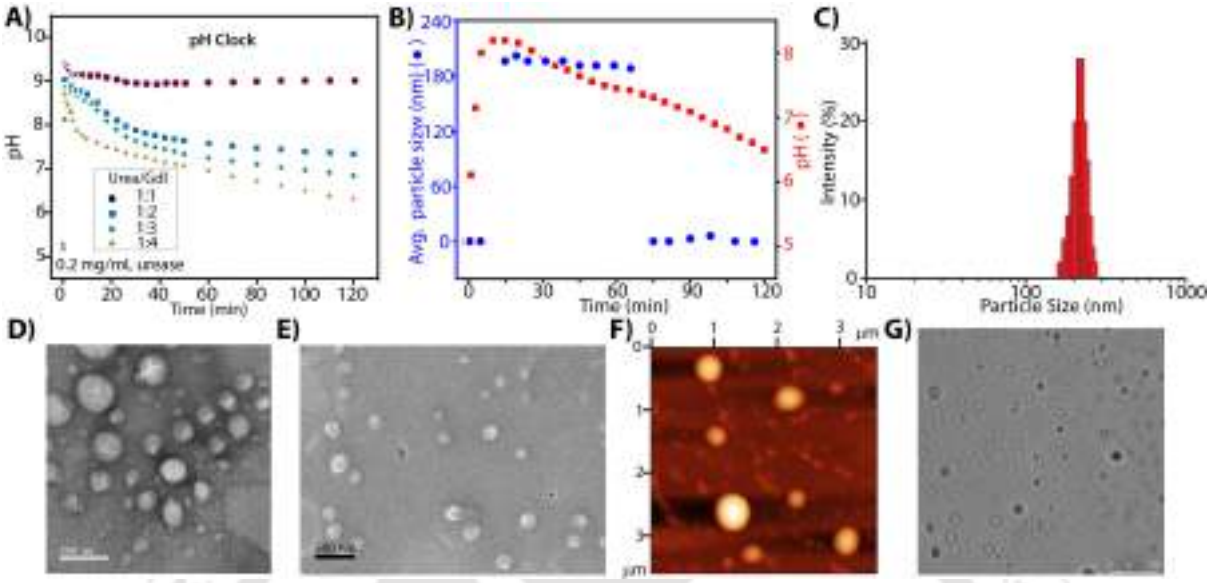

Figure 2.2. A) Optimizing the pH clock. The change in pH with time for four different urea/Gdl compositions. **B)** Appearance of particles of different sizes (from DLS) as a function of time for the transient system constructed by **1** and DA in presence of 0.2 mg/mL urease, and 1:3 urea/Gdl showing the response toward the pH clock. **C)** Representative plot of DLS measurements during the transient formation of vesicles in response to the pH clock. **D)** FETEM, **E)** FESEM, **F)** AFM, and **G)** CLSM images of the transient vesicles formed during the cycle mentioned in (B).

The kinetics of the transient formation of the SPA was then assessed under the influence of the pH clock. A 0.1 mM solution of the ternary complex, **1**, in water containing 0.2mg/ml of urease and an equivalent amount (0.1 mM) of DA (dissolved in THF to facilitate solubilisation) showed an initial pH of 7.0-7.2. The presence of the amine might be responsible for this higher initial pH. The pH of the solution was adjusted to ~5 in order to avoid any SPA formation. The pH jump induced by the addition of urea and GdL (1:3) led to the transient generation of the SPA through the formation of imine bond under alkaline pH conditions.

The aggregation process of the so formed amphiphiles were monitored using Dynamic Light Scattering (DLS) measurements. Figure 2.2B shows the appearance of particles of different sizes and change in pH of the system as a function of time. Prior to the addition of the triggers, no particular size distribution was observed in the DLS profile. However, aggregates with a hydrodynamic diameter of ~220 nm started (Figure 2.2C) appearing soon after the pH clock started (addition of urea/Gdl). Peaks corresponding to 220 nm distribution continued appearing until the pH of the system remain above 7.4 (~ 60 mins). However, after that the distribution disappeared completely. Even though the pH jump takes place almost instantaneously, aggregation takes place in a relatively slower and delayed fashion. This might be due to the reason that the ammonium ions

present in the system might compete with the long chain amines for imine formation.[32] However, DA, owing to its stronger hydrophobic interactions in the assembled state form stronger imine bonds and outweigh the effect of ammonium ions. The aggregation pattern clearly demonstrates a pH dependent behaviour.

In order to determine the morphology of the supramolecular aggregates, microscopic techniques like FETEM, FESEM, AFM and CLSM were employed. The FETEM image of the sample at pH 7.8 showed nearly mono-dispersed hollow spherical aggregates with a thin dark boundary which is indicative of the formation of vesicles (Figure 2.2D). The diameter of the vesicles was found to be 200 nm which is in good agreement with the DLS data obtained. Furthermore, the absence of any specific morphology for the samples at pH below 7.5 corroborates the transient formation of vesicles. FESEM, AFM and CLSM experiments also showed the formation of spherical aggregates with similar dimensions (Figure 2.2E, F, G).

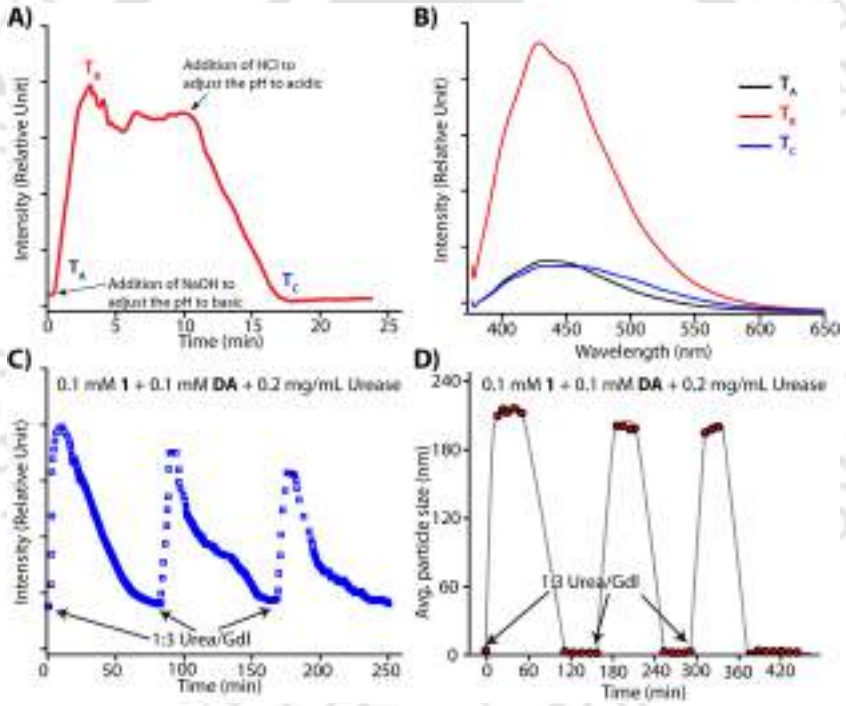

Figure 2.3. A) Time dependent emission of DPH at 438 nm (λex = 355 nm) in presence of **1** and DA in water at room temperature. To trigger the vesicle formation, NaOH was added and then to disrupt the vesicles, HCl was added. **B)** The emission spectra of the same system at different times as mentioned in (A). Three consecutive cycles of the transient SPA and its vesicle formation as monitored by **C)** emission spectra of DPH and, **D)** appearance of particles of different sizes as a function of time (from DLS).

Ternary complexation induced formation of supramolecular amphiphiles and their vesicles are already demonstrated by our group and in the present case, the microscopic images also indicate the formation of vesicles.[127] However, it is important to confirm that the spherical aggregates are indeed vesicles. To prove the vesicular nature of the aggregates, diphenylhexatriene

(DPH) was used which is well-known for the enhancement of emission upon encapsulation in the lipid bi-layer of vesicles.[21] In the present case, when the pH of the system (**1** + DA) is increased to ~8 by the addition of NaOH solution, significant enhancement in the emission (at 438 nm; λ_{ex} = 355 nm) was observed which confirms the vesicular nature of the system (Figure 2.3A, B). Upon addition of HCl to this system, the emission returns back its original position. Further, to confirm the transient nature, similar experiments were performed (**1** + DA + DPH + urease) in presence of GdL and urea and a prominent enhancement in the emission of DPH was observed until 5 min followed by a decay to its original position afterward within 90 min (Figure 2.3C).

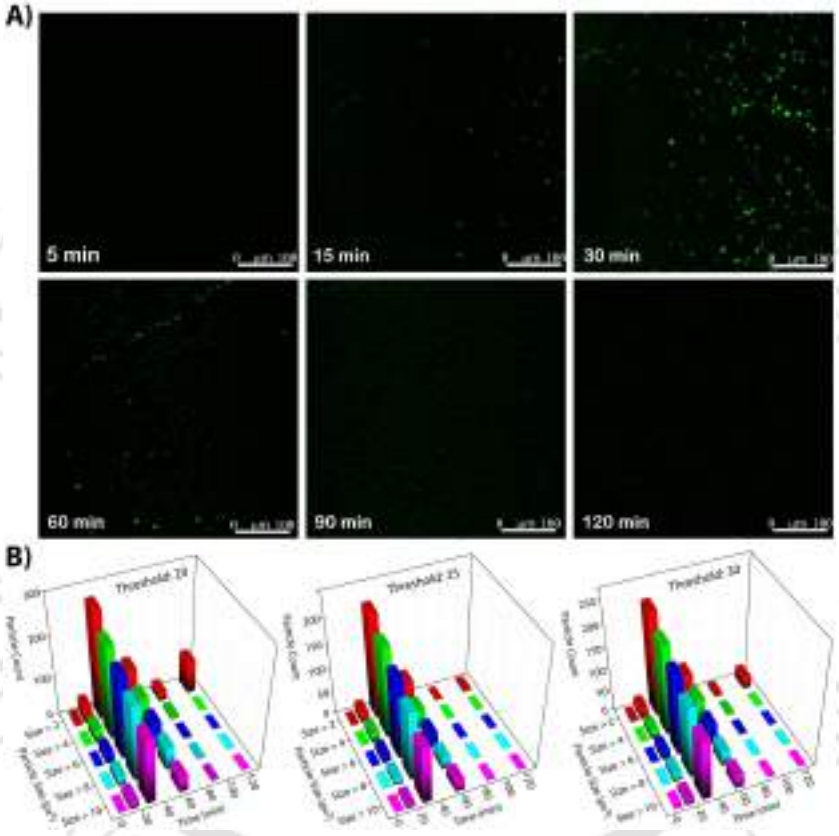

Figure 2.4. A) CLSM images of the transient system constructed by **1**, DA, 0.2 mg/mL urease, and 1:3 urea/Gdl in presence of NR at different times showing the temporal formation of the vesicles, **B)** Statistical analysis of the images shown in (A)

It is worth mentioning that, control experiments in the absence of CB[8] showed the formation of imine bonds at higher pH. However, neither any size distribution nor any particular morphology could be found for this system. The attachment of DA with MV-CHO certainly created an amphiphile which presumably could not form any vesicular aggregates as no particular morphology could be seen from microscopic experiments. Experiment with DPH also showed no change in the emission of the dye upon increasing the pH from 5 to 8 confirming the absence of vesicles (data not shown). It is well-established that asymmetric viologen amphiphiles are not capable of forming vesicular assembly alone but ternary complexation with CB[8] assists the aggregation to vesicles.[140]

To have a conclusive evidence for the transient formation of the vesicles, confocal laser scanning microscopy (CLSM) was performed to directly visualize the assembly as well as the disassembly processes. A hydrophobic dye, Nile red (NR) was used to facilitate the visualization of the aggregates. A control experiment with **1** and DA at pH 8 showed that fluorescent spots of the vesicular aggregates remained unchanged for 2 hours ensuring no photobleaching. During the experiment under pH clock, initially, no fluorescence was observed in the absence of pH triggers due to the absence of vesicles (Figure 2.4A). However, the fluorescence intensity of NR increased abruptly after 15 minutes from the addition of the fuel indicating the formation of vesicles and entrapment of NR in the bilayer. As the reaction proceeds further, the fluorescence intensity diminishes slowly indicating the breakdown of the vesicular assemblies. One cycle of vesicle formation and dissociation was visualized by recording an image every 30 s. The number of fluorescent objects (Figure 2.4B) was then counted to quantify the analyses. From the Figure 2.4B, the formation and dissociation of the vesicles is clearly visible as the number of fluorescent particles increased and then disappeared following the pH clock.

2.2.3. Repeatability of the Transient Cycles

An interesting property of natural dissipative systems is their reusability or repeatability without significant fatigue. Having established the transient formation of vesicles, we were interested to check the repeatability of the transient assembly by refuelling after each cycle. Refuelling after the first cycle reproduced similar cycle of events and the aggregation in subsequent cycles was studied using fluorescence spectroscopy (using DPH) and DLS as shown in Figure 2.3C and D. In subsequent cycles, a lower rise in initial pH followed by a rapid decay in pH was observed (Figure 2.5A). The DLS data also showed a steady decrease in the lifetime of the assembled state in consecutive cycles (Figure 2.3D). This fall in efficiency of the pH clock is due to the accumulation of gluconic acid in the system after each cycle which increases the overall acidity of the system. Fluorescence studies using DPH as the hydrophobic probe also showed an increase in the fluorescence intensity followed by a steady decay. The second reaction cycle shows a nearly identical variation in the fluorescence intensity which indicates the stability of the system under repeated pH cycles.

To gain further insight into the dynamics of the aggregation, DLS studies were performed with aliphatic amines of varying chain lengths (Figure 2.5B). The chain length had no significant effect on the aggregation behaviour and time scale. However, a direct proportionality between the size of the aggregates and the chain lengths could be observed as the average diameter increases with the chain length of the amine.

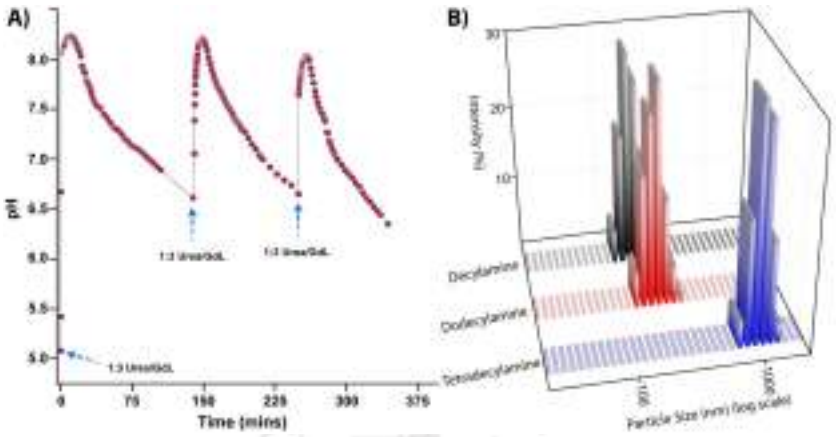

Figure 2.5. A) Representative plot showing the change in pH during the transient vesicle formation across three consecutive cycles, **B)** Representative plot of DLS measurements during the transient formation of vesicles in response to the pH clock by amines of different chain lengths.

2.3. Conclusion

In conclusion, we have shown the transient formation of a SPA which subsequently forms a vesicular assembly in response to a pH clock. The formation of the SPA is assisted by the ternary complexation by CB[8]. The pH clock is established by combining urea/urease based fast biocatalytic processes and slow hydrolysis of GdL. The imine bond formation under basic conditions and its hydrolysis under an acidic medium are the key chemical transformations used for the construction of the SPA and its transient assembly. The temporal formation of the vesicle requires chemical fuel to maintain the out-of-equilibrium state and several cycles of the transient assembly can be achieved by supplying the fuel to the system.

2.4. Experimental Section

2.4.1. General Information and Materials

2-Naphthaldehyde, 4,4'-Bipyridyl, Phosphorus Tribromide (PBr_3) and Gluconolactone (GdL) were purchased from Sigma-Aldrich (USA). Imidazole, Sodium Hydride, Methyl Iodide and Urea were obtained from Spectrochem (India). Methyl Bromoacetate and Terephthalaldehyde were acquired from TCI Chemicals (India). Sodium Borohydride and Urease from *Canavalia ensiformis* (Jack bean; Activity=345 u/mg) were procured from SRL (India). Cucurbit[8]uril (CB[8]) was synthesized following a previously published protocol and characterized accordingly.[141] Rink amide MBHA resin, protected amino acids and coupling reagents were purchased from Novabiochem. HPLC-grade dimethylformamide (DMF), dichloromethane (DCM), and acetonitrile (ACN) were procured from Spectrochem (India) and Fisher Scientific (India). Solvents were dried whenever required according to the reported procedures. Milli-Q water with a conductivity of less than 2 μScm^{-1} was used for all sample preparations. 60-120 mesh silica gel (SRL) was used from column chromatography.

Chromatographic purifications were performed on a Luna 5 μm (C18) column (Phenomenex) using a Dionex Ultimate 3000 HPLC. ^{1}H NMR and ^{13}C NMR spectra were recorded using a Bruker Ascend 600 MHz (Bruker, Coventry, UK) spectrometer and referenced to deuterated solvents. Coupling constants (J values) are reported in hertz, and chemical shifts are reported in parts per million (ppm). Multiplicities are reported as follows: s (singlet), d (doublet), t (triplet), m (multiplet), and br (broadened). Electrospray ionization mass spectrometry (ESI-MS) were performed with a Q-Tof-Micro Quadrupole mass spectrometer (Micromass) and data were analyzed using the built-in software. MALDI analysis were performed with Bruker Daltonics - autoflex™ speed MALDI-TOF instrument.

2.4.2. Synthesis and Characterization

MV-CHO and Nap-P were synthesized following Scheme 2.2.

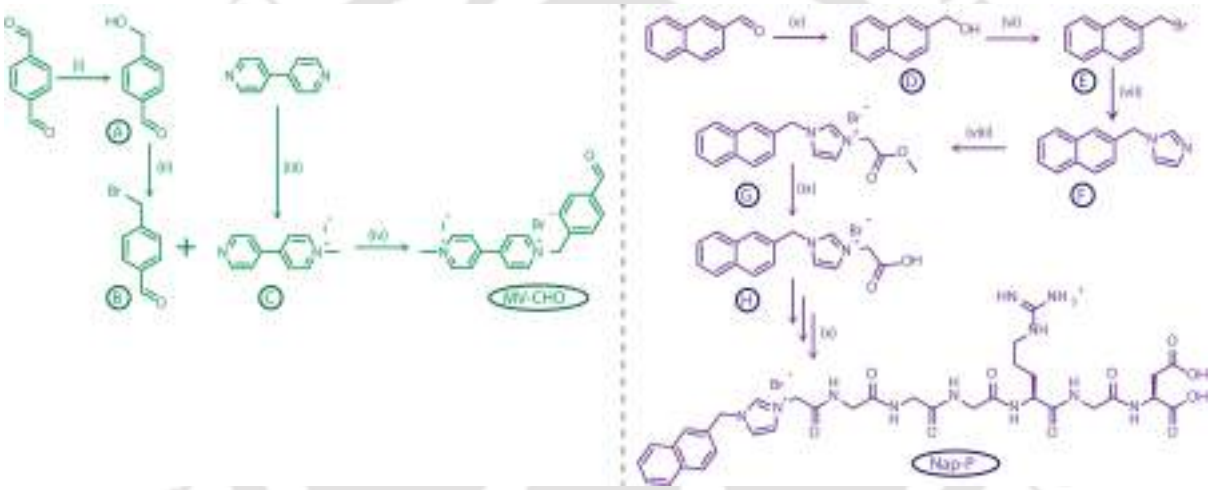

Scheme 2.2. Synthetic route for MV-CHO and Nap-P.(i) $NaBH_4$, Ethanol/THF, 0°C, 6 h; (ii) HBr, Toluene, Reflux, 3 h; (iii) MeI, Dry DCM, Reflux, Overnight; (iv) Dry Acetonitrile, 80°C, Overnight; (v) $NaBH_4$, Dry Methanol, RT, 2 h; (vi) PBr_3, Dry DCM, 0°C to RT, 4 h; (vii) Imidazole, NaH, Dry THF, RT (1 hr) to Reflux (Overnight); (viii) Methyl bromoacetate, Toluene, 100°C, Overnight; (ix) 1M HCl, 105 °C, 3 h; (x) Solid Phase Peptide Synthesis (SPPS).

4-(Hydroxymethyl)benzaldehyde (A):

$NaBH_4$ (70.5 mg, 1.86 mmol, 0.25 eqv.) was slowly added to a solution of terepthalaldehyde (1 g, 7.45 mmol, 1 eqv.) in a mixture of ethanol and THF (1:1.5; 10 mL) at 0°C in an ice bath over a period of 30 minutes with constant stirring. The solution was then stirred at 0°C for 6 hours. The reaction mixture was acidified to pH 5 using 2M HCl and the solvent was evaporated using a rotary evaporator. Water was added to the residue and the product was extracted using ethyl acetate. The organic fractions were collected, dried over anh. Na_2SO_4, filtered and evaporated. The crude product was purified using column chromatography (50% Ethyl Acetate/Hexane) to give the product as a white solid. Yield=751.1 mg; 74%. ^{1}H NMR (600 MHz, $CDCl_3$) δ (ppm) 9.99 (s, 1H), 7.86 (d, J = 8.1 Hz,

2H), 7.52 (d, J = 7.9 Hz, 2H), 4.79 (s, 2H). ^{13}C NMR (151 MHz, $CDCl_3$) δ (ppm) 192.30, 148.09, 130.12, 130.10, 127.80, 127.08, 127.04, 64.51.

4-(Bromomethyl)-benzaldehyde (B):

1.2 mL of 48% aqueous HBr was added to a solution of **Compound A** (447 mg, 3.28 mmol) in toluene (4 mL) and refluxed for 3 hours. The reaction mixture was cooled to room temperature, DCM was added to it and the organic phase was washed with saturated $NaHCO_3$ until neutral. The organic phase was dried over anh. Na_2SO_4, filtered and evaporated to give the crude product as a yellow solid. Upon further purification using column chromatography (3% Ethyl acetate/Hexane), the product was obtained as a white crystalline solid. Yield= 477 mg; 73%. ^{1}H NMR (600 MHz, $CDCl_3$) δ (ppm) 10.01 (s, 1H), 7.86 (d, J = 8.2 Hz, 2H), 7.56 (d, J = 8.1 Hz, 2H), 4.51 (s, 2H). ^{13}C NMR (151 MHz, $CDCl_3$) δ (ppm) 191.67, 144.39, 136.26, 130.32, 129.83, 32.11.

1-methyl-[4,4'-bipyridin]-1-ium iodide (C):

Methyl Iodide (585 uL, 3.85 mmol, 1.2 eqv.) was added to a solution of 4 4'-bipyridyl (500 mg, 3.2 mmol, 1 eqv.) in dry DCM and refluxed overnight. The precipitate so obtained was washed with copious amounts of ether to give the product as a yellow solid. Yield=715.8 mg, 75%. ^{1}H NMR (600 MHz, D_2O) δ (ppm) 8.86 (d, J = 6.2 Hz, 2H), 8.72 (d, J = 4.2 Hz, 2H), 8.34 (d, J = 6.2 Hz, 2H), 7.86 (d, J = 4.5 Hz, 1H), 4.40 (s, 3H). ^{13}C NMR (151 MHz, D_2O) δ (ppm) 153.50, 149.89, 145.55, 142.59, 125.71, 122.42, 47.77. Mass (ESI-MS): m/z calcd. for $C_{11}H_{11}N_2^+$ $[M]^+$: 171.092, found 171.093.

1-(4-formylbenzyl)-1'-methyl-[4,4'-bipyridine]-1,1'-diium (MV-CHO):

Compound B (674 mg, 2.26 mmol, 1 eqv.) and **C** (450 mg, 2.26 mmol, 1 eqv.) were dissolved in dry acetonitrile and stirred at 80°C overnight under an inert atmosphere of argon. The resultant precipitate was filtered and washed multiple times with ether to give the product as an orange colored solid. Yield=1.09 g; 97%. ^{1}H NMR (400 MHz, D_2O) δ (ppm) 10.00 (s, 1H), 9.22 (d, J = 6.7 Hz, 2H), 9.07 (d, J = 6.3 Hz, 2H), 8.60 (d, J = 6.4 Hz, 2H), 8.54 (d, J = 6.4 Hz, 2H), 8.06 (d, J = 8.0 Hz, 2H), 7.71 (d, J = 8.0 Hz, 2H), 6.08 (s, 2H), 4.51 (s, 3H). ^{13}C NMR (101 MHz, D_2O) δ (ppm) 195.62, 150.80, 149.61, 146.36, 145.85, 138.97, 136.63, 130.97, 129.70, 127.33, 126.77, 64.19, 48.42. Mass (ESI-MS): m/z calcd. for $C_{19}H_{18}BrIN_2O^{2+}$ $[M]^{2+}$: 495.965, for $C_{19}H_{17}N_2O^+$ $[M\text{-}Br\text{-}I\text{-}H]^+$:289.134, found $[M\text{-}Br\text{-}IH]^+$: 289.135.

Naphthalen-2-ylmethanol (D):

2-Naphthaldehyde (1 g, 6.4 mmol, 1 eqv.) was dissolved in dry MeOH and was cooled to 0 °C. To this cooled solution, sodium borohyride (266.4 mg, 7.04 mmol, 1.1 eqv.) was added in one portion, and the reaction mixture was allowed to come to room temperature and then stirred at room temperature for 2 hours. After completion of the reaction (confirmed by TLC), the solvent was removed under reduced pressure. To the resulting reaction mixture saturated $NaHCO_3$ was added

and it was extracted with DCM. The organic phase was dried over Na_2SO_4, filtered and concentrated under reduced pressure to give the desired material as a white solid. Yield = 891.4 mg, 88 %. ^{1}H NMR (600 MHz, $CDCl_3$) δ (ppm) 7.87 – 7.76 (m, 4H), 7.52 - 7.43 (m, 3H), 4.83 (s, 2H). ^{13}C NMR (151 MHz, $CDCl_3$) δ (ppm) 138.43, 133.50, 133.06, 128.42, 128.00, 127.82, 126.28, 126.00, 125.54, 125.28, 65.50.

2-(bromomethyl)naphthalene (E):

PBr_3 (457.5 μL, 4.87 mmol, 1.1 eqv.) was added dropwise to the cooled DCM solution of **Compound-D** (700 mg, 4.42 mmol,1 eqv.). Then the reaction mixture was warmed up to room temperature and stirred for 4 hours. Sat. $NaHCO_3$ was added to the reaction mixture and the solution was extracted with DCM. The organic phase was collected, dried over anh. Na_2SO_4, filtered and evaporated with the help of rotary evaporator. The residue was then purified by silica gel chromatography with DCM to yield the desired product as a greyish solid. Yield = 802.2 mg, 82%. ^{1}H NMR (600 MHz, $CDCl_3$) δ (ppm) 10.01 (s, 1H), 7.86 (d, J = 8.2 Hz, 2H), 7.56 (d, J = 8.1 Hz, 2H), 4.51 (s, 2H). ^{13}C NMR (151 MHz, $CDCl_3$) δ (ppm) 191.67, 144.39, 136.26, 130.32, 129.83, 32.11.

1-(naphthalen-2-ylmethyl)-1H-imidazole (F):

Imidazole (585.6 mg; 8.6 mmol; 3 eqv.) was taken in dry THF and the solution was cooled to 0°C in an ice bath. Pre-dried NaH (206.46 mg; 8.6 mmol; 3 eqv.) was added to the solution at 0°C with constant stirring. The ice bath was then removed and the solution was allowed to stir at room temperature for 1 hour. **Compound E** (634 mg; 2.87 mmol; 1 eqv.) dissolved in dry THF was then added to the solution drop wise using a dropping funnel with constant stirring. The solution was allowed to stir for 3 hours at room temperature and then refluxed at 70°C overnight. THF was evaporated from the pale-yellow suspension so obtained and ethyl acetate was added to the reaction mixture. The organic phase was washed multiple times with water followed by brine, dried over anh. Na_2SO_4, filtered and the organic phase was evaporated to give the product as a white solid. The product was taken to the next step without further purification. Yield=531.5 mg; 89%. ^{1}H NMR (600 MHz, $CDCl_3$) δ (ppm) 7.86 – 7.75 (m, 3H), 7.58 (d, J = 10.4 Hz, 2H), 7.53 – 7.45 (m, 2H), 7.24 (dd, J = 8.5, 1.8 Hz, 1H), 7.13 – 7.09 (m, 1H), 6.93 (d, J = 1.4 Hz, 1H), 5.24 (s, 2H). ^{13}C NMR (151 MHz, $CDCl_3$) δ (ppm) 137.59, 133.62, 133.34, 133.08, 129.93, 129.03, 127.92, 127.83, 126.74, 126.55, 126.37, 124.93, 119.45, 51.03. Mass (ESI-MS): m/z calcd. for $C_{14}H_{13}N_2^+$ $[M+H]^+$: 209.107, found 209.109.

3-(2-methoxy-2-oxoethyl)-1-(naphthalen-2-ylmethyl)-1H-imidazol-3-ium (G):

Compound F (555.6 mg, 2.67 mmol, 1 eqv.) was dissolved in toluene in a round-bottomed flask and methyl bromoacetate (378.8 uL, 4 mmol, 1.5 eqv.) was added to it. The solution was then stirred at 100°C overnight. The white precipitation so formed was collected and washed multiple times with ether and finally dried under high vacuum to give the product as a white solid. Yield=950

mg, 98.6%. ^{1}H NMR (600 MHz, DMSO-d_6) δ (ppm) 9.36 (s, 1H), 8.02 – 7.98 (m, 2H), 7.97 – 7.90 (m, 3H), 7.81 (t, J = 1.8 Hz, 1H), 7.60 – 7.52 (m, 3H), 5.71 (s, 2H), 5.30 (s, 2H), 3.74 (s, 3H). ^{13}C NMR (151 MHz, DMSO-d_6) δ (ppm) 167.28, 137.50, 132.74, 132.68, 132.06, 128.84, 127.84, 127.68, 127.64, 126.79, 126.77, 125.66, 124.19, 122.39, 52.79, 52.20, 49.65. Mass (ESI-MS): m/z calcd. for $C_{17}H_{17}N_2O_2^+$ $[M]^+$: 281.128, found 281.132.

3-(carboxymethyl)-1-(naphthalen-2-ylmethyl)-1H-imidazol-3-ium bromide (H):

Compound G (900 mg, 2.49 mmol) was dissolved in 25mL 1M HCl and the solution was refluxed at 105°C for 3 hours. Water in the reaction mixture was then evaporated on a rotary evaporator and the solid so obtained was washed multiple times with ether and dried under high vacuum to give the product as a white solid. Yield= 846 mg, 97.8%. ^{1}H NMR (600 MHz, D_2O) δ (ppm) 8.77 (s, 1H), 7.85 (dd, J = 9.9, 6.3 Hz, 3H), 7.78 (d, J = 1.9 Hz, 1H), 7.54 – 7.49 (m, 2H), 7.38 (d, J = 1.9 Hz, 2H), 7.34 (dd, J = 8.5, 1.9 Hz, 1H), 5.41 (s, 2H), 4.92 (s, 2H). ^{13}C NMR (151 MHz, D_2O) δ (ppm) 170.18, 136.84, 133.03, 132.92, 130.87, 129.24, 128.10, 128.05, 127.81, 127.25, 127.11, 125.59, 123.94, 122.29, 53.18, 50.40. Mass (ESI-MS): m/z calcd. for $C_{16}H_{15}N_2O_2^+$ $[M]^+$: 267.113, found 267.115.

Synthesis of the Peptide (Nap-P):

The peptide was synthesized on Rink amide MBHA resin using standard Fmoc (9-fluorenylmethoxycarbonyl) solid phase peptide synthesis (SPPS) protocol. In a typical coupling, 3 equiv. of protected amino acid (with respect to the loading of the resin), 3 equiv. of HBTU, and 6 equiv. of DIPEA were taken in 5 mL of DMF (for 0.1 mmol scale with respect to the resin loading) and stirred for 5 minutes prior to addition of the mixture to the swelled deprotected resin. The reaction mixture was shaken for 60 min and the resin was washed several times with DMF. The Fmoc-deprotection was achieved by treatment of the resin thrice with 5 ml of 20% piperidine in DMF for 5 minutes followed by thorough washing of the resin with DMF and DCM. The Fmoc-deprotection and coupling steps were repeated until the designed peptide sequence was obtained. The resin with the loaded peptide was washed several times with DMF and DCM and dried. The dried resin was then treated with a mixture of freshly prepared mixture of 8.5:1:0.5 (TFA/TES/H_2O) and stirred for 1 h. The resin was finally washed with DCM several times. The cleavage cocktail and the washings combined were concentrated to a minimum volume on a rotary evaporator. The cleaved peptide was then precipitated from cold dry ether, centrifuged and lyophilized to get the crude peptide. Purification was done in a semi-preparative HPLC using a Luna 5 μm (C18) column (Phenomenex) and an eluent of acetonitrile and water starting at 5% ACN in H2O reaching at 100% ACN in 30 mins) to complete the chromatogram in 35 mins. (Yield = 65%)

MALDI-TOF: m/z calcd. for $C_{34}H_{45}N_{12}O_9^+$ $[M]^+$, 765.808; found 765.418.

2.4.3. Methods and Instrumentations

UV-Visible and Fluorescence Spectroscopy: UV-Visible spectra were recorded on a PerkinElmer Lambda 750 spectrometer, while fluorescence measurements were performed on a Cary Eclipse (Agilent) spectrophotometer.

Isothermal Titration Calorimetry (ITC): ITC was performed using a Nano-ITC instrument from MicroCal for determining the formation constants and thermodynamic parameters for the inclusion complexes. 1mM Nap-P solution in buffer (10 mM phosphate, pH 7) was injected in parts (each injection, 1.3 uL) at an interval of 2 mins from a 40 uL micro-syringe into the MV-CHO@CB[8] s(1:1) solution (0.05 mM, 200 uL) with constant stirring (300 rpm) at 298K. All the solutions were degassed prior to titration. The ITC thermogram showed a 1:1 binding ratio between MV-CHO@CB[8] and Nap-P, thus indicating the formation of the ternary complex.

Dynamic Light Scattering (DLS) Studies: The particle sizes of the assemblies were obtained at 298 K using a 632.8 nm He–Ne laser using Zetasizer Nano-ZS90 (Malvern). The stock solutions of assemblies were prepared in water and filtered through appropriate filters to remove dust particles, if present before the measurement. All the measurements were performed in triplicates.

pH Measurements: The pH curves were recorded on a Hanna HI 2210 pH meter equipped with HI1131 pH probe from Hanna.

Field Emission Scanning Electron Microscopy (FESEM): 5 μL of appropriate sample solution at specific time intervals during the pH cycle were cast on a silicon wafer and immediately freeze-dried to cease the kinetics of the pH cycle. FESEM images were then taken on a Gemini SEM 300 (Sigma Zeiss) instrument.

Field Emission Transmission Electron Microscopy (FETEM): 5 μL of the sample solution at specific time intervals during the pH cycle were cast on the carbon coated copper grid (300 mesh Cu grid with thick carbon film from Pacific Grid Tech, USA) and allowed to air dry for 2 minutes and then the excess sample was bloated with a tissue paper. The grid was then immediately freeze-dried and the FETEM images were taken in JEOL 2100F microscopes.

Atomic Force Microscopy (AFM): Sample solution at specific time intervals during the pH cycle were casted on a silicon wafer and freeze-dried before the experiment. AFM images were then taken on Oxford Cypher microscope.

Confocal Laser Scanning Microscopy (CLSM): Confocal laser scanning microscopic (CLSM) images and videos were recorded on a TCS SP8 microscope from Leica, Germany.

Preparation of CB[8] stabilized Host-Guest Ternary Complex:

To prepare 2 mL of 0.75 mM MV@CB[8] stock solution, appropriate amount of CB[8] (2.6 mg) and MV-CHO (0.75 mg) were taken in a 2 mL volumetric flask and MilliQ water was added to the mixture. The heterogeneous solution was then sonicated for 1 hour at 298 K. An equivalent amount of the peptide (Nap-P) was added to the solution of the binary complex and sonicated for 1 hour at 298 K. The solution was then kept undisturbed at 298 K for 1 day before utilizing for further experiments. The formation of the CB[8] stabilized charge-transfer ternary complex was confirmed by the appearance of a CT band at 390 nm as well as by ITC (Figure 2.1).

NMR Study for the pH dependent reversible formation of the supramolecular peptide amphiphile:

Stock solutions of the ternary complex (**1**) (1 mM in D_2O) and DA (100 mM in THF-d_8) were prepared. Solution containing equimolar amounts (0.5mM) of the ternary complex (**1**) and DA was prepared in D_2O and its NMR spectra was recorded. A drop (1 μL) of NaOD was then added to the above solution to induce the formation of imine bonds and thus the supramolecular peptide amphiphile and the NMR spectra was recorded again. Finally, few drops (5 μL) of DCl was added to the above solution to neutralize NaOD and break the imine linkages and the NMR spectra was recorded again. The disappearance of the aldehyde peak and the appearance of the imine peak and vice versa in basic and acidic medium, respectively indicate the formation and breakdown of the supramolecular peptide amphiphile.

Programming of the transient pH states for establishing a tunable pH Cycle:

Stock solution of Urease enzyme (2 mg/mL) was prepared in MilliQ water and stored at -20°C for further use. Gluconolactone (GdI) and urea were used in the solid form for all experiments. Urea beads were ground to a fine powder to facilitate easy dissolution in water. The required amount of urease (final concentration : 0.2 mg/mL) was added to MilliQ water and the pH of the solution was adjusted to ~5 using 1 M HCl solution. A solid mixture of GdL and urea in the required ratio was added in one portion to solution and were immediately dissolved by simple hand shaking. The change in pH was then monitored over time at 298 K.

pH Kinetics Study of transient vesicle formation:

Stock solutions of the ternary complex (**1**) (1 mM in water) and DA (100 mM in THF) were prepared. Equimolar amounts (0.1mM) of the ternary complex and DA were taken in water and mixed thoroughly. The requisite amount of urease (final concentration: 0.2 mg/mL) was added to the solution and the pH of the solution was adjusted to ~5 using 1M HCl solution. The pH cycle was initiated by addition of a 1:3 mixture of GdL and urea in solid state to the solution at 298 K. The solids

were dissolved in the solution by simple hand shaking and the pH changes were monitored over time.

Dynamic Light Scattering Kinetics Study of transient vesicle formation:

The solution containing equimolar amounts (0.1 mM) of the ternary complex and DA along with the required amount of urease (0.2 mg/mL) was acidified to pH 5 using 1M HCl solution and then filtered through a 0.22 μm syringe filter into a 3 mL quartz cuvette with 1 cm path length. A 1:3 mixture of GdL and urea were added to the solution and the solution was sonicated briefly to facilitate dissolution. DLS measurements were performed immediately and the change in the hydrodynamic size distribution with time was monitored at 298 K. All measurements were performed with a constant angle of 90° and the results were reported as Number Distribution to reflect the number of aggregates formed. All measurements were performed in triplicates.

Fluorescence Kinetics Study of the repeatability of the formation of the transient vesicle:

Stock solution (10 mM) of the hydrophobic dye DPH (Diphenylhexatriene) was prepared in THF. Equimolar amounts (0.1 mM) of the ternary complex (**1**) and DA were dissolved in MilliQ water containing 0.2 mg/mL urease and the pH of the solution was adjusted to 5 using 1M HCl solution. 10 μM of the hydrophobic dye DPH (Diphenylhexatriene) was added to the solution and then the pH cycle was started by addition of a 1:3 mixture of GdL and Urea. The solution was excited at 355nm (slit width= 10 nm) and the emission intensity was monitored at 438 nm (slit width= 10 nm) over a period of 250 mins.

Fluorescence Confocal Microscopy Studies:

Transient vesicle formation was performed as mentioned earlier but in the presence of Nile red and the phenomenon was monitored through CLSM. Nile red was used as a hydrophobic dye for fluorescence imaging as it specifically accumulates in the hydrophobic vesicle bilayer and shows fluorescence upon vesicle formation. The sample was excited at 488 nm and the fluorescence emission was observed at 549 nm - 662 nm over a period of 120 mins at 298 K.

Particle Count Analysis from CLSM:

The particle count from the CLSM images obtained at different time points were analysed using ImageJ software. In particular, the images were converted to 8-bit format and visible particles were counted with threshold level set at 20, 25 and 30. The particles having a minimum object dimension of 2, 4, 6, 8 and 10 px^2 were considered for particle count analysis.

भारतीय प्रौद्योगिकी संस्थान गुवाहाटी
Indian Institute of Technology Guwahati

Chapter 3

Controlling the Lifetime of Cucurbit[8]uril based Self-Abolishing Nanozymes

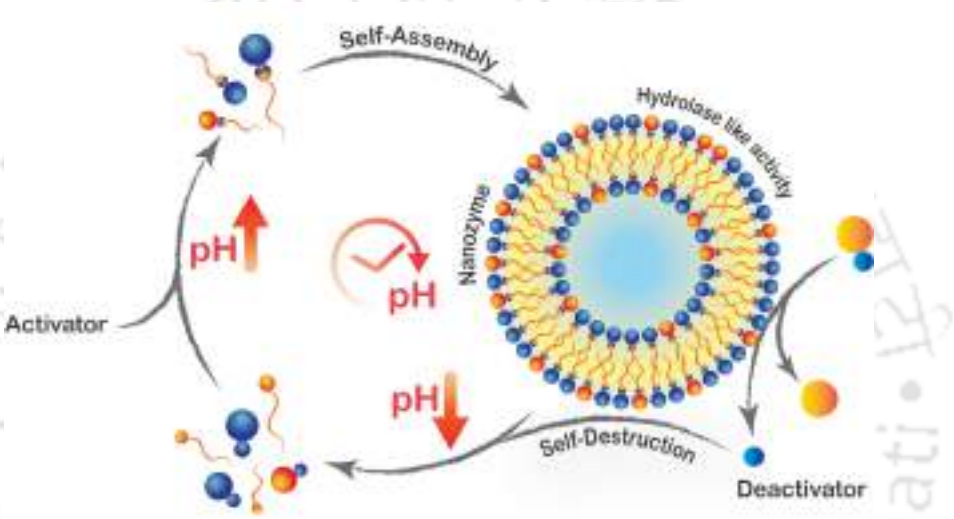

भारतीय प्रौद्योगिकी संस्थान गुवाहाटी
Indian Institute of Technology Guwahati

3.1. Introduction

Self-regulatory feedback and feedforward mechanisms are ubiquitous in living systems. These feedback loops help in maintaining homeostasis by controlling various chemical signalling pathways.[142-144] For example, signal amplification in positive feedback loops leads to enhanced secretion of oxytocin during child birth[145] and rapid activation of platelets for clotting[146] in the event of an injury. On the other hand, negative feedback loops exert a decelerating effect on certain metabolic processes that help in maintaining a stable physiological environment through regulation of body temperature, blood pressure, and blood sugar level, among other processes.[147] Likewise, in the self-inhibitory feedback mechanism, the activity of certain enzymes is inhibited by their own metabolic end product. Feedback inhibition helps in modulating the activity of the enzymes according to the need of the cell and prevents accumulation of harmful metabolites in the cellular micro-compartments.

Akin to the biochemical reaction networks, a few instances of chemically triggered feedback loops have been exploited in synthetic organic systems as well.[148-151] Chemical reaction relays in synthetic systems have profusely been used for designing out-of-equilibrium self-assemblies wherein rationally designed feedback mechanisms regulate the lifetime of the assemblies.[8, 38, 41, 49, 152-155] These non-equilibrium systems, however, invariably employ a slow deactivating agent as a key component of the dissipating reaction and thus, the concentration of the deactivator and/or the rate of the backward dissipative reaction dictates the lifetime of the self-assembly. Biomimetic transient self-assembly processes driven by negative feedback reaction relays wherein the self-assembled structures catalyse their own decomposition have rarely been explored and thus, development of autocatalytic self-destructive molecular assemblies that follow non-equilibrium kinetic pathways still remain highly elusive. Moreover, with proper adjustment of the self-inhibitory activity, control over the lifetime of the assemblies can be achieved without the need of any external deactivating agent.

Environmental factors such as pH, temperature, ionic and redox strength play key roles in driving the self-assembly of supramolecular ensembles with emergent functional attributes and have been exploited on many occasions to generate transient self-assembled nanostructures.[29, 30, 91, 96, 156] Chemically triggered cyclic pH changes have been exploited as an efficient technique to instigate self-assemblies in a temporally controlled fashion.[31, 81, 86, 157-159] Following our previous findings[158], herein, we report a cucurbit[8]uril (CB8)[124, 131] based supramolecular peptide amphiphile (SPA)[160, 161] with an intermediate pH responsive imine linkage that assembles into transient vesicles with hydrolase like catalytic properties (nanozyme) under alkaline conditions. The nanozyme catalyses its own degradation owing to the generation of deactivating acidic products (and thereby

changing the pH) in the system (Scheme 3.1). Moreover, by simple changes in the headgroup composition or by changing the substrate for the catalysis, control over the lifetime of the nanozyme can be achieved for a wide time range.

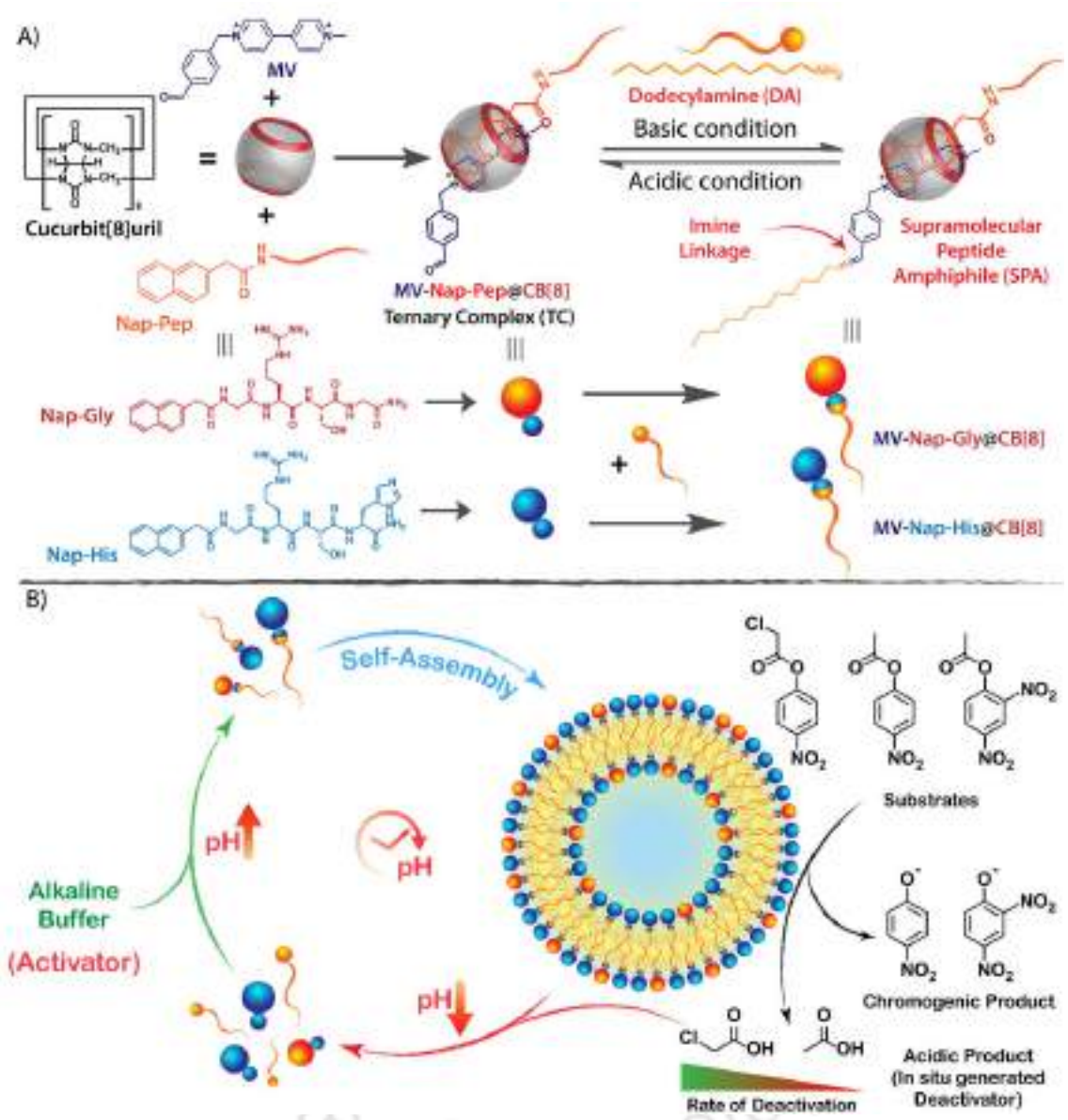

Scheme 3.1. Chemical structures of different components and graphical presentation of the self-inhibitory feedback driven temporal formation of a CB[8] assisted supramolecular peptide amphiphile and its vesicles.

3.2. Results and Discussion

3.2.1. Design of the SPA and the Corresponding Vesicle Formation

The vesicle formation by CB[8] assisted ternary complexation of the asymmetric viologen amphiphile and an electron rich second guest is very well documented in the literature.[125-127, 132, 140] We took the help of this phenomenon and designed our transient nanozyme accordingly. As depicted in Scheme 3.1A, the head group of the SPA was constructed with the help of well-established hetero-ternary complex formation by CB[8].[125, 127, 141] An electron rich guest for CB[8] was

designed wherein naphthalene is connected to a hydrophilic catalytic peptide sequence bearing Histidine (His) at the C-terminal (Nap-His). The naphthalene unit of the peptide forms a 1:1:1 heteroternary complex (termed TC, hereafter) with electron deficient viologen (MV) units inside the hydrophobic cavity of CB[8]. The complexation is stabilized through charge transfer interaction between the naphthalene and viologen units.[133] It is worth mentioning here that entrance of both the guests from the same side of CB[8] is not energetically favourable mainly because of the steric crowding. Moreover, the ternary complexation where guests enter the CB[8] cavity from opposite directions is very well documented in the literature.[124, 162, 163] The peptide was designed in a way to incorporate catalytic amino acid residues His and Serine (Ser) commonly found in the catalytic pockets of hydrolases to induce hydrolase like catalytic activity.[164, 165] The presence of Arginine (Arg) unit not only provides hydrophilicity but also enhances substrate binding because of its strong H-bond donating propensity.[165] On the other hand, the viologen units (MV) carry an aldehyde group at one end. The incorporation of this aldehyde unit was judicially done to form imine linkages with alkyl amine (dodecylamine, DA) and form the SPA as discussed later.

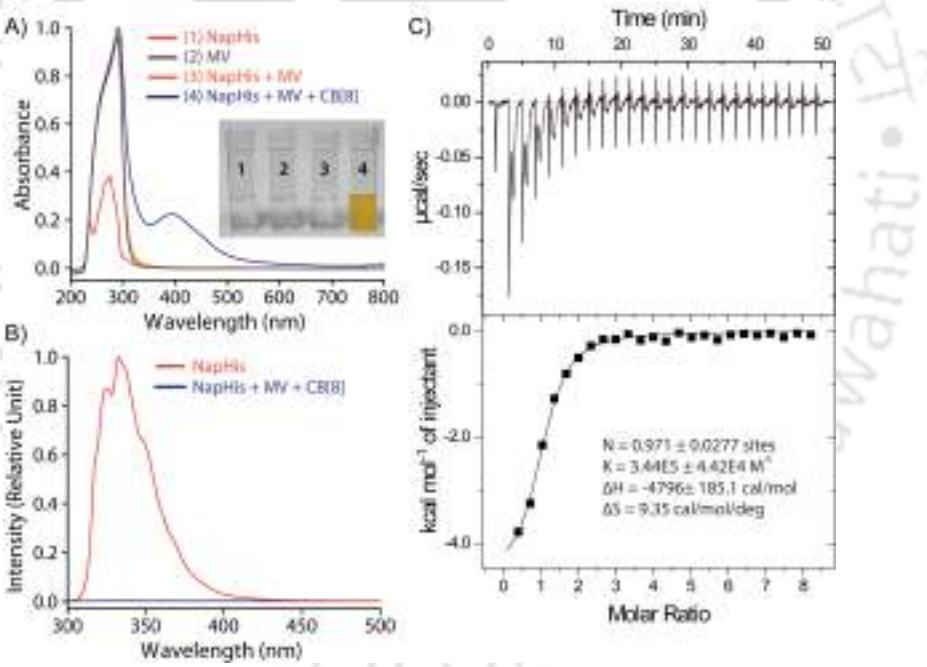

Figure 3.1. Formation of charge transfer complex as observed from **A)** UV-Visible spectra, and **B)** Fluorescence spectra of different components of TC (0.2 mM), **C)** Isothermal Titration Calorimetry (ITC) thermograms (top) and binding isotherms (bottom) of Nap-His@CB[8] with MV at 298 K

Formation of the TC was monitored utilizing various standard techniques. UV-Visible absorption spectra of 1:1:1 CB[8], Nap-His and MV showed the appearance of the characteristic charge transfer band at 394 nm which was not present for any other combinations as can be seen in Figure 3.1A.[133] A prominent colour change was also observed when all these three components were mixed and confirms the formation of the CT complex (inset of Figure 3.1A). Further, the

emission of the naphthalene moiety of Nap-His at 333 nm decreased drastically upon formation of TC with MV and CB[8] which indicates the incorporation of MV and Nap units of the peptide inside the CB[8] cavity (Figure 3.1B).[134, 166] Moreover, isothermal titration calorimetric (ITC) titration of the 1:1 Nap-His@CB[8] solution with the MV solution shows a 1:1 binding between these two components with a binding constant of 3.44×10^5 M^{-1} and thereby confirm the formation of TC (Figure 3.1C).

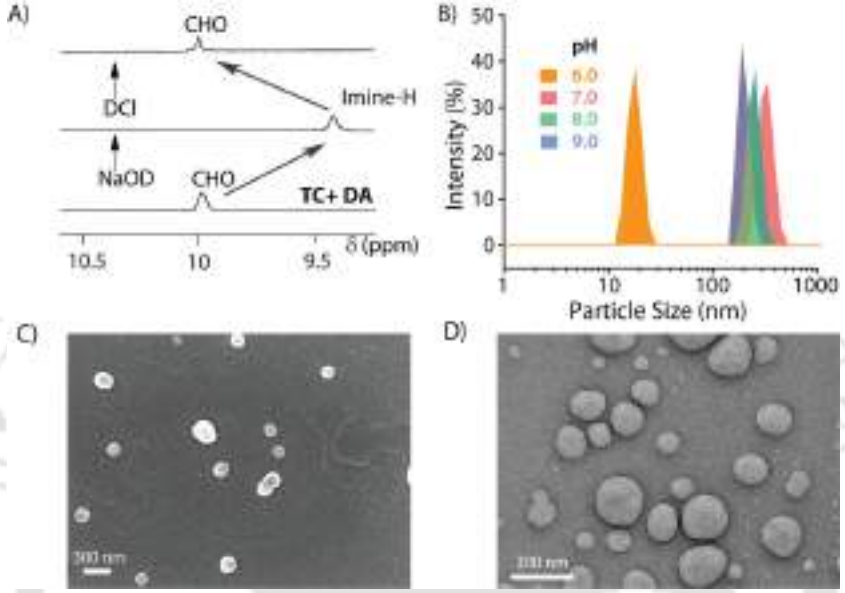

Figure 3.2. Formation of the SPA vesicles. **A)** ^{1}H-NMR showing formation/disruption of the imine linked SPAs, **B)** DLS profile of assemblies formed at different pH values, **C)** FESEM, and **D)** FETEM images of the vesicles formed at pH 8.

Next, the formation of the SPA and the corresponding vesicles was confirmed. The imine bond formation under aqueous basic pH and hydrolysis of the same at lower pH are well documented in the literature.[138] We have previously shown that such head groups result in SPAs upon linking with dodecylamine (DA) at basic pH and assembles into higher order aggregates.[158, 167] The ^{1}H NMR study shows the disappearance of the aldehyde signal (δ = 9.96 ppm) and appearance of the imine peak (δ = 9.38 ppm) as we move from neutral to basic condition and confirms the formation of the imine bond between the aldehyde group of MV and the amine of DA (Figure 3.2A). Upon acidification of the system, the disappearance of the imine signal and reappearance of the aldehyde proton peak demonstrates the instability of the imine linkage under acidic conditions. Dynamic light scattering (DLS) studies showed an increase in the hydrodynamic size of the assemblies generated by TC and DA from ~20 nm at pH 6 to ~250 nm at pH 7-9, indicating the formation of ordered assemblies under alkaline conditions (Figure 3.2B). The vesicular nature of the assemblies was ascertained by microscopic techniques like field emission scanning electron microscopy (FESEM) and field emission transmission electron microscopy (FETEM) (Figure 3.2C and

D). A thin dark boundary around the spherical aggregates of ~200 nm size in the FETEM images confirmed the formation of vesicles.

3.2.2. Catalytic Activity of the Vesicular Nanozymes

It is well known that the enzyme mimicking peptides show significant improvement in the catalytic efficiency when they are in the aggregated state compared to that in the monomeric state.[168] In the present case, the proximate localization of the His groups on the surface of the vesicles was expected to show cooperative interactions amongst them wherein a pair of neighbouring His units simultaneously can act as a nucleophile and proton donor and thereby enhance the rate of hydrolysis. To establish the catalytic ability of the SPA vesicles, a pH irresponsive control viologen derivative, hexadecylmethylviologen (HDMV, Synthesized and characterized following literature protocol)[169], was used to form the control SPA using CB[8] and Nap-His. The resultant pH insensitive SPA vesicles were used to assess the catalytic proficiency of the proximal histidine units. A bell-shaped curve for the rate of hydrolysis of *p*-nitrophenylacetate (pNPA) at different pH values was obtained with a maximum at around pH 7 (close to the pK_a of His) (Figure 3.3A). These observations pointed towards the cooperative catalysis mechanism.[170-172]

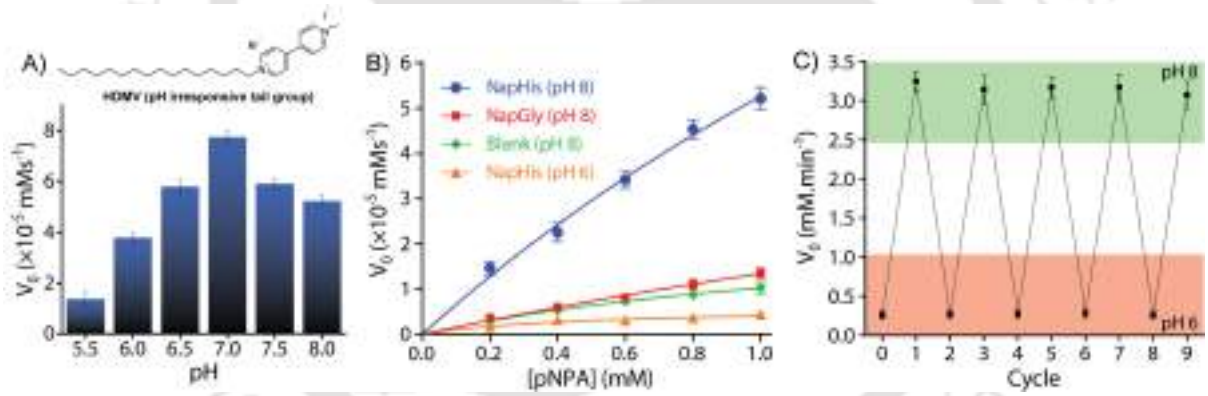

Figure 3.3. pH dependent catalytic activity of the nanozymes **A)** Rate of hydrolysis of p-nitrophenyl acetate (pNPA) substrate using Nap-His head group and pH irresponsive (HDMV) tail group at different pH values. [CB[8]]/ [Nap-His]/ [HDMV]=100 µM, [pNPA]= 1mM. **B)** Michaelis Menten plot for hydrolysis of pNPA using NapHis/NapGly (Control) head group by the assembled/disassembled nanozyme (100 µM) at pH 8/6, respectively. **C)** Switchable catalytic activity of the nanozyme (100 µM) at pH 6 and 8 using 0.5 mM pNPA.

However, when the catalytic activity was monitored in the pH responsive system (TC + DA), it displayed negligible catalytic activity at pH 6 (V_{max} = 0.378 µM min^{-1}, Figure 3.3B). At this pH, the formation of the SPA and the consequent vesicles is not possible as the imine bonds are cleaved under acidic condition.[158] Thus, the molecules (TC and DA) remain in non-associated form and thereby the cooperative interactions are essentially absent to promote effective catalysis. Formation of the vesicles at pH 8, however, led to a 38-fold jump in activity (V_{max} = 14.388 µM min^{-1}) signifying the cooperative effect in the vesicular aggregates. Moreover, switching the pH of the solution

between acidic and alkaline range allowed efficient switching of the activity of the nanozyme over multiple cycles (Figure 3.3C). To confirm that the values obtained are not arising from the auto-hydrolysis due to the basic conditions, two control experiments were performed. The hydrolysis rates in pH 8 buffer (V_{max} = 1.562 μM min^{-1}) and the activity of the catalytically inert control SPA (V_{max} = 5.01 μM min^{-1}) containing glycine (Gly) instead of histidine (Nap-Gly, Scheme 3.1) in the head group were found to be significantly lower than those of the vesicles with Nap-His at the surface.

3.2.3. Temporal Existence and Self-destruction of the Nanozyme

To introduce transient and self-destructing features into the hydrolase nanozyme, a self-inhibitory pH feedback response was established by using *p*-nitrophenol and 2,4-dinitrophenol ester substrates that generate acidic entities upon hydrolysis. These esters remain stable in a solution of the inactive nanozyme components (TC and DA) at pH ~5 but undergo hydrolysis as soon as the nanozyme formation is triggered by the addition of a specified amount of alkaline TRIS buffer (pH 9) as an activator. The nanozyme catalyses the generation of acid from the esters which in turn perturbs the environment conducive to its own existence. Thus, a pH drop is registered as long as the nanozyme is active and below a certain pH value, the nanozyme is dissipated by its own catalytic by-products. pNPA underwent very slow hydrolysis in the presence of the nanozyme at pH 8 (V_0 = 3.327 ± 0.148 μM min^{-1}) as compared to *p*-nitrophenylchloroacetate (pNPCAA) (V_0 = 19.719 ± 0.255 μM min^{-1}) (Figure 3.4A). However, both the esters displayed meagre hydrolytic decomposition at acidic pH. The pH clock established by adding 1 mM pH 9 TRIS buffer to 100 μM nanozyme solution at pH 5 containing 5 mM pNPA or pNPCAA led to a rapid jump in pH followed by a slow decay. It is to be noted that the concentrations mentioned (for buffer and substrates) here and hereafter represent the overall concentrations of the components in the system and not of the stock solutions added.

Owing to the slow hydrolysis of pNPA to acetic acid, the pH dropped to 6 in 194 mins whereas pNPCAA (chloroacetic acid as the hydrolysis product) presented a much faster pH drop to 5.73 in 34 mins and thereafter a gradual decline owing to slow background hydrolysis of pNPCAA at low pH (Figure 3.4B). The faster drop in pH in case of choloracetic acid (pKa = 2.68) as compared to acetic acid (pKa = 4.56) may also be attributed to the stronger acidic nature of the former.[173] On account of the faster kinetics and more prominent pH change by pNPCAA, it was used as a substrate for subsequent pH kinetic studies. Time-gated formation of the SPAs and their subsequent hydrolysis were further monitored through FESEM microscopic analysis. In this case, freeze dried samples of the system (Nap-His + CB[8] + MV + DA + pNPCAA) collected at different time points along the course of the pH cycle were analysed and as can be seen from Figure 3.4C, no self-assembled structures were visible prior to the initiation of the pH cycle. After initiation, as the pH

clock progressed, vesicular assemblies were observed which slowly disintegrated with the course of time, indicating the transient formation of the nanozymes.

The in situ generated *p*-nitrophenol (pNP) chromogenic product served as a pH indicator and enabled visual monitoring of the pH cycles. pNP is colourless at acidic pH (pH < 6) and shows absorption maxima at 318 nm. *p*-Nitrophenolate ions, formed in alkaline solution (pH > 7), however, strongly absorbs at λ_{max} = 400 nm and appears yellow in colour. The absorption intensity at 318 nm and 400 nm, thus, gives an approximation of the pH of the solution. The isosbestic point of pNP at 348 nm, on the other hand, is pH independent and allows quantification of the amount of pNP present/generated in the solution. UV-visible spectrophotometric analyses of the designed pH clock showed that upon adding 0.5 mM pH 9 TRIS buffer to 1 mM pNPCAA, the nanozyme (100 μM) resulted in a significant decrease in absorbance at 400 nm and an enhancement in absorbance at 318 nm over a period of 70 minutes (Figure 3.4D and 4E). The blank solution (without nanozyme), however, displayed only slight fall in the absorbance at 400 nm (Figure 3.4D (inset) and 3.4E). Although, both systems showed increment in absorbance at 348 nm indicating the formation of pNP, as expected, the extent of the increment in case of the nanozyme was significantly higher.

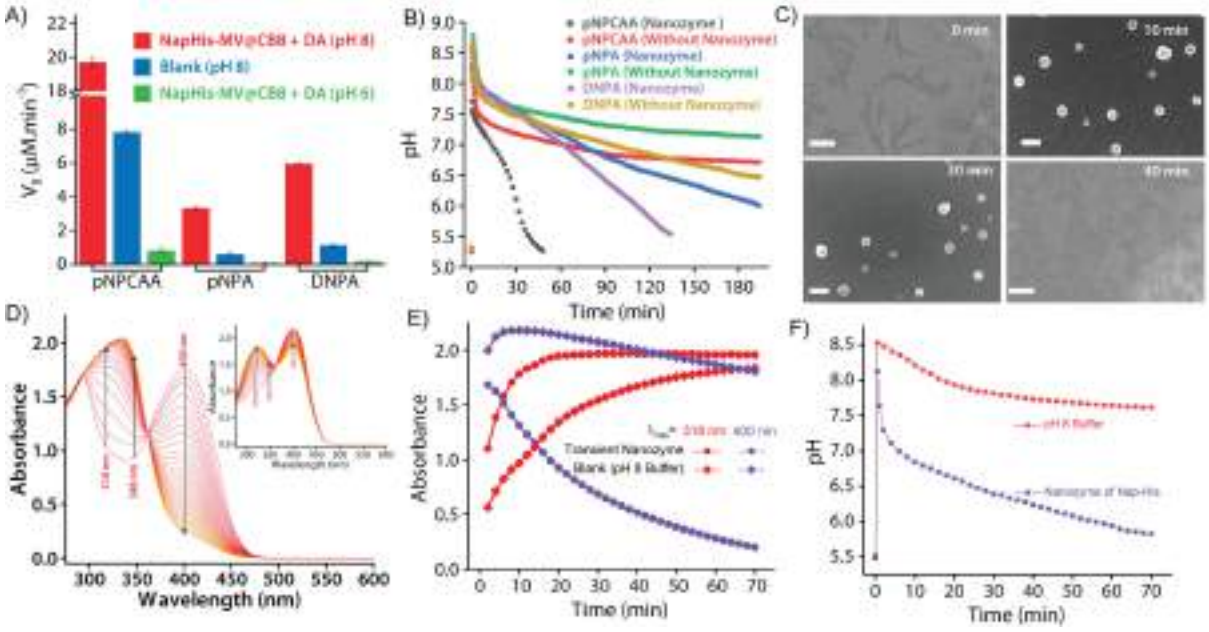

Figure 3.4. A) Rate of hydrolysis of pNPA/pNPCAA (0.5 mM) by the assembled/ disassembled nanozyme (100 μM) at pH 8/6, respectively. **B)** pH clock with/without the nanozyme (100 μM) using pNPA/pNPCAA/DNPA (5 mM) as substrates and 1mM pH 9 TRIS buffer as the activator. **C)** FESEM images of the transient vesicles furnished by SPAs accommodating equimolar (0.1 mM) amounts of CB[8], Nap-His and MV–DA formed during the course of the pH cycle (scale bar = 500 nm). [pH 9 TRIS buffer] = 1 mM, [pNPCAA] = 5 mM. **D)** Time dependent UV-Visible spectra obtained at different time intervals after the addition of 0.5 mM pH 9 TRIS buffer to a solution of 1 mM pNPCAA in the presence, and (Inset of **D**) absence of the nanozyme (100 μM), respectively. **E)** Change in absorbance at λ_{max}= 318 nm and 400 nm as observed from D. **F)** Time dependent variation in pH for the systems in **D**.

Furthermore, HPLC kinetics studies using the nanozyme indicated gradual consumption of pNPCAA and formation of pNP as the pH cycle progressed (Figure 3.5A-C). These results show that the nanozyme simultaneously catalyses the hydrolysis of pNPCAA and leads to a fall in the pH of the solution to the point when the nanozyme is no more existent. The uncatalyzed alkali mediated hydrolysis of pNPCAA in the absence of the nanozyme failed to produce similar results. These observations were further corroborated by the pH kinetics experiment where a significant drop in pH (8.29 to 5.81) was observed in case of the nanozyme as compared to the blank solution (8.51 to 7.23) (Figure 3.4F).

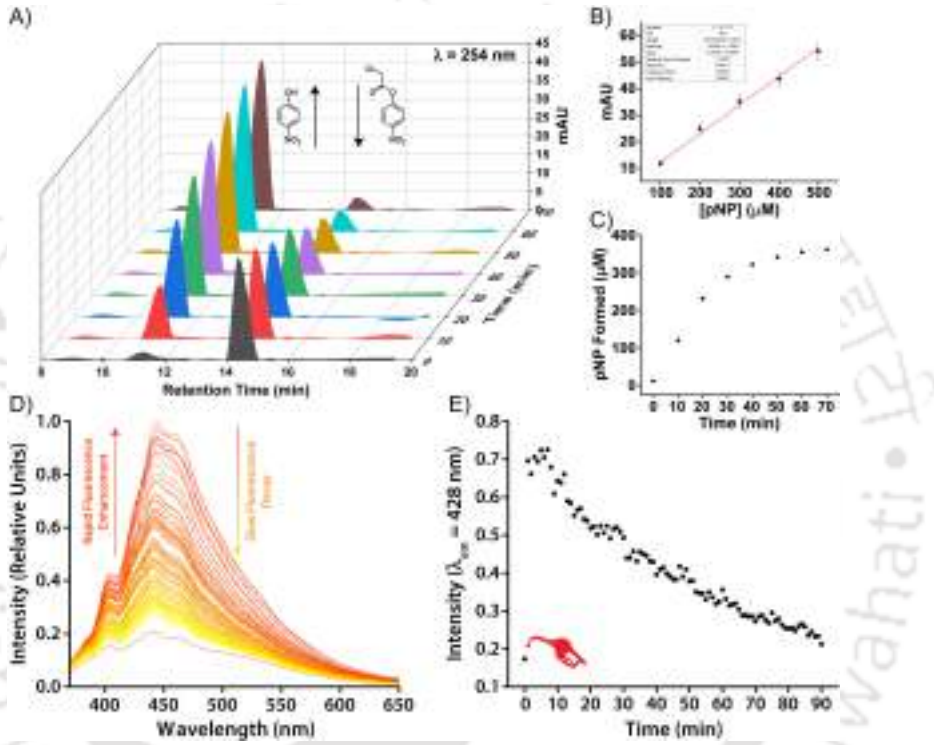

Figure 3.5. A) Time dependent HPLC chromatograms showing the nanozyme catalysed hydrolysis of pNPCAA to pNP, **B)** Standard plot for pNP from HPLC, **C)** Time course generation of pNP from pNPCAA through the nanozyme catalysed ester hydrolysis reaction, **D)** Time dependent emission spectra of DPH (10 μM) at different time intervals during the course of the pH cycle. [pH 9 TRIS Buffer] = 0.5 mM, [pNPCAA] = 1 mM, **E)** Change in the emission intensity at λ_{em} = 428 nm (λ_{ex} = 355 nm, Slit width (Ex./Em. = 5/5 nm) along the course of the pH cycle.

Also, the transient formation of the nanozyme was confirmed by time dependent fluorescence kinetics studies using diphenylhexatriene (DPH) as a lipophilic probe.[21] The emission intensity of DPH enhances when trapped in vesicular aggregates.[21, 158] In the present case, as expected, DPH showed enhanced emission upon addition of the activator as it gets trapped inside the vesicles (Figure 3.5D and E). The enhanced emission was followed by a slow decay indicating the disruption of the vesicles. The transient aggregation process was also monitored through confocal laser scanning microscopy (CLSM) using Nile Red as fluorescent probe which shows enhanced emission upon intercalation in lipid bilayers.[158] Appearance of fluorescent assemblies shortly after

the addition of the activator that slowly disappeared within 60 minutes indicated the formation of transient vesicular nanozymes. (Figure 3.6A). Particle count analysis of the CLSM images also confirmed the transient emergence of vesicular aggregates (Figure 3.6B).

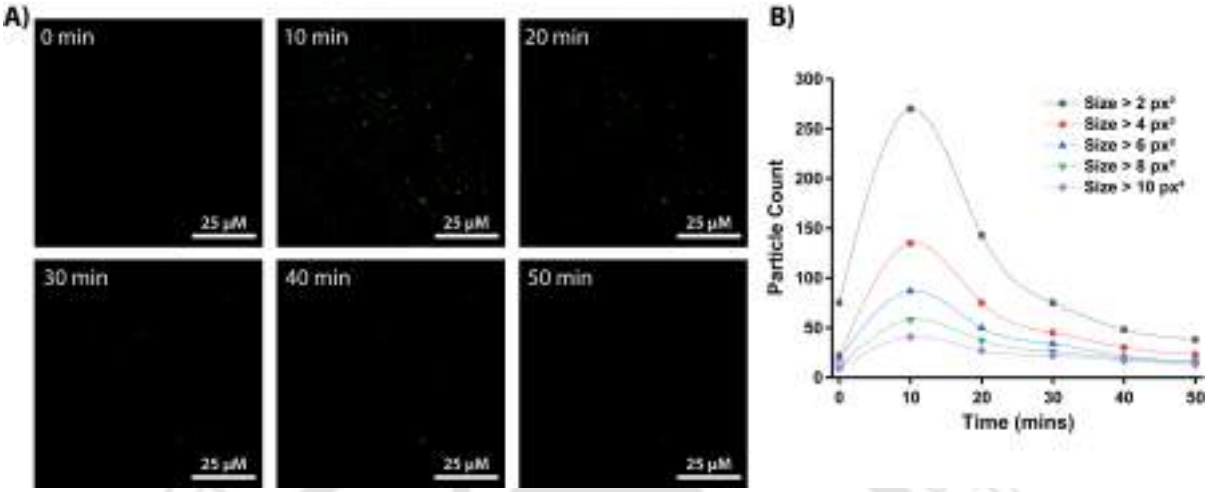

Figure 3.6. A) CLSM images showing the transient formation of Nile Red (NR) (10 μM) encapsulated vesicular nanozymes. [CB8]/[Nap-His]/[MV]/[DA]= 100 μM, [pNPCAA]= 5 mM, [pH 9 TRIS buffer]= 1 mM, **B)** Statistical analysis of the images obtained by confocal fluorescence microscopy.

3.2.4. Controlling the Lifetime

As discussed in the Introduction, though creation of artificial transient assemblies has been reported on several occasions in the last decade, not much attention has been paid to create systems where the lifetime of these assemblies can be catalytically controlled by the assemblies itself. In the present work, we put an effort to gain control over the lifetime of the formed nanozyme through a self-inhibitory mechanism. The change in the pH of the system is a good indicator of the existence/disappearance of the nanozyme. As no particle distribution corresponding to the vesicles was observed at pH 6 in the DLS measurement (Figure 3.2B), we consider reaching pH 6 by the system during the deactivation process as a good consideration of the complete destruction of the nanozymes. Thus, the corresponding timeframe can be considered as the lifetime of the transient nanozymes.

As mentioned earlier, Nap-Gly containing vesicles displayed little catalytic behaviour and thus we envisioned that a combination of Nap-His and Nap-Gly peptides to construct the nanozyme may allow us to tune the lifetime of the nanozyme. As can be seen from Figure 3.7A, various combinations of Nap-His/Nap-Gly containing head groups were tested for this purpose using 3 mM pNPCAA as the substrate. With the increase in Nap-Gly content, the nanozymes displayed progressively lowering activities and longer lifetimes (Figure 3.7A and B). The presence of Nap-Gly along with Nap-His disrupts the cooperative effect that was gained by the assembly process in case of the Nap-His based nanozyme. Thus, by varying the head group composition, a wide range of

lifetime (52 min to 145 min) could be achieved. Moreover, the purely NapGly containing nanozyme presented an insignificant fall in pH (similar to the blank solution) and retained its vesicular form over an extended period of time.

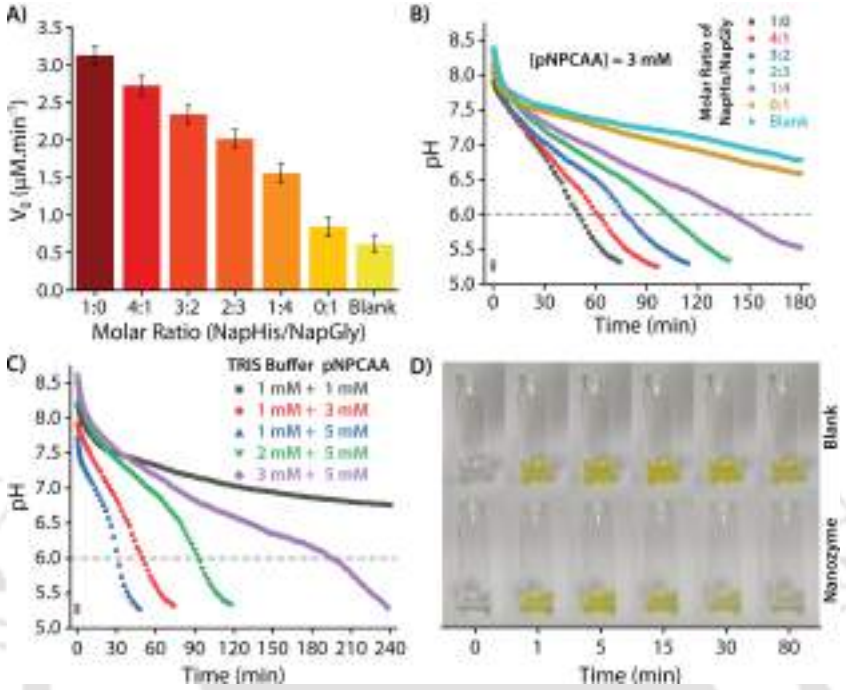

Figure 3.7. A) Rate of hydrolysis of pNPA (0.5 mM) using different molar ratio of NapHis/NapGly ([Nanozyme]= 100 µM) in pH 8 buffer, **B)** pH clock using different molar ratios of NapHis/NapGly nanozyme (100 µM), 1 mM pH 9 TRIS buffer and 3 mM pNPCAA, **C)** pH clock using various molar ratios of pH 9 TRIS buffer and pNPCAA in the presence of 100 µM nanozyme, **D)** Photographic images of the nanozyme and blank (without nanozyme) solution captured along the course of the pH clock triggered by using 0.5 mM pH 9 TRIS buffer and 1 mM pNPCAA.

Another approach to tune the lifetime of the transient state is to vary the molar ratio of the activator (pH 9 TRIS buffer) and the substrate (pNPCAA). For a fixed concentration of TRIS buffer (1 mM), higher concentration of pNPCAA resulted in shorter lifetimes of the nanozymes owing to the faster rate of hydrolysis (Figure 3.7C). Higher concentrations of TRIS buffer against a fixed concentration of pNPCAA (5 mM), however, resulted in longer lifetimes on account of decrease in the ability of the generated acid to neutralize higher concentrations of the alkaline buffer. Visual inspection of the nanozyme and blank (without nanozyme) solutions subjected to the pH cycle by adding 0.5 mM pH 9 TRIS buffer and 1 mM pNPCAA showed that the nanozyme as well as the blank solution, both turned yellow soon after the addition of the activator owing to the formation of pNP (Figure 3.7D). However, as the pH became acidic in case of the nanozyme solution, the solution slowly turned clear whereas the blank solution retained its yellow colour over a prolonged duration of time. This clearly indicates the hydrolytic prowess of the nanozyme which is in fact responsible for driving the pH cycle.

As we were able to construct nanozymes with a lifetime range of 34 mins to more than 3 hours, we focused on preparing systems that can exist for a much shorter period. Working with esters of stronger acids like trifluoroacetic acid (pK_a = 0.0), trinitrobenzoic acid (pK_a = 0.42) or dichloroacetic acid (pK_a = 0.87) etc. is extremely difficult both in terms of synthesis and extremely fast hydrolysis of the corresponding esters.[173] In this regard, we realized that the hydrolysis product, *p*-Nitrophenol, though acidic in nature, is not necessarily contributing toward the acidification of the system mainly because of its higher pKa value (7.2).[173] However, if both the products can contribute (the acid and the phenol) to the self-destruction of the nanozyme, a much lower lifetime can be achieved. We found that dinitrophenol (DNP) has a much lower pK_a (4.09)[174] compared to the lowest pH (< 6)where the nanozyme can exist. Based on this fact, acetic acid ester of DNP was prepared (DNPA) and used as a substrate for the nanozyme. The chloroacetic ester derivative of DNP, however, was hydrolytically unstable and underwent hydrolysis even in the absence of the vesicular nanozyme. Based on the results obtained from experiments with pNPCAA, a combination of 1 mM TRIS buffer and 5 mM DNPA were used (Figure 3.4B). As expected, a fast decrease in the pH was observed as compared to the case of pNPA (lifetime, 194 mins) and the entire process took ~110 mins to reach a pH value of 6. Although, we were not able to achieve a shorter lifetime than that in the case of pNPCAA, the use of different substrates significantly enhanced the scope of tuning the lifetimes of the nanozymes.

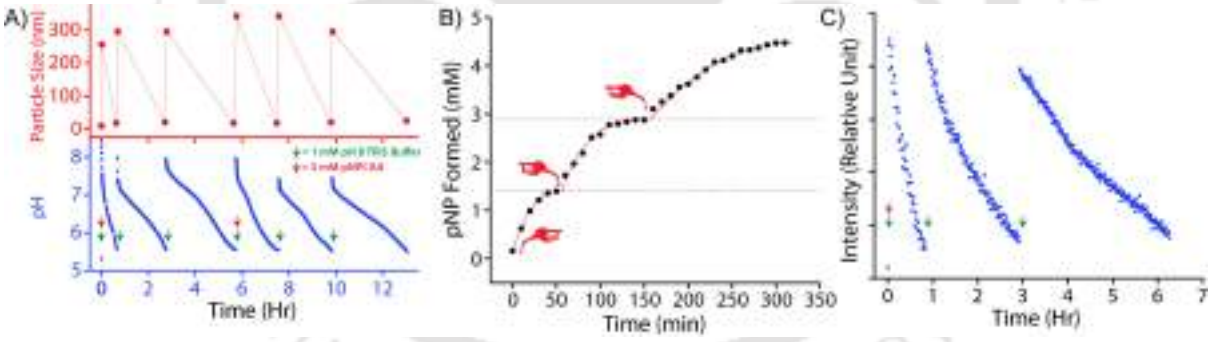

Figure 3.7. A) Time dependent variation in pH (Bottom) and particle size (Top) across six consecutive pH cycles. Note: 1 mM pH 9 TRIS buffer was added to 100 µM nanozyme solution to initiate each cycle and 5 mM pNPCAA was added before initiating the 1st and 4th cycle, **B)** Time dependent generation of pNP from pNPCAA by the nanozyme across three pH cycles as determined by HPLC measurements, **C)** Fluorescence kinetics across three consecutive cycles using DPH lipophilic probe. [DPH]= 10 µM, λ_{ex}(DPH) = 355 nm, λ_{em}(DPH) = 428 nm.

3.2.5. Recyclability

An interesting feature of natural enzymes is their reactivation and recyclability under favourable environmental conditions. Akin to natural counterparts, the vesicular nanozymes could be reactivated by fresh addition of the activator after consecutive pH cycles. Briefly, addition of 1 mM TRIS buffer (pH 9) to the nanozyme solution (100 µM) containing 5 mM pNPCAA triggered a pH cycle that ended in 34 mins (Figure 3.8A). Subsequent addition of 1 mM TRIS buffer enacted two

more consecutive pH cycles without any further addition of pNPCAA. The lifetimes of the successive pH cycles, however, increased owing to the consumption of pNPCAA in each cycle. Fresh addition of 5 mM pNPCAA and 1 mM TRIS buffer after the third cycle produced similar cyclic changes to those observed initially (first cycle).DLS measurements at different time points along the course of the pH clocks indicated the transient and repeated formation of the nanozymes. HPLC kinetics experiment also presented progressive formation of pNP towards the beginning of the pH cycle and slower kinetics at the end of the pH clock (Figure 3.8B). Addition of TRIS buffer after the first pH cycle again resulted in a jump in the rate of formation of pNP, indicating the regeneration of the nanozymes. Kinetic fluorescence experiment using DPH also indicated the reproducibility of the system across three pH cycles (Figure 3.8C). It is worth mentioning that although the nanozyme displayed appreciable reproducibility owing to the self-catalysed degradation pathway, the accumulation of wastes in the system led to minor dampening in subsequent pH cycles.

3.3. Conclusions

In conclusion, an imine linked CB[8] based pH responsive SPA is reported which displays alkaline buffer (activator) triggered vesicular assembly in aqueous medium. The histidine groups localized on the surface of the vesicles impart catalytic properties to the vesicle through a cooperative mechanism. The catalytic prowess of the assembled nanozyme leads to in situ generation of the deactivating agent (acid) from the substrates and results in disintegration of the nanozyme due to hydrolysis of the imine linkages at acidic pH. The denatured nanozymes could be reactivated by adding fresh pulses of the activator and the transient formation of the nanozymes could be repeated across multiple pH cycles. Importantly, we have shown how to modulate the lifetime of the nanozymes. By varying the composition of catalytic groups on the nanozyme surface, the catalytic efficiency can be controlled and thereby formation of acid and subsequent self-destruction of the nanozyme can be manipulated. Another approach is to vary the substrate for the catalytic reaction and thereby increase or decrease the strength of the generated acid. The rate of production of the acid and its strength eventually determines the lifetime of the nanozyme. In another approach, the ratio of the activator (buffer) and the substrates was varied to achieve a wide range of lifetime for the nanozyme. The self-inhibitory feedback mechanism employed herein presents a new approach to generation of transient functional assemblies and may serve as a novel addition to the progressively developing field of out-of-equilibrium systems chemistry.

3.4. Experimental Section

3.4.1. General Information and Materials

2-Naphthaleneacetic acid, 4,4'-Bipyridyl, Methyl Iodide, 4-Nitrophenol, 2,4-Dinitrophenol, Triethylsilane (TES), 1,6-Diphenyl-1,3,5-hexatriene (DPH) and dodecylamine were purchased from Sigma-Aldrich (USA). Trifluoroacetic acid (TFA) were obtained from Spectrochem (India). Terephthalaldehyde, Chloroacetic acid were acquired from TCI Chemicals (India). Sodium Borohydride were procured from SRL (India). Cucurbit[8]uril (CB[8]) was synthesized following a previously published protocol[141] and characterized accordingly. Rink amide MBHA resin, protected amino acids and coupling reagents were purchased from Novabiochem. HPLC-grade dimethylformamide (DMF), dichloromethane (DCM) and acetonitrile (ACN) were procured from Spectrochem (India) and Fisher Scientific (India). Solvents were dried whenever required according to the reported procedures. Milli-Q water with a conductivity of less than 2 μScm^{-1} was used for all sample preparations. 60-120 mesh silica gel (SRL) was used for column chromatography. Chromatographic purifications were performed on a Luna 5 µm (C18) column (Phenomenex) using a Dionex Ultimate 3000 HPLC. ^{1}H NMR and ^{13}C NMR spectra were recorded using a Bruker Ascend 600 MHz (Bruker, Coventry, UK) spectrometer and referenced to deuterated solvents. Coupling constants (J values) are reported in hertz, and chemical shifts are reported in parts per million (ppm). Multiplicities are reported as follows: s (singlet), d (doublet), t (triplet), m (multiplet), and br (broadened). Electrospray ionization mass spectrometry (ESI-MS) were performed with a Q-Tof-Micro Quadrupole mass spectrometer (Micromass) and data were analyzed using the built-in software.

3.4.2. Synthesis and Characterization

1-(4-formylbenzyl)-1'-methyl-[4,4'-bipyridine]-1,1'-diium (MV):

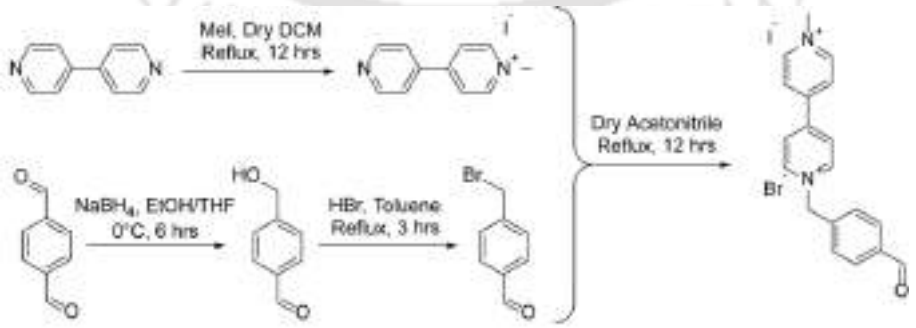

Scheme 3.2: Synthetic procedure of MV

The aldehyde appended viologen derivative, MV, was synthesized following our previously reported protocol[158] and subsequently characterised.

4-nitrophenyl 2-chloroacetate (pNPCAA):

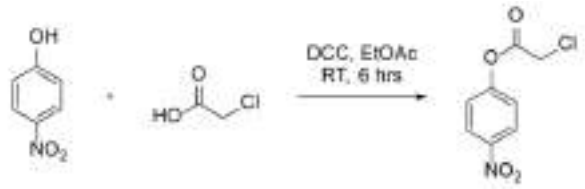

2-chloroacetic acid (500 mg, 5.291 mmols, 1 eqv.) and N,N′-dicyclohexylcarbodiimide (1.20 g, 5.82 mmols, 1.1 eqv.) was measured in a clean and dry 100 mL round bottom flask equipped with a magnetic stirrer. It was then sealed and purged with argon. To it 15 mL of dry EtOAc was added and then stirred at 0°C in an ice bath for 1 hour. To this continuously stirring reaction mixture a 10 mL solution of p-nitrophenol (810 mg, 5.822 mmols, 1.1 eqv.) dissolved in dry EtOAc was slowly added dropwise in the inert ice-cold condition. It was then allowed to stir at 0°C for 1 hour and then gradually allowed to reach room temperature and stirred furthermore for 3 hours. The white precipitate obtained in the reaction mixture was discarded out by suction filtration. The reaction mixture was then concentrated by rotary evaporation to give a light-yellow sticky compound as the crude product. The crude product was purified by column chromatography over silica with an isocratic elution of 10% ethyl acetate in hexane to give a white crystalline solid compound as the pure product (462.02 mg, 40.5% yield). ^{1}H NMR (600 MHz, Chloroform-d) δ (ppm) 8.97 (d, J = 2.7 Hz, 1H), 8.53 (dd, J = 8.9, 2.7 Hz, 1H), 7.48 (d, J = 8.9 Hz, 1H), 2.43 (s, 3H).

2,4-dinitrophenyl acetate (DNPA):

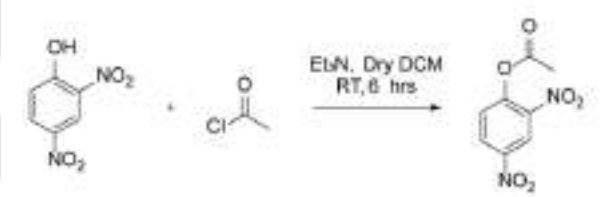

2,4-dinitrophenol (500 mg, 2.717 mmols, 1 eqv.) was measured in a clean and dry 100 mL round bottom flask equipped with a magnetic stirrer. It was then sealed and purged with argon. To it 10 mL of dry DCM was added and then stirred at 0°C in an ice bath. Triethyl amine (500 µL, 3.592 mmols, 1.32 eqv.) was then added dropwise under the continuously stirring inert condition at 0°C which gave a clear yellow solution, which was then further allowed to stir for 30 minutes. To this continuously stirring cold reaction mixture, acetyl chloride (252 µL, 3.532 mmols, 1.30 eqv.) was slowly added dropwise. The reaction mixture was stirred for 1 hour in the inert ice-cold condition and then gradually allowed to reach room temperature, wherein it was further allowed to stir for 3 hours. A clear yellow reaction mixture was obtained which was then further diluted with 30 mL of dry DCM. This organic phase was then washed thrice with equal volumes of distilled water, once with brine and then collected and dried over anhydrous Na_2SO_4. It was then filtered and

concentrated by rotary evaporation to give the crude product as a clear yellow oily liquid. The crude product was then purified by column chromatography over neutral alumina with an isocratic elution in 15% ethyl acetate in hexane to give a white solid compound as the pure product. (371.9 mg, 60.5% yield). ^{1}H NMR (600 MHz, Chloroform-d) δ (ppm) 8.30 (d, J = 9.1 Hz, 1H), 7.35 (d, J = 9.1 Hz, 1H), 4.34 (s, 1H).

General Synthesis of the Peptide (Nap-His/Nap-Gly):

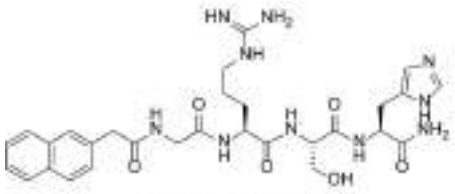

Nap-GRSH (Nap-His)

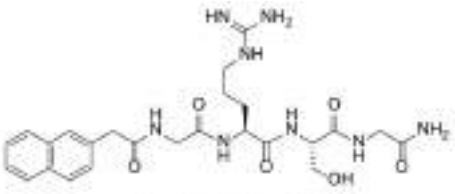

Nap-GRSG (Nap-Gly)

The peptides were synthesized on Rink amide MBHA resin using standard Fmoc (9-fluorenylmethoxycarbonyl) solid phase peptide synthesis (SPPS) protocol. In a typical coupling, 3 equiv. of protected amino acid (with respect to the loading of the resin), 3 equiv. of HBTU, and 6 equiv. of DIPEA were taken in 5 mL of DMF (for 0.1 mmol scale with respect to the resin loading) and stirred for 5 minutes prior to addition of the mixture to the swelled deprotected resin. The reaction mixture was shaken for 60 min and the resin was washed several times with DMF. The Fmoc-deprotection was achieved by treatment of the resin thrice with 5 ml of 20% piperidine in DMF for 5 minutes followed by thorough washing of the resin with DMF and DCM. The Fmoc-deprotection and coupling steps were repeated until the desired peptide sequence was obtained. The resin with the loaded peptide was washed several times with DMF and DCM and dried. The dried resin was then treated with a mixture of freshly prepared mixture of 8.5:1:0.5 (TFA/TES/H_2O) and stirred for 1 h. The resin was finally washed with DCM several times. The cleavage cocktail and the washings combined were concentrated to a minimum volume on a rotary evaporator. The cleaved peptide was then precipitated from cold dry ether, centrifuged and lyophilized to get the crude peptide. Purification was done in Dionex Ultimate 3000 HPLC using a Luna 5 µm (C18) column (Phenomenex) and using acetonitrile and water (containing 0.1% TFA each) as the mobile phase. (HPLC Program= 5% Acetonitrile/Water to 100% Acetonitrile in 25 minutes.)

Nap-His: ^{1}H NMR (600 MHz, DMSO-d_6) δ (ppm) 8.89 (s, 1H), 8.40 (t, J = 5.8 Hz, 1H), 8.18 (d, J = 8.3 Hz, 1H), 8.10 (dd, J = 21.8, 7.3 Hz, 1H), 7.86 (d, J = 7.7 Hz, 1H), 7.83 (d, J = 8.0 Hz, 2H), 7.74 (d, J = 18.5 Hz, 1H), 7.57 – 7.40 (m, 4H), 7.32 (d, J = 10.8 Hz, 3H), 4.46 (d, J = 5.0 Hz, 1H), 4.31 (d, J = 6.7 Hz, 1H), 4.21 (d, J = 6.3 Hz, 1H), 3.77 (d, J = 5.8 Hz, 3H), 3.64 (d, J = 16.3 Hz, 3H), 3.15 (dd, J = 15.4, 5.2 Hz, 1H), 3.06 (d, J = 7.4 Hz, 2H), 2.93 (dd, J = 15.5, 8.3 Hz, 1H), 1.67 (t, J = 6.1 Hz, 1H), 1.47 (dd, J = 13.8, 7.7 Hz, 3H).

Mass (ESI-MS): m/z calcd. for $C_{35}H_{42}N_9O_5^+$ $[M+H]^+$: 624.308, found 624.081; $C_{35}H_{43}N_9O_5^{2+}$ $[M+2H]^{2+}$: 312.156, found 312.567; HPLC R_T = 9.25 min.

Nap-Gly: ^{1}H NMR (600 MHz, DMSO-d_6) δ (ppm) 8.39 (s, 1H), 8.11 (q, J = 6.8, 6.3 Hz, 3H), 7.91 – 7.81 (m, 3H), 7.77 (s, 1H), 7.52 – 7.40 (m, 3H), 7.32 – 7.11 (m, 5H), 4.36 (q, J = 7.3 Hz, 3H), 4.24 (q, J = 6.3 Hz, 2H), 3.13 – 2.99 (m, 4H), 1.68 (dd, J = 15.1, 8.0 Hz, 2H), 1.59 – 1.38 (m, 4H). Mass (ESI-MS): m/z calcd. for $C_{31}H_{38}N_7O_5^+$ $[M+H]^+$: 543.267, found 543.193; HPLC R_T = 10.37 min.

2.4.3. Methods and Instrumentations

UV-Visible and Fluorescence Spectroscopy: UV-Visible spectra were recorded on a PerkinElmer Lambda 750 spectrometer, while fluorescence measurements were performed on a Fluoromax 4 Plus spectrophotometer.

pH Measurements: The pH curves were recorded on a Hanna HI 2210 pH meter equipped with HI1131 pH probe from Hanna.

Field Emission Scanning Electron Microscopy (FESEM): 5 μL of the sample solution at specific time interval during the pH cycle was casted on a silicon wafer and immediately freeze-dried to arrest the kinetics of the pH cycle. FESEM imaging and Energy Dispersive X-ray (EDX) mapping analysis were then performed on a Gemini SEM 300 (Sigma Zeiss) instrument.

Field Emission Transmission Electron Microscopy (FETEM): 5 μL of the sample solution at specific time interval during the pH cycle was casted on carbon coated copper grid (300 mesh Cu grid with thick carbon film from Pacific Grid Tech, USA) and allowed to air dry for 2 minutes and then the excess sample was bloated with a tissue paper. The grid was then immediately freeze-dried and the FETEM images were taken in JEOL 2100F microscopes.

Isothermal Titration Calorimetry (ITC): ITC was performed using a Nano-ITC instrument from MicroCal for determining the formation constants and thermodynamic parameters for the inclusion complexes. 1 mM MV solution in buffer (10 mM phosphate, pH 7) was injected in parts (each injection, 1.3 μL) at an interval of 2 mins from a 40 μL micro-syringe into the Nap-His@CB[8] (1:1) solution (0.02 mM, 200 μL) with constant stirring (500 rpm) at 298K. All the solutions were degassed prior to titration. The ITC thermogram showed a 1:1 binding ratio between Nap-His@CB[8] and MV, thus indicating the formation of the ternary complex.

Preparation of CB[8] stabilized Host-Guest Ternary Complex:

To prepare 2 mL of 1 mM MV@CB[8] stock solution, 3.5 mg of CB[8] (the overall molecular weight of the used CB[8] was found to be 1730 from the elemental analysis data) and 1 mg of MV

were accurately weighed into a 2 mL volumetric flask and 1.8 mL of MilliQ water was added to it. The heterogeneous solution was then sonicated for 1 hour at 298 K. An equivalent amount of the peptide (Nap-His/Nap-Gly) was added to the solution of the binary complex, the volume was made up to 2 mL using MilliQ water and the solution was further sonicated for 1 hour at 298K. The light-yellow colored solution was then kept undisturbed at 298 K for 1 day before utilizing for further experiments. The formation of the CB[8] stabilized charge-transfer ternary complex was confirmed by the appearance of a CT band at 394 nm and a significant drop in the fluorescence intensity of naphthalene. ITC experiment also confirmed the formation of the ternary complex.

Assessment of pH Dependent Hydrolase Activity (Figure 3.3A and B):

Hydrolase activity of the vesicular nanozyme at pH 8 and 6, respectively, were assessed by spectrophotometrically monitoring the hydrolysis of p-nitrophenylacetate (pNPA) to p-nitrophenol (pNP). Briefly, 0.1 mM each of the TC (1 mM stock solution in water) and dodecylamine (10 mM stock solution in THF) were taken in 1 mL of pH 6 phosphate buffer (20 mM) or pH 8 TRIS buffer (20 mM) in a quartz cuvette of 1 cm path length and varying concentrations of pNPA (0.2, 0.4, 0.6, 0.8, 1.0 mM from 0.2 M stock solution in acetonitrile) were added to the solution. Following mixing, the absorbance changes corresponding to the chromogenic product, pNP were monitored at the pH independent isosbestic point for pNP, λ_{max}= 348 nm (ε_{348nm}= 6.75 $mM^{-1}.cm^{-1}$ in water) over a period of 5 minutes. The catalysis experiments were performed in triplicates and the kinetics of the reactions at different pH values were calculated via nonlinear regression using GraphPad Prism 9 software, under an assumption of Michaelis-Menten kinetics.

pH Gated Switching of Hydrolase Activity of the Nanozyme (Figure 3.3C):

The pH reversible nature of the nanozyme was assessed by alternatively switching the pH of an aqueous solution of the nanozyme (containing 0.1 mM each of TC and DA) between pH 6 and 8 using 0.01M HCl and NaOH, respectively. 1mL aliquots of the solutions at different pHs were checked for hydrolase activity by treating with pNPA (0.5 mM) and monitoring the absorbance of the hydrolised product, pNP at 348 nm. Disruption of the vesicular assembly at pH 6 led to a fall in the hydrolase activity of the nanozyme underpinning the critical role of the vesicular assembly in the catalysis reaction. Reconstitution of the nanozyme, however, restored the activity of the nanozyme over multiple cycles.

Programming of the pH Cycle:

Stock solutions of the fuel, pH 9 TRIS buffer (1 M), was prepared in MilliQ water and stored at 4°C for further use. For pH clock optimization, 1mL aqueous solution containing 0.1 mM each of the TC (1 mM stock solution in water) and dodecylamine (10 mM stock solution in THF), and the

required amount of substrate (pNPA/pNPCAA/DNPA) was first acidified to a pH ~5 using 1 mM HCl (to ensure disassembled state of the vesicles) and then the pH clock was initiated by addition of the required amount of pH 9 TRIS buffer. The change in pH was then monitored over time at 298K.

Time Dependent Dynamic Light Scattering (DLS) Studies:

The particle sizes of the assemblies were obtained at 298 K using a 632.8 nm He–Ne laser using Zetasizer Nano-ZS90 (Malvern). Briefly, 1mL aqueous solution containing equimolar amounts (0.1 mM) of the TC (1 mM stock solution in water) and dodecylamine (10 mM stock solution in THF) was first acidified to a pH ~5 using 1 mM HCl (to ensure disassembled state of the vesicles). The solution was filtered through appropriate filters to remove dust particles, if any, and the hydrodynamic size of the aggregates prior to the initiation of the pH clock (i.e., at 0 min) was found to be ~10 nm. DLS measurements were performed immediately after the addition of the fuel (1 mM pH 9 TRIS buffer) and the substrate (5 mM pNPCAA) and the hydrodynamic size distribution was monitored at specific time points at 298 K. All measurements were performed with a constant angle of 90° and the results were reported as Number Distribution to reflect the number of aggregates formed. All measurements were performed in triplicates.

Fluorescence Kinetics Study for Transient Vesicle Formation (Figure 3.5D and E):

Equimolar amounts (0.1 mM) of TC and dodecylamine along with 1 mM pNPCAA were dissolved together in MilliQ water and the pH of the solution was adjusted to ~5 prior to the initiation of the pH clock. 10 µM of the lipophilic dye, DPH (Diphenylhexatriene), was added to this solution and the initial fluorescence intensity was determined. The pH clock was then initiated by addition of pH 9 TRIS buffer (0.5 mM) and the emission intensity at 428 nm (λ_{ex}=355 nm, Slit width (Ex./Em.)= 5/5 nm) was monitored across three pH cycles over a period of 90 minutes.

Fluorescence Confocal Microscopy Studies:

Transient nanozyme formation was performed as mentioned earlier but using Nile Red (10 µM) as the fluorescent probe as it specifically accumulates in the hydrophobic vesicle bilayer and shows fluorescence upon vesicle formation. Post initiation of the pH clock (1 mM pH 9 TRIS buffer and 5 mM pNPCAA), the assembly/disassembly process was monitored through CLSM wherein the transient vesicular nanozymes appeared as fluorescent aggregates and slowly disappeared as the nanozyme assemblies disassembled. The sample was excited at 488 nm and the fluorescence emission was observed at 549 – 662 nm over a period of 60 min at 298 K.

Particle Count Analysis from CLSM:

The particle count from the CLSM images obtained at different time points were analysed using ImageJ software. In particular, the images were converted to 8-bit format and visible particles

were counted. The particles having a minimum object dimension of 2, 4, 6, 8 and 10 px^2 were considered for particle count analysis. As anticipated, the number of fluorescent particles first increased upon initiation of the pH clock and then declined steadily as the pH clock concluded.

Evidence for Cooperative mechanism for the hydrolase activity of the nanozyme:

As the pH sensitive nanozyme containing imine linked MV-DA tail group is highly susceptible to pH changes, in order to assess the catalytic mechanism of the nanozymes, a pH irresponsive nanozyme containing HDMV as the tail group was synthesized. The pH irresponsive nanozyme displayed a bell-shaped curve for the pH dependent hydrolase activity with the maximum rate at pH 7 (close to the pK_a of histidine units) (Figure 3.3A). This pH dependent behaviour of the nanozyme is indicative of cooperative interaction amongst the neighbouring histidine units immobilized on the surface of the vesicular nanozyme.[175] As a result of disruption of the pH sensitive nanozymes (MV-DA) at acidic pH, the cooperative effect is lost and protonation of the free histidine units (pKa~6) at acidic pH leads to the loss of catalytic of the dissociated nanozymes.

FESEM images of transient vesicles formed during the pH cycle (Figure 3.4C):

Imine linkage between the aldehyde appended viologen (MV) unit of the TC and dodecylamine in pH 8 TRIS buffer was found to generate vesicles, which is in line with our previous observations.[158] To visualize the morphology of the assembled nanostructures at different time intervals during the course of the pH cycle, microscopic images of freeze dried samples of the nanozymes collected at specific time points were analysed using FESEM technique. The FESEM images showed no specific aggregation pattern before the initiation of the pH clock. However, upon addition of fuel, vesicles were observed as long as the pH of the solution was in the alkaline region. The vesicles, however, disappeared as the solution became acidic after 40 mins, indicating the transient nature of the vesicles.

HPLC Kinetics for the Hydrolysis of pNPCAA to pNP (Figure 3.5A-C):

The hydrolysis of pNPCAA to pNP was monitored through Analytical High-Performance Liquid Chromatography (HPLC) using Dionex Ultimate 3000 HPLC system equipped with Luna 5 µm C18 column (Phenomenex) and using acetonitrile and water (containing 0.1% TFA each) as the mobile phase (HPLC Program= 0% Acetonitrile/Water to 100% Acetonitrile in 20 minutes). Briefly, 1 mL solution containing 0.1 mM each of the TC (1 mM stock solution in water) and dodecylamine (10 mM stock solution in THF) was prepared 1 mM pNPCAA was added to it. The pH of the solution was adjusted to ~5 and the hydrolysis reaction was initiated by adding 0.5 mM pH 9 TRIS buffer (1 M stock solution in water) to the solution. 50 µl aliquots of the solution were collected at specific time

intervals and the reaction was quenched by acidifying the collected aliquots. The rate of hydrolysis was thereby monitored through HPLC at different time intervals and the amount of product formed was quantified using a standard plot prepared with known concentrations of pNP.

Time Dependent Fluorescence Kinetics Study (Figure 3.5D and E):

DPH (Diphenylhexatriene) is a lipophilic probe that shows enhanced emission when entrapped in the hydrophobic nanodomains of vesicular assembly. The transient entrapment and resultant fluorescence enhancement of DPH (10 µM) was monitored at an interval of 1-minute post initiation of pH clock (0.5 mM pH 9 TRIS buffer, 1 mM pNPCAA). A rapid initial jump in emission intensity was followed by a gradual decay over a course of 90 minutes indicating the transient formation of the vesicular nanozymes.

Formation of pNP during the pH cycle (Figure 3.8B):

Owing to considerable spectral overlap between the absorbance of the substrate, pNPCAA and the hydrolysed product, pNP, the time dependent kinetics for the hydrolysis of pNPCAA to pNP was monitored through HPLC. Briefly, 10 mL aqueous solution containing 0.1mM each of the TC and DA, along with 5 mM pNPCAA was initially maintained at pH ~5 and then subjected to the pH clock by addition of 1 mM pH 9 TRIS buffer. 50 µL aliquots of the solution were collected at different time points and acidified to quench the catalysis reaction. The aliquots were subsequently subjected to chromatographic separation and the amount of pNP generated across three pH cycles was estimated using the calibration plot shown in Figure 3.9B.

Determination of Molar Extinction Coefficient of p-Nitrophenol/ 2,4-Dinitrophenol:

The molar extinction coefficient of pNP/DNP in water were determined by plotting the absorbance of known concentrations of pNP/DNPA in water at 348 nm and 355 nm, respectively. The slope of the linearly fitted concentration vs absorbance plot yielded the value ε_{348nm}= 6.75 $mM^{-1}.cm^{-1}$ for pNP and ε_{355nm}= 9.62 $mM^{-1}.cm^{-1}$ for DNP in water. All measurements were performed in triplicates.

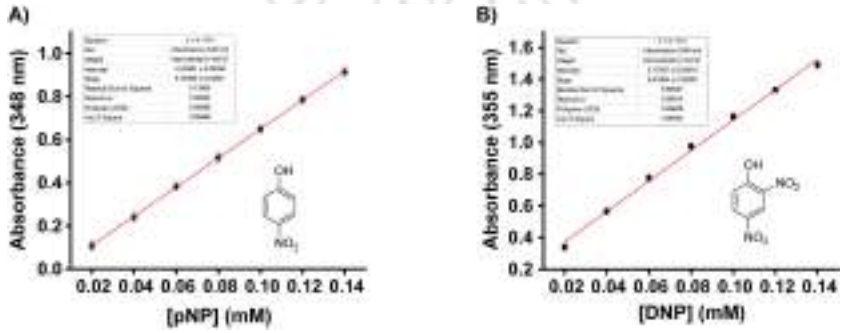

Figure 3.8. Calibration plot for **A)** p-nitrophenol, and **B)** 2,4-dinitrophenol in water.

Chapter 4

Bi-Directional Feedback Controlled Transience in Cucurbituril Based Tandem Nanozyme

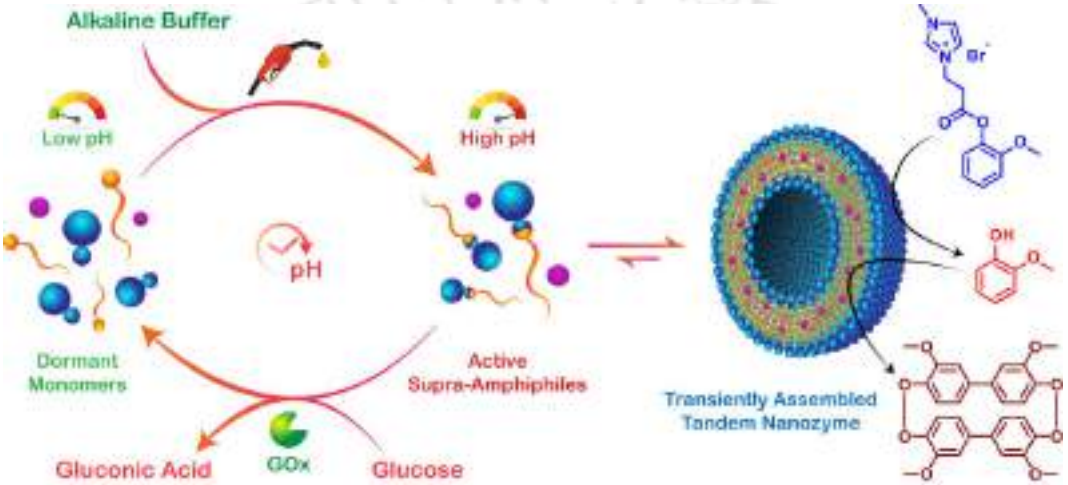

भारतीय प्रौद्योगिकी संस्थान गुवाहाटी
Indian Institute of Technology Guwahati

4.1. Introduction

Multicomponent and multienzymatic tandem transformations are at the heart of nature's intricate biochemical processes.[176, 177] The extreme sophistication, yet the extraordinary synergy in biological tandem reactions such as cellular metabolism, signal transduction, etc. have fascinated and inspired synthetic chemists for long to devise synthetic tandem reaction networks for complex chemical transformations. Multistep sequential chemical reactions in a single system requires the catalytic steps involved to be mutually orthogonal and feasible under the same reaction settings. Incompatible catalysts, lack of substrate selectivity and specificity, undesirable competing side reactions and non-specific reaction sequences, however, present major issues while designing synthetic tandem reactors.[178]

Although much progress has been made in translating bioinspired compartmentalization and confinement strategies to self-assembled tandem nanoreactors based on micelles,[179, 180] vesicles,[181] hydrogels,[182, 183] nanorods,[184, 185] etc., artificial tandem nanoreactors still lack certain unique features that make the natural counterparts far more robust and self-sustaining. Unlike thermodynamically driven supramolecular nanozymes, natural catalytic processes follow non-equilibrium pathways where regulatory signals direct transient membrane permeabilization and dissipative assembly of catalysts in a kinetically driven spatiotemporal order.[186-188] This ensures a time-gated in-and-out movement of substrates and wastes and helps in maintaining an optimal substrate concentration at the site of catalysis. Lessons learnt from nature have been implemented for developing chemical fuel driven out-of-equilibrium self-assembled nanoreactors that can amass substrates and/or catalysts together within catalytically active nano-domains and catalyse otherwise non-viable reactions in aqueous environment.[21, 36, 99, 114, 120-122] However, on account of difficulty in simultaneously fuelling catalytic reaction cycles and periodically assembling/disassembling the nanoreactors, only single step transformations have been accomplished in non-equilibrium settings to date. Moreover, the fuels used so far work in one direction controlling mainly the assembly/disassembly processes. A single fuel that offers dual feedback by generating two components that regulate the self-assembly as well as the output (catalysis that happens in the assembled state) of the self-assembly process will be extremely beneficial.

In this work, we present a chemoenzymatically fuelled transient nanozyme with the ability to perform a tandem catalytic process. The lifetime and activity of the nanozyme is controlled by the dual feedback mechanism emerging from the GOx mediated oxidation of glucose as shown in Scheme 4.1.

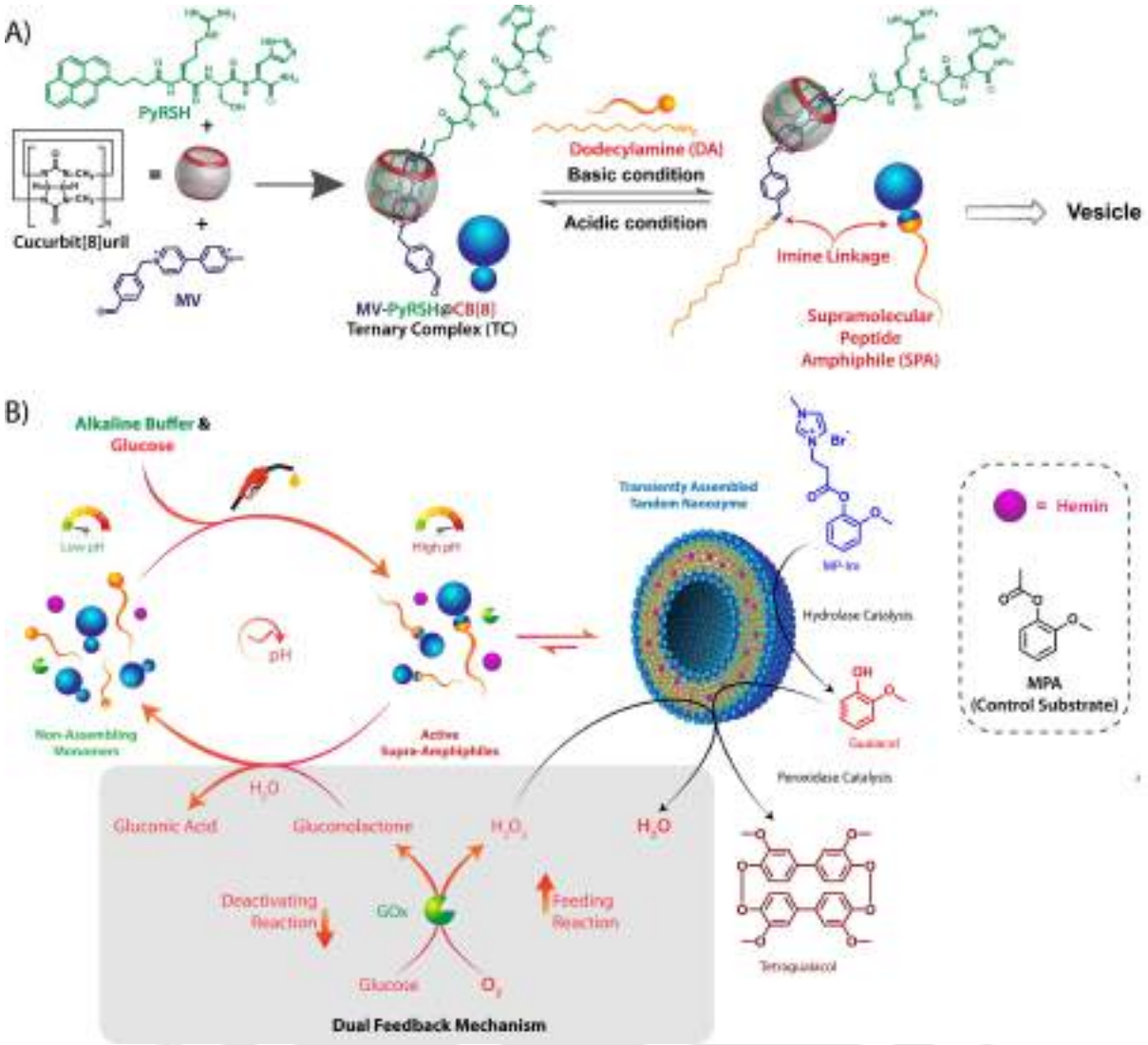

Scheme 4.1. Graphical representation of **A)** CB[8] assisted pH responsive SPA and the corresponding vesicle formation and, **B)** pH clock driven transient assembly of vesicular nanozymes for tandem hydrolase-peroxidase catalysis, and chemical structures of the different components of the transient nanozyme.

4.2. Results and Discussion

4.2.1. System Design and CB[8] Assisted SPA and the Corresponding Nanozyme Formation

We envisioned that confinement of functionally divergent catalytic units capable of sequential chemical transformations in a transient supramolecular assembly might produce a biomimetic and transient tandem nanozyme. To this end, we realized that the unique charge transfer complexation[189] mediated ternary complex[132, 140, 190] formation by Cucurbit[8]uril (CB[8]), [124, 130, 131] could be an ideal platform to construct such transient systems. The ability of CB[8] based supramolecular peptide amphiphile (SPA) vesicles[125, 127, 158] to simultaneously place hydrophilic catalytic peptide segments on its outer surface and host hydrophobic catalysts in its hydrophobic lipid bilayer prompted us to design a transient SPA based vesicular tandem nanozyme.

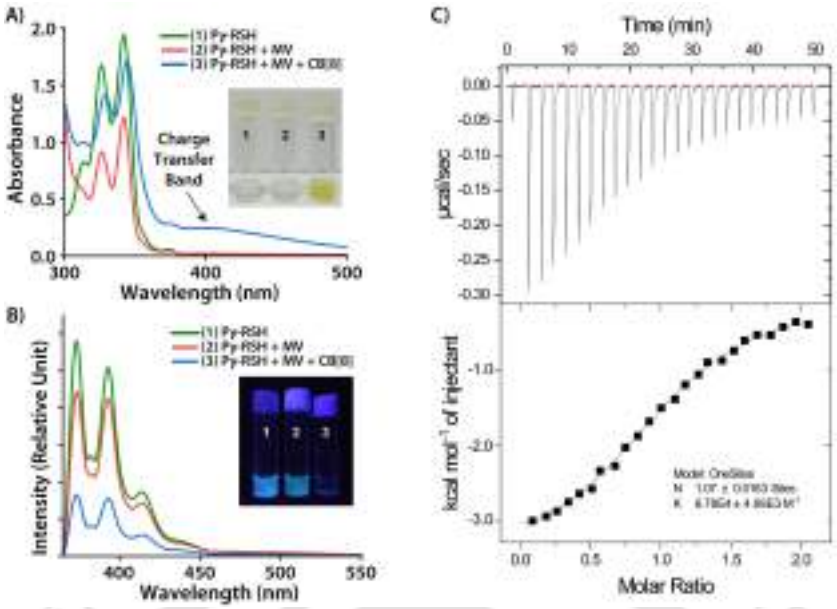

Figure 4.1. Formation of TC, confirmed through **A)** UV-Vis spectrum of equimolar (5 mM) combination of CB[8], MV and Py-RSH, exhibiting a CT band at ~400 nm, **B)** Fluorescence spectra showing quenching of emission for the TC. (Inset: Images of the solutions 1, 2 and 3 as observed under A. normal light, B. UV light). λ_{ex} = 340 nm. **C)** Isothermal Titration Calorimetry (ITC) thermograms (top) and binding isotherms (bottom) of Py-RSH@CB[8] with MV at 298 K.

We have recently shown the pH clock[31, 32, 81, 158] regulated transient formation of CB[8] based vesicles. Herein, we have endowed the transient vesicles with dual catalytic properties by incorporating a catalytic peptide in the head group and a hydrophobic catalyst in the lipid bilayer. Transient vesicular aggregation is expected to briefly activate both the catalytic units and enable tandem catalysis in a transient fashion. Scheme 4.1A schematically describe the CB[8] assisted pH sensitive SPA formation. An aldehyde containing viologen (MV) a pyrene containing peptide (PyRSH) can form heteroternary [89, 191] complex (TC) inside CB[8] where the viologen and pyrene units work as the first and second guest respectively. Since, the formed TC contains an appended aldehyde group, in presence of an amine, under basic condition, it will form imine linkages and thereby the SPA.[138] The SPA subsequently assembles to form vesicles. The dynamic and reversible imine bond formation and hence the vesicular assembly can be transiently regulated by the change in pH of the medium. The incorporation of a catalytic group at the head of the TC and presence of Hemin group in the lipid bilayer was anticipated to allow the formation of a transient tandem nanozyme (Scheme 4.1B).[158] Hemin,[192] was chosen as the hydrophobic catalyst as it shows low activity in aqueous medium but upon compartmentalization in hydrophobic domains of self-assembled structures, it catalyses the oxidation of a wide range of phenolic compounds.[99, 193] The phenolic substrates, on the other hand, can be generated in situ from the corresponding phenolic esters by Histidine (His) mediated ester hydrolysis. His groups, however, display efficient hydrolase activity when immobilized on the surface of multivalent supramolecular assemblies owing to

cooperative effects amongst neighbouring catalytic entities.[165, 170-172] Integrating the catalytic activities of His and hemin in the confined architectures of SPA vesicle can thus furnish a novel hydrolase-peroxidase tandem nanozyme in a pH-gated fashion.

The catalytic group for hydrolase activity was constructed through the peptide, PyRSH where the His serves as the main catalytic unit. Ser was rationally placed near the terminal His moiety as it is known to reinforce hydrolase activity in esterase mimics.[165] Also, Arg was introduced to enhance substrate binding affinity owing to its strong H-bond donating propensity and enhance aqueous solubility.[165] The formation of the TC (Scheme 4.1A) was confirmed by the appearance of characteristic charge transfer (CT) band[140] at ~400 nm in the absorption spectra and a drop in pyrene fluorescence intensity owing to host enhanced CT interaction between MV and Py-RSH (Figure 4.1A and B).[134, 158] Moreover, a red shift in the absorbance maxima owing to the stabilization of the charge transfer complex in the cavity of CB[8] indicated the formation of the ternary complex.[194] Isothermal Titration Calorimetry (ITC) also displayed a 1:1:1 complexation between CB[8], MV and Py-RSH (Figure 4.1C).

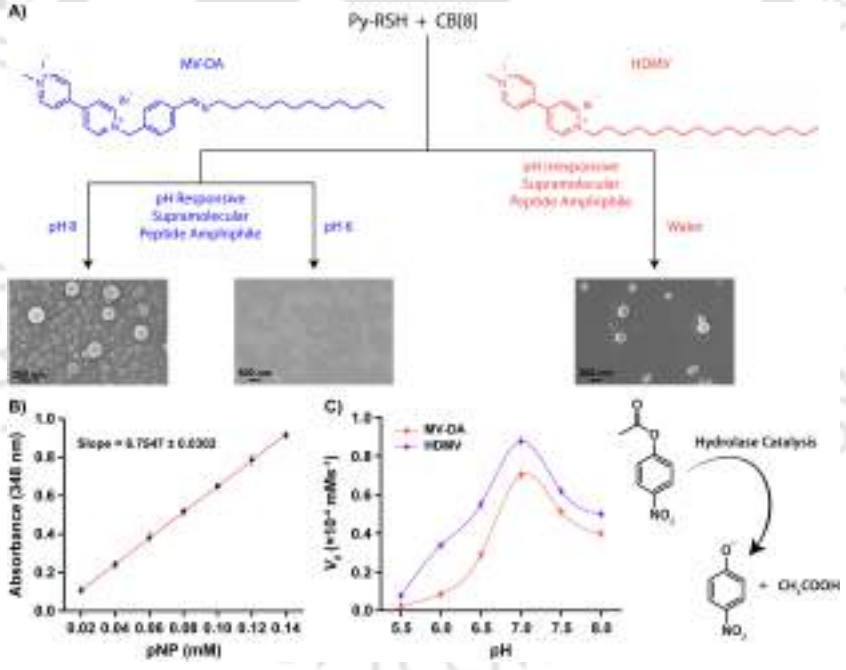

Figure 4.2. A) FESEM images of the vesicles furnished by SPAs accommodating equimolar (0.1 mM) amounts of CB[8], Py-RSH and MV-DA (in pH 8 TRIS buffer/ pH 6 phosphate buffer) (Images at the left) and HDMV (in Water) (Image at the right). **B)** Calibration plot for p-nitrophenol from the absorbance at 348 nm (isosbestic point) in water, **C)** Rate of hydrolysis of p-nitrophenyl acetate (pNPA) substrate using Py-RSH head group and pH responsive (MV-DA)/irresponsive (HDMA) tail group at different pH values. [CB[8]]/ [Py-RSH]/ [HDMV]/ [MV-DA]/ [Dodecylamine]=100 μM, [pNPA]= 1mM.

4.2.2. Hydrolase and Peoxidase Activity in the Nanozyme

Alkaline pH mediated association of the hydrophilic heads with dodecylamine through imine linkage afforded SPAs which rapidly assembled into vesicles (Figure 4.2A) and displayed

hydrolase activity at pH 8. pH dependent hydrolase activity of the nanozyme displayed a bell-shaped curve with the maxima at pH 7, indicative of a cooperative mechanism for the hydrolase activity (Figure 4.2C).[175] Disassembly of the vesicle at pH 6 (Figure 4.2A), however, deactivated the nanozymes owing to loss of cooperativity amongst the free His units.

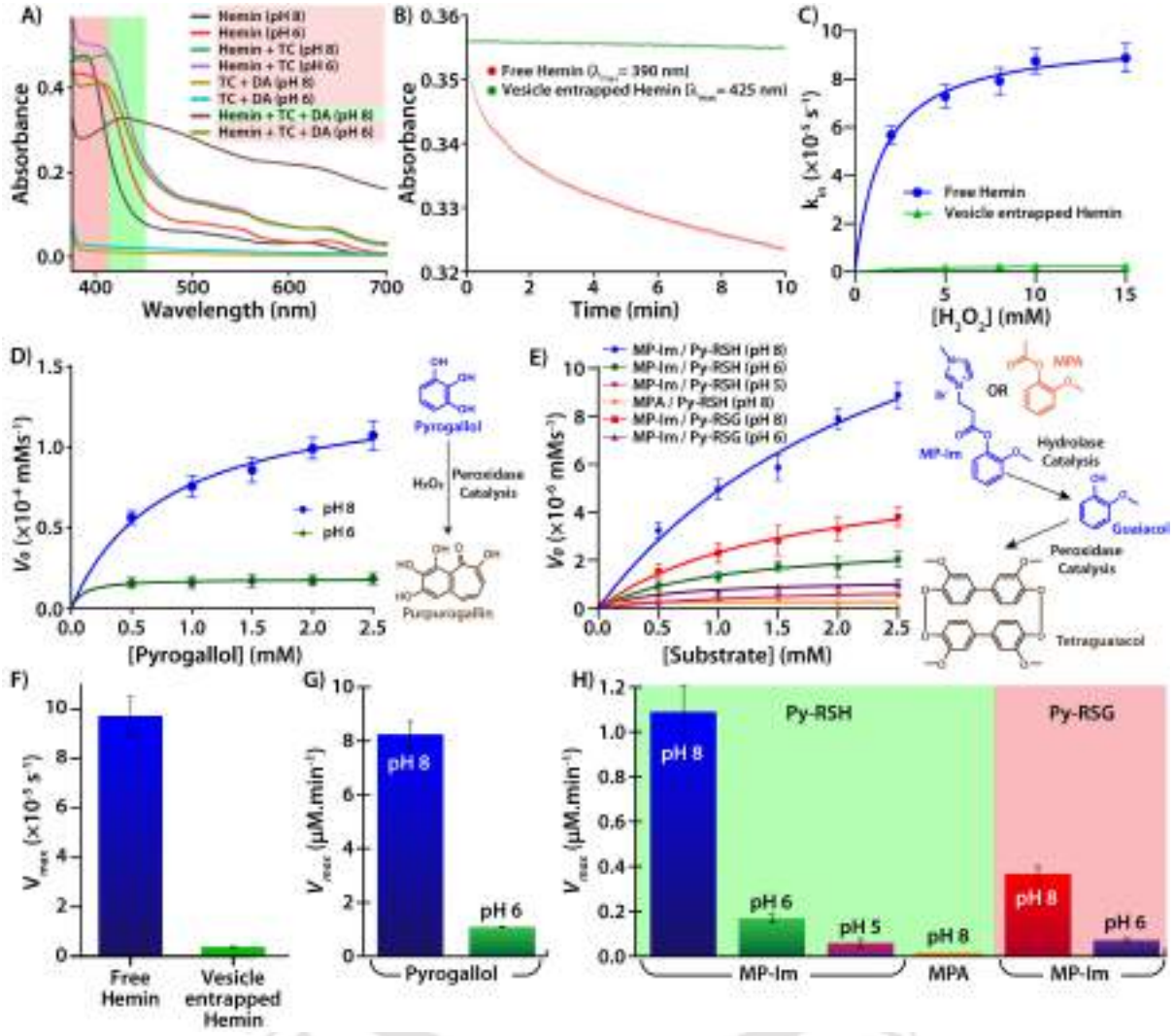

Figure 4.3. A) UV-Vis spectra for Hemin entrapment in the assembled/disassembled SPA vesicles at pH 8/6, respectively, **B)** Time dependent variation of absorbance at the Soret peaks for free hemin and vesicle entrapped hemin treated with 5 mM H_2O_2 in pH 8 TRIS buffer, **C)** Inactivation kinetics of free and vesicle entrapped hemin in the presence of varying concentrations of H_2O_2,). [CB[8]]/[Py-RSH]/[Dodecylamine]=100 µM, [Hemin]= 5 µM, [H2O2]= 2, 5, 8, 10, 15 mM, **D)** Michaelis Menten plot for oxidation of pyrogallol by the assembled/disassembled nanozyme at pH 8/6, respectively, **E)** Michaelis Menten plot for cascade reactions employing MPA/MP-Im substrates and Py-RSH/Py-RSG (Control) head group by the assembled/disassembled nanozyme at pH 8/6, respectively. Bar diagrams showing **F)** Maximum initial velocity of hemin degradation (from C), **G)** Peroxidase activity (from D), and **H)** Cascade activity (from E) of the nanozyme. [CB[8]]/ [Py-RSH]/ [Py-RSG]/ [Dodecylamine]= 100 µM, [Hemin]= 5 µM, [H_2O_2]= 5 mM.

The vesicular nanozymes presented hydrophobic domains similar to the proteinaceous envelopes in enzymes that protect and preserve the activity of the catalytic centers.[158, 193] Therefore,

the ability of the SPA vesicles to encapsulate hemin was followed with UV-Vis spectroscopy (Figure 4.3A). Hemin retains its catalytic activity in monomeric form (within enzymes) but gets deactivated in aqueous medium owing to formation of μ-Oxo-bridged dimers, as indicated by the presence of a Soret band at 390 nm and Q bands around 610-640 nm in both acidic (pH 6) as well as alkaline (pH 8) buffers.[99, 193] A well pronounced red shift of the Soret band to 425 nm in the presence of vesicles formed in pH 8 buffer suggested possible localization of monomeric hemin units within/around the lipid bilayer.[99, 184, 193, 195] The lipid bilayer also shielded and protected hemin from irreversible oxidative damage by its substrate, H_2O_2, required for peroxidase catalysis. The absorbance at the Soret band of H_2O_2 treated free hemin (λ_{max}= 390 nm) displayed a steady fall, indicating rapid deactivation of the bare catalyst, whereas the vesicle trapped hemin presented no change in the Soret peak absorbance (λ_{max}= 425 nm) under similar conditions (Figures 4.3B, C and F).[195, 196]

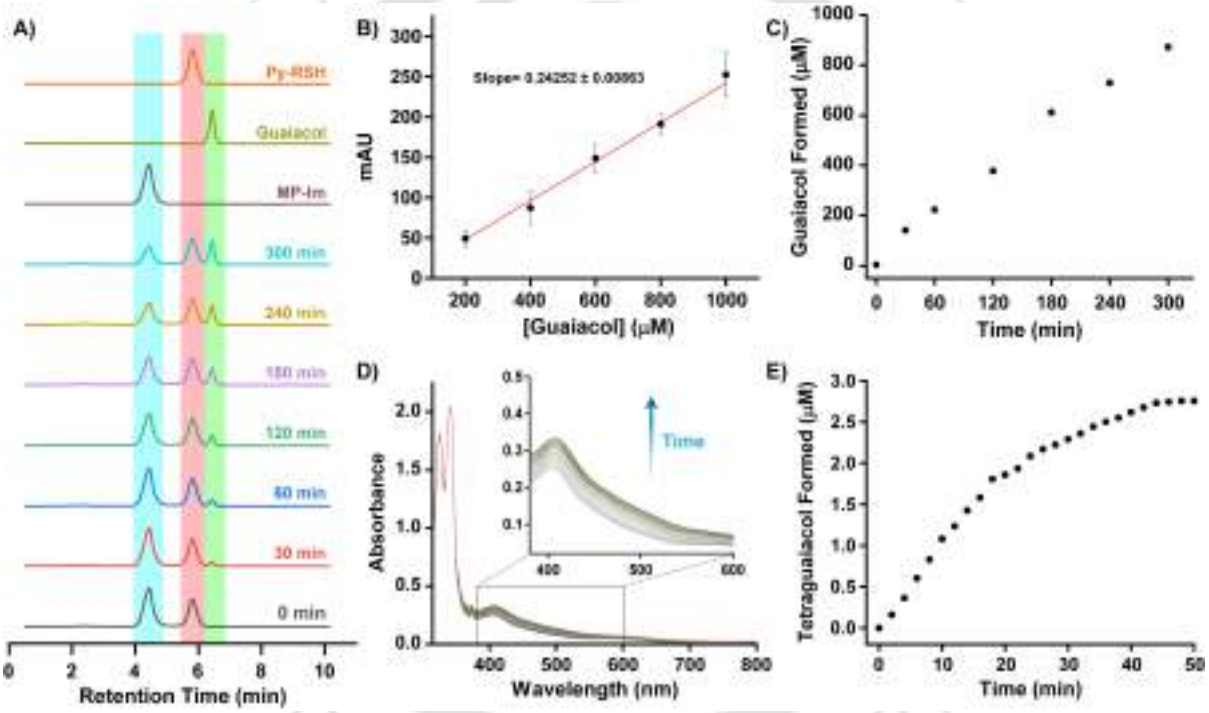

Figure 4.4. A) Time dependent HPLC chromatograms showing the nanozyme catalysed hydrolysis of MP-Im to guaiacol, **B)** Standard plot for guaiacol from HPLC, and **C)** Time course generation of guaiacol from MP-Im through the nanozyme catalyzed ester hydrolysis reaction (Data obtained from HPLC chromatograms in A), **D)** UV spectra showing the formation of tetraguaiacol (λ_{max}= 470 nm) from MP-Im via tandem hydrolase-peroxidase catalysis, and **E)** Time course generation of tetraguaiacol from MP-Im (Data calculated from the absorbance values in D).

The effect of pH directed formation/disruption of the SPA vesicle on the peroxidase activity of hemin was then evaluated using H_2O_2 assisted oxidation of pyrogallol to the chromogenic oxidation product, purpurogallin (λ_{max}= 420 nm).[99, 193] In the absence of vesicular assembly at pH 6, hemin displayed nominal peroxidase activity (V_{max}= 1.0968 μmol/min) as it predominantly formed dimers and/or loosely bound aggregates with hydrophobic dodecylamine chains in aqueous

medium (Figures 4.3D and G). Schiff base formation at pH 8, however, enacted vesicle formation wherein the trapped hemin molecules displayed ~7.5-fold higher activity (V_{max}= 8.244 µmol/min). In order to assess the multitasking capabilities of the nanozyme, an acetylated derivative of guaiacol, methoxyphenyl acetate (MPA) was prepared, which was projected to undergo subsequent hydrolase and peroxidase catalysis in a sequential fashion to generate the oxidized product, tetraguaiacol, which can be easily visualized through UV-Vis spectroscopy (λ_{max}= 470 nm).[185] However, no catalytic conversion by the nanozyme at pH 8 was observed. This is presumably because of the entrapment of the hydrophobic MPA molecules in the lipid bilayer of the vesicles which restricted the His-mediated hydrolysis of ester bonds to generate the active substrate for hemin. An amphiphilic ester derivative of guaiacol, MP-Im, however, localized on the surface of the vesicles and underwent His mediated hydrolysis to generate guaiacol for the subsequent peroxidase catalysis (Figure 4.4A and C). Thus, MP-Im was efficiently converted to tetraguaiacol via tandem hydrolase-peroxidase catalysis (V_{max}= 1.0896 µmol/min) at pH 8 (Figure 4.4D and E) and the activity declined by a factor of ~6.4 (V_{max}= 0.1696 µmol/min) and ~18.4 (V_{max}= 0.0591 µmol/min) at pH 6 and 5, respectively, owing to the disruption of the nanozyme assembly (Figures 4.3E and H).

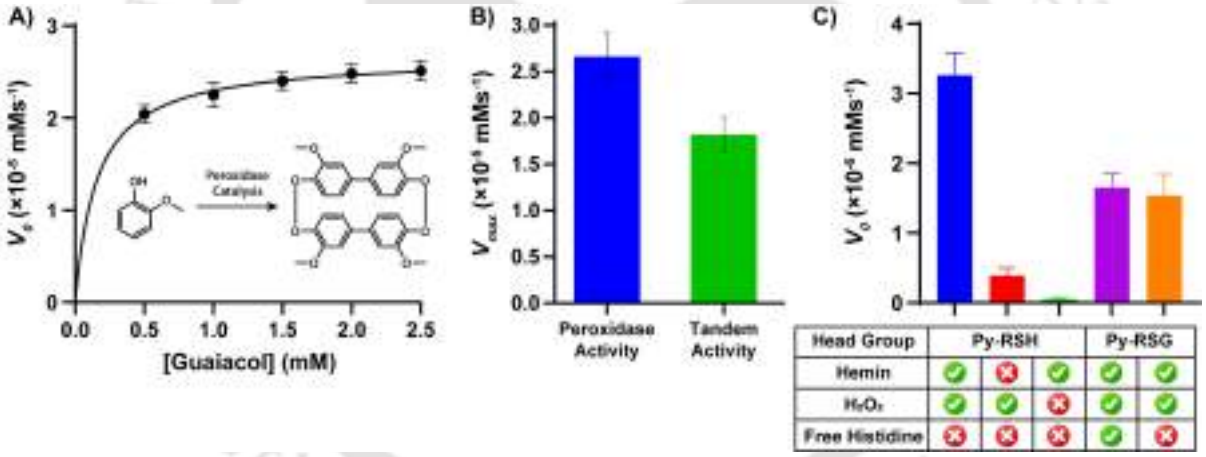

Figure 4.5. A) Michaelis Menten plot for peroxidase catalysis by the assembled nanozyme at pH 8 using varying concentrations of Guaiacol, and **B)** Bar diagram showing comparison between the peroxidase activity (from A) and tandem activity (From Figure 4.3E and H). **C)** Bar diagram showing the implication of Hemin, H_2O_2 and free/surface-bound histidine on the rate of tandem hydrolase-peroxidase catalysis. [CB[8]]/[Py-RSH]/[Py-RSG]/[Dodecylamine]=100 µM, [Hemin]= 5 µM, [H_2O_2]= 5 mM , [Free Histidine]= 100 µM.

A slower rate of tandem catalysis as compared to the rate of peroxidation of guaiacol (Figure 4.5A and B) suggested that the rate of the hydrolysis reaction dictates the overall catalytic activity of the tandem nanozyme. To understand the implication of His containing head group in the tandem sequence, a catalytically inert control peptide, Py-RSG, was prepared. At pH 8, the Py-RSG containing nanozyme displayed significantly lower tandem activity, signifying the critical role of His units in the tandem catalysis (Table 4.1). Also, control experiments using various combinations of

the catalytic components validated the critical role of hemin, H_2O_2 and surface bound His for the tandem catalysis reaction (Figure 4.5C). Moreover, both the peroxidase as well as the tandem catalysis reactions displayed enhanced catalytic activity with increase in the concentration of the oxidizing substrate, H_2O_2 (Figures 4.6A and B). Further, the nanozyme showed efficient on-off switching of catalytic activity across multiple pH cycles (Figure 4.6C and D).

	Peroxidase Catalysis		**Tandem Hydrolase-Peroxidase Catalysis**					
Peptide	**Py-RSH**						**Py-RSG**	
Substrate	**Pyrogallol**		**MP-Im**			**MPA**	**MP-Im**	
pH	**8**	**6**	**8**	**6**	**5**	**8**	**8**	**6**
V_{max} (μmol.min^{-1})	8.244 ± 0.490	1.097 ± 0.032	1.089 ± 0.124	0.169 ± 0.018	0.059 ± 0.019	0.015 ± 0.001	0.366 ± 0.034	0.072 ± 0.007

Note: All measurements were performed in triplicates.

Table 4.1: Kinetics Data for the Peroxidase and Tandem Hydrolase-Peroxidase Catalysis Reactions.

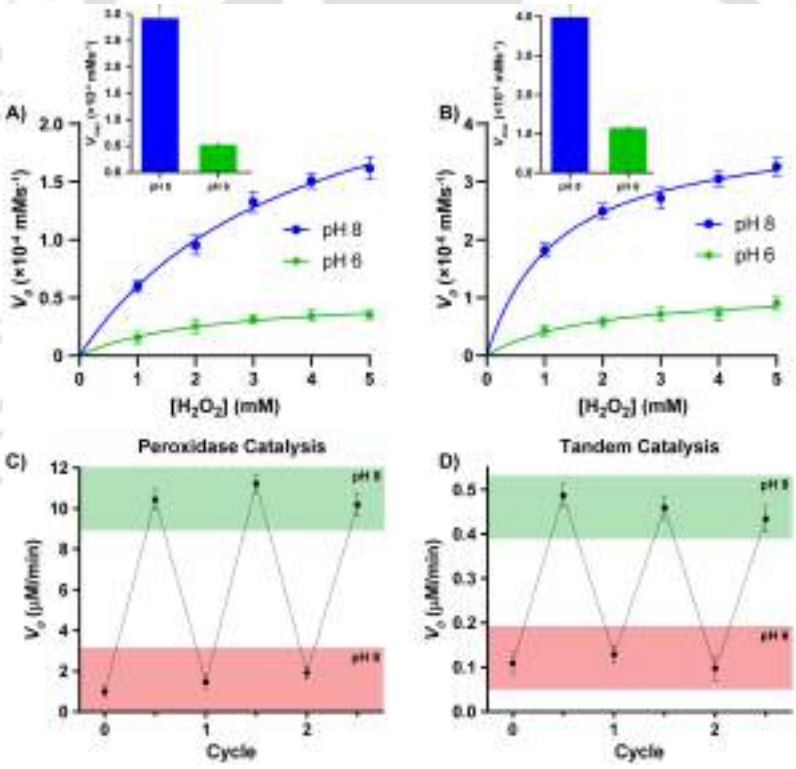

Figure 4.6. A) Michaelis Menten plot for oxidation of pyrogallol by the assembled/disassembled nanozyme at pH 8/6 using varying concentrations of H_2O_2 (Inset: Bar diagram showing the peroxidase activity (from A) at different pH values.) [Pyrogallol]= 0.5 mM, **B)** Michaelis Menten plot for tandem hydrolase-peroxidase catalysis by the assembled/disassembled nanozyme at pH 8/6 using varying concentrations of H_2O_2 (Inset: Bar diagram showing the tandem activity (from B) at different pH values.) [MP-Im]= 0.5 mM, The reversible switching of **C)** Peroxidase activity of the nanozyme determined through the oxidation of pyrogallol (2 mM), and the **D)** Tandem activity of the nanozyme determined through the hydrolase-peroxidase tandem conversion of MP-Im (2 mM) to tetraguaiacol, at pH 6 and 8. [CB[8]]/[Py-RSH]/[Dodecylamine]=100 µM, [Hemin]= 5 µM, [H_2O_2]= 5 mM.

4.2.3. Transient Formation of the Nanozyme and Bi-Directional Feedback by the Fuel

To establish non-equilibrium dynamics into the tandem nanozymes, the nanozyme building blocks along with the enzyme, Glucose Oxidase (GOx), initially maintained at pH ~5 (to ensure inactive state of the nanozyme), were subjected to a chemoenzymatic reaction network fueled by simultaneous addition of pH 9 TRIS buffer and glucose in a definite ratio. TRIS buffer triggered the formation of imine linked SPAs and their subsequent assembly to tandem nanozymes. GOx mediated oxidation of glucose, most importantly, steered the non-equilibrium kinetics bi-directionally in two opposite directions by generating (A) H_2O_2, which promoted the peroxidase activity of the nanozyme, and (B) Gluconolactone, which slowly hydrolysed to gluconic acid and disrupted the nanozyme owing to acidification of the medium. In this manner, the designed GOx powered pH clock, presented an easy yet unique approach to in situ generation of substrate (H_2O_2) and deactivating agent (Gluconic acid) from a single fueling agent (Glucose). As anticipated, a higher concentration of promoter (TRIS buffer) was found to increase the lifetime of the pH clock whereas higher concentration of glucose declines the longevity of the transient phase (Figure 4.7A). The progression of the pH clock was visualized with the help of the pH indicator, Bromothymol Blue (BTB) (Figure 4.8A-C). A 1:5 molar ratio of TRIS buffer (1 mM) and glucose (5 mM) along with 25 U/mL of GOx was identified as the ideal composition to constrain the lifetime of the transient cycle and the production of H_2O_2 within practicable limits.

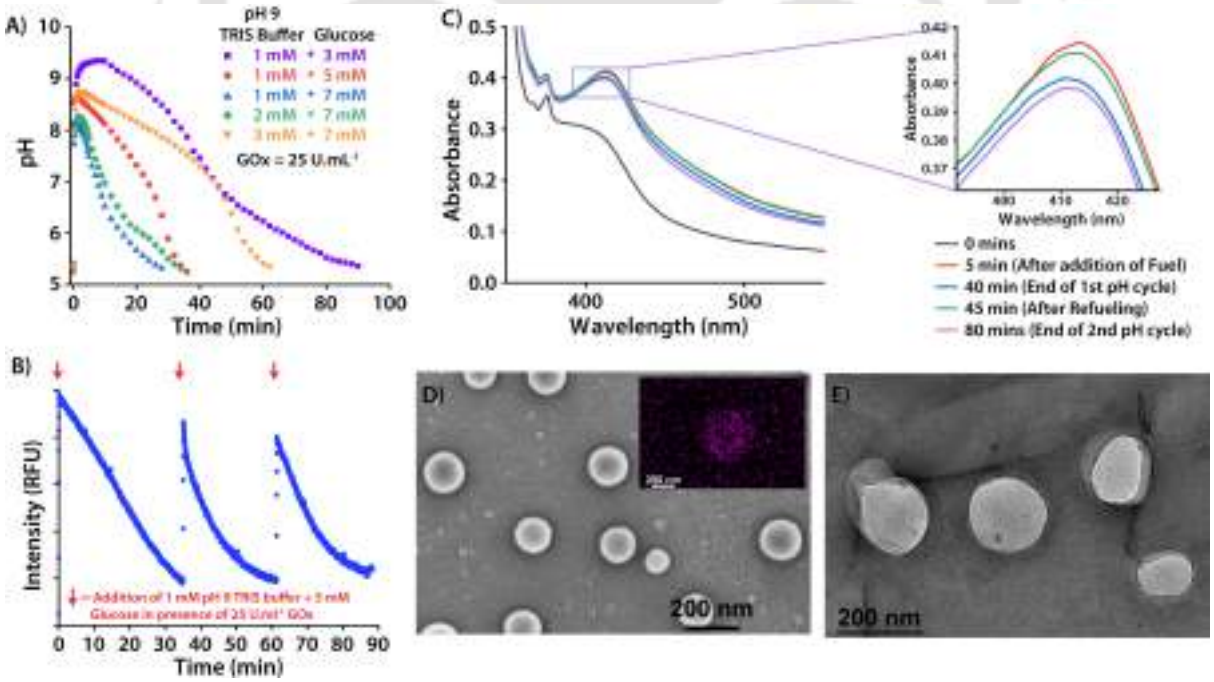

Figure 4.7. Transient assembly of vesicular nanozyme. **A)** pH clock optimization using varying ratios of pH 9 TRIS buffer and glucose in the presence of 25 U/mL GOx, **B)** Fluorescence kinetics for three consecutive pH cycles using DPH lipophilic probe, **C)** UV-Vis spectra displaying the vesicular entrapment of hemin under the influence of the pH clock, **D)** FESEM and

E) FETEM images of the nanozymes. Inset of D) EDX mapping of Fe element in one of the nanozymes observed in (D). [CB[8]]/[Py-RSH]/[Dodecylamine] = 100 μM, [Hemin] = 5 μM, [DPH] = 10 μM, λ_{ex}(DPH) = 355 nm, λ_{em}(DPH) = 428 nm.

pH clock mediated imine bond formation was monitored through ^{1}H-NMR spectroscopy wherein the disappearance of the aldehyde peak and appearance of imine peak at the begining of the pH cycle indicated the formation of the SPAs. The imine peak, however, disappeared and the aldehyde peak reappeared towards the end of the pH clock indicating the disruption of the SPAs (Figure 4.8D). The transient vesicular aggregation was followed through fluorescence kinetics experiment using diphenylhexatriene (DPH), a well-known lipophilic probe which exhibits enhanced emission when intercalated within lipid domains of vesicles.[158] The initially weakly-fluorescent probe at acidic pH (~5), upon addition of the fuels, exhibited sharp fluorescence enhancement followed by a gradual decay, indicating the formation of transient vesicular aggregates in the alkaline region (Figure 4.7B). Refueling produced similar cyclic responses for three consecutive cycles with mild dampening after each successive cycle, as observed in case of the pH kinetics profile (Figure 4.9A), owing to accumulation of gluconic acid in the medium.

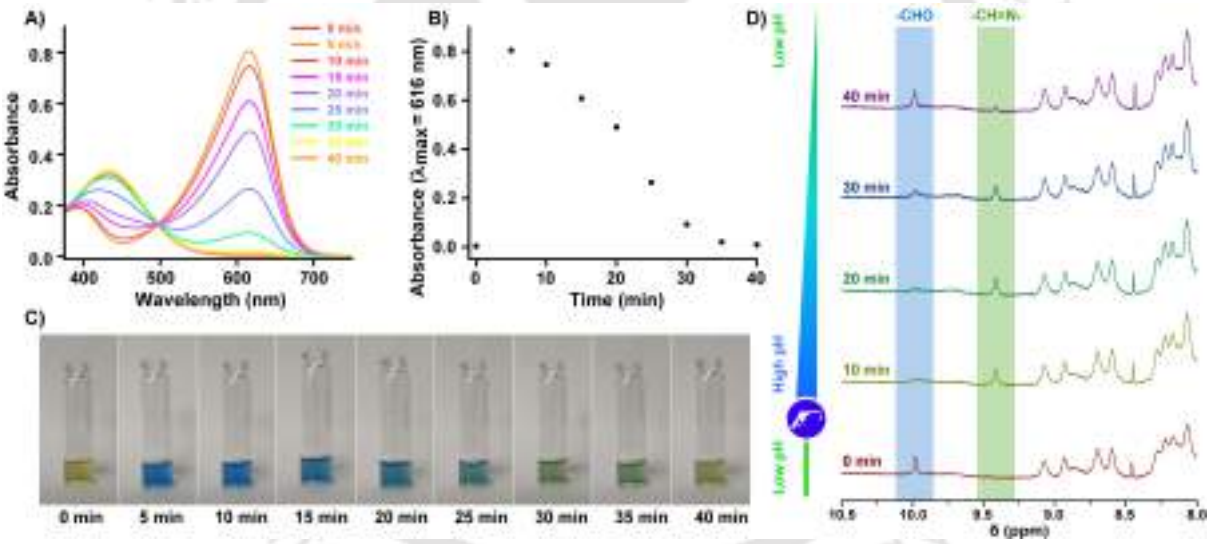

Figure 4.8. A) UV-Visible spectra of BTB at different time intervals of the pH clock constituted by 1 mM pH 9 TRIS buffer, 5 mM glucose and 25 U/mL GOx enzyme, **B)** Change in the absorbance at λ_{max} = 616 nm during the course of the pH cycle (Data obtained from A), and **C)** Photographic images of the BTB solution captured at different time points during the progression of the pH clock. **D)** ^{1}H NMR of TC and DA at different time points post-initiation of the pH clock showing the formation and disappearance of the imine linkage as a function of the pH of the medium.

Transient entrapment of hemin in the SPA vesicles under the influence of pH clock was then assessed through UV-Vis spectroscopy. Soret peak at 390 nm for free hemin at acidic pH (~5) shifted to 413 nm upon initiation of pH clock, indicating entrapment of hemin in monomeric form in the vesicular bilayer (Figure 4.7C). Slightly blue shifted Soret band of lower intensity at the end of the pH cycle implied that the hemin molecules retain their monomeric state and form loosely bound aggregates, possibly with dodecylamine chains, after the collapse of the transient vesicles. A second

refuelling cycle presented similar cycle of changes in the absorbance pattern. It is worth mentioning that although the hemin molecules retain their monomeric state at the end of the pH cycle, they display very low activity owing to the lack of a suitable hydrophobic environment necessary for the activity of the catalyst.[99, 185] Visual evidence of pH clock triggered vesicle formation was obtained through electron microscopic techniques (Figures 4.7D and E) wherein samples collected at pH 8 displayed vesicular aggregates with diameter of ~200 nm, which is in line with the observation from the time dependent Dynamic Light Scattering (DLS) experiment (Figure 4.9B).

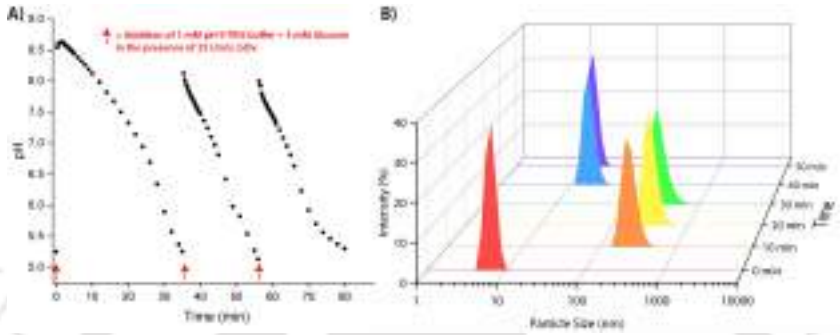

Figure 4.9. A) Representative plot showing the change in pH during the transient vesicle formation through three consecutive. [CB[8]]/[Py-RSH]/[Dodecylamine]=100 µM, **B)** Representative plots of DLS measurements during the transient formation of vesicles in response to the pH clock. [CB[8]]/[Py-RSH]/[Dodecylamine]=100 µM, [Hemin]= 5 µM.

The assembly/disassembly process was also monitored through confocal laser scanning microscopy (CLSM) technique using Nile Red (NR) as the fluorescent probe. Appearance of fluorescent aggregates after 10 minutes of addition of the fuels, which gradually disappeared over a period of 40 minutes, validated the transient formation of the vesicular nanozymes (Figures 4.10A-D).

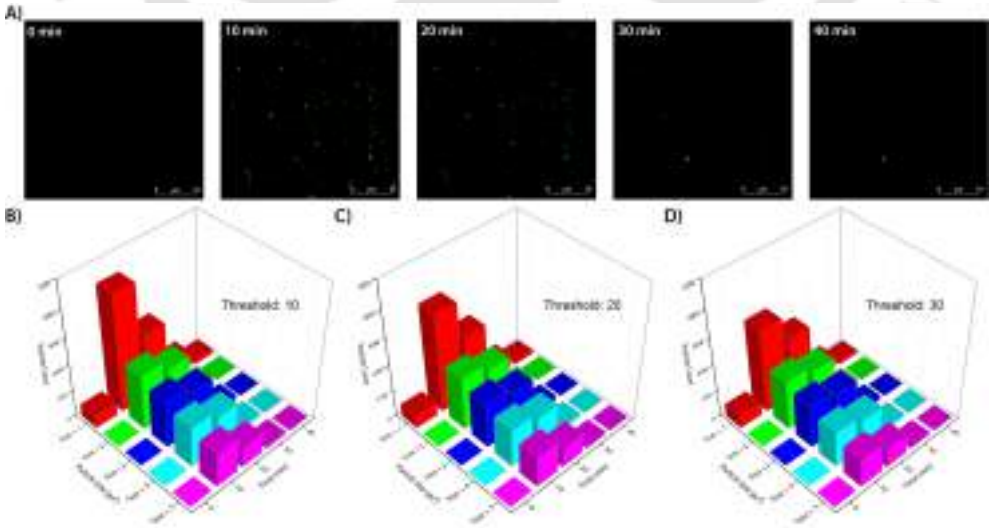

Figure 4.10. A) CLSM images of the transient nanozymes formed under the influence of a pH clock constituted by 25 U/mL GOx, 1 mM pH 9 TRIS buffer and 5 mM Glucose in the presence of 10 µM nile red (NR) at different time points showing the temporal formation of the vesicles. **B)** Statistical analysis of the images obtained by confocal fluorescence microscopy (Data obtained from A). [CB[8]]/[Py-RSH]/[Dodecylamine]=100 µM, [NR]= 10 µM.

Furthermore, Energy Dispersive X-ray (EDX) mapping analysis revealed extensive localization of iron in the vesicular aggregates, substantiating the preferential entrapment of hemin in the transiently formed vesicles (Inset of Figure 4.7D).

4.2.4. Transient Tandem Catalysis by the Nanozyme

Next, the dual feedback-controlled regulation of activity of the transient nanozyme was assesed through peroxidation of pyrogallol using different concentrations of glucose. With increase in concentration of glucose the activity increases as can be seen from Figure 4.11A. Here, the initial high activity of the nanozyme can be attributed to the free hemin molecules (in addition to trapped hemin) in the system which display high catalytic activity in alkaline medium.[197] However, deactivation of the free hemin molecules by H_2O_2 leads to lowering of activity after a brief period as only the trapped hemin molecules now contribute to the catalytic activity. Following the initial burst reaction kinetics, the rate of peroxidase catalysis using 1mM pH 9 TRIS buffer and 3,5 and 7 mM glucose was found to be 0.84 ± 0.04, 1.44 ± 0.1 and 1.82 ± 0.02 µM/min, respectively. This rise in activity is due to the increase in the concentration of in situ generated H_2O_2 with increase in the concentration of glucose in the medium. However, the lifetime of the nanozyme decreased with glucose concentration.

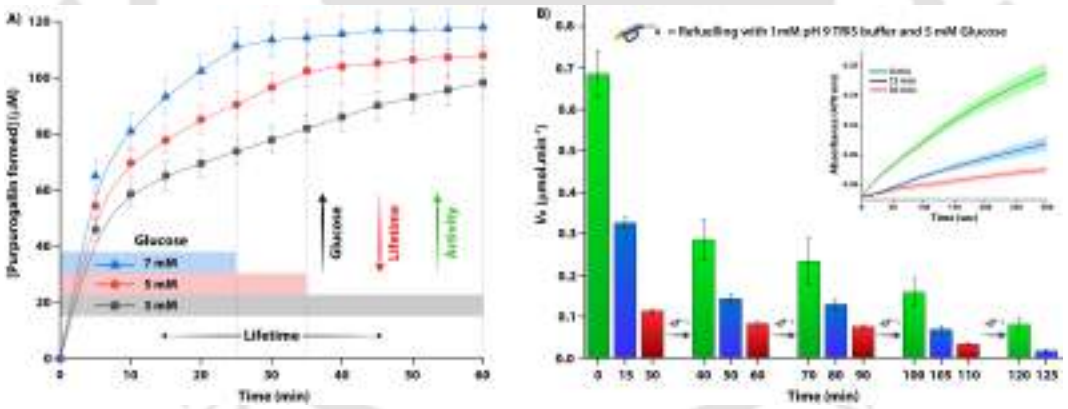

Figure 4.11. A) Time dependent formation of purpurogallin via peroxidase catalysis of pyrogallol in response to the H_2O_2 formed by oxidation of varying concentration of glucose by GOx under the influence of pH clock. [Pyrogallol] = 1 mM. Monitored at 420 nm. **B)** Transient tandem activity of the nanozyme across five consecutive pH cycles. (Inset: Kinetics spectra for the 1st pH cycle monitored at λ_{max}= 470 nm) [CB[8]]/[Py-RSH]/[Dodecylamine] = 100 µM, [Hemin]= 5 µM, [GOx]= 25 U/mL, [MP-Im]= 0.5 mM.

In Figure 4.11A, the region of the curve indicating the progressive formation of purpurogallin represents the active state of the nanozyme and the flattening of the curve represents the inactive state of the nanozyme. The lifetime of the nanozyme as indicated by this curve correlates well with that observed from the pH kinetics study (Figure 4.7A) and substantiate the fact that the lifetime of the nanozyme declines with increasing glucose concentration. All these observations can be explained in light of the glucose oxidation products generated as discussed

earlier for the pH clock optimization. Here, the in situ generated H_2O_2 works as the oxidizing agent for the peroxidase reaction and thereby higher glucose content resulted in higher activity. On the other hand, gluconic acid generation dissipates the nanozyme. This explains the shorter lifetime of the nanozyme at higher glucose concentration. In this manner, the dual feedback mechanism enabled the transient generation of nanozymes with higher activity/ shorter lifetimes and vice versa.

The dual feedback mechanism was then used to transiently upregulate tandem catalysis by the nanozyme. This was followed through UV-Vis kinetics experiment by monitoring the conversion of MP-Im to tetraguaiacol (Figure 4.11B). Following the initiation of the pH clock, the initially high tandem activity decayed with time indicating the course of deactivation of the nanozyme as the pH clock reached its end. Reinitiation of the pH clock by addition of fresh fuel reactivates the nanozymes, however, with lower activity owing to poisoning of the system with excessive amounts of gluconic acid and H_2O_2, which unfortunately could not be removed out of the system. After the first three cycles, the dissipation of the nanozyme took place rapidly in the fourth cycle and more so in the fifth cycle. No more cycles could be performed after five cycles. Owing to the chemically fuelled dynamic self-assembly process of the transient nanozyme and the limited supply of in-situ generated H_2O_2, the transient nanozyme showed slightly lower activity than the thermodynamically stable nanozyme at pH 8. Also similar to the peroxidase catalysis reaction, high concentration of free hemin molecules resulted in a comparitively high tandem activity in the first pH cycle and lowered activity in the subsequent cycles. Nevertheless, the transient tandem catalysis could be repeated across multiple pH cycles, marking the reproducibility of the system.

4.3. Conclusion

In summary, a novel transient nanozyme is presented which displays an efficient hydrolase-peroxidase tandem catalysis event by enhancing the activities of catalytically distinct units- His and hemin through separately placing them in discrete nano-confinements. Dual feedback controlled asymmetric relationship between the tandem nanozyme and the chemoenzymatic pH clock ensured a boosted catalytic activity of the nanozyme for a transient life time. Also, the nanozyme displayed marked substrate specificity and reproducibility over multiple pH cycles, which is a key distinguishing feature of natural enzymes. The nano-compartmentalization strategy employed here can be extended for combining incompatible catalysts in multicompartment nanozymes for efficient one-pot tandem transformations. Further, the results depicted here will allow us to go for life-like systems with more complex and multistep catalytic processes.

4.4. Experimental Section

4.4.1. General Information and Materials

1-Pyrenebutyric acid, 4,4'-Bipyridyl, Guaiacol, 3-Bromopropionic acid, Triethylsilane (TES), 1,6-Diphenyl-1,3,5-hexatriene (DPH), 4-Nitrophenyl acetate and dodecylamine were purchased from Sigma-Aldrich (USA). 1-Methylimidazole, 4-Dimethylaminopyridine, Thionyl chloride and Trifluoroacetic acid (TFA) were obtained from Spectrochem (India). Hemin, D-(+)-Glucose and Terephthalaldehyde were acquired from TCI Chemicals (India). Sodium Borohydride and Glucose Oxidase from *Aspergillus Niger* (Activity=280 U/mg) were procured from SRL (India). Cucurbit[8]uril (CB[8]) was synthesized following a previously published protocol[141] and characterized accordingly. Rink amide MBHA resin, protected amino acids and coupling reagents were purchased from Novabiochem. HPLC-grade dimethylformamide (DMF), dichloromethane (DCM) and acetonitrile (ACN) were procured from Spectrochem (India) and Fisher Scientific (India). All chemicals were used as received without further purification. Solvents were dried whenever required according to the reported procedures. Milli-Q water with a conductivity of less than 2 μScm^{-1} was used for all sample preparations. 60-120 mesh silica gel (SRL) was used for column chromatography. Chromatographic purifications were performed on a Luna 5 µm (C18) column (Phenomenex) using a Dionex Ultimate 3000 HPLC. ^{1}H NMR and ^{13}C NMR spectra were recorded using a Bruker Ascend 600 MHz (Bruker, Coventry, UK) spectrometer and referenced to deuterated solvents. Coupling constants (J values) are reported in hertz, and chemical shifts are reported in parts per million (ppm). Multiplicities are reported as follows: s (singlet), d (doublet), t (triplet), m (multiplet), and br (broadened). Electrospray ionization mass spectrometry (ESI-MS) were performed with a Q-Tof-Micro Quadrupole mass spectrometer (Micromass) and data were analyzed using the built-in software. UV-Visible spectra were recorded on a PerkinElmer Lambda 750 spectrometer, while fluorescence measurements were performed on a Cary Eclipse (Agilent) spectrophotometer. The pH curves were recorded on a Hanna HI 2210 pH meter equipped with HI1131 pH probe from Hanna. Unless otherwise mentioned, all experiments were performed at room temperature.

4.4.2. Synthesis and Characterization

2-methoxyphenyl acetate (MPA)[198]:

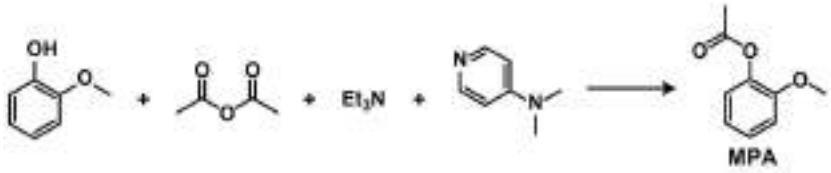

Guaiacol (500 mg, 4.03 mmol, 1 eqv.) was dissolved in dried dichloromethane in a round bottom flask and triethylamine (842 µL, 6.04 mmol, 1.5 eqv.) followed by 4-dimethylaminopyridine

(49.2 mg, 0.41 mmol, 0.1 eqv.) were added to it. The solution was cooled to ~0°C in an ice-bath and acetic anhydride (418.8 μL, 4.43 mmol, 1.1 eqv.) was added to it dropwise with constant stirring. The solution was then allowed to stir at room temperature for 24 hours. Upon completion of reaction (monitored through TLC), the reaction mixture was washed several times sequentially using saturated $NaHCO_3$, water, HCl (2N), water and brine. The organic fraction was collected, dried over anhydrous Na_2SO_4, filtered and evaporated under reduced pressure to give the product, **MPA**, as a clear liquid which required no further purification. Yield= 587 mg, 87.7%. ^{1}H NMR (400 MHz, $CDCl_3$) δ (ppm) 7.21 (td, J = 7.9, 1.8 Hz, 1H), 7.04 (dd, J = 7.8, 1.7 Hz, 1H), 7.00 – 6.92 (m, 2H), 3.83 (s, 3H), 2.32 (s, 3H).

3-(3-(2-methoxyphenoxy)-3-oxopropyl)-1-methyl-1H-imidazol-3-ium bromide (MP-Im):

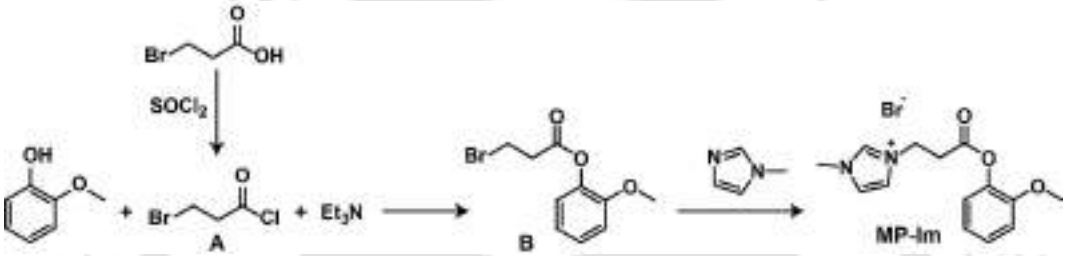

3-bromopropionic acid (1 g, 6.54 mmol, 1 eqv.) and anhydrous DMF (1 drop) were taken in thionyl chloride (5 mL) in a round bottom flask and the solution was refluxed for 5 hours under argon atmosphere. $SOCl_2$ was removed in vacuo to give the acyl chloride, **A,** as a light-yellow viscous liquid which was immediately used for the next step. Guaiacol (720 μL, 6.54 mmol, 1 eqv.) and triethylamine (1.09 mL, 7.85 mmol, 1.2 eqv.) were dissolved in dried dichloromethane in a round bottom flask and the solution was cooled to ~0°C in an ice bath. A solution of **A** in dichloromethane was added drop wise to the above solution at 0°C with constant stirring and then the mixture was allowed to stir overnight at room temperature. The reaction mixture was washed with copious amount of water and brine to remove excess triethylamine and the crude product was purified through column chromatography (10% Ethyl acetate/Hexane) to yield the product, **B**, as a pale-yellow viscous liquid. (Yield= 881 mg, 52%). Compound **B** (870 mg, 3.36 mmol, 1 eqv.) was then dissolved in dried acetonitrile along with 1-Methylimidazole (402 μL, 5.04 mmol, 1.5 eqv.) and the solution was refluxed overnight. The resultant reaction mixture was then purified through column chromatography (7-10% Methanol/DCM) to yield the compound, **MP-Im**, as a light brown viscous liquid. (Yield= 538 mg, 46.9%) ^{1}H NMR (600 MHz, DMSO-d_6) δ (ppm) 9.21 (s, 1H), 7.84 (s, 1H), 7.74 (s, 1H), 7.24 (t, J = 7.8 Hz, 1H), 7.13 (d, J = 8.2 Hz, 1H), 7.07 (dd, J = 7.9, 1.6 Hz, 1H), 6.96 (t, J = 7.7 Hz, 1H), 4.51 (t, J = 6.6 Hz, 2H), 3.87 (s, 3H), 3.71 (s, 3H), 3.29 (t, J = 6.6 Hz, 2H). ^{13}C NMR (151 MHz, DMSO-d_6) δ (ppm) 168.40, 150.55, 138.85, 137.12, 127.18, 123.53, 122.56, 122.40, 120.59, 112.92, 55.72, 44.49, 35.73, 33.44.

1-(4-formylbenzyl)-1'-methyl-[4,4'-bipyridine]-1,1'-diium (MV):

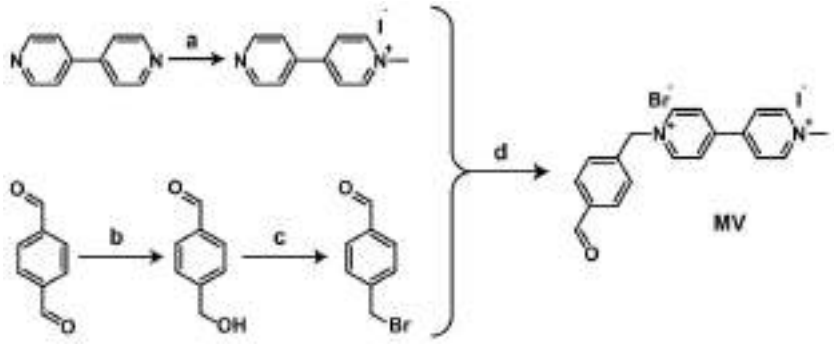

Scheme 4.2: (a) MeI, Dry DCM, Reflux, Overnight (b) $NaBH_4$, Ethanol/THF, 0°C, 6 hrs (c) HBr, Toluene, Reflux, 3 hrs (d) Dry Acetonitrile, 80°C, Overnight

The aldehyde appended viologen derivative, **MV**, was synthesized following our previously reported protocol[158] and subsequently characterised.

Cucurbit[8]uril (CB[8]): CB[8] was synthesized following a previously published protocol.[141] ^{1}H NMR (600 MHz, $D_2O/CF_3CO_2D/D_2SO_4$ (1:1:0.15)): δ 4.25 (d, 16H), 5.55 (s, 16H), 5.86 (d, 16H); MS (ESI): m/z 1461.41 $(CB[8] + Cs)^+$.

General Synthesis of the Peptide (Py-RSH/Py-RSG):

The peptides were synthesized on Rink amide MBHA resin using standard Fmoc (9-fluorenylmethoxycarbonyl) solid phase peptide synthesis (SPPS) protocol. In a typical coupling, 3 equiv. of protected amino acid (with respect to the loading of the resin), 3 equiv. of HBTU, and 6 equiv. of DIPEA were taken in 5 mL of DMF (for 0.1 mmol scale with respect to the resin loading) and stirred for 5 minutes prior to addition of the mixture to the swelled deprotected resin. The reaction mixture was shaken for 60 min and the resin was washed several times with DMF. The Fmoc-deprotection was achieved by treatment of the resin thrice with 5 ml of 20% piperidine in DMF for 5 minutes followed by thorough washing of the resin with DMF and DCM. The Fmoc-deprotection and coupling steps were repeated until the desired peptide sequence was obtained. The resin with the loaded peptide was washed several times with DMF and DCM and dried. The dried resin was then treated with a mixture of freshly prepared mixture of 8.5:1:0.5 (TFA/TES/H_2O) and stirred for 1 h. The resin was finally washed with DCM several times. The cleavage cocktail and the washings combined were concentrated to a minimum volume on a rotary evaporator. The cleaved peptide was then precipitated from cold dry ether, centrifuged and lyophilized to get the crude peptide. Purification was done in Dionex Ultimate 3000 HPLC using a Luna 5 μm (C18) column (Phenomenex) and using acetonitrile and water (containing 0.1% TFA each) as the mobile phase. (HPLC Program= 5% Acetonitrile/Water to 100% Acetonitrile in 25 minutes.)

Py-RSH: ^{1}H NMR (600 MHz, DMSO-d_6) δ (ppm) 8.92 (s, 1H), 8.37 (d, J = 9.2 Hz, 1H), 8.27 (dd, J = 7.6, 4.7 Hz, 2H), 8.24 – 8.18 (m, 3H), 8.14 (m, 3H), 8.06 (t, J = 7.7 Hz, 2H), 7.93 (d, J = 7.8 Hz, 1H), 7.67 (s, 1H), 7.35 – 7.29 (m, 3H), 4.46 (m, 1H), 4.33 (m, 1H), 4.24 (m, 1H), 3.66 (m, 1H), 3.55 (m, 2H), 3.32 (t, J = 7.8 Hz, 2H), 3.16 (m, 1H), 3.09 (m, 2H), 2.93 (m, 1H), 2.32 (d, J = 7.5 Hz, 2H), 2.01 (t, J = 7.7 Hz, 2H), 1.68 (s, 1H), 1.51 (m, 3H). ^{13}C NMR (151 MHz, DMSO-d_6) δ (ppm) 172.63, 172.01, 171.83, 170.13, 156.79, 136.50, 133.60, 130.89, 130.43, 129.56, 129.32, 128.16, 127.58, 127.46, 127.24, 126.54, 126.17, 124.96, 124.81, 124.24, 124.15, 123.51, 116.73, 61.42, 55.29, 52.35, 51.69, 40.42, 34.78, 32.23, 28.88, 27.47, 26.41, 25.06. Mass (ESI-MS): m/z calcd. for $C_{35}H_{42}N_9O_5^+$ $[M+H]^+$: 668.330, found 668.343; $C_{35}H_{43}N_9O_5^{2+}$ $[M+2H]^{2+}$: 334.669, found 334.675; HPLC R_T = 10.44 min.

Py-RSG: ^{1}H NMR (600 MHz, DMSO-d_6) δ (ppm) 8.38 (d, J = 9.2 Hz, 1H), 8.27 (t, J = 7.6 Hz, 2H), 8.22 (t, J = 8.1 Hz, 2H), 8.14 (m, 4H), 8.07 (d, J = 7.3 Hz, 2H), 7.94 (d, J = 7.7 Hz, 1H), 7.53 (t, J = 5.7 Hz, 1H), 7.23 (s, 1H), 7.17 (s, 1H), 5.11 (t, J = 5.4 Hz, 1H), 4.39 (d, J = 7.1 Hz, 1H), 4.26 (m, 1H), 3.65 (m, 3H), 3.58 (m, 1H), 3.10 (m, 2H), 2.32 (t, J = 7.2 Hz, 2H), 2.01 (m, 2H), 1.70 (d, J = 8.5 Hz, 1H), 1.50 (m, 3H). ^{13}C NMR (151 MHz, DMSO-d_6) δ (ppm) 172.36, 171.83, 171.06, 170.23, 156.66, 136.57, 130.89, 130.43, 129.31, 128.16, 127.59, 127.46, 127.23, 126.52, 126.15, 124.96, 124.81, 124.24, 124.15, 123.53, 61.58, 55.18, 52.06, 42.07, 40.44, 34.78, 32.24, 29.05, 27.55, 25.03. Mass (ESI-MS): m/z calcd. for $C_{31}H_{38}N_7O_5^+$ $[M+H]^+$: 588.293, found 588.289; HPLC R_T = 11.28 min.

4.4.3. Methods and Instrumentations

Field Emission Scanning Electron Microscopy (FESEM): 5 µL of the sample solution at specific time interval during the pH cycle was casted on a silicon wafer and immediately freeze-dried to arrest the kinetics of the pH cycle. FESEM imaging and Energy Dispersive X-ray (EDX) mapping analysis were then performed on a Gemini SEM 300 (Sigma Zeiss) instrument.

Field Emission Transmission Electron Microscopy (FETEM): 5 µL of the sample solution at specific time interval during the pH cycle was casted on carbon coated copper grid (300 mesh Cu grid with thick carbon film from Pacific Grid Tech, USA) and allowed to air dry for 2 minutes and then the excess sample was bloated with a tissue paper. The grid was then immediately freeze-dried and the FETEM images were taken in JEOL 2100F microscopes.

Isothermal Titration Calorimetry (ITC): ITC was performed using a Nano-ITC instrument from MicroCal for determining the formation constants and thermodynamic parameters for the inclusion complexes. 1 mM **MV** solution in buffer (10 mM phosphate, pH 7) was injected in parts (each injection, 1.3 µL) at an interval of 2 mins from a 40 µL micro-syringe into the Py-RSH@CB[8] (1:1) solution (0.08 mM, 200 µL) with constant stirring (500 rpm) at 298K. All the solutions were degassed

prior to titration. The ITC thermogram showed a 1:1 binding ratio between Py-RSH@CB[8] and MV, thus indicating the formation of the ternary complex.

Preparation of CB[8] stabilized Host-Guest Ternary Complex: To prepare 2mL of 1mM MV@CB[8] stock solution, 3.5 mg of CB[8] (the overall molecular weight of the used CB[8] was found to be 1730 from the elemental analysis data) and 1mg of MV were accurately weighed into a 2 mL volumetric flask and 1.8 mL of MilliQ water was added to it. The heterogeneous solution was then sonicated for 1 hour at 298K. An equivalent amount of the peptide (Py-RSH/Py-RSG) was added to the solution of the binary complex, the volume was made up to 2 mL using MilliQ water and the solution was further sonicated for 1 hour at 298K. The light yellow colored solution was then kept undisturbed at 298K for 1 day before utilizing for further experiments. The formation of the CB[8] stabilized charge-transfer ternary complex was confirmed by the appearance of a CT band at 400 nm and a significant drop in the fluorescence intensity of pyrene.

Comparison of pH Dependent Hydrolase Activity of pH Responsive/Irresponsive Nanozyme (Figure 4.2B and C): The hydrolase activity of the vesicular nanozyme at pH 5.5, 6.0, 6.5, 7.0, 7.5 and 8 were assessed by spectrophotometrically monitoring the hydrolysis of *p*-nitrophenyl acetate (pNPA) to the chromogenic product, *p*-nitrophenolate anions (pNP). The extinction coefficient of pNP in water was determined using a standard calibration curve of the absorbance at the pH independent isosbestic point, 348 nm for varying concentrations of pNP and was found to be 6.75 $mM^{-1}cm^{-1}$. For determining the hydrolase activity, 0.1 mM each of the **TC** (1 mM stock solution in water) and dodecylamine (10 mM stock solution in THF) were taken in 1 mL of the respective buffer solution (20 mM) in a quartz cuvette of 1 cm path length and 1mM pNPA (200 mM stock solution in acetonitrile) was added to the solution. The solution was mixed briefly and the absorbance change corresponding to the chromogenic product, pNP was monitored at λ_{max}= 348 nm over a period of 5 minutes. Similarly, hydrolase activity of the pH irresponsive nanozyme containing HDMV as the hydrophobic tail was analysed at different pH values. The velocities of the hydrolysis reactions were calculated from the average slope in the first minute of the reaction and all the catalysis experiments were performed in triplicates.

Both the pH sensitive (MV-DA) as well as the pH irresponsive nanozyme (HDMV) displayed a bell shaped curved for the pH dependent hydrolase activity with the maximum rate at pH 7, which is close to the pKa of histidine units. This indicates that cooperative interaction amongst the neighbouring histidine units immobilized on the surface of the vesicular nanozyme account for the efficient hydrolase activity of the nanozymes.[175] On account of disruption of the nanozymes (MV-DA) at acidic pH, the cooperativity is lost and protonation of the free histidine units (pKa~6) at acidic

pH leads to the loss of nucleophilicity and thus the hydrolytic ability of the histidine groups falls much rapidly at acidic pH in case of the pH responsive transient nanozymes.

Note: 20 mM phosphate buffer was prepared for pH 5.5 - 7.5 and 20 mM TRIS-HCl buffer was prepared for pH 8.

Inactivation Kinetics of Free/Vesicle Trapped Hemin (Figure 4.3C): As the structural and electronic features of the catalytically active iron core are reflected in the Soret band of hemin, the rate of inactivation of hemin in the presence/absence of the vesicular nanozyme was analysed by monitoring the change in absorbance at the Soret band of free hemin (λ_{max} = 390 nm) and vesicle entrapped hemin (λ_{max}= 425 nm) upon treatment with varying concentrations of H_2O_2 in pH 8 TRIS buffer. Free hemin displayed rapid decomposition upon addition of increasing amounts of H_2O_2 whereas the trapped hemin displayed negligible inactivation even at higher concentrations of H_2O_2. The inactivation kinetics of hemin in the presence/absence of vesicular nanozyme were calculated via nonlinear regression using GraphPad Prism 9 software, under an assumption of Michaelis-Menten kinetics and the vesicle entrapped hemin was found to exhibit ~26-fold slower inactivation rate as compared to free hemin in the presence of H_2O_2 in alkaline medium.

HPLC Kinetics for the Hydrolysis of MP-Im to Guaiacol (Figure 4.4A-C): The hydrolysis of MP-Im to guaiacol was monitored through Analytical High-Performance Liquid Chromatography (HPLC) using Dionex Ultimate 3000 HPLC system equipped with Luna 5 µm C18 column (Phenomenex) and using acetonitrile and water (containing 0.1% TFA each) as the mobile phase (HPLC Program= 30% Acetonitrile/Water to 100% Acetonitrile in 20 minutes). Briefly, solution containing 0.1 mM each of the TC (1 mM stock solution in water) and dodecylamine (10 mM stock solution in THF) was prepared in pH 8 TRIS buffer and the hydrolysis reaction was initiated by adding 5 mM MP-Im (0.5 M stock solution in DMSO) to the solution. The rate of hydrolysis was subsequently monitored through HPLC at different time intervals and the amount of product formed was quantified using a standard plot prepared with known concentrations of guaiacol.

UV Spectrophotometric Analysis of Tandem Catalysis Reaction (Figure 4.4D and E): The formation of tetraguaiacol oxidation product from MP-Im via tandem hydrolase-peroxidase catalysis was monitored by recording the UV-Visible spectra of the solution (pH 8 TRIS buffer) containing the nanozyme (0.1 mM each of TC and DA, 5 µM Hemin), MP-Im (0.5 mM) and H_2O_2 (5 mM) at an interval of 2 minutes. An enhancement in the absorbance around 470 nm indicated the formation of tetraguaiacol.

Note: Owing to the unstable nature of tetraguaiacol in the presence of light and high concentrations of guaiacol,[199-201] the quantitative analysis of the tandem reaction could not be

performed using techniques like ^{1}H-NMR spectroscopy and HPLC. For obtaining best results, the tandem catalysis reaction was performed in dark and the quantitative determination of the amount of product formed was done through UV-Visible spectroscopy (ε_{470nm}= 26600 $M^{-1}.cm^{-1}$ in water). All absorbance measurements were corrected for background contributions that may arise on account of minor changes in the turbidity of the solution. No obvious enhancement in the absorbance near 750-800 nm as well as around 320-350 nm shows that the enhancement in absorbance around 470 nm originates solely on account of formation of tetraguaiacol[184, 202] and not due to changes in turbidity of the solution or due to changes in the absorbance of any other component.

Comparison of Peroxidase and Tandem Activity (Figure 4.5A and B): Peroxidase activity of hemin in the presence the vesicular nanozyme at pH 8 was assessed by spectrophotometrically monitoring the oxidation of guaiacol to tetraguaiacol in the presence of H_2O_2. Briefly, 0.1 mM each of the TC (1 mM stock solution in water) and dodecylamine (10 mM stock solution in THF) along with 5 μM Hemin (1.5 mM stock solution in DMSO) were taken in 1 mL of pH 8 TRIS buffer (20 mM) in a quartz cuvette of 1 cm path length and varying concentrations of guaiacol (0.5, 1.0, 1.5, 2.0, 2.5 mM from 0.5 M stock solution in acetonitrile) were added to the solution. The reaction was initiated by addition of 5 mM H_2O_2 (1 M stock solution in water) and following mixing, the absorbance changes corresponding to the chromogenic product, tetraguaiacol was monitored at λ_{max}= 470 nm (ε_{470nm}= 26600 $M^{-1}.cm^{-1}$ in water) over a period of 5 minutes. The catalysis experiments were performed in triplicates and the kinetics of the reactions at different pH values were calculated via nonlinear regression using GraphPad Prism 9 software, under an assumption of Michaelis-Menten kinetics. The peroxidase catalysis reaction displayed ~1.5-fold higher activity than the tandem catalysis reaction which implies that the hydrolysis reaction dictates the overall rate of the tandem reaction.

Control Experiments (Figure 4.5C): In order to assess the catalytic role of the various catalytic components of the nanozyme, kinetic studies were performed by monitoring the conversion of MP-Im to tetraguaiacol using varying combinations of the catalytic head group (0.1 mM), hemin (5 μM) and H_2O_2 (5 mM) in pH 8 TRIS buffer (20 mM). Py-RSH containing nanozyme displayed only nominal activity in the absence of hemin and almost no activity in the absence of H_2O_2, thereby substantiating the critical role of hemin and H_2O_2 in the tandem catalysis reaction. The Py-RSG containing nanozyme displayed lower activity than the Py-RSH containing nanozyme. The activity observed in the case of Py-RSG containing nanozyme may be attributed to the background hydrolysis of MP-Im at alkaline pH. Also, the Py-RSG containing nanozyme displayed meagre activity even in the presence of free histidine implying the critical role of surface bound histidine in the hydrolase catalysis reaction.

pH Gated Switching of Peroxidase/Tandem Activity of the Nanozyme (Figure 4.6C and D): The pH reversible nature of the nanozyme was assessed by alternatively switching the pH of an aqueous solution of the nanozyme (containing 0.1 mM each of TC and DA, and 5 μM Hemin) between pH 6 and 8 using 0.01M HCl and NaOH, respectively. 1mL aliquots of the solutions at different pHs were checked for peroxidase activity by treating with pyrogallol (2 mM) and H_2O_2 (5 mM) and monitoring the absorbance of the oxidised product, purpurogallin at 420 nm. Likewise, the tandem activity at different pHs were scrutinized by monitoring the absorbance of tetraguaiacol (at 470 nm) formed as a result of tandem hydrolase-peroxidase catalysis of MP-Im (2 mM) in the presence of H_2O_2 (5 mM). Disruption of the vesicular assembly at pH 6 led to a fall in the peroxidase as well as tandem activity of the nanozyme underpinning the critical role of the vesicular assembly in the catalysis reaction. Reconstitution of the nanozyme, however, restored the activity of the nanozyme over multiple cycles.

Programming of the Chemoenzymatic pH Cycle (Figure 4.7A): Stock solutions of the fuels, pH 9 TRIS buffer (1M) and glucose (1M), as well as the enzyme, glucose oxidase (560 U/mL) were prepared in MilliQ water and stored at 4°C for further use. For pH clock optimization, 1mL aqueous solution containing 0.1 mM each of the TC (1 mM stock solution in water) and dodecylamine (10 mM stock solution in THF), 5 μM Hemin (1.5 mM stock solution in DMSO), and 25 U/mL GOx was first acidified to a pH ~5 using 1mM HCl (to ensure disassembled state of the vesicles) and then the pH clock was initiated by simultaneous addition of aqueous solutions of pH 9 TRIS buffer and glucose in appropriate molar ratios. The change in pH was then monitored over time at 298K.

For a given concentration of pH 9 TRIS buffer (1mM), the lifetime of the pH clock declined with the increase in the concentration of glucose owing to GOx mediated faster production of higher concentrations of the deactivating agent, gluconolactone. Likewise, for a given concentration of glucose (7mM), the lifetime of the pH clock increased with the increase in the concentration of pH 9 TRIS buffer.

The decay trend of the pH clock is primarily dictated by the pH dependent activity of GOx enzyme. GOx exhibits low activity at alkaline pH (8-9)[81] and thus the initial drop in pH is slow. As the pH drops down to ~7, a rapid fall in pH is observed owing to the higher activity of GOx and thus, faster rate of generation of gluconolactone. However, as the concentration of the substrate, glucose decreases overtime, the pH clock displays a slow and gradual decay towards the end of the pH cycle. A higher concentration of glucose (e.g., 7 mM) in comparison to pH 9 TRIS buffer, however, presented a rapid decline in pH over the course of the pH cycle as in this case the high concentration of glucose predominantly accelerated the rate of generation of gluconolactone.

Fluorescence Kinetics Study for Transient Vesicle Formation (Figure 4.7B): Equimolar amounts (0.1 mM) of TC and dodecylamine along with 5 μM Hemin and 25 U/mL GOx were dissolved together in MilliQ water and the pH of the solution was adjusted to ~5 prior to the initiation of the pH clock. 10 μM of the lipophilic dye, DPH (Diphenylhexatriene), was added to this solution and the initial fluorescence intensity was determined. The pH clock was then initiated by addition of 1:5 mixture of pH 9 TRIS buffer (1 mM) and glucose (5 mM) and the emission intensity at 428 nm (λ_{ex}=355 nm, Slit width (Ex./Em.)= 5/5 nm) was monitored across three pH cycles over a period of 90 minutes.

pH Kinetics Study using Bromothymol Blue (BTB) pH indicator (Figure 4.8A-C): Bromothymol Blue (pK_a = 7.1) was employed for visualizing pH changes during the pH cycle as it shows wide colour variation at different pH values ranging from yellow under acidic conditions (pH < 6) to a greenish blue (cerulean) at neutral pH and an intense blue colour under alkaline (pH > 7.6) pH. Briefly, the pH kinetics experiment was performed using 1 mM pH 9 TRIS buffer and 5 mM glucose in the presence of 25 U/mL GOx and 25 μM BTB. The absorbance spectra of BTB was acquired at different time intervals during the course of the pH cycle. A rapid jump in the absorbance at λ_{max} = 616 nm upon initiation of the pH clock followed by a slow decay over a period of 40 minutes indicated initial rise in pH followed by a gradual decay as observed in Figure 4.9A. Also, photographic images of the BTB containg solution captured at different time points during the pH cycle provided visual evidence of the changes in pH during the pH cycle.

^{1}H-NMR analysis showing the pH reversible formation of the imine linked SPA (Figure 4.8D): The reversible formation of imine linkage between the aldehyde appended head group (TC) and aliphatic amine was followed by monitoring the changes in the ^{1}H-NMR peak for the imine and aldehyde protons in response to the pH clock. The imine bonds of the SPAs are buried and shielded in the hydrophobic bilayer of the vesicles and thus are barely visible through ^{1}H-NMR spectroscopy. Therefore, a short chain amine (n-butylamine) was used instead of dodecylamine to avoid vesicular aggregation and facilitate detection of the imine peaks. Briefly, solution containing 0.1 mM each of the TC (1 mM stock solution in D_2O) and n-butylamine (10 mM stock solution in THF-d_8) along with 25 U/mL GOx was prepared in D_2O and its NMR spectrum was recorded. Subsequently, 1 mM pH 8 TRIS buffer and 5 mM glucose (stock solutions prepared in D_2O) were added to the solution above and it's NMR spectra were recorded at an interval of 10 minutes. The disappearance of the aldehyde peak and the appearance of the imine peak indicated the formation of imine linkages. The imine peak, however, slowly disappeared and the aldehyde peak reappeared over a course of 40 minutes as the pH reverted back to the acidic range at the end of the pH cycle.

Assessment of Catalytic Activity:

pH Dependent Peroxidase Activity: Peroxidase activity of hemin in the presence or absence of the vesicular nanozyme at pH 8 and 6, respectively, were assessed by spectrophotometrically monitoring the oxidation of pyrogallol to purpurogallin in the presence of H_2O_2. Briefly, 0.1 mM each of the TC (1 mM stock solution in water) and dodecylamine (10 mM stock solution in THF) along with 5 μM Hemin (1.5 mM stock solution in DMSO) were taken in 1 mL of pH 6 phosphate buffer (20 mM) or pH 8 TRIS buffer (20 mM) in a quartz cuvette of 1 cm path length and varying amounts of pyrogallol (0.5 M stock solution in acetonitrile used to attain final concentrations of 0.5, 1.0, 1.5, 2.0, and 2.5 mM) were added to the solution. The reaction was initiated by addition of 5 mM H_2O_2 (1 M stock solution in water) and following mixing, the absorbance change corresponding to the chromogenic product, purpurogallin was monitored at λ_{max}= 420 nm (λ_{420nm}= 2640 $M^{-1}.cm^{-1}$ in water)[99] over a period of 5 minutes. The catalysis experiments were performed in triplicates and the kinetics of the reactions at different pH values were calculated via nonlinear regression using GraphPad Prism 9 software, under an assumption of Michaelis-Menten kinetics.

pH Dependent Hydrolase-Peroxidase Tandem Activity: Tandem catalytic activity of the nanozyme at different pH values was evaluated by spectrophotometrically monitoring the formation of tetraguaiacol from MP-Im/MPA through a two-step hydrolase-peroxidase catalysis. The activity measurements were performed using the same procedure as that in case of peroxidase catalysis, but using varying concentrations of MP-Im/MPA (0.5 M stock solution in DMSO used to attain final concentrations of 0.5, 1.0, 1.5, 2.0, and 2.5 mM) substrate instead of pyrogallol. The absorbance change corresponding to tetraguaiacol was monitored at λ_{max}= 470 nm (ε_{470nm}= 26600 $M^{-1}.cm^{-1}$ in water)[184] over a period of 5 minutes and the kinetics of the reactions were plotted using GraphPad Prism 9 software, under an assumption of Michaelis-Menten kinetics. Kinetics experiments using the control peptide, Py-RSG, were performed similarly but using a heteroternary complex of CB[8], MV and Py-RSG. All experiments were performed in triplicate.

Time Dependent Dynamic Light Scattering (DLS) Studies (Figure 4.9B): The particle sizes of the assemblies were obtained at 298 K using a 632.8 nm He–Ne laser using Zetasizer Nano-ZS90 (Malvern). Briefly, 1mL aqueous solution containing equimolar amounts (0.1 mM) of the **TC** (1 mM stock solution in water) and dodecylamine (10 mM stock solution in THF), 5μM Hemin (1.5 mM stock solution in DMSO), and 25 U/mL GOx was first acidified to a pH ~5 using 1mM HCl (to ensure disassembled state of the vesicles). The solution was filtered through appropriate filters to remove dust particles, if any, and the hydrodynamic size of the aggregates prior to the initiation of the pH clock (i.e., at 0 min) was found to be ~6nm, probably due to the aggregation of dodecylamine chains and hemin molecules. DLS measurements were performed immediately after the addition of the

fuels (1mM pH 9 TRIS buffer and 5mM glucose) and the hydrodynamic size distribution was monitored at specific time intervals at 298K. All measurements were performed with a constant angle of 90° and the results were reported as Number Distribution to reflect the number of aggregates formed. All measurements were performed in triplicates.

Fluorescence Confocal Microscopy Studies (Figure 4.10A): Transient nanozyme formation was performed as mentioned earlier but using Nile Red (10 μM) as the fluorescent probe as it specifically accumulates in the hydrophobic vesicle bilayer and shows fluorescence upon vesicle formation. Post initiation of the pH clock (1mM pH 9 TRIS buffer and 5mM glucose in the presence of 25 U/mL GOx), the assembly/disassembly process was monitored through CLSM wherein the transient vesicular nanozymes appeared as fluorescent aggregates and slowly disappeared as the nanozyme assemblies disassembled. The sample was excited at 488nm and the fluorescence emission was observed at 549 – 662 nm over a period of 60 min at 298K.

Particle Count Analysis from CLSM (Figure 4.10B-D): The particle count from the CLSM images obtained at different time points were analyzed using ImageJ software. In particular, the images were converted to 8 bit format and visible particles were counted with threshold level set at 10, 20 and 30. The particles having a minimum object dimension of 1, 2, 3, 4 and 5 px^2 were considered for particle count analysis. As anticipated, the number of fluorescent particles first increased upon initiation of the pH clock and then declined steadily as the pH clock culminated.

Transient Peroxidase Activity (Figure 4.11A): Equimolar mixture (0.1 mM) of the TC and dodecylamine, 5 μM Hemin and 25 U/mL GOx were taken together in 1 mL MilliQ water (maintained at a pH of ~5) in a quartz cuvette of 1 cm path length and to it pyrogallol (1 M in ACN) was added to maintain a final concentration of 1 mM. The pH clock was initiated by adding a combination of pH 9 TRIS buffer (1 mM final concentration) and varying concentrations of glucose (3, 5, and 7 mM final concentrations) to the solutions. Following mixing, the absorbance changes at λ_{max}= 420 nm (ε_{420nm}= 2640 $M^{-1}.cm^{-1}$ in water) was monitored immediately over a period of 60 minutes. The experiments were performed in triplicate.

Transient Hydrolase-Peroxidase Tandem Activity (Figure 4.11B): Equimolar mixture (0.1 mM) of the TC and dodecylamine, 5 μM Hemin and 25 U/mL GOx were taken together in 10 mL MilliQ water, maintained at a pH of ~5, and the pH clock was initiated by adding a combination of 1 mM pH 9 TRIS buffer and 5 mM glucose to the solution. 1 mL aliquots of the solution were transferred to a 1 mL quartz cuvette at certain time intervals and 0.5 mM MP-Im was added to the solution. Following mixing, the absorbance change at λ_{max}= 470 nm was monitored immediately over a period of 5 minutes and the velocity of the tandem catalysis reaction at different time points was calculated

from the average slope in the first minute of the reaction. Kinetics were measured for five consecutive pH cycles and the experiments were performed in triplicates.

Note: All kinetics measurements were corrected for interference from various components of the system as well as from changes in turbidity of the solution by subtracting the background contribution prior to fitting using GraphPad Prism 9 software.

भारतीय प्रौद्योगिकी संस्थान गुवाहाटी
Indian Institute of Technology Guwahati

Chapter 5

Transiently Breathing Multi-Luminescent Vesicles with Broad-Spectrum Tunability

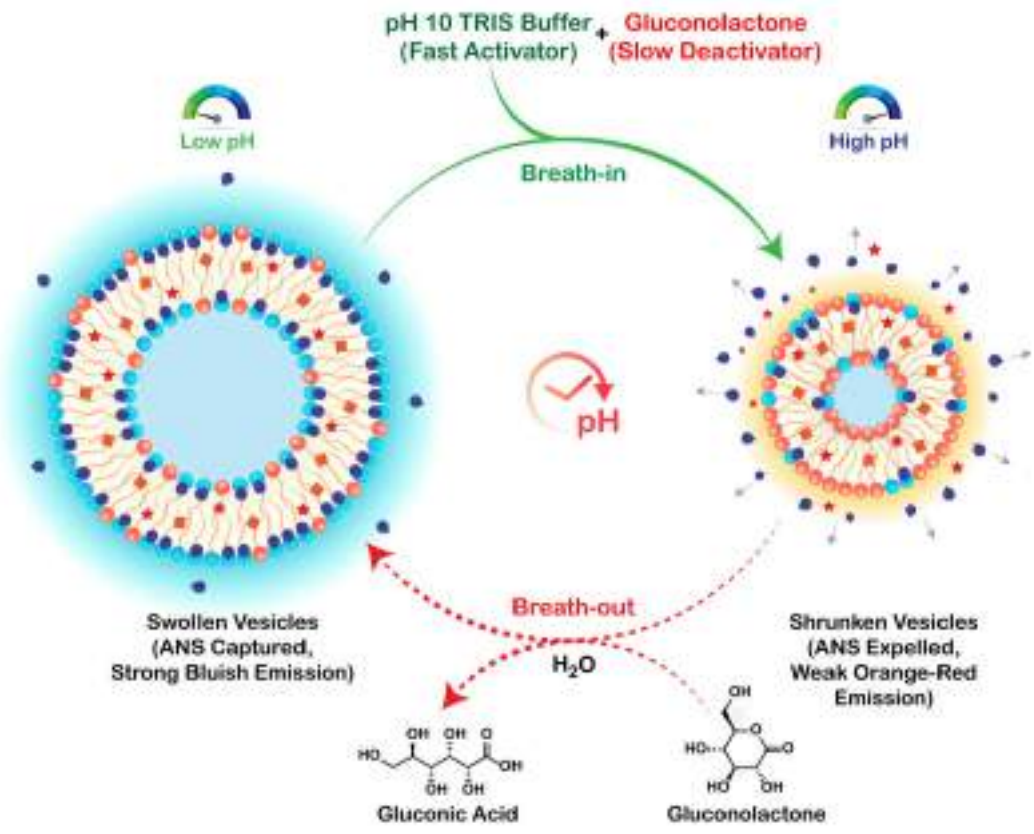

भारतीय प्रौद्योगिकी संस्थान गुवाहाटी
Indian Institute of Technology Guwahati

5.1. Introduction

Along the evolutionary pathway, lipids have emerged as one of the simplest yet indispensable building elements of life. When organized into well-ordered dynamic cellular membranes via self-assembly, they work together to accomplish complex life-sustaining functions. The advent of lipid membranes undeniably accelerated the pace of molecular evolution by compartmentalizing primitive building blocks such as amino acids, sugars, and nitrogen bases in confined nano-spaces and facilitating the development of complex polymeric macromolecules such as enzymes, proteins, and RNA.[203] Owing to their close resemblance to cell membranes, synthetic vesicles have been extensively employed as protocell models to uncover the mysteries of the genesis of life and to simulate complex cellular events in abiotic settings.[204, 205] In response to various chemical and physiological signals, synthetically engineered vesicles have been demonstrated to exhibit life-like features such as fission, fusion, budding, birthing, adhesion, and aggregation.[206, 207] Interestingly, certain deliberately constructed polymeric vesicles have been found to display stimuli-responsive dynamic "breathing" cycles with concomitant variations in hydrodynamic size and membrane permeability.[208-214] This breathing feature has been utilized for controlled release of payload,[210-212] temporal activation of nanoreactors,[212, 213] and modulation of luminescence output.[208, 209] However, these breathing vesicles do not act autonomously and require repetitive chemical/physical stimulation for the “breath-in” and “breath-out” events. Furthermore, only polymeric vesicles have been found to be capable of demonstrating breathing cycles.

Living cells, on the other hand, are predominantly made up of much simpler phospholipids and have highly autonomous and adaptable breathing (i.e. expansion and contraction) cycles that follow out-of-equilibrium dynamics. In recent years, advances in non-equilibrium systems chemistry have prompted the development of life-like vesicles and coacervate-based protocell models that feature fuel-driven transient assembly-disassembly processes with exquisite spatiotemporal control.[47, 115, 158, 167, 215] In an attempt to bridge the gap between chemistry and biology, the transiently generated membrane and organelle mimics are designed to exhibit transitory functional attributes such as growth, replication, confinement and catalysis.[21, 114, 120, 216-219] Although it has received little attention, bioluminescence is another fascinating transient biological process wherein the breathing cycles are concurrently coupled with the conversion of chemical energy to light energy. Certain species of jellyfish (Coelenterates) take up Ca^{2+} ions (i.e. the activator) during the breath-in event, triggering the conversion of non-fluorescent coelenterazine into excited coelenteramide (Scheme 5.1A). The transiently generated excited fluorophore thereafter emits blue light as it relaxes back to the ground state during the breath-out event.[220-222] Likewise, in fireflies, ATP (i.e. the fuel)

drives the oxidation of luciferin to excited state oxyluciferin during the breath-in event, followed by emission of light and CO_2 during the breath-out process (Scheme 5.1B).[223-225]

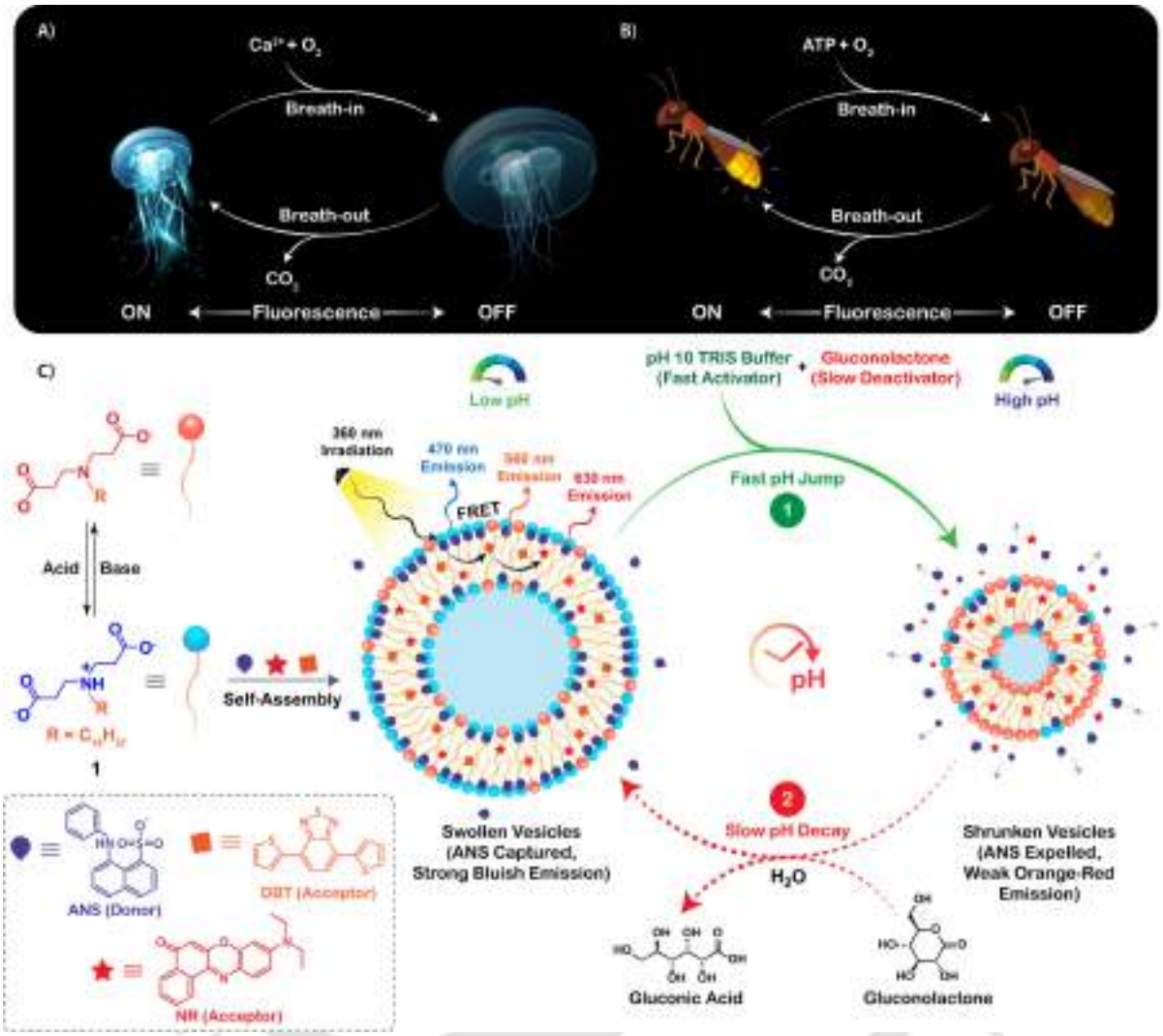

Scheme 5.1. Schematic illustration of transient luminescence in **A)** Jelly-fish, using Ca^{2+} (as activator) and O_2 (as fuel); **B)** Firefly, using ATP and O_2 as fuel; and **C)** the pH responsive breathing vesicles, 1, under the influence of a pH clock.

Converging the concepts of transient breathing and luminescence in a single abiotic ensemble is an enticing and challenging task that has not yet been accomplished under non-equilibrium conditions. To address this unmet goal, herein, we describe a pH responsive vesicular assembly that exhibits jellyfish-like breathing behavior and broad-spectrum transient fluorescence oscillations under the influence of a chemically driven pH cycle (Scheme 5.1C). The vesicular architecture acts as a versatile platform for entrapping and showing Förster resonance energy transfer (FRET) interaction between complementary donor and acceptor fluorophores.[226-230] The spontaneously changing interfacial charge of the vesicles during the pH cycle caused constant fluctuations in vesicle size, resulting in the breathing effect. It also altered the emission intensity of the donor fluorophore, and therefore the efficacy of FRET interactions amongst the donor-acceptor

pairs. The continuously changing ratiometric fluorescence output from different donor-acceptor pairs allowed for broad-spectrum tunability of multicolor luminescence during the breathing events. Furthermore, by altering the activator/deactivator ratio, the lifespan of the breathing cycles may be simply and effectively regulated across several pH cycles, emphasizing the adaptability of the vesicles to the surrounding environment.

5.2. Results and Discussion

5.2.1. pH Responsive Breathing

The charge and size of the amphiphile head group are crucial in determining the amphiphile's hydrophilic-lipophilic balance, the degree of hydration at the vesicular interface as well as the lipid packing arrangement within the vesicular architecture.[231, 232] Thus, to create a pH responsive breathing system, we anticipated using a previously reported pH responsive vesicle.[233] The amphiphile is made up of a single tail lipid with a pH responsive dendritic head group (**1**, Scheme 5.1C). These lipids, unlike polymeric amphiphiles, are easily accessible via a two-step synthetic protocol (Scheme 5.2) and form vesicles across a wide pH range (pH>5). The head group of **1** comprises three pH responsive functional groups, one tertiary amine and two carboxylic acids, which can be protonated and deprotonated reversibly at different pHs. Previous findings[233] suggest that the pH responsive amphiphile with octadecyl tail displayed noticeable and wide variations in hydrodynamic size in response to varying pHs, thus we opted for lipid **1** with octadecyl aliphatic chain to construct our breathing vesicles.

The critical aggregation concentration (CAC) of **1** in aqueous medium was determined using a Nile red (NR) solubilization fluorescence assay (Figure 5.1A-C) and was found to be 2.42×10^{-5} M in pH 7 phosphate buffer (20 mM), which is consistent with the previously reported value.[233] Dye encapsulation and release experiment performed using carboxyfluorescein (CF) also confirmed the formation of stable vesicles under ambient conditions (Figure 5.1D).[127, 234] As previously stated, the pH of the medium has a significant impact on the size of the vesicles produced by **1**, hence Dynamic Light Scattering (DLS) analysis was used to assess the size variations at different pHs. At pH 6, the hydrodynamic diameter of the vesicles was observed to be ~700 nm, but at pH 10, it decreased to ~200 nm (Figure 5.1E). Similar results were depicted by microscopic imaging techniques like FETEM (Figure 5.1G) and FESEM (Figure 5.1H). Furthermore, by simply altering the pH of the media with NaOH/HCl, the inflation-deflation of the vesicles may be readily and reversibly regulated across multiple cycles (Figure 5.1F). The size variations of vesicles as a function of pH can be described using Israelachvili's theoretical framework of critical packing parameter (P).[235] The structure of amphiphilic aggregates can be predicted using the equation, $P = v/A_{min}l_c$ where v is the effective volume

occupied by hydrophobic chains, l_c is the maximum effective length (critical chain length), and A_{min} is the effective hydrophilic head group surface area at the aggregate-solution interface. Fluctuations in the effective charge of the head group at different pHs alter the P of the surfactants, causing size changes. For conclusive argument, the P values of **1** at pH 6 and 10 were obtained experimentally using surface tension measurements (Figure 5.1I)[140], and as expected, the Cpp of **1** at pH 10 (0.54) was found to be lower than that at pH 6 (0.66) (Table 5.1). Furthermore, for both pHs, the P values were well within the vesicular aggregation range (0.5-1).[235]

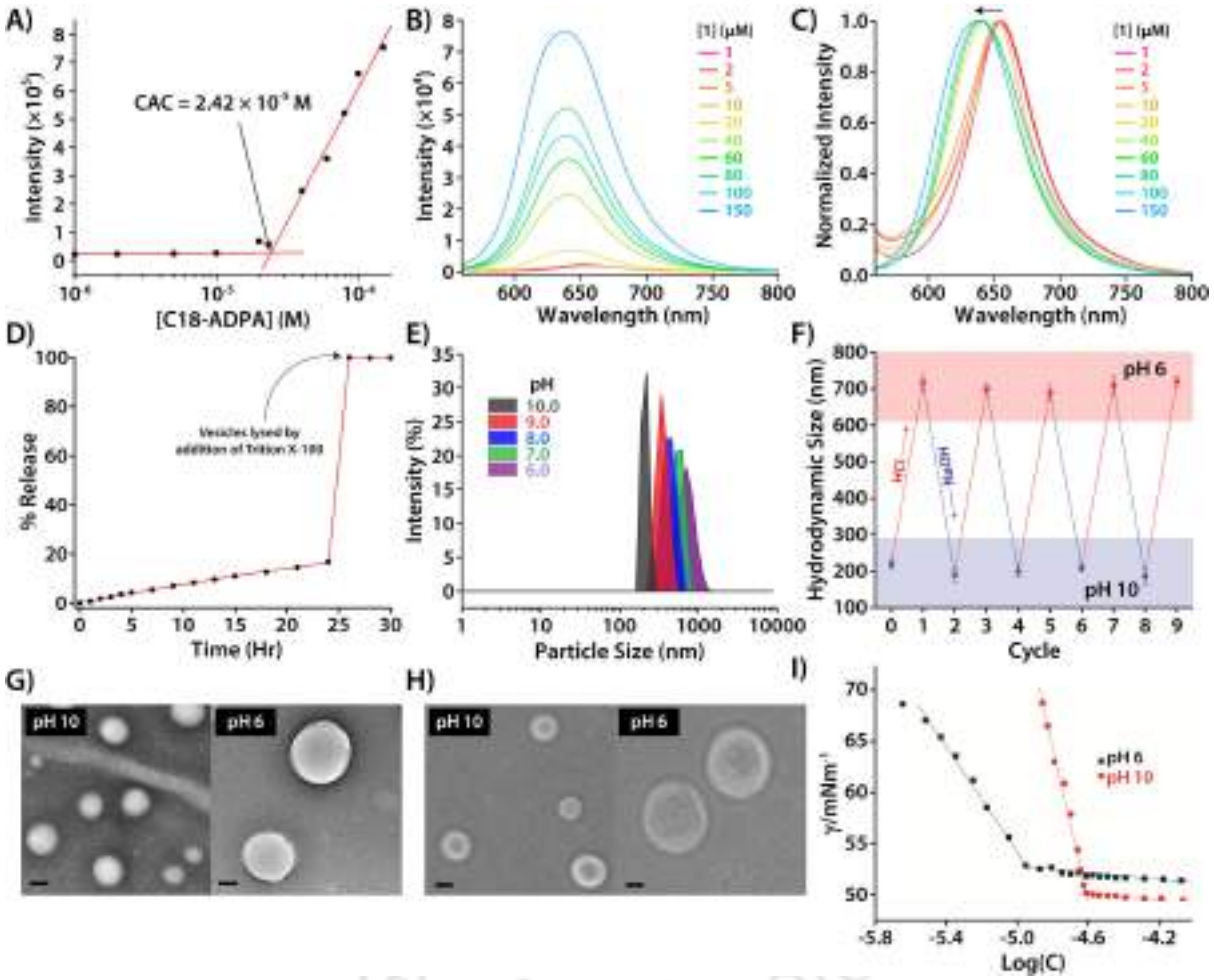

Figure 5.1. pH-responsive breathing. **A)** Critical aggregation concentration (CAC) analyses for **1** using NR in pH 7 buffer (20 mM), **B)** Fluorescence spectra of 1 μM NR taken in pH 7 phosphate buffer (20 mM) upon titrating with increasing concentrations of the amphiphile **1**, **C)** Normalized fluorescence spectra corresponding to **B** showing blue shift in the NR emission with increase in the concentration of **1**, indicating vesicle formation. (λ_{ex}= 550 nm, Slit width (Ex./Em.) = 5/5 nm), **D)** Dye release profile for CF from the vesicles over a period of 24 hours at room temperature. Release of only 16.4% dye in 24 hours suggested the formation of stable and robust vesicles of **1**. **E)** DLS analysis of the vesicles at different pHs, **F)** DLS analysis of HCl/NaOH triggered size changes across multiple cycles, **G)** FETEM, and **H)** FESEM images of the vesicles at pH 6 and 10, **I)** Surface tension versus log [**1**] plot at pH 6 and 10. (For G and H, Scale Bar = 200 nm)

In order to introduce transient out-of-equilibrium breathing feature, we subjected the pH-responsive vesicles to a chemically driven pH clock powered by two opposing triggers, i) Activator:

pH 10 TRIS buffer, which rapidly raises the pH of the medium, and ii) Deactivator: Glucono delta-lactone (GdL), which generates gluconic acid via a comparatively slow base-catalyzed saponification reaction, reducing the pH.[31] The lifetime of the breathing cycles can be easily tuned by varying the ratio of activator and deactivator (Figure 5.2A). As anticipated, higher concentration of the activator increases the lifetime whereas a high concentration of the deactivator lowers the lifetime of the breathing cycles. To analyze the breathing cycle, the swollen vesicles of **1** (~700 nm) maintained at pH ~6 in water were treated simultaneously with 2 mM pH 10 TRIS buffer and 5 mM GdL, and the size fluctuations were recorded using DLS. The vesicles rapidly contracted to ~200 nm within 1 – 2 minutes after starting the pH clock, as the pH jumped to ~10, and then gradually inflated again to ~800 nm over a 60-minute period as the pH steadily declined to ~6 (Figure 5.2B). Also, the formation of bigger size vesicles resulted in a rise in the turbidity of the solution as the pH dropped below ~7 (Figure 5.2C). FESEM images of freeze-dried vesicle samples obtained at different time intervals during the pH cycle also revealed that the vesicles shrink at first, then slowly expand as the pH of the solution changes over the breathing cycle (Figure 5.2D).

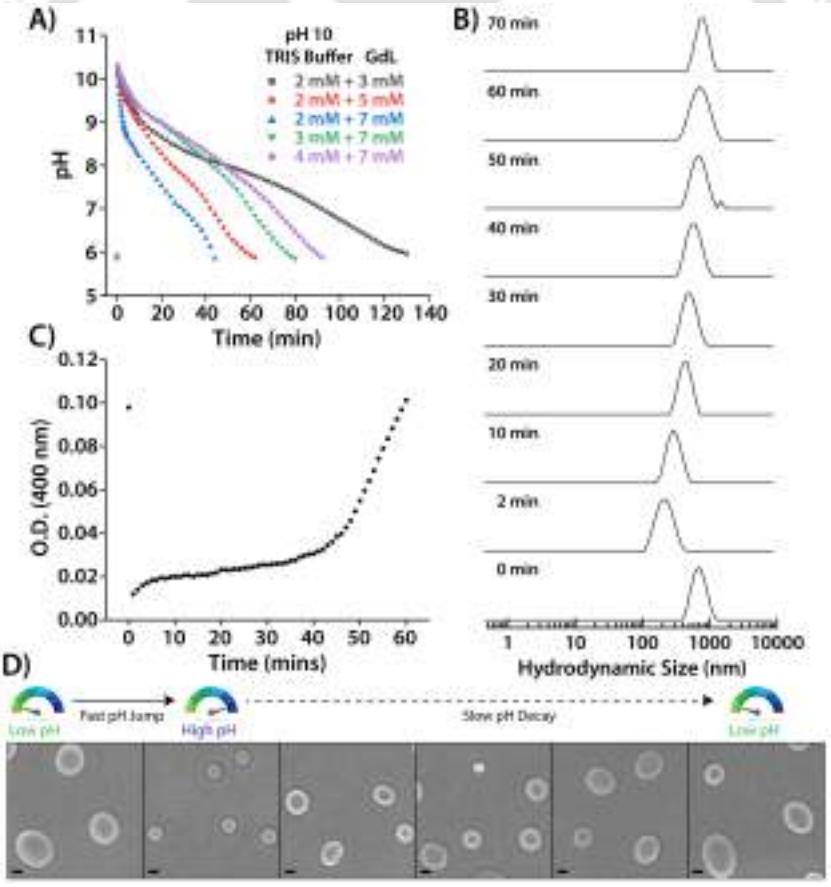

Figure 5.2. A) pH clock optimizations using different concentrations of pH 10 TRIS buffer and GdL, in the presence of 500 μM **1** in water, **B)** Representative plots of DLS measurements during the transient breathing of the vesicles in response to the pH clock triggered by adding 2 mM pH 10 TRIS buffer and 5 mM GdL, **C)** Changes in turbidity of the vesicle solution monitored by measuring the absorbance at 400 nm during the pH cycle. [**1**] = 500 μM, **D)** FESEM images of freeze-dried samples of the vesicles collected along the course of the pH cycle. (Scale Bar = 200 nm)

5.2.2. Vesicles as a Platform for FRET

Vesicles have the remarkable ability of immobilizing hydrophobic dyes in their lipid bilayer and hydrophilic dyes on their surface through various non-covalent interactions. As a result, they've been widely used as a modular framework for generating FRET interactions amongst numerous donor-acceptor pairings. Herein, we have used a polarity sensitive dye, 1-anilinonaphthalene-8-sulfonic acid (ANS) as the donor fluorophore. ANS is a hydrophobic dye that has been frequently utilized to analyze protein unfolding and enzyme binding interactions.[236] It has a low fluorescence intensity in aqueous solution, which increases significantly when it binds to hydrophobic binding sites in proteins/enzymes.[237] ANS binds particularly to cationic amino acid residues in proteins such as lysine and arginine via electrostatic interactions.[236, 238, 239] In the present study, the quantum yield of ANS increased from 0.003 in pH 7 phosphate buffer to 0.205 in the presence of the vesicles (500µM of **1**, 20mM pH 7 buffer) with a ~21-fold enhancement in fluorescence intensity (Figure 5.3A). A similar fluorescence enhancement was observed when ANS was taken in presence of positively charged micelles of CTAB, Cetyl Trimethyl Ammonium Bromide (5 mM) (Figure 5.3B). However, negligible enhancement was observed when ANS was taken with negatively charged micelles of Sodium dodecyl sulfate (SDS, 20mM). This indicates that the weakly hydrophobic ANS binds with protonated amine residues of **1** and exhibits intense fluorescence following sequestration in the palisade layer of the vesicles (The region between the charged head group and the first few carbon atoms of the tail).[240-244]

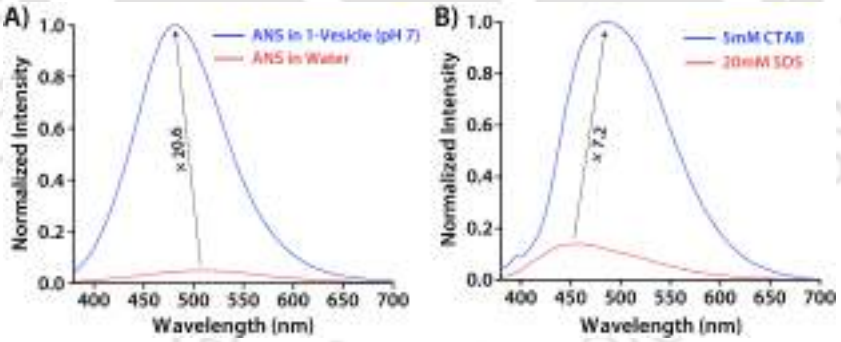

Figure 5.3. A) Fluorescence spectra of 10 µM ANS in water and in the presence of vesicles formed by 500 µM of the amphiphile, **1**. **B)** Fluorescence spectra of 10 µM ANS taken in the presence of cationic micelles of CTAB and the anionic micelles of SDS. (λ_{ex}= 360 nm, Slit width (Ex./Em.) = 5/5 nm)

To construct light harvesting system with ANS as the donor fluorophore, the hydrophobic dyes, 4,7-dithien-2-yl-2,1,3-benzothiadiazole (DBT) and Nile red (NR), were chosen as acceptor fluorophores because of three reasons, i) All three fluorophores emit only when entrapped in the hydrophobic lipid bilayer, ii) Within the vesicular architecture, the fluorophores can be brought close together, which is required for FRET interactions, and iii) There is significant spectral overlap between the absorption spectra of DBT/NR and the emission spectrum of ANS. (Figure 5.4A-C).

When 20 μM ANS (in a solution of 500 μM **1** in pH 7 phosphate buffer, 20 mM) was selectively excited at 360 nm and titrated with increasing concentrations of DBT, ANS emission at 480 nm declined progressively while DBT emission at 565 nm increased (Figure 5.4D). Concurrently, the fluorescence color shifted from blue to yellowish-orange (Figure 5.4I). Similarly, titration with increasing concentrations of NR lowered ANS emission while enhancing NR emission at 635 nm (Figure 5.4F). The fluorescence color, in this case, changed from blue to red. Also, both DBT and NR showed only weak emission in the absence of ANS due to their inherent aggregation caused quenching (ACQ) behavior, ruling out the possibility of direct excitation of the acceptor at the donor excitation wavelength and substantiating the presence of a FRET mechanism in the system (Figure 5.5A, B)

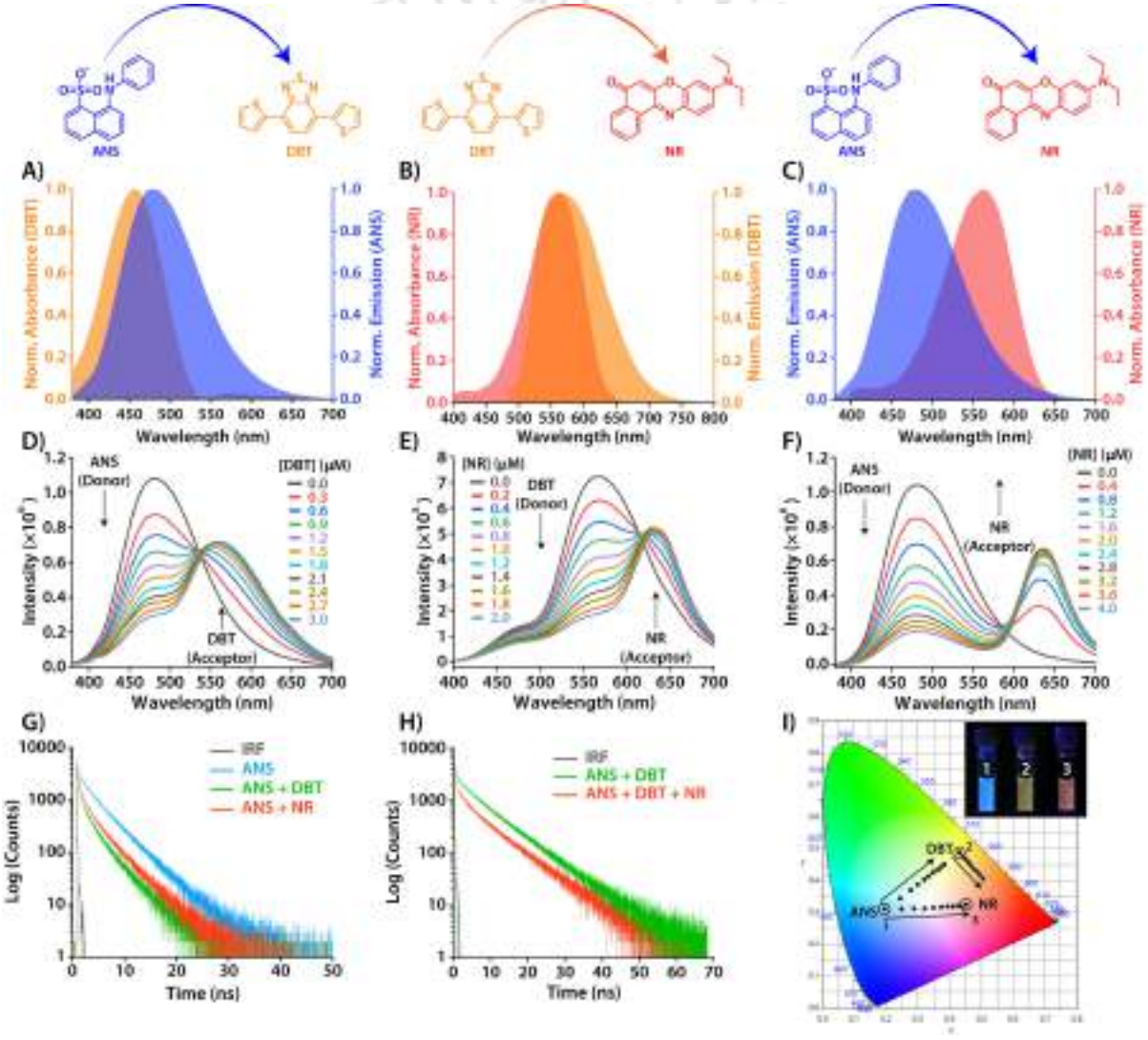

Figure 5.4. Spectral overlap between the **A)** Normalized emission spectrum of ANS and normalized absorption spectrum of DBT, **B)** Normalized emission spectrum of DBT and normalized absorption spectrum of NR, and **C)** Normalized emission spectrum of ANS and normalized absorption spectrum of NR, in pH 7 phosphate buffer (20 mM). **D)** Fluorescence spectra (λ_{ex} = 360 nm) of 20 μM ANS in 500 μM **1** (pH 7 buffer, 20 mM) upon addition of increasing concentrations of DBT (One-step FRET), **E)** Fluorescence spectra (λ_{ex} = 360 nm) of 5 μM DBT taken in presence of 20 μM ANS and 500 μM **1** (pH 7 buffer, 20 mM) upon addition of increasing concentrations of NR (Two-step FRET), **F)** Fluorescence spectra (λ_{ex} = 360 nm) of 20

μM ANS in 500 μM **1** (pH 7 buffer, 20 mM) upon addition of increasing concentrations of NR (One-step FRET), **G)** Fluorescence decay profile of ANS in presence of DBT and NR at 480 nm (λ_{ex} = 375 nm), **H)** Fluorescence decay profile of ANS/DBT in presence of NR at 565 nm (λ_{ex} = 375 nm), and **I)** The CIE chromaticity diagram , showing the luminescent color changes corresponding to the titrations in D, E and F.

Quantitative assessment of the titration process revealed that an energy transfer efficiency (Φ_{ET}) of 72.8% was reached and antenna effect (AE) of 5.4 was attained upon adding 3 μM DBT to 20 μM ANS (Table 5.2). Similarly, addition of 4 μM NR to 20 μM ANS yielded Φ_{ET} value of 82% and AE of 4.9 (Table 5.3). Owing to the overlap of absorption spectra of NR with the emission spectra of DBT, the system also supports two-step sequential FRET from ANS to NR via DBT. When a 500 μM solution of **1** (containing 20 μM ANS and 5 μM DBT (Φ_{ET} = 87.7%)) was titrated with increasing concentrations of NR, the DBT emission at 565 nm declined steadily while the NR emission at 635 nm increased, when excited at the ANS excitation wavelength of 360 nm (Figure 5.4E). The Φ_{ET} and AE value upon adding 2 μM NR were found to be 75.2% and 3.5, respectively (Table 5.4). Furthermore, when titrated with increasing concentrations of DBT or NR, the absorption of ANS at 350 – 390 nm remained constant while that of DBT (at 290 – 340 and 400 – 540 nm), and NR (at 420 – 670 nm), increased continuously, indicating the absence of any ground state interactions between the donor (ANS) and acceptor (DBT/NR) molecules (Figure 5.5C,D).

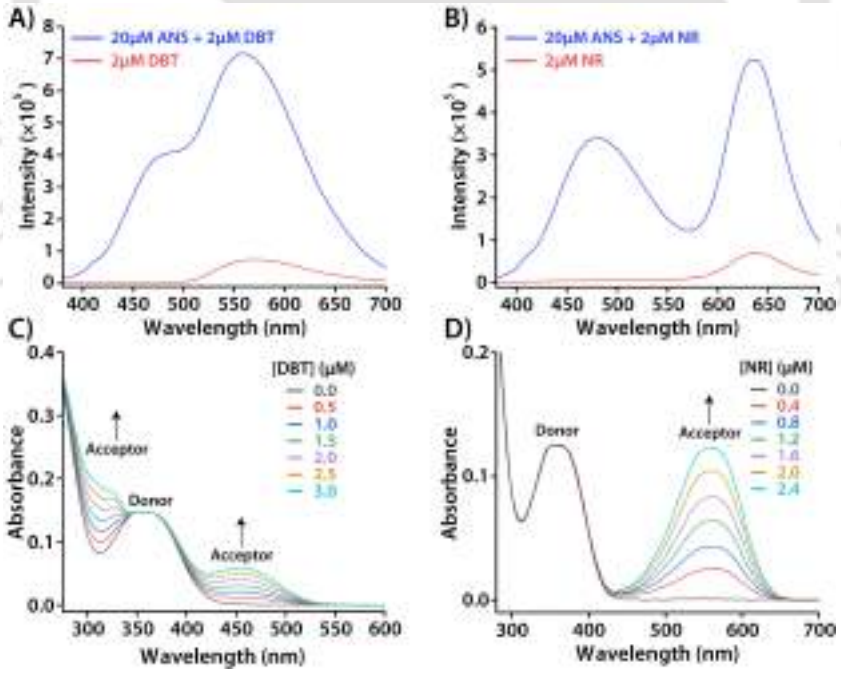

Figure 5.5. Fluorescence spectra of **A)** DBT, and **B)** NR in the presence and absence of ANS. (λ_{ex}= 360 nm, Slit width (Ex./Em.) = 5/5 nm). Changes in the absorption spectra of ANS upon addition of increasing concentrations of **C)** DBT, and **D)** NR, in presence of the vesicles, **1** (500 μM in pH 7 buffer). [ANS] = 20 μM

The energy transfer process was further validated by fluorescence decay experiments wherein a marked reduction in the lifetime of ANS was observed upon addition of DBT, NR as well

as a combination of DBT/NR (Figure 5.4G,H; Table 5.5). This clearly indicates efficient transfer of the excited state energy of the donor to the acceptors and thus the vesicles enabled the construction of one-step as well as two-step sequential light harvesting systems with broad-spectrum tunability of luminescence.

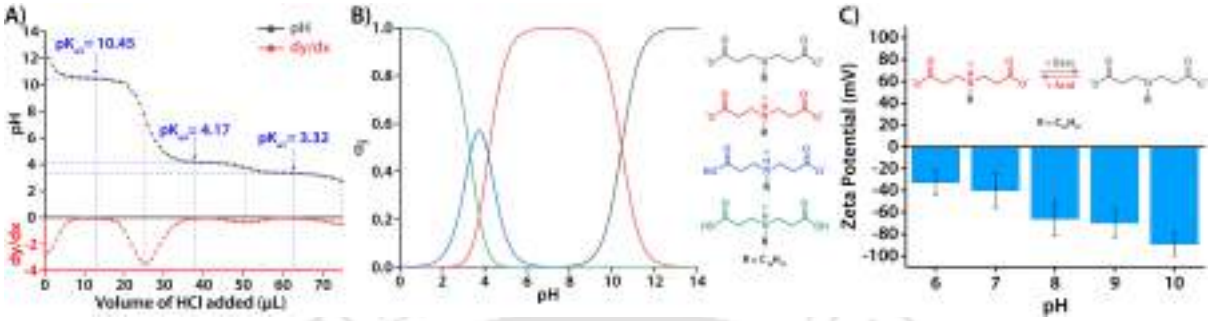

Figure 5.6. A) Changes in the pH of the solution containing 1mM of **1** (adjusted to pH ~ 13 by addition of NaOH) upon consecutive addition of 1 M HCl solution. The lower, red colored curve represents the derivative plot of the pH titration curve. **B)** Microspecies distribution plot showing the distribution of the various charged species of the amphiphile, **1**, as a function of pH. This plot was generated using the pKa values from **A**. **C)** Zeta potential of the vesicles formed by **1** (500 μM) at different pH values.

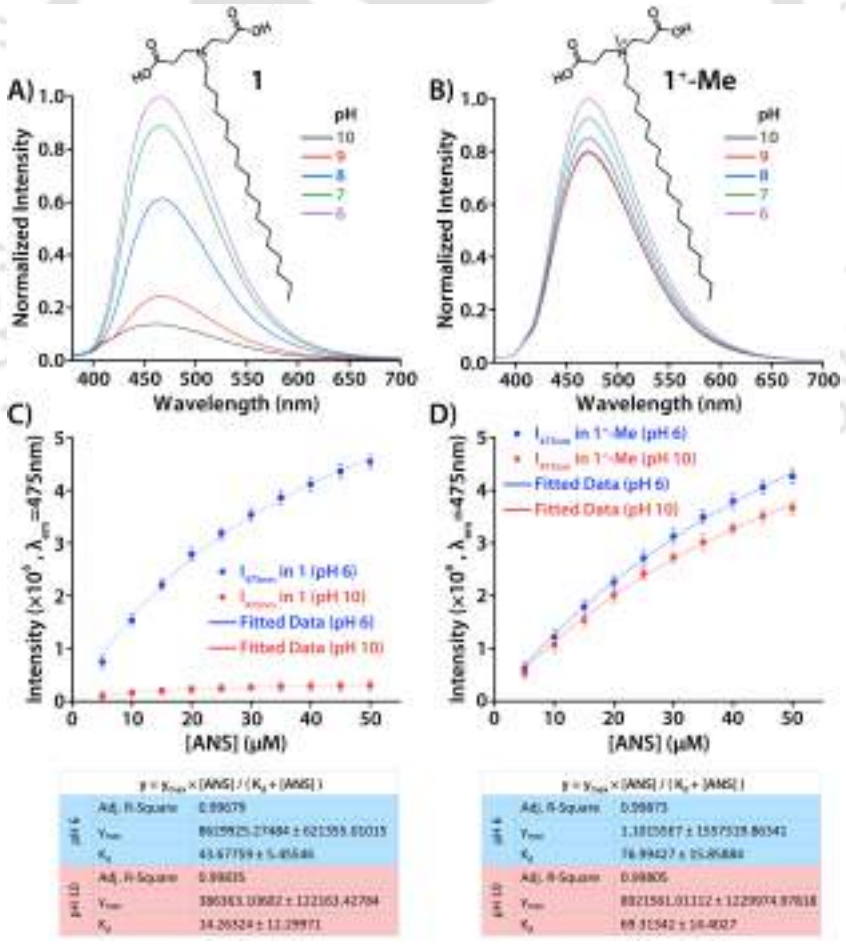

Figure 5.7. Changes in fluorescence intensity of 5 μM ANS at different pH values in presence of the vesicles furnished by 500 μM of **A)** the amphiphile, **1**, and **B)** the control amphiphile, **1⁺-Me**. (λ_{ex}= 360 nm, Slit width (Ex./Em.) = 5/5 nm). Changes in fluorescence intensity at λ_{em}= 475 nm upon addition of increasing concentrations of ANS to a solution containing

vesicles furnished by 500 μM of **C)** the amphiphile, **1**, and **D)** the control amphiphile, **1⁺-Me**, at pH 6 and 10. (λ_{ex}= 360 nm, Slit width (Ex./Em.) = 5/5 nm).

5.2.3. Tuning Transient Multicolor Luminescence

As the head group of **1** contains three pH sensitive moieties, the extent of binding ANS varies linearly with the pH of the system. The apparent pKa of the two carboxylic acids and one tertiary amine group were found to be pK_{a1} = 3.32, pK_{a2} = 4.17 and pK_{a3} = 10.45, respectively (Figure 5.6A), and as can be seen from the microspecies distribution curve, the degree of protonation of the amine group increases as the pH decreases from 10 to 6 (Figure 5.6B). This explains the drop in the negative zeta potential of the vesicles (Figure 5.6C) as well as the enhancement in the emission of ANS (in presence of **1**) as the pH decreases from 10 to 6 (Figure 5.7A). A control amphiphile, **1⁺-Me** (Scheme 5.2), bearing a quaternary ammonium ion in the head group, on the other hand, presented minimal changes in ANS fluorescence with pH fluctuations (Figure 5.7B). This is due to the fact that **1** bind strongly to ANS at acidic pH (K_d = 43.67 ± 5.45) and has weak interactions at basic pH (K_d = 14.26 ± 12.29), whereas **1⁺-Me,** with a permanent positive charge, has comparable K_d values at pH 6 and pH 10 (Figure 5.7C, D).

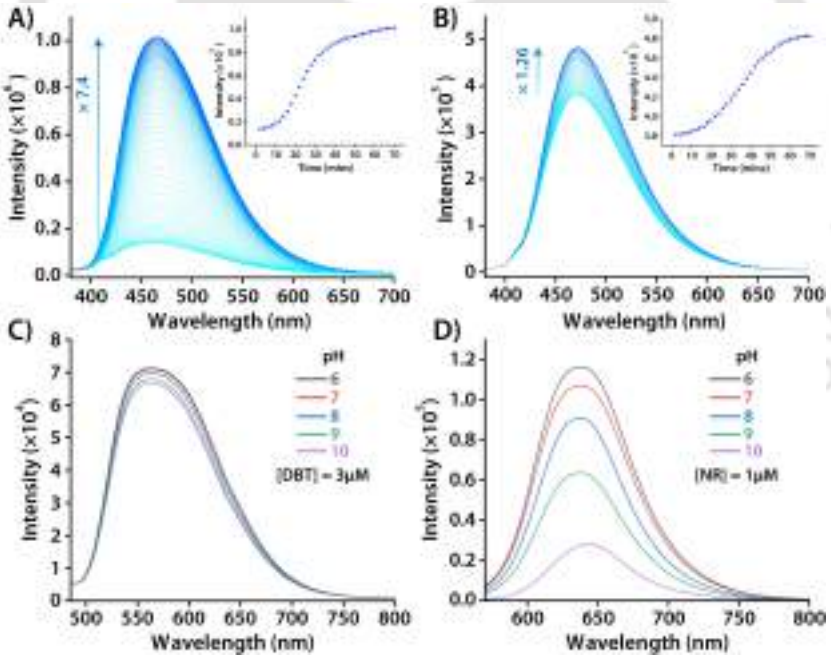

Figure 5.8. Time-dependent fluorescence spectra of ANS (5 μM) in presence of vesicles furnished by 500 μM of **A)** the amphiphile, **1**, and **B)** the control amphiphile, **1⁺-Me**, and under the influence of the pH clock triggered by adding 2 mM pH 10 TRIS buffer and 5 mM GdL. The insets show the change in fluorescence intensity at 460 nm as a function of time. Changes in fluorescence intensity of **C)** 3 μM DBT (λex= 465 nm), and **D)** 1 μM NR ((λex= 550 nm), at different pH values in presence of the vesicles furnished by 500 μM of the amphiphile, **1**.

As expected, when exposed to the pH cycle (2 mM pH 10 TRIS buffer and 5 mM GdL), **1** caused a rapid initial drop followed by a gradual and significant increase in ANS fluorescence, but **1⁺-Me** only produced minor alterations (Figure 5.8A, B). pH variations had negligible impact on the

fluorescence of DBT (Figure 5.8C) as it remains deeply buried in the hydrophobic domains of the vesicles, **1**.[245] The comparatively less hydrophobic NR molecules, however, presented weak emission at higher pH values as they lie closer to the hydrophilic head groups and experience a much polar environment at alkaline pH owing to hydration of the bilayer (Figure 5.8D).[245, 246]

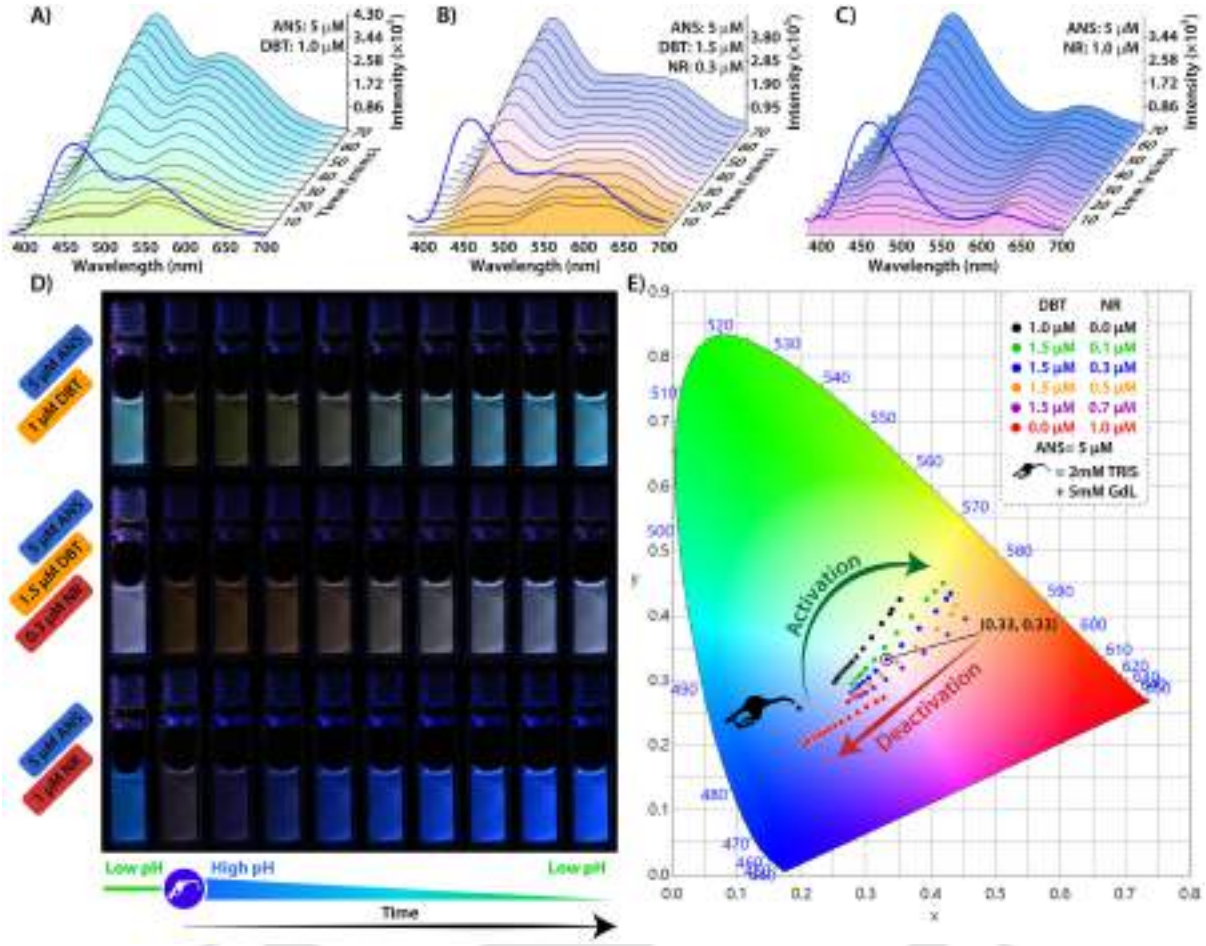

Figure 5.9. Multimodal luminescence by the breathing vesicle under pH cycle. Fluorescence spectral changes of the pH-responsive breathing vesicles of **1**, containing **A)** 5 µM ANS and 1 µM DBT, **B)** 5 µM ANS, 1.5 µM DBT and 0.3 µM NR, and **C)** 5 µM ANS and 1 µM NR, under the influence of pH clock triggered by adding 2 mM pH 10 TRIS buffer and 5 mM GdL. **D)** Photographic images of the vials corresponding to **A-C**, showing changes in luminescence color and intensity, **E)** The CIE diagram showing the transient changes in luminescence for different combinations of the FRET pairs.

After determining the pH-dependent behavior of the different fluorophores in the vesicles, we investigated the feasibility of generating life-like transient multicolor luminescence. We utilized 2 mM pH 10 TRIS buffer and 5 mM GdL for the pH cycles and used different combinations of the fluorophores. A solution containing 500 µM **1**, 5 µM ANS and 1 µM DBT, maintained at pH 6, showed strong bluish fluorescence initially. When the pH cycle was started, the rapid jump in pH caused the expulsion of ANS molecules from the vesicular interface, and the solution emitted weak orange fluorescence, which was mostly produced by the entrapped DBT molecules. Later, as the pH decreased gradually, the uptake of ANS molecules resulted in the transfer of excitation energy from

ANS to DBT and thus an increase in overall fluorescence intensity (Figure 5.9A). The above argument was also corroborated by time-dependent excitation spectra collected along the course of the pH cycle (5.10F). Finally, at the end of the pH cycle, the solution again emitted bluish fluorescence, arising predominantly from the ANS molecules. Remarkably, we were also able to control the spectral range spanned by the transient cycles by altering the DBT concentration for a given concentration of ANS (5 μM) (Figure 5.10A-E).

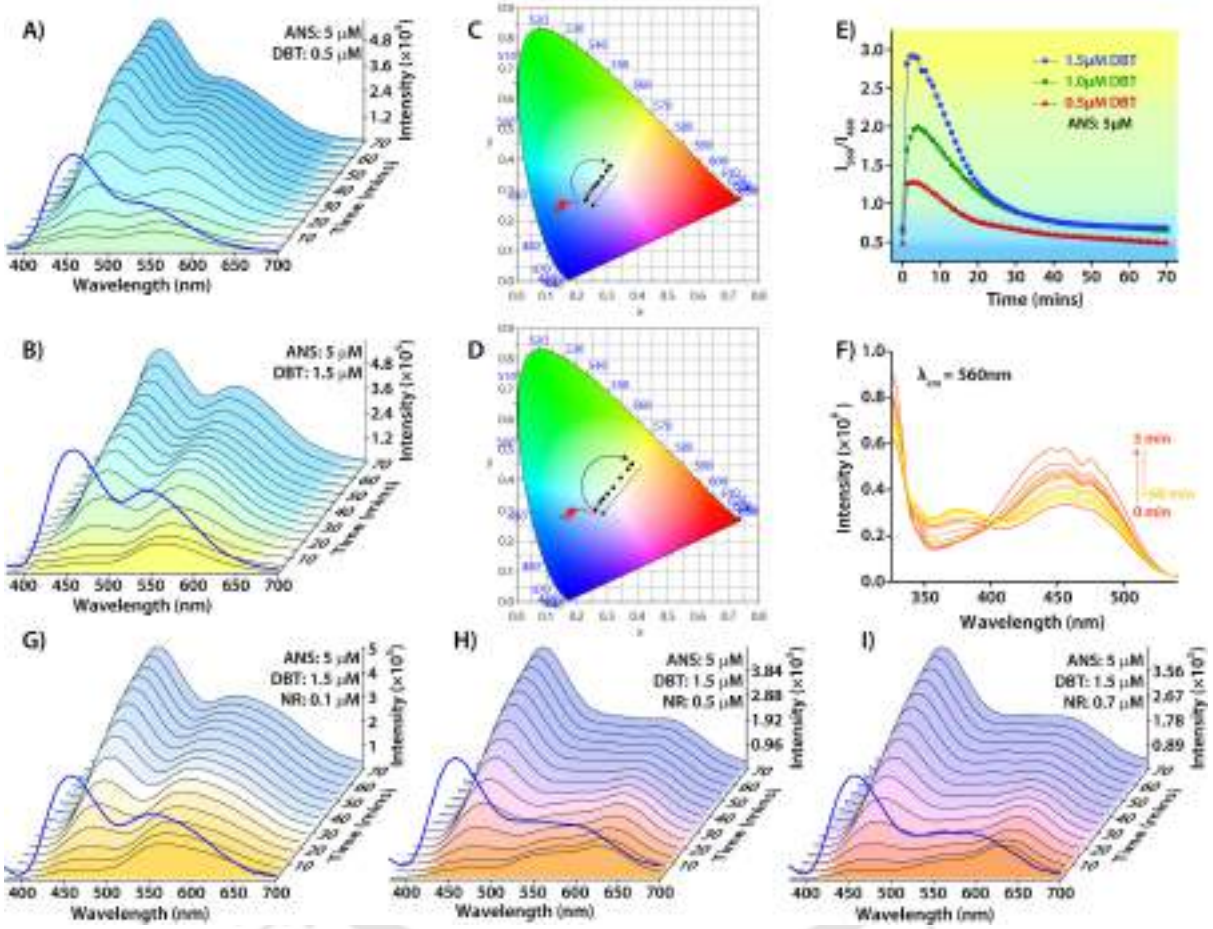

Figure 5.10. Fluorescence spectra changes of the pH responsive breathing vesicles, **1**, containing **A)** 5μM ANS and 0.5μM DBT, **B)** 5μM ANS, 1.5μM DBT, under the influence of pH clock triggered by adding 2mM pH 10 TRIS buffer and 5 mM GdL. The CIE diagram showing the transient changes in luminescence corresponding to **C)** the Figure **A**, and **D)** the Figure **B**. (λ_{ex}= 360 nm, Slit width (Ex./Em.) = 5/5 nm). **E)** Time-dependent variation of the ratio of ANS emission (I_{460}) and DBT emission (I_{560}) along the course of the pH cycle. The I_{560}/I_{460} plotted here correspond to Figure **5.9A** and **5.10A, B**. The I_{560}/I_{460} values indicate the luminescence colours spanned during the pH cycle, as shown in the background of the figure. **F)** Time-dependent excitation fluorescence spectra of 5 μM ANS and 1 μM DBT taken with 500 μM vesicles of **1** under the influence of the pH clock triggered by adding 2 mM pH 10 TRIS buffer and 5 mM GdL. Fluorescence spectra changes of the pH responsive breathing vesicles, **1**, containing 5μM ANS, 1.5 μM DBT and **G)** 0.1μM NR, **H)** 0.5μM NR, and **I)** 0.7μM NR, under the influence of pH clock triggered by adding 2mM pH 10 TRIS buffer and 5 mM GdL. (λ_{ex}= 360 nm, Slit width (Ex./Em.) = 5/5 nm).

Continuously changing ratiometric fluorescence output from the ANS-DBT and ANS-NR (Figure 5.9B) one-step FRET processes, as well as the ANS-DBT-NR two-step FRET process (Figure 5.9C, 5.10G-I), allowed for broad-spectrum tunability of multicolor luminescence during the breathing events (Figure 5.9D, E). To our pleasing surprise, we were also able to achieve transient pure white light emission with CIE coordinates (0.33, 0.33) using 5 μM ANS, 1.5 μM DBT and 0.3 μM NR, during the transient cycle. Quantitative analysis of the FRET process at the two extreme pHs revealed that the fluorophores exhibit high Φ_{ET} at alkaline pH but display low Φ_{ET} at acidic pH (Figure 5.11, Table 5.6). This is due to the fact that at alkaline pH, lesser number ANS molecules are imbedded on the vesicle surface and they transfer most of the absorbed excitation energy to the acceptor fluorophores. At acidic pH, however, the ANS molecules are abundant and thus the acceptor molecules can take up only a portion of the available excitation energy. NR, however, anomalously displayed lower Φ_{ET} with ANS at alkaline pH because it is weakly entrapped in the vesicle under alkaline conditions and is not present in sufficient amount to effectively receive the excitation energy from the available ANS molecules. Thus, although the ANS-NR FRET system spans a broad spectral range at pH 7 (Figure 5.4I), during the transient cycle, the system performed inadequately.

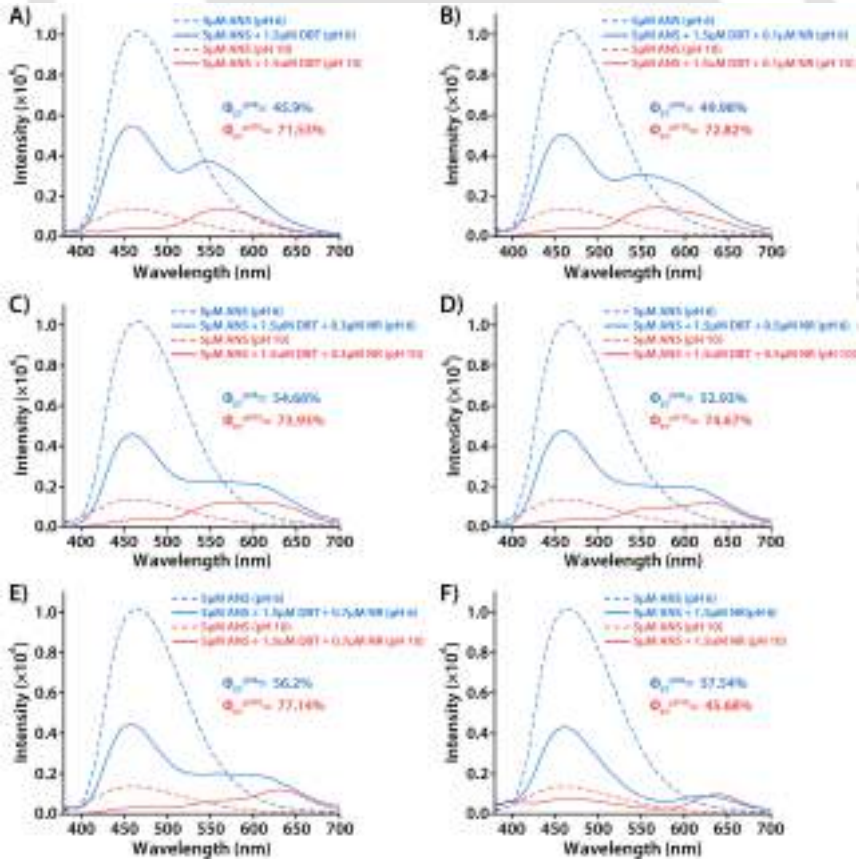

Figure 5.11. Fluorescence spectra of 5 μM ANS, taken with 500 μM **1**, at pH 6 and 10, in presence and absence of **A)** 1.5 μM DBT, **B)** 1.5 μM DBT and 0.1 μM NR, **C)** 1.5 μM DBT and 0.3 μM NR, **D)** 1.5 μM DBT and 0.5 μM NR, **E)** 1.5 μM DBT and 0.7 μM NR, and **F)** 1.5 μM NR. (λ_{ex}= 360 nm, Slit width (Ex./Em.) = 5/5 nm).

5.2.4. Adaptability and Repeatability

Natural systems have an amazing ability to adapt to their environment. On the other hand, artificially created out-of-equilibrium systems have drawbacks such as waste generation, increasing ionic strength, and dilution in consecutive cycles. To mitigate the effect of waste generation, we estimated the amount of GdL that remained unused after the pH cycle (using HPLC, Figure 5.12) and accounted for it when adding triggers for following cycles. Regardless of the amount of GdL added, each pH cycle triggered using 2 mM pH 10 TRIS buffer was found to consume ~1.9-2.1 mM GdL.

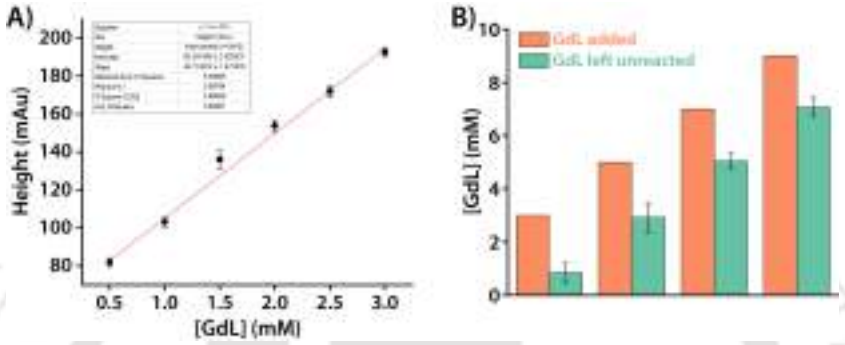

Figure 5.12. A) Standard plot for GdL from HPLC, and **B)** Bar diagrams showing amount of GdL added and amount of GdL left unreacted upon triggering the pH cycle using 2mM pH 10 TRIS buffer.

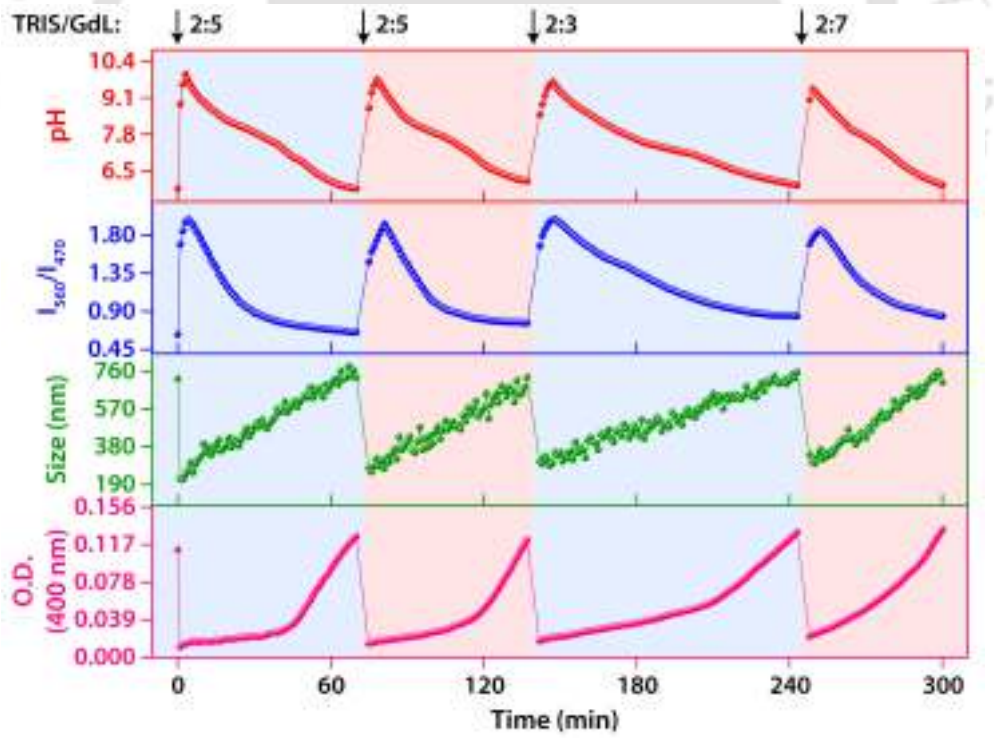

Figure 5.13. Time dependent variation in pH, I_{560}/I_{470} emission ratio, hydrodynamic size and optical density across four consecutive pH cycles triggered using varying ratios of the activator/deactivator.

To check the adaptability of our system, we subjected a solution containing 500 µM **1**, 5 µM ANS and 1 µM DBT to four consecutive pH cycles, but using different ratios of the activator and deactivator. The transient changes in the system were monitored using time dependent pH, I_{560}/I_{470}

emission ratio, DLS and turbidity measurements (Figure 5.13). The system demonstrated excellent reproducibility and had highly adaptive lifetimes that correspond well to the ratio of triggers added during consecutive cycles. This level of control over transient cycles is extremely rare and reflects the system's remarkable adaptability and robustness.

5.3. Conclusion

In summary, we have utilized a minimalistic single tail amphiphile based vesicle to demonstrate pH gated autonomous breathing cycles under the influence of a chemically driven pH clock. The vesicle provided a modular framework to discreetly localize the donor fluorophore (ANS) at the vesicular interface and the acceptor fluorophores (DBT/NR) in the hydrophobic lipid bilayer. Using a unique pH responsive catch and release mechanism, the concentration of ANS in the vesicular ensemble fluctuates during the pH cycle and allows transient luminescence color and intensity changes along the course of the pH cycle. Remarkably, we were also able to achieve transient pure white light emission during the breathing cycles. This system's exceptional versatility, robustness, broad-spectrum transient luminescence, adaptability, and reversibility make it an excellent mimic of naturally occurring bioluminescent systems. Multi-luminescent materials that function in an out-of-equilibrium fashion are particularly rare and, hence this new concept may open new avenues in the field non-equilibrium systems chemistry. This may also find applications in the development of smart fluorescent inks capable of storing cryptic information and other intelligent luminous materials.

5.4. Experimental Section

5.4.1. General Information and Materials

1-anilinonaphthalene-8-sulfonic acid (ANS), 4,7-dithien-2-yl-2,1,3-benzothiadiazole (DBT) and Nile red (NR) were purchased from TCI Chemicals (India). Octadecylamine, Methyl acrylate, Methyl Iodide and Glucono delta-lactone (GdL) were acquired from Sigma-Aldrich (USA). HPLC-grade dimethyl sulfoxide (DMSO), dichloromethane (DCM) and acetonitrile (ACN) were procured from Spectrochem (India) and Fisher Scientific (India). Solvents were dried whenever required according to the reported procedures. Milli-Q water with a conductivity of less than 2 μScm^{-1} was used for all sample preparations. 60-120 mesh silica gel (SRL) was used for column chromatography. Chromatographic purifications were performed on a Luna 5 µm (C18) column (Phenomenex) using a Dionex Ultimate 3000 HPLC. ^{1}H NMR and ^{13}C NMR spectra were recorded using a Bruker Ascend 600 MHz (Bruker, Coventry, UK) spectrometer and referenced to deuterated solvents. Coupling constants (J values) are reported in hertz, and chemical shifts are reported in parts per million (ppm).

Multiplicities are reported as follows: s (singlet), d (doublet), t (triplet), m (multiplet), and br (broadened).

5.4.2. Synthesis and Characterization

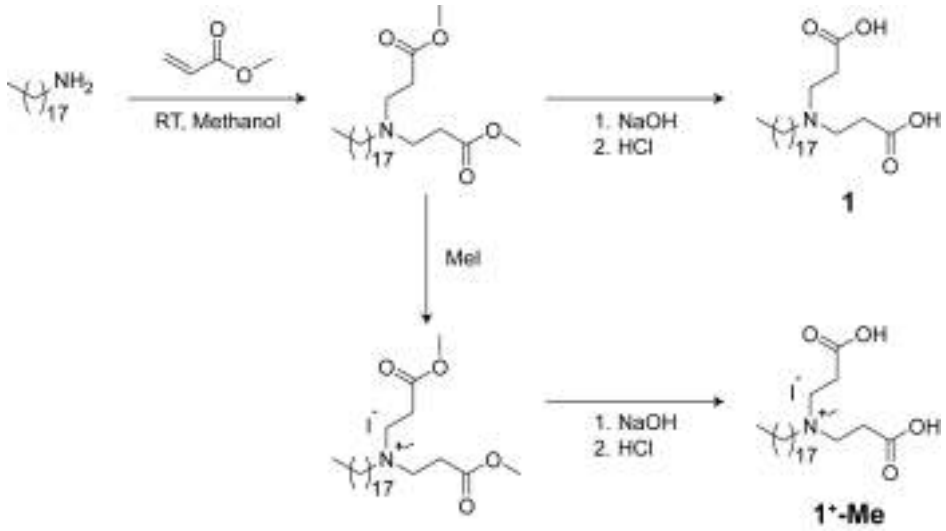

Scheme 5.2: Synthetic procedure of **1** and **1⁺-Me**

Compound **1** was synthesized using a previously reported protocol.[233] Briefly, 5g (0.018 mol) of octadecylamine was dissolved in 25 mL of methanol and excess methyl acrylate (6.7 mL, 4 eqv.,0.074 mol) was added to the solution dropwise with constant stirring. The solution was stirred at room temperature for 48 hours and then the solvent was evaporated at 40°C using a rotary evaporator to yield a colorless oil. The oily residue was taken in dichloromethane and washed with 0.01M HCl solution. The organic fraction was then collected and evaporated. The resulting oily residue was then stirred with 50 mL 1M NaOH solution at 80°C for 10 hours to hydrolyze the methyl ester. The pH of the solution was then adjusted to 5 using HCl and the resulting precipitate was collected by filtration. The precipitate was then dried under reduced pressure and recrystallized in a mixed solvent of hexane and methanol to yield the pure product, **1**, as a white powder. ^{1}H NMR (600 MHz, $CDCl_3$) δ (ppm) 3.45 (d, J = 9.9 Hz, 3H), 3.14 (t, J = 8.3 Hz, 2H), 2.92 (d, J = 7.9 Hz, 4H), 1.83 – 1.70 (m, 2H), 1.25 (d, J = 3.0 Hz, 30H), 0.88 (t, J = 6.9 Hz, 3H). ^{13}C NMR (151 MHz, $CDCl_3$) δ 173.70, 54.01, 49.36, 32.09, 29.96, 29.94, 29.92, 29.84, 29.78, 29.54, 29.47, 29.29, 26.91, 23.77, 22.85, 14.27.

Compound **1⁺-Me** was prepared by first treating octadecylamine (1 g, 0.004 mol) with methyl acrylate (4 eqv.) as mentioned above and then methylating the resulting oily residue with excess MeI. Briefly, the oily residue obtained after first step was stirred with excess methyl iodide (4 eqv.) in DCM for 72 hours. The solvent was then evaporated using rotary evaporator and the resulting oily liquid was stirred with 50 mL 1M NaOH solution at 80°C for 10 hours to hydrolyze the methyl ester. The solution was then neutralized using HCl and the water was evaporated using rotary evaporator.

The resulting crude product was washed multiple times with diethyl ether to give the pure product as a sticky white solid. MALDI-TOF: m/z calcd. for $C_{25}H_{50}NO_4^+$ $[M]^+$, 428.373; found 428.675.

5.4.3. Methods and Instrumentations

UV-Visible spectra were recorded on a PerkinElmer Lambda 750 spectrometer, while fluorescence measurements were performed on a Fluoromax 4 Plus spectrophotometer. pH data were recorded on a Hanna HI 2210 pH meter equipped with HI1131 pH probe from Hanna. FESEM imaging was performed on a Gemini SEM 300 (Sigma Zeiss) instrument. FETEM images were taken in JEOL 2100F microscopes. The particle sizes and zeta potential analysis of the assemblies were performed at 298 K using Zetasizer Nano-ZS90 (Malvern). A He-Ne LASER (λ = 632.8 nm) was used as an excitation source for dynamic light scattering (DLS) measurements. Surface tension measurements were done using a tensiometer (Jencon, India) applying Du Noüy ring method at 25 ± 0.1° C in water. Fluorescence decay was measured using a time-correlated single-photon counting (TCSPC) setup (Horiba instruments) equipped with a 375 nm picosecond LASER diode (Horiba instruments), and a microchannel plate photomultiplier tube (MCP-PMT) for photon detection.

Time-dependent FESEM analysis: 5 µL of the sample solution at specific time interval during the pH cycle was casted on a silicon wafer and immediately freeze-dried to arrest the kinetics of the pH cycle. The dried samples were then analyzed through FESEM.

Time-dependent FETEM analysis: 5 µL of the sample solution at specific time interval during the pH cycle was casted on carbon coated copper grid (300 mesh Cu grid with thick carbon film from Pacific Grid Tech, USA) and allowed to air dry for 2 minutes and then the excess sample was bloated with a tissue paper. The grid was then immediately freeze-dried and then the FETEM images were taken.

Determination of Critical Aggregation Concentration (CAC): 1 µM NR (1 mM stock solution in DMSO) was taken in pH 7 phosphate buffer (20 mM) and increasing concentrations of the amphiphile 1 was added to the solution. After each addition, the solution was mixed briefly and the fluorescence spectra was recorded (λ_{ex}= 550 nm, Slit width (Ex./Em.) = 5/5 nm). Beyond a certain concentration of 1, an abrupt rise in the NR emission was observed indicating the entrapment of NR in the formed vesicles (Figure 5.1A-C). Also, the normalized fluorescence spectra of NR with increasing concentrations of 1 showed an obvious shift to lower wavelengths, indicating increase in the hydrophobicity of the lipid bilayer and thus, the formation of stable vesicles. The CAC was estimated from the point of interception beyond which a sharp increase in the fluorescence intensity and a blue shift was observed.

Dye encapsulation and release: 1 mL of 0.1 mg mL^{-1} solution of Carboxyfluorescein (CF) was prepared in MilliQ water (pH 7) and 1 mM of 1 was added to it. The solution was vortexed for 5 minutes and then sonicated for 30 minutes. The resulting dye containing vesicle solution was passed through a column of Sephadex G-25 using water as the eluent to remove the extravesicular CF. Fluorescence spectra of the eluted solution was measured at specific time intervals over a period of 24 hours (λ_{ex}= 492 nm, Slit width (Ex./Em.) = 5/5 nm). After 24 hours, the vesicles were completely lysed by addition of 20 µL of Triton X-100 (1%) and the fluorescence spectrum was recoded again. The % CF release was calculated using the following equation,

$$\text{Release } \% = \left(\frac{I_t - I_0}{I_a - I_0}\right) \times 100 \qquad \text{(Equation 5.1)}$$

where, I_0 and I_t are the fluorescence intensities initially and at time t, respectively, and I_a is the fluorescence intensity when all the fluorophore molecules were released from the vesicles upon getting lysed by the addition of Triton X-100.

Packing parameter at different pH:

To estimate the packing parameter of the vesicles formed at pH 6 and 10, the CAC was determined using surface tension. The surface tension of the surfactants at the air/water interface was measured using a tensiometer (Jencon, India) following the du Noüy ring detachment method. Previously prepared concentrated aqueous solution of **1** in the respective buffers were added progressively with Hamilton syringes to a measured quantity of the same buffer, gently stirred for 2 min, and kept in a constant-temperature bath for 10 min without disturbance to reach equilibrium. The surface tensions (g) of these solutions were then measured in triplicate while maintaining the temperature. The dependence of the surface tension on the total surfactant concentration (C) at 298 K are shown in Figure 5.1I. The plots of g versus log (C) show breaks at concentrations corresponding to CAC of 1. The surface excess (Γ_{max}) and the minimum surface area (A_{min}) were calculated using equations 5.2 and 5.3 respectively from the least-squares slopes of the g versus log C plots.[247] The packing parameter (P) was calculated using equations 5.4-5.6. All the values are listed in Table 5.1.

$$\Gamma_{max} = \frac{1}{2.303nRT} \lim_{C \to C_{CAC}} \frac{d\gamma}{d \log C} \qquad \text{(Equation 5.2)}$$

where n is the number of species generated by the amphiphile in the solution. For the present case, at pH 10, n = 3 and at pH 6, n = 2 (considering the counterions).

$$A_{min} = 10^{18}[N_A \Gamma_{max}]^{-1} \qquad \text{(Equation 5.3)}$$

$$P = \frac{v}{l_c A_{min}} \qquad \text{(Equation 5.4)}$$

$$v = (0.0274 + 0.0269 n_c) nm^3 \qquad \text{(Equation 5.5)}$$

$$l_c = (0.154 + 0.1265 n_c)\ nm \qquad \text{(Equation 5.6)}$$

Where, v is the volume of the hydrophobic chain, which can be considered to be fluid and incompressible, and l_c is the maximum effective length, called the critical chain length. For a saturated hydrophobic chain with n_c number of carbon atoms which is 18 in the present case.

Parameters	pH6	pH10
CAC (10^{-5}M)	1.05	2.52
Γ_{max} (10^{-6} mol m^{-2})	5.22	3.18
A_{min} (nm^2)	0.318	0.526
P	0.66	0.54

Table 5.1. Interfacial parameters of aggregates formed by **1** at pH 6 and 10.

Quantum yield calculations: The fluorescence quantum yields were determined using the following equation.

$$\phi i = \phi s . \frac{n^2}{n_s^2} . \frac{I_i}{I_s} . \frac{1-10^{-A_S(\lambda_{exc})}}{1-10^{-A_i(\lambda_{exc})}} \qquad \text{(Equation 5.7)}$$

where Φ is fluorescence quantum yield, *A* is the absorbance at the excitation wavelength, *I* the area under the fluorescence spectra, and *n* is the refractive index of the solvent in which the sample was collected. The subscripts "*i*" and "*s*" refer to the sample of interest and the standard, respectively. Coumarin 153 in EtOH (Φ = 0.54) was used as a standard for ANS (in presence of the vesicles), and quinine sulphate in 0.05 M H_2SO_4 (Φ = 0.51) was used for free ANS in pH 7 buffer. Coumarin 153 and quinine sulphate were excited at 411 and 310 nm, respectively.

Energy transfer efficiency (Φ_{ET}) and antenna effect (AE) calculations:

Energy-transfer efficiency, Φ_{ET}, may be defined as the fraction of the absorbed energy that is transferred to the acceptor and is experimentally measured as a ratio of the fluorescence intensities of the donor in the absence and presence of the acceptor (I_D and I_{DA}).[248] Φ_{ET} is calculated using the following equation 5.8.

$$\emptyset_{ET} = 1 - \frac{I_{DA}}{I_A} \qquad \text{(Equation 5.8)}$$

For one-step FRET interactions between ANS and DBT, I_{DA} and I_D are the fluorescence intensities at 480 nm of ANS/DBT and ANS, respectively, when excited at 360 nm.

Antenna effect (AE), is the ability of the acceptor to harvest energy from the donor. AE for the ANS-DBT pair can be calculated using the following equation 5.9.

$$AE = \frac{I_{DA-360} - I_{D-360}}{I_{DA-465}} \qquad \text{(Equation 5.9)}$$

where I_{DA-360} is the fluorescence intensity at 560 nm of ANS/DBT when indirect excitation of the DBT is performed at 360 nm, I_{D-360} is the fluorescence intensity at 560 nm of ANS, which is normalized with ANS/DBT at 480 nm. I_{DA-465} is the fluorescence intensity at 560 nm of ANS/DBT, when direct excitation of the acceptor is performed at 465 nm.

ANS (μM)	DBT (μM)	I_{DA} (I_D)	I_{DA-360}	I_{D-360}	I_{DA-465}	Φ_{ET} (%)	AE
20	0	1079891	-	408326.2	-	-	-
20	0.3	870297.5	515627.3	329839.6	28211.78	19.40876	6.585466
20	0.6	754035.9	595854.4	285914.2	46179.67	30.1748	6.711617
20	0.9	658999.5	645550.1	254047.8	58833.58	38.97536	6.654402
20	1.2	576828.4	681256.5	261558.5	67682.47	46.58457	6.200985
20	1.5	511507.9	701009.7	266365.6	72747.23	52.63337	5.974717
20	1.8	450441.3	712452.3	269809.4	76305.51	58.28826	5.80093
20	2.1	402720.2	716388.3	271443.2	79039.06	62.70733	5.629434
20	2.4	368953.5	718136	271540.2	80529.3	65.83419	5.545756
20	2.7	327241.2	716553.3	271179.5	81246.82	69.69683	5.481738
20	3	294068.4	712213.1	269624.1	81651.57	72.76869	5.420459

Table 5.2. Quantitative analysis of Energy-transfer efficiency, Φ_{ET}, and Antenna effect (AE) for the ANS-DBT one-step FRET process.

For one-step FRET interactions between ANS and NR, I_{DA} and I_D are the fluorescence intensities at 480 nm of ANS/NR and ANS, respectively, when excited at 360 nm.

Antenna effect (AE), for the ANS-NR pair can be calculated using the following equation 5.10.

$$AE = \frac{I_{DA-360} - I_{D-360}}{I_{DA-550}} \qquad \text{(Equation 5.10)}$$

where I_{DA-360} is the fluorescence intensity at 630 nm of ANS/DBT when indirect excitation of the NR is performed at 360 nm, I_{D-360} is the fluorescence intensity at 630 nm of ANS, which is normalized with ANS/NR at 480 nm. I_{DA-550} is the fluorescence intensity at 630 nm of ANS/NR, when direct excitation of the acceptor is performed at 550 nm.

ANS (μM)	NR (μM)	I_{DA} (I_D)	I_{DA-360}	I_{D-360}	I_{DA-550}	Φ_{ET} (%)	AE
20	0	1038878	-	62588.17	-	-	-
20	0.4	844127.3	335846.3	50855.24	57510.82	18.74624	4.955433
20	0.8	696716.4	489399.8	41974.33	88834.97	32.93568	5.036592
20	1.2	567996.5	578541.2	34219.48	106235.8	45.32596	5.123712
20	1.6	475668.6	630395.2	28657.1	114345.1	54.21323	5.262476
20	2	391963.1	648021.8	23614.18	118568.4	62.27054	5.266223
20	2.4	333462.8	659177.3	20089.78	120378.2	67.90163	5.308998

20	2.8	283391.8	652605.3	17073.2	120815.2	72.72136	5.260365
20	3.2	246946	642669.4	14877.49	121245.5	76.22955	5.177859
20	3.6	214622.9	627689	12930.16	121290.7	79.34089	5.068474
20	4	186395	609562.1	11229.54	121494.8	82.05804	4.924758

Table 5.3. Quantitative analysis of Energy-transfer efficiency, Φ_{ET}, and Antenna effect (AE) for the ANS-NR one-step FRET process.

For the two-step FRET interactions between ANS and NR via DBT, I_{DA} and I_D are the fluorescence intensities at 480 nm of ANS-DBT/NR and ANS, respectively, when excited at 360 nm.

Antenna effect (AE), for the ANS-DBT/NR pair can be calculated using the equation 5.10 where I_{DA-360} is the fluorescence intensity at 630 nm of ANS-DBT/NR when indirect excitation of the NR is performed at 360 nm, I_{D-360} is the fluorescence intensity at 630 nm of ANS-DBT, which is normalized with ANS-DBT/NR at 565 nm. I_{DA-550} is the fluorescence intensity at 630 nm of ANS-DBT/NR, when direct excitation of the acceptor is performed at 550 nm.

Note: ANS-DBT corresponds to a combination of 20 μM ANS and 5 μM DBT (Φ_{ET}=87.7%), taken together in 500 μM solution of **1** in pH 7 buffer.

DBT (μM)	NR (μM)	I_{DA} (I_D)	I_{DA-360}	I_{D-360}	I_{DA-550}	Φ_{ET} (%)	AE
5	0	716295.8	-	364811.8	-	-	-
5	0.2	621540.8	424937.3	316552.7	37284.45	14.06133	2.906964
5	0.4	539054.6	459582.9	274542.3	60791	25.46646	3.043882
5	0.6	465981.9	488780.9	237326.1	78629.65	35.57001	3.197964
5	0.8	398832.2	502513.7	203126.5	90586.74	44.85461	3.304978
5	1	347330.2	513614.4	176896.4	99231.74	51.97564	3.393249
5	1.2	304086.9	516329.6	154872.4	104825.4	57.95477	3.448184
5	1.4	266009.6	513852.3	135479.5	108816.1	63.21961	3.477175
5	1.6	233815.1	511033.5	119082.8	111690.5	67.67105	3.509256
5	1.8	202453.6	499202.9	103110.2	113320.1	72.00733	3.495343
5	2	179094.9	491530.9	91213.63	114576.2	75.23705	3.493896

Table 5.4. Quantitative analysis of Energy-transfer efficiency, Φ_{ET}, and Antenna effect (AE) for the ANS-DBT/NR two-step FRET process.

Time-Resolved Photoluminescence (TRPL) Analysis: Fluorescence decays were collected in a Time-Correlated Single-Photon Counting (TCSPC) setup from Horiba instruments using a 375 nm laser diode. The fluorescence lifetimes were measured by fitting the decay curve into a tri-exponential function as given below.

$$I(t) = A_1 e^{(-t/\tau_1)} + A_2 e^{(-t/\tau_2)} + A_3 e^{(-t/\tau_3)} \qquad \text{(Equation 5.11)}$$

where τ_i is the decay time of components, and A_i is the corresponding contributions. The average decay time can be further calculated by the following equation.

$$T = {(A_1\tau_1 + A_2\tau_2 + A_3\tau_3)}/{(A_1 + A_2 + A_3)} \qquad \text{(Equation 5.12)}$$

λ_{em}	Sample	τ_1	τ_2	τ_3	A_1	A_2	A_3	τ_{avg}	X^2
480 nm	ANS (20 μM)	1.55	5.26	1.61	21 %	29 %	50 %	1.93	1.07
	ANS (20 μM) + DBT (5 μM)	0.85	4.27	0.09	21 %	7 %	72 %	0.56	1.04
	ANS (20 μM) + NR (5 μM)	0.84	4.67	0.08	21 %	9 %	70 %	0.66	1.08
565 nm	ANS (20 μM) + DBT (5 μM)	3.37	10.15	0.25	13 %	26 %	61 %	3.27	1.17
	ANS (20 μM) + DBT (5 μM) + NR (2 μM)	2.11	9.77	0.23	14 %	13 %	73 %	1.77	1.21

Table 5.5. Fluorescence lifetimes for varying combinations of ANS, DBT and NR at 480 nm (One-step FRET) and 565 nm (Two-step FRET) in presence of the vesicles of **1** (500 μM)

Programming of the pH cycle: Stock solution of the activator, pH 10 TRIS buffer (1 M), and the deactivator, GdL (1 M), were prepared in MilliQ water and DMSO, respectively, and stored at 4°C for further use. For pH clock optimization, 1 mL aqueous solution containing 500 μM of **1** (100 mM stock solution in DMSO) was prepared, and the solution was first acidified to a pH ~6 using 1 mM HCl (to achieve inflated and protonated state of the vesicles). The pH clock was then initiated by the simultaneous addition of the required amount of pH 10 TRIS buffer and GdL. The change in pH was then monitored over time at 298 K.

Time-dependent DLS analysis: A slightly acidic (pH ~6) solution of 500 μM **1** was taken and a combination of 2 mM pH 10 TRIS buffer and 5 mM GdL was added to it. After swirling briefly, the solution was placed immediately in the DLS instrument and the hydrodynamic size distribution was monitored at specific time points at 298 K. All measurements were performed in triplicates with a constant angle of 90°.

Time-dependent turbidity measurements: The absorbance of 500 μM solution of **1** in water (pH~6) at 400 nm was first determined and then the solution was subjected to a pH cycle by addition of 2 mM pH 10 TRIS buffer and 5 mM GdL. The absorbance of the solution at 400 nm (where no absorbance peak appears from the sample) was then monitored at an interval of 1 minute and plotted as a function of time.

pKa determination: 1mM of **1** was taken in 5 mL water and completely solubilized by adjusting the pH to ~13 using NaOH. The pH of the solution was then recorded after each subsequent addition of 1 μL of 1 M HCl, under constant stirring, at 25°C. The derivative plot of the titration curve indicated

the equivalence points in the curve and the pK_a values were estimated from the half-equivalence points.

Determination of dissociation constant (K_d): 1 mL of 500 μM solution of **1** was prepared in the respective buffer (pH 6/10) and fluorescence spectra were recorded with successive additions of increasing concentrations of ANS to the solution (λ_{ex}= 360 nm, Slit width (Ex./Em.) = 5/5 nm). The emission at 475 nm was plotted as a function of ANS concentration and the dissociation constant, K_d, was determined by fitting the data to the following equation,

$$y = \frac{y_{max} \times [ANS]}{K_d + [ANS]} \qquad \text{(Equation 5.13)}$$

General protocol for time-dependent fluorescence kinetics: 2 mL aqueous solution (pH~6) containing 500 μM of **1** and the desired concentrations of ANS, DBT and NR were taken in a quartz cuvette of 1 cm path length and the fluorescence spectrum prior to the addition of triggers was recorded. Next, the desired ratio of pH 10 TRIS buffer and GdL were added to the solution in the cuvette and mixed briefly. The cuvette was then immediately placed in the fluorescence spectrophotometer and fluorescence spectra were recorded at an interval of 1 minute along the course of the pH cycle (λ_{ex}= 360 nm, Slit width (Ex./Em.) = 5/5 nm).

Explanation for changes in ANS fluorescence in water and buffer:

The emission maxima of ANS in the presence of the vesicles. **1**, in water appears at 460 nm (As can be seen during the transient pH cycles, Figure 5.8A, 5.9A-C, 5.10A, B, G-I). The emission maxima, however, shifts to 480 nm when ANS is taken in buffer (Figure 5.4D-F). Also, for the same pH, a given concentration of ANS shows enhanced emission in water as compared to that in buffer. This is because the emission intensity of ANS increases and the emission maxima shows a blue shift as the electrostatic interaction between the sulfonate group of ANS and cationic head group of the vesicles increase.[238, 239] In buffered solution, the buffer ions partially shield the head group charges, lowering the ionic interactions with ANS. Water, however, permits strong electrostatic interactions between the cationic head groups and ANS and result in blue-shifted enhanced emission.

Time-dependent excitation kinetics: 2mL aqueous solution (pH~6) containing 500 μM of **1**, 5 μM ANS and 1 μM DBT were taken in a quartz cuvette of 1 cm path length and the steady state excitation spectrum prior to the addition of triggers was recorded (λ_{em}= 560 nm, Slit width (Ex./Em.) = 5/5 nm). Next, 2 mM pH 10 TRIS buffer and 5 mM GdL were added to the solution in the cuvette simultaneously and mixed briefly. The cuvette was then immediately placed in the fluorescence spectrophotometer and excitation spectra were recorded at an interval of 1 minute along the course of the pH cycle.

Estimation of GdL used during the pH cycle: pH cycles were performed in 1 mL aqueous solution containing 500 µM of **1** (pH~6) using varying ratio of pH 10 TRIS buffer and GdL. The concentration of TRIS buffer was kept constant (2 mM) in each case, whereas the concentration of GdL was changed (3, 5, 7, 9 mM). Towards the end of the pH cycle, as the pH reached ~6, 10 µL aliquot was withdrawn from the solution and diluted to 1 mL using pH 6 buffer, to cease the hydrolysis of GdL. GdL that remained unreacted was analyzed through HPLC by monitoring the absorbance at λ= 214 nm, R_t= 3.5 min and the amount of GdL was quantified using a standard plot prepared with known concentrations of GdL. (HPLC Program= 5% Acetonitrile/Water to 100% Acetonitrile in 10 minutes, Flow rate= 1 mL min^{-1}.)

Energy-transfer efficiencies, Φ_{ET}, for the systems mentioned in Figure 5.11, at different pHs, were calculated as follows.

pH	ANS (uM)	DBT (uM)	NR (uM)	IDA (ID)	ET (%)
6	5	0	0	1009077	-
6	5	1.5	0	545924	45.89867
6	5	1.5	0.1	504720.8	49.98193
6	5	1.5	0.3	457534.3	54.65813
6	5	1.5	0.5	474952.8	52.93195
6	5	1.5	0.7	442004.6	56.19713
6	5	0	1.5	428491.7	57.53627
10	5	0	0	135850.2	-
10	5	1.5	0	38673.25	71.53243
10	5	1.5	0.1	36922.21	72.82138
10	5	1.5	0.3	35410.79	73.93394
10	5	1.5	0.5	34411.23	74.66972
10	5	1.5	0.7	31056.09	77.13946
10	5	0	1.5	73797.33	45.67742

Table 5.6. Quantitative analysis of Energy-transfer efficiency, Φ_{ET}, for different combinations of ANS, DBT and NR at pH 6 and 10, in water.

6. Characterization Data of the Synthesized Compounds

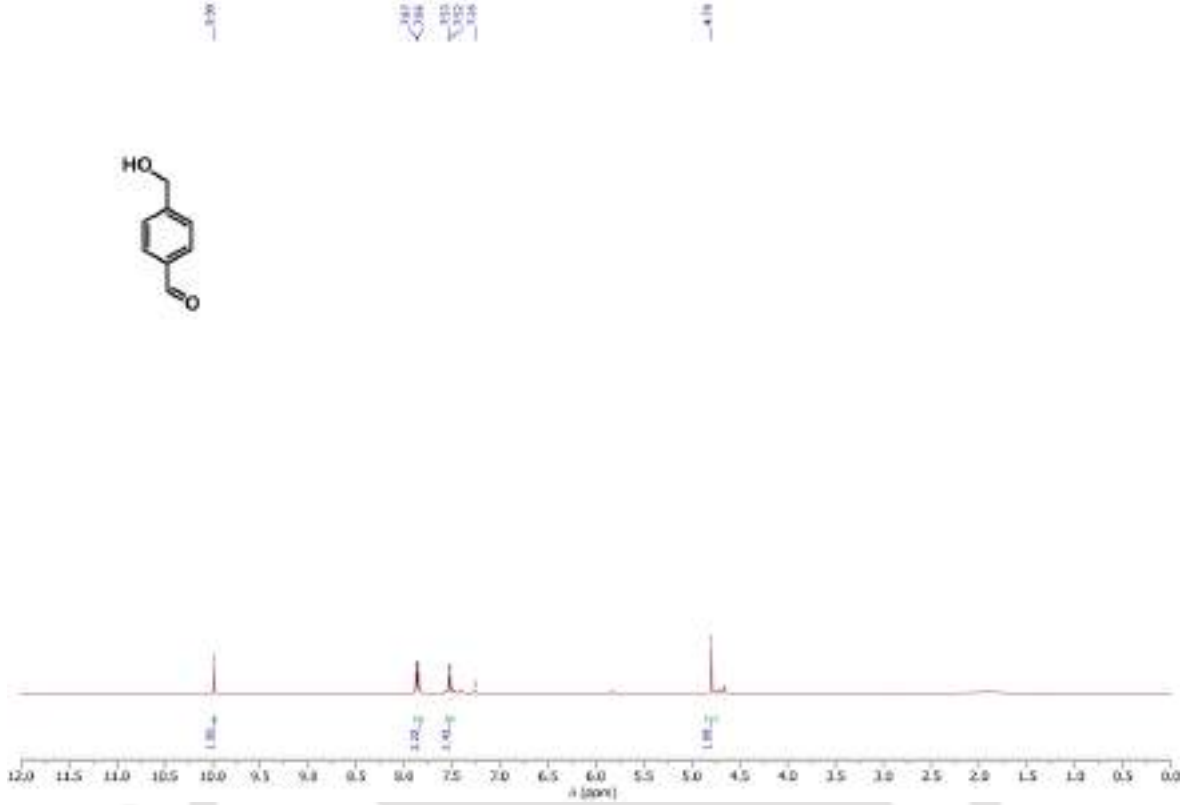

Figure 6.1. ^{1}H NMR spectrum of 4-(Hydroxymethyl)benzaldehyde **(A)** in $CDCl_3$

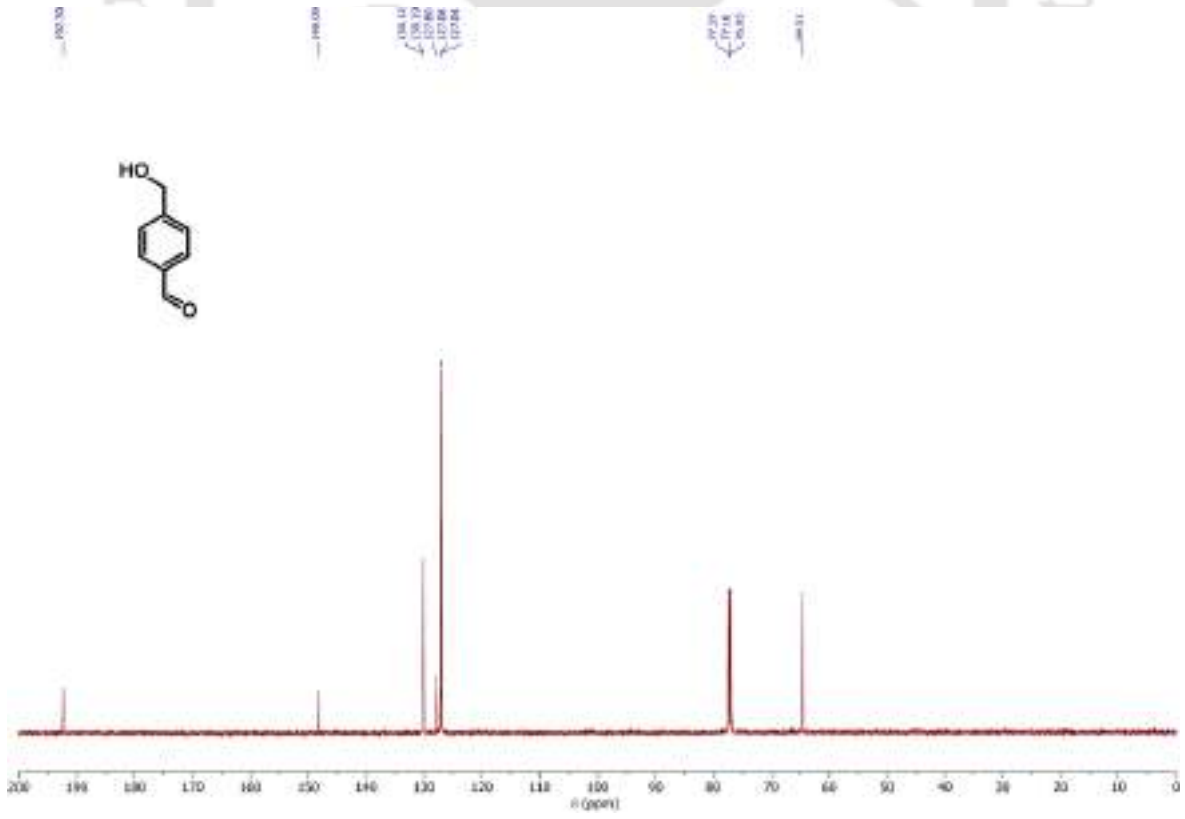

Figure 6.2. ^{13}C NMR spectrum of 4-(Hydroxymethyl)benzaldehyde **(A)** in $CDCl_3$

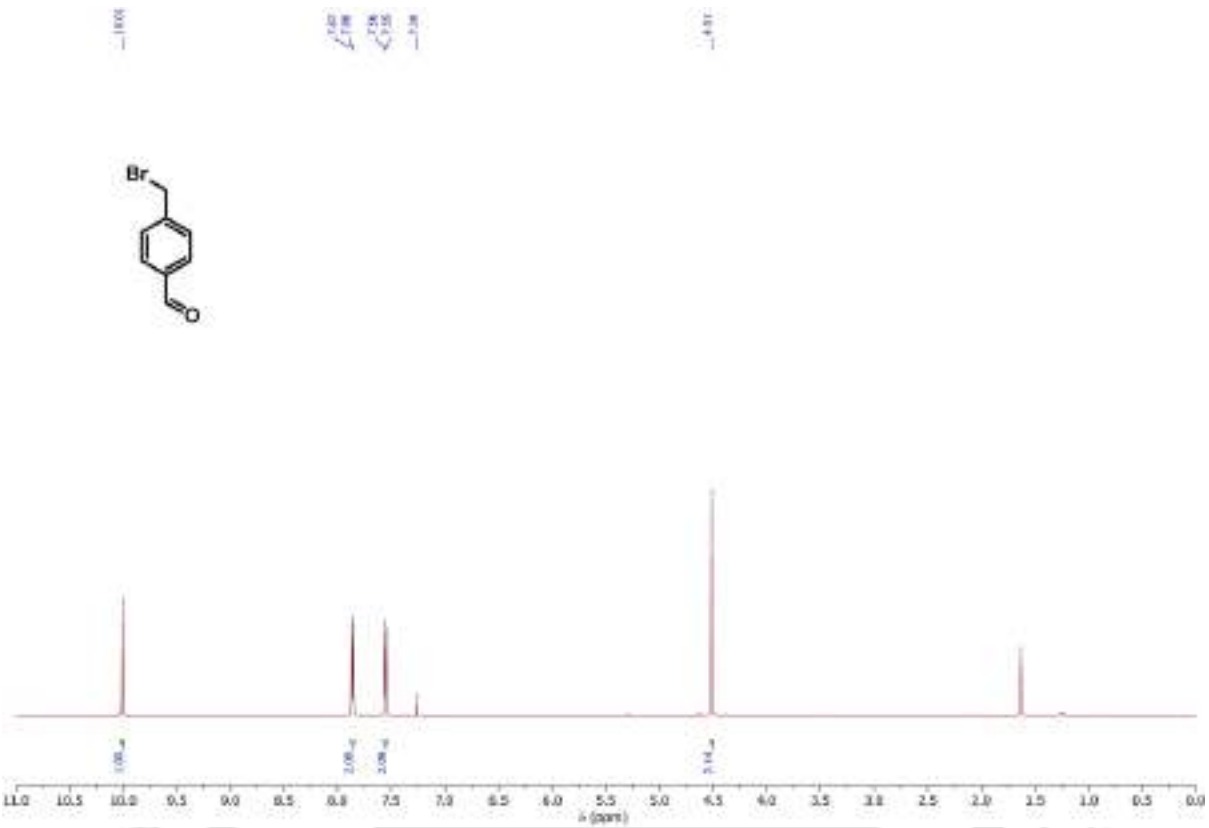

Figure 6.3. ^{1}H NMR spectrum of 4-(Bromomethyl)-benzaldehyde **(B)** in $CDCl_3$

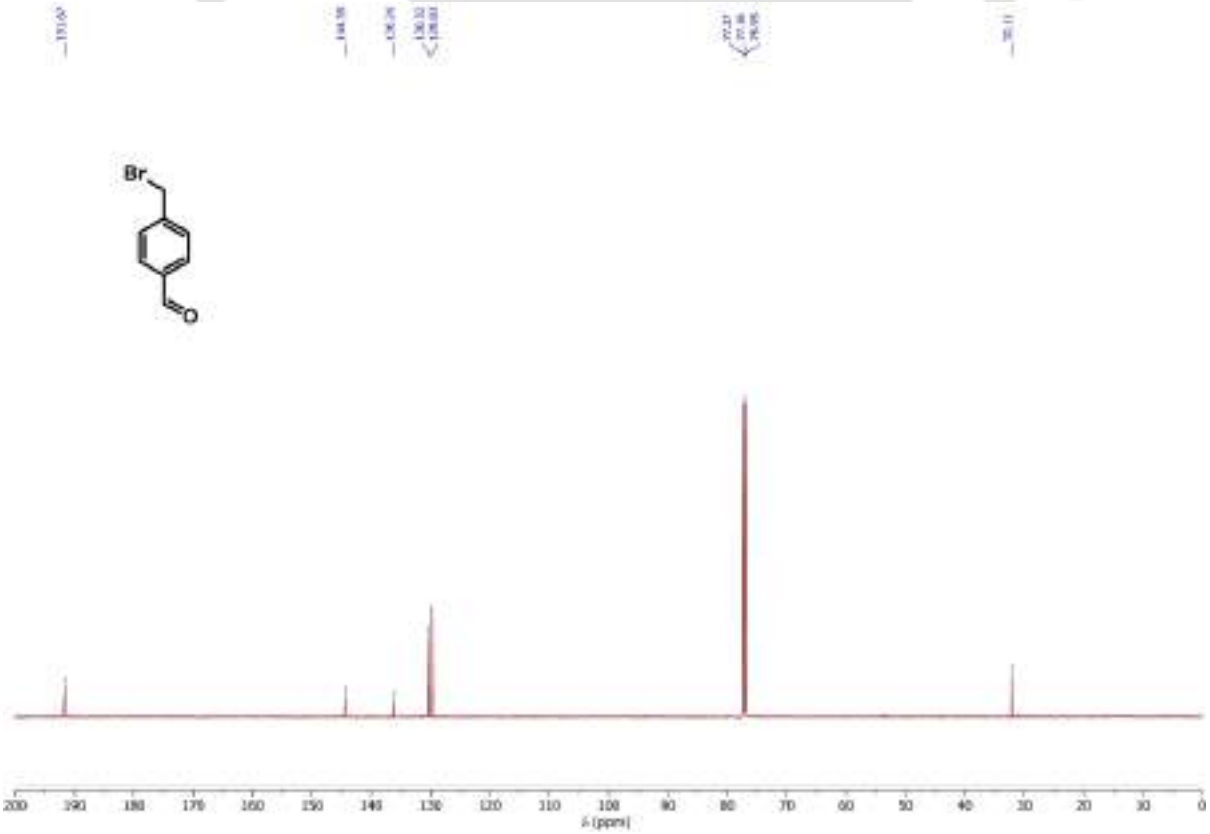

Figure 6.4. ^{13}C NMR spectrum of 4-(Bromomethyl)-benzaldehyde **(B)** in $CDCl_3$

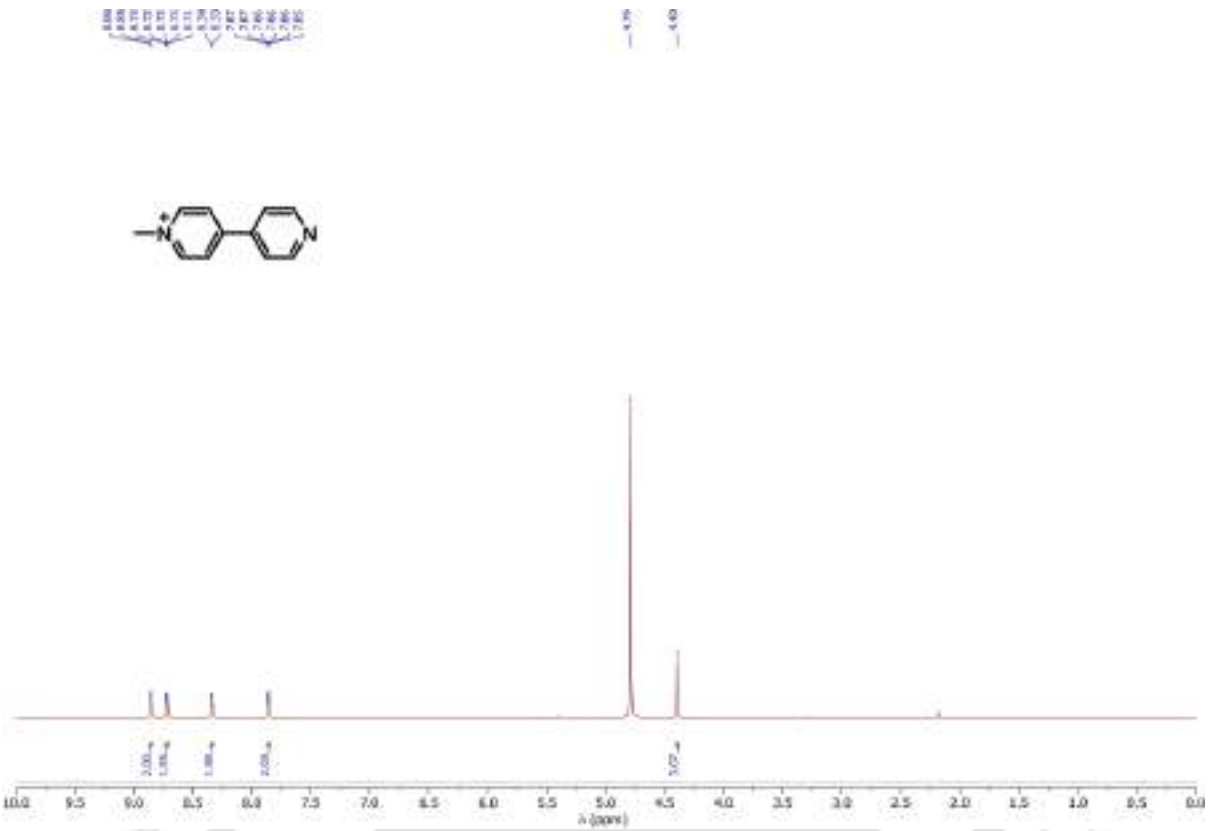

Figure 6.5. ^{1}H NMR spectrum of 1-methyl-[4,4'-bipyridin]-1-ium iodide **(C)** in D_2O

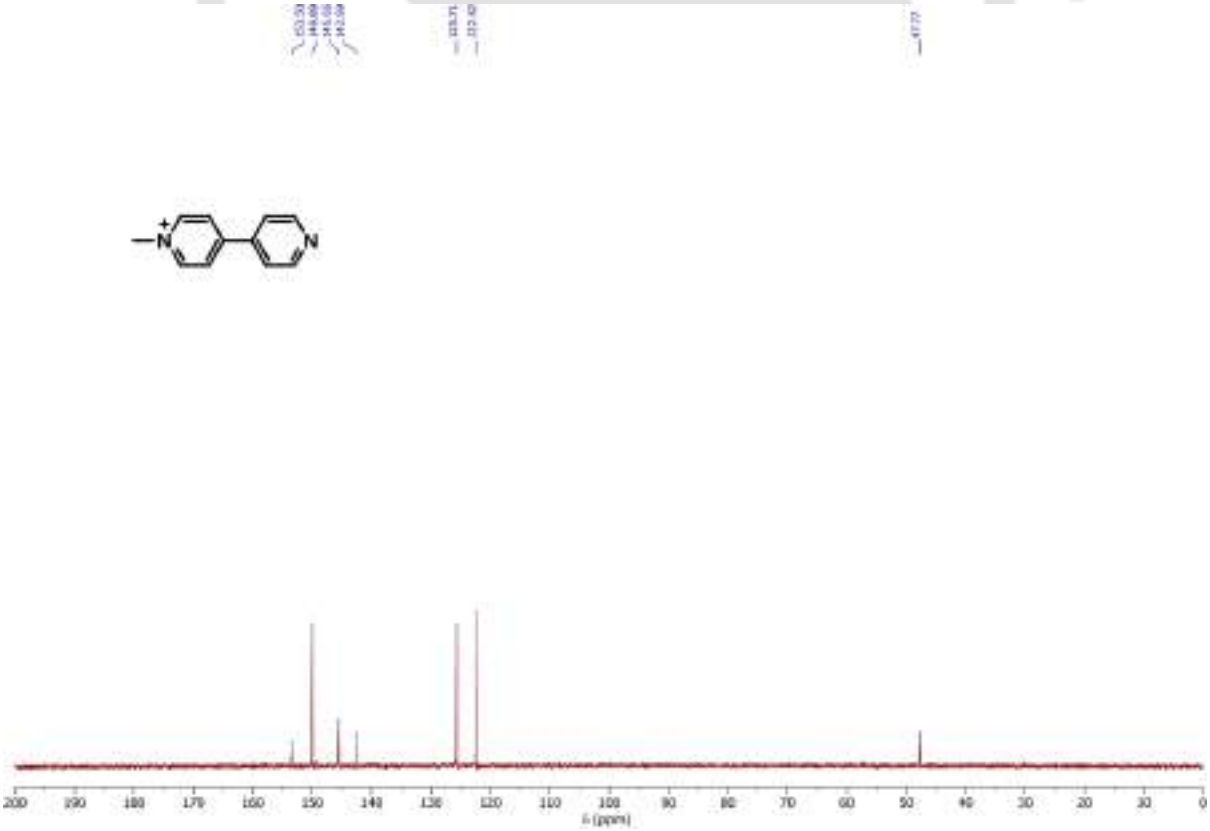

Figure 6.6. ^{13}C NMR spectrum of 1-methyl-[4,4'-bipyridin]-1-ium iodide **(C)** in D_2O

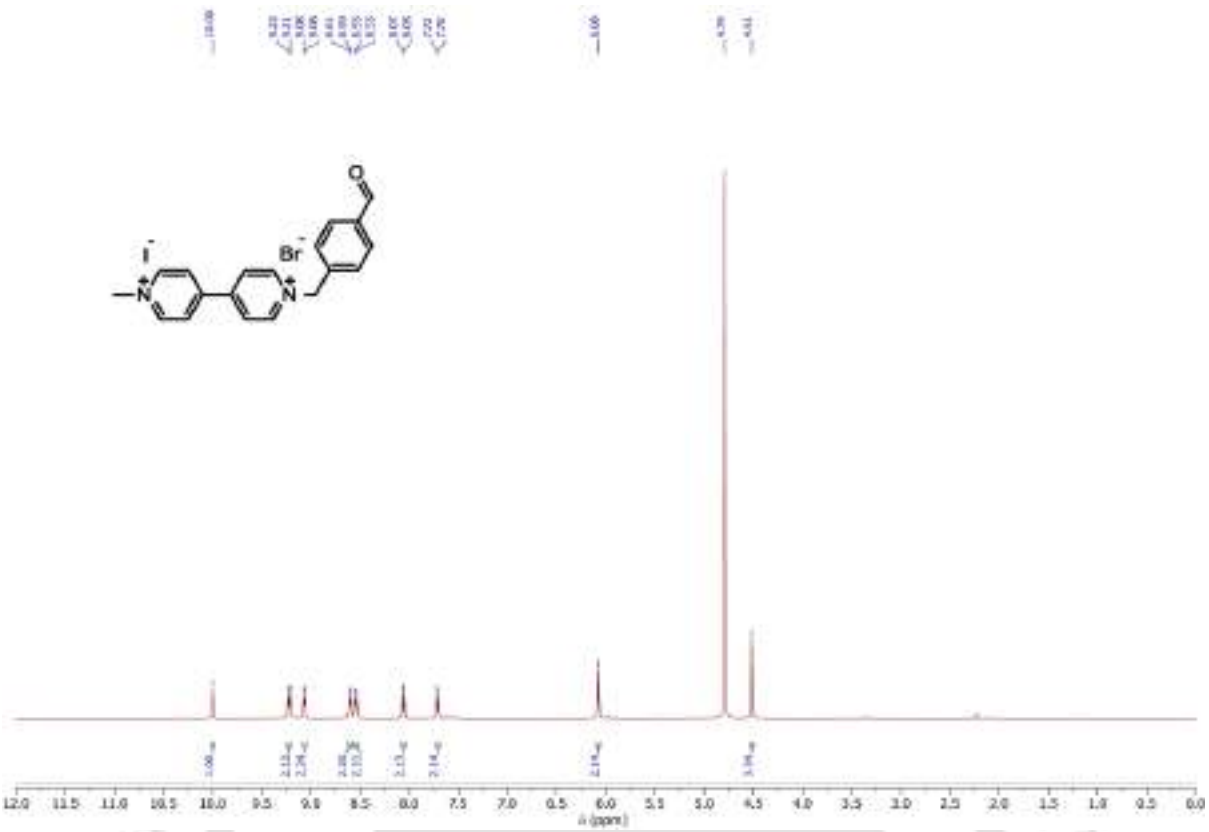

Figure 6.7. ^{1}H NMR spectrum of 1-(4-formylbenzyl)-1'-methyl-[4,4'-bipyridine]-1,1'-diium **(MV-CHO)** in D_2O

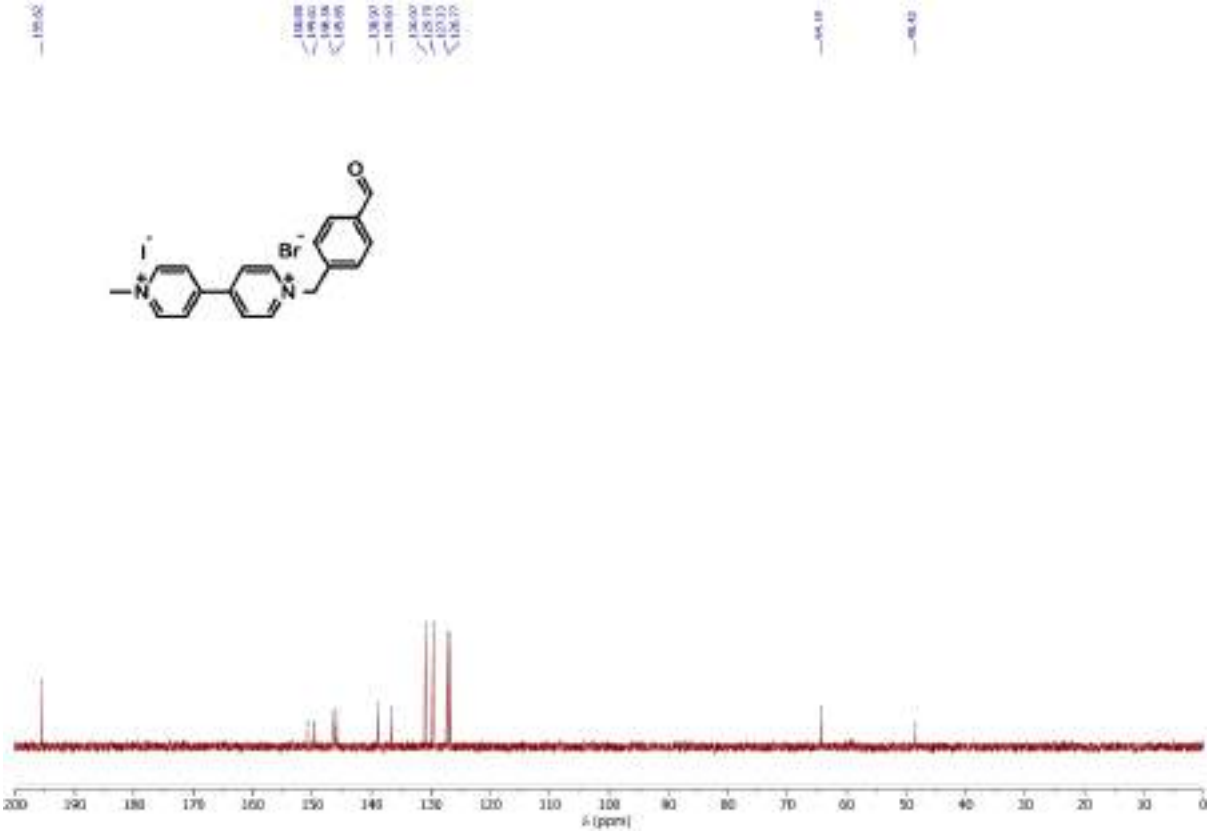

Figure 6.8. ^{13}C NMR spectrum of 1-(4-formylbenzyl)-1'-methyl-[4,4'-bipyridine]-1,1'-diium **(MV-CHO)** in D_2O

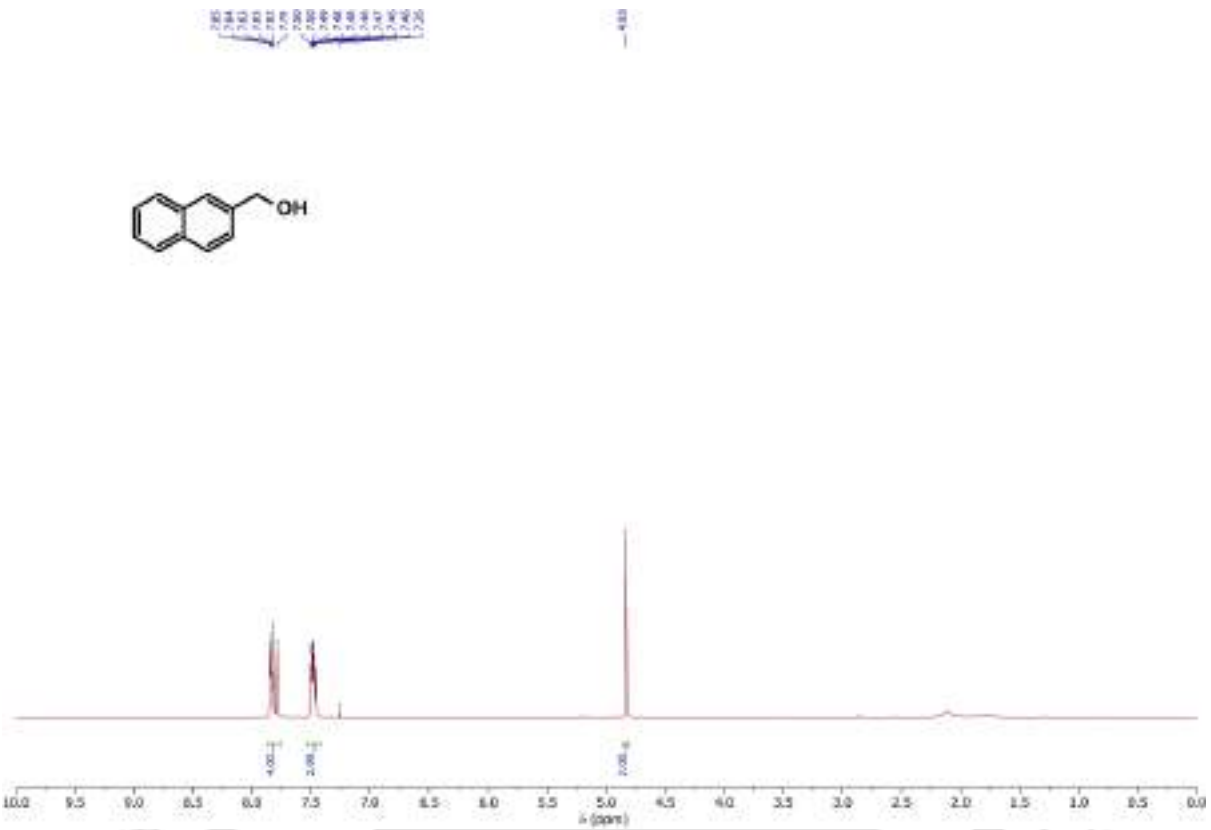

Figure 6.9. ^{1}H NMR spectrum of Naphthalen-2-ylmethanol **(D)** in $CDCl_3$

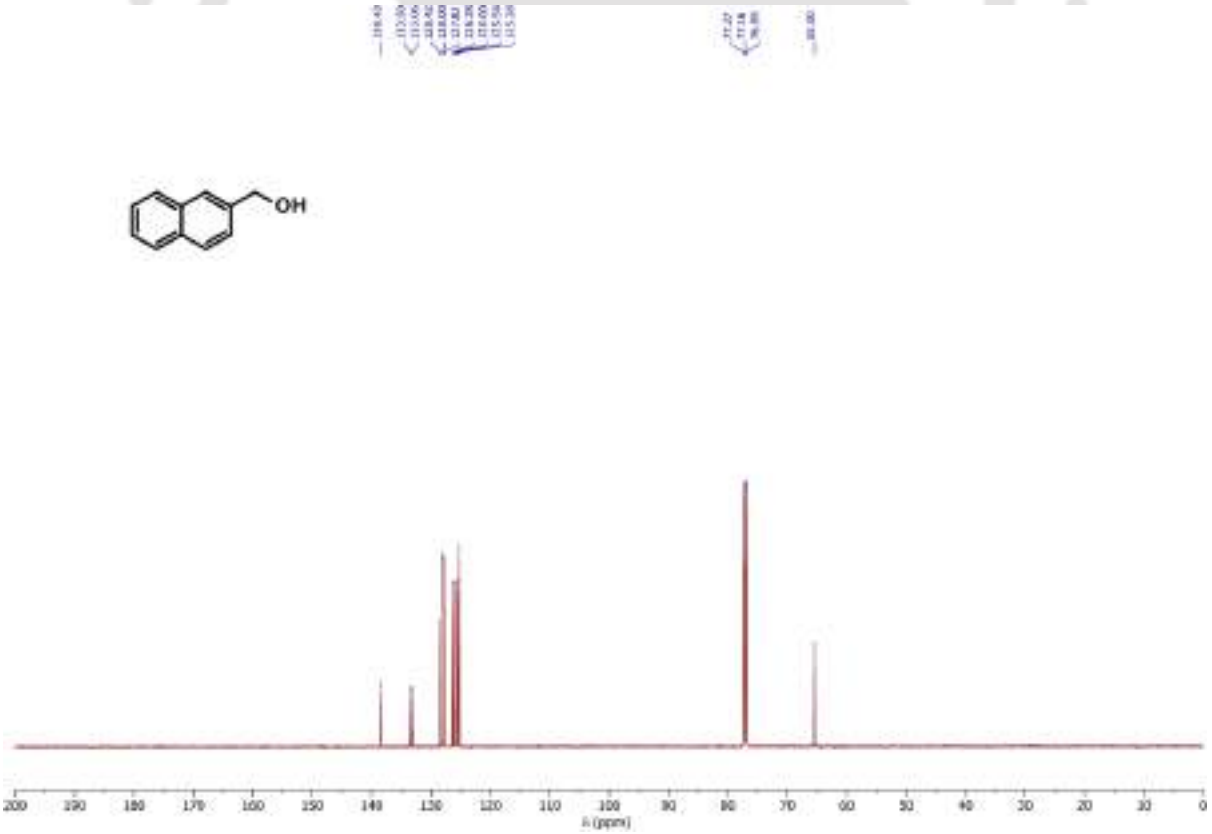

Figure 6.10. ^{1}H NMR spectrum of Naphthalen-2-ylmethanol **(D)** in $CDCl_3$

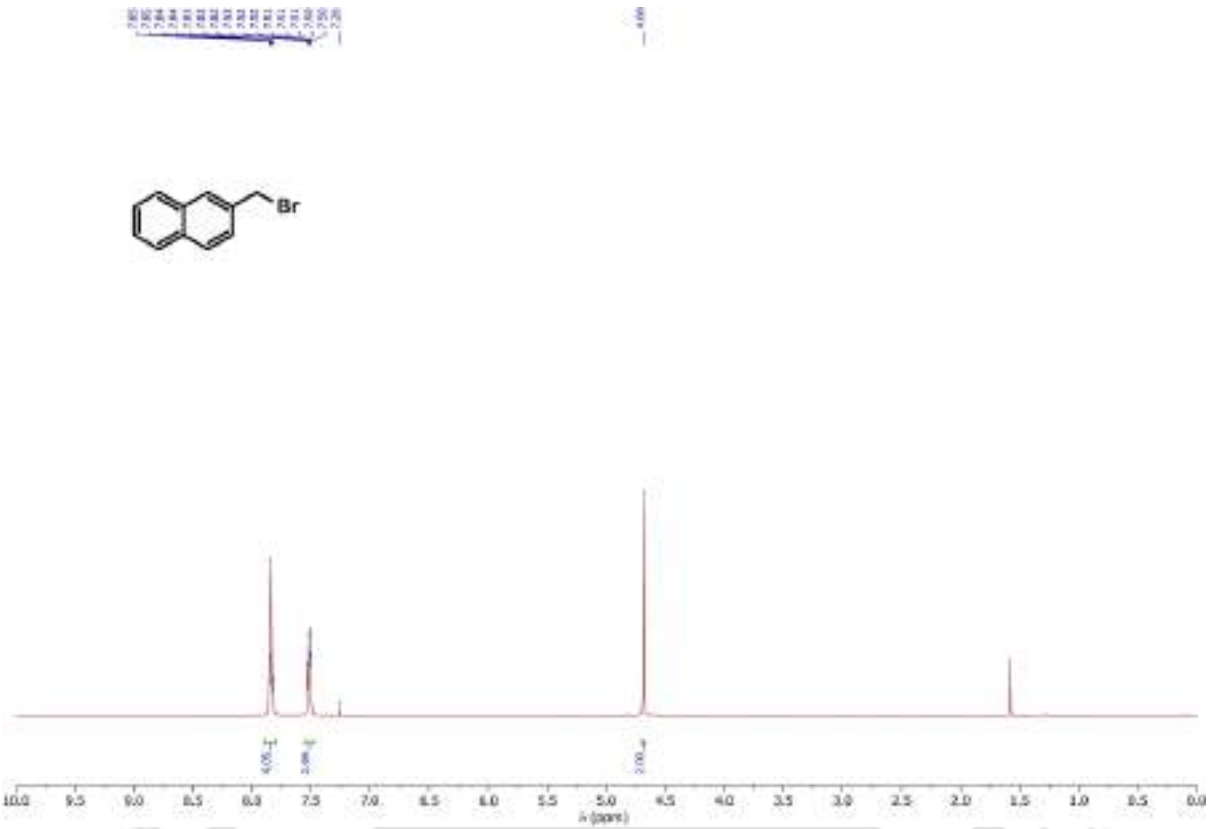

Figure 6.11. ^{1}H NMR spectrum of 2-(bromomethyl)naphthalene **(E)** in $CDCl_3$

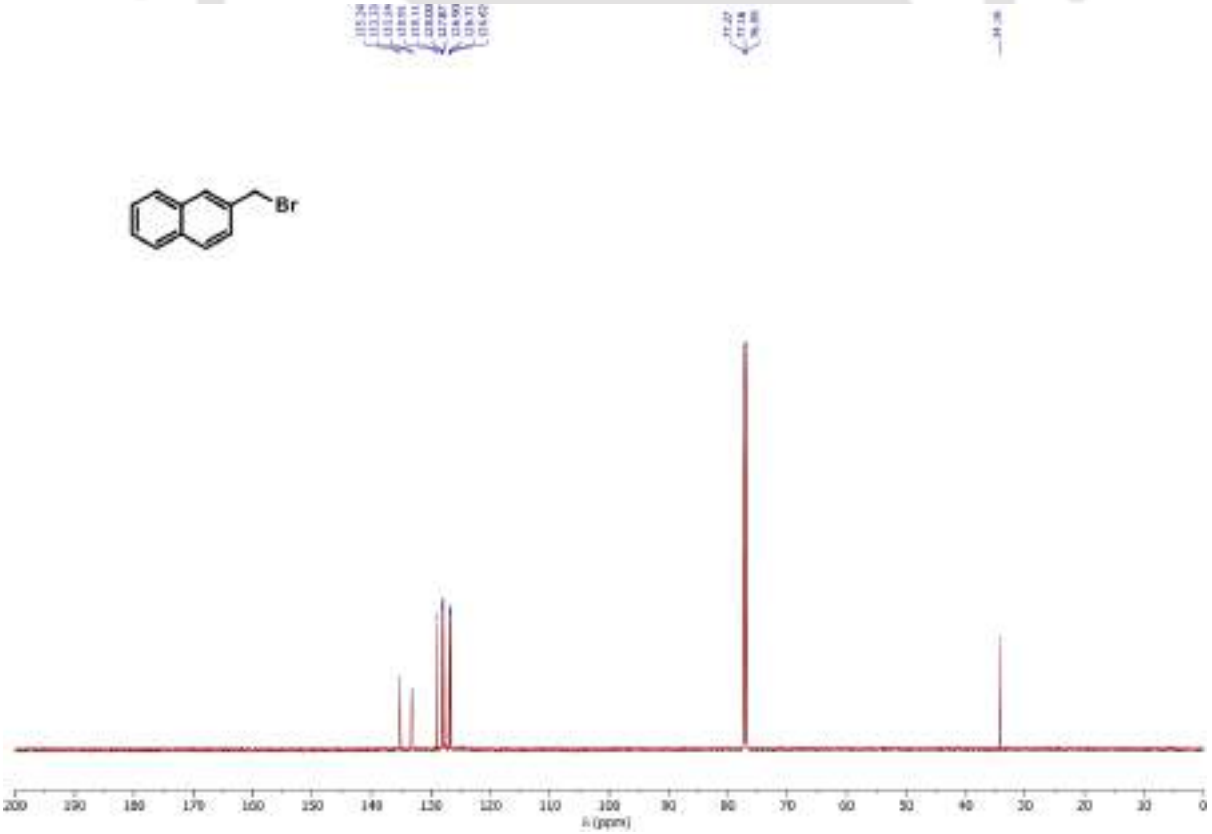

Figure 6.12. ^{13}C NMR spectrum of 2-(bromomethyl)naphthalene **(E)** in $CDCl_3$

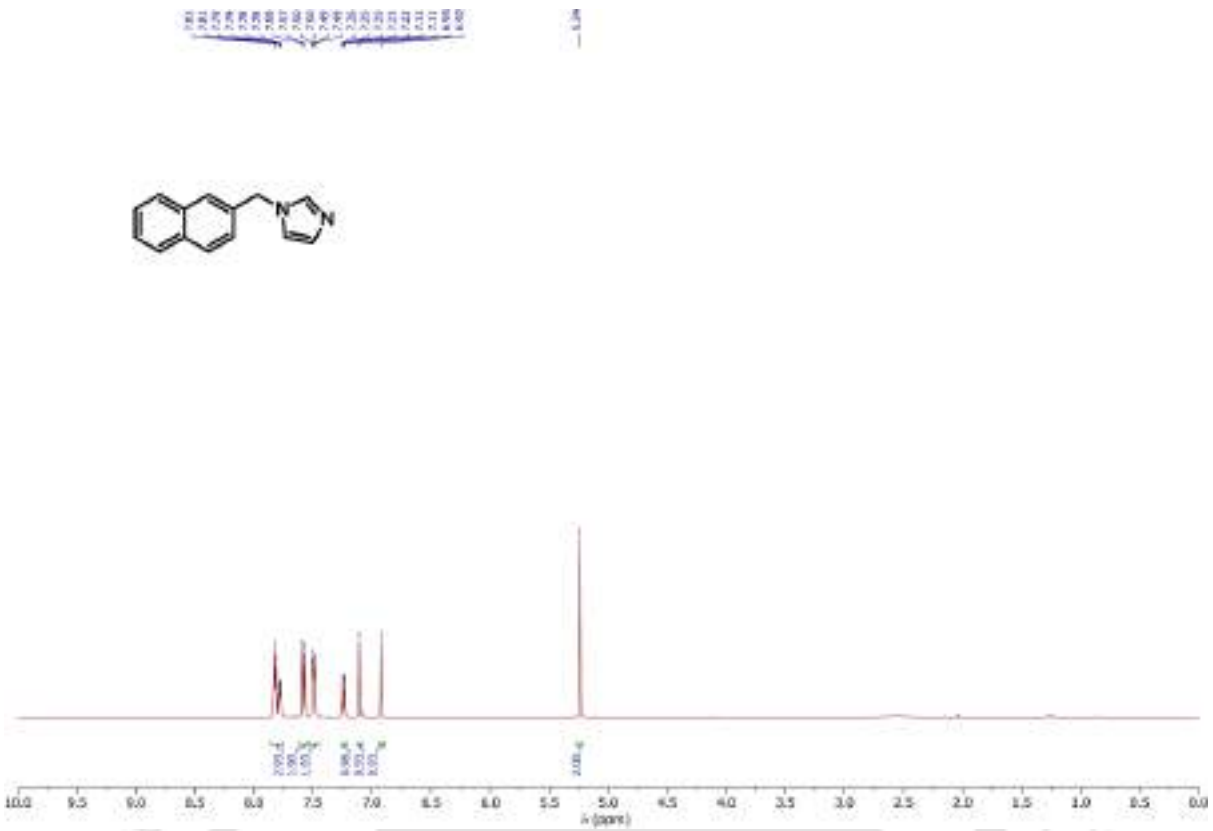

Figure 6.13. ^{1}H NMR spectrum of 1-(naphthalen-2-ylmethyl)-1H-imidazole **(F)** in $CDCl_3$

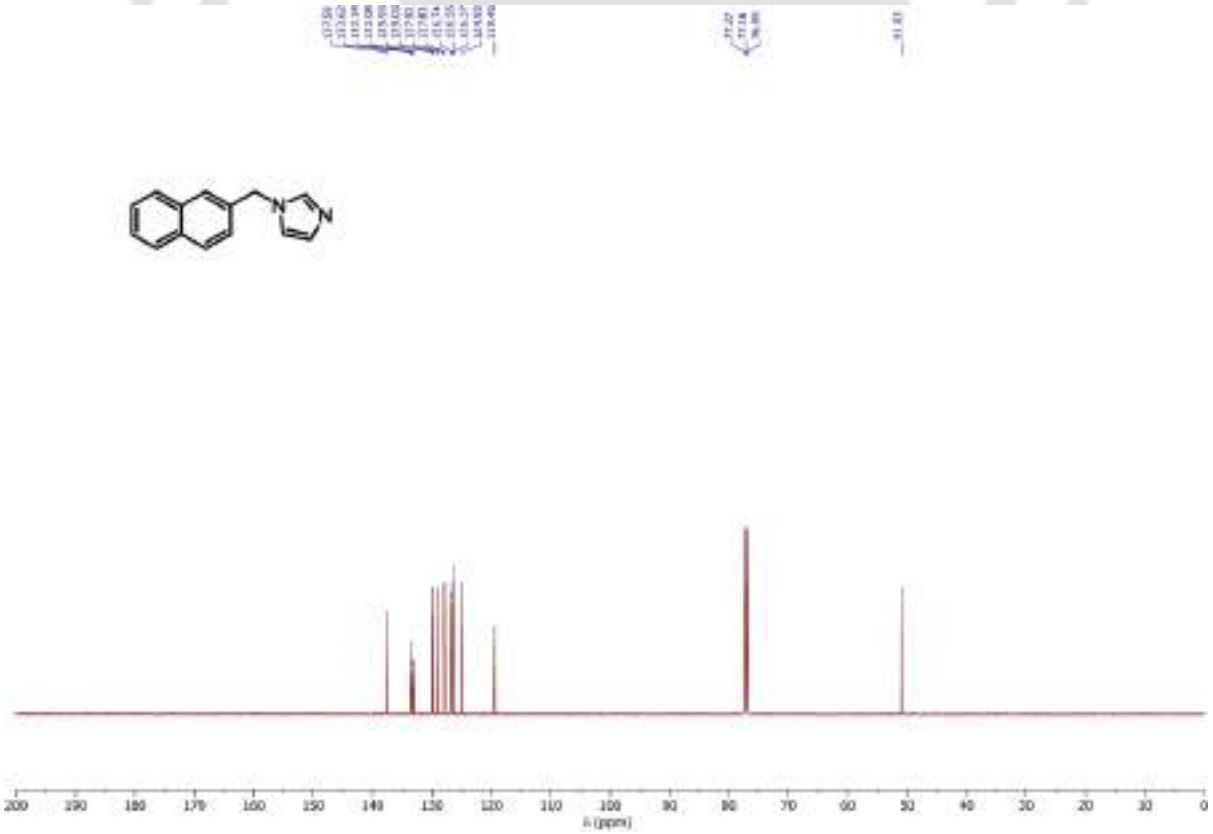

Figure 6.14. ^{13}C NMR spectrum of 1-(naphthalen-2-ylmethyl)-1H-imidazole **(F)** in $CDCl_3$

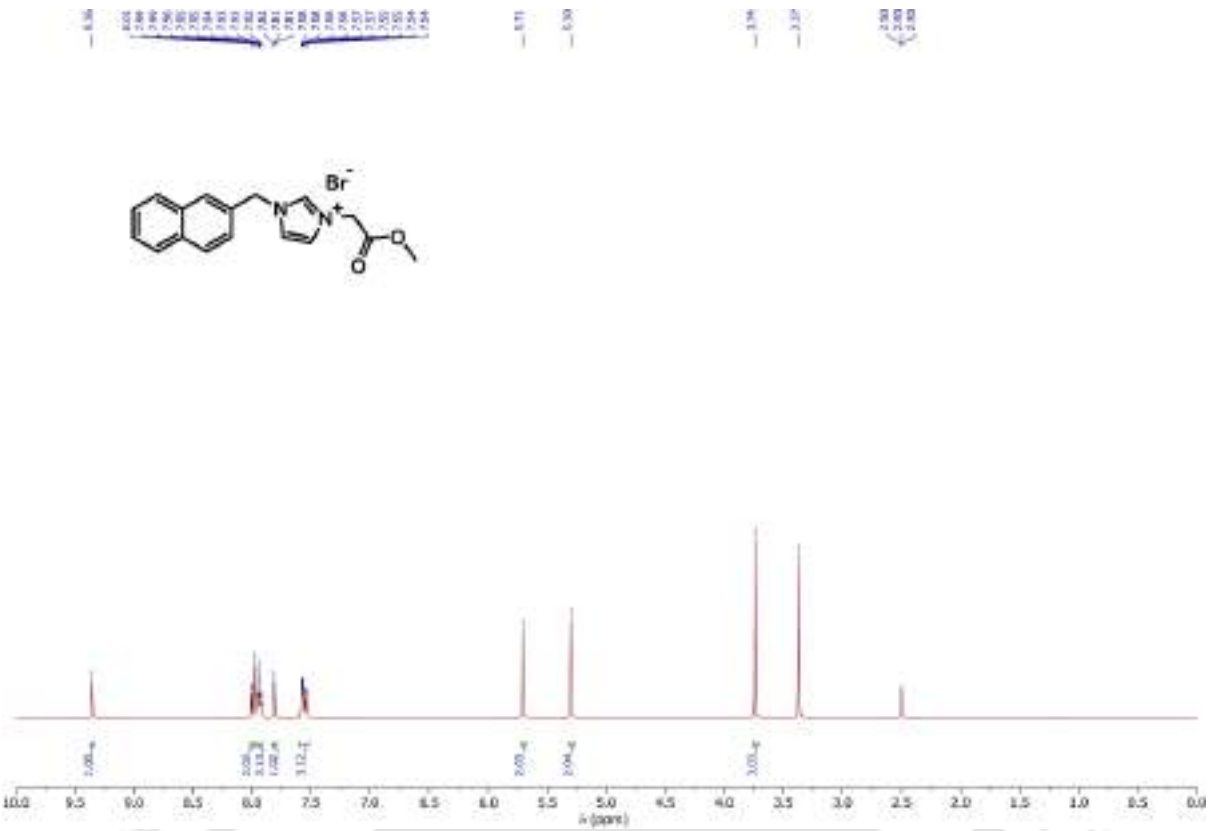

Figure 6.15. ^{1}H NMR spectrum of 3-(2-methoxy-2-oxoethyl)-1-(naphthalen-2-ylmethyl)-1H-imidazol-3-ium **(G)** in $CDCl_3$

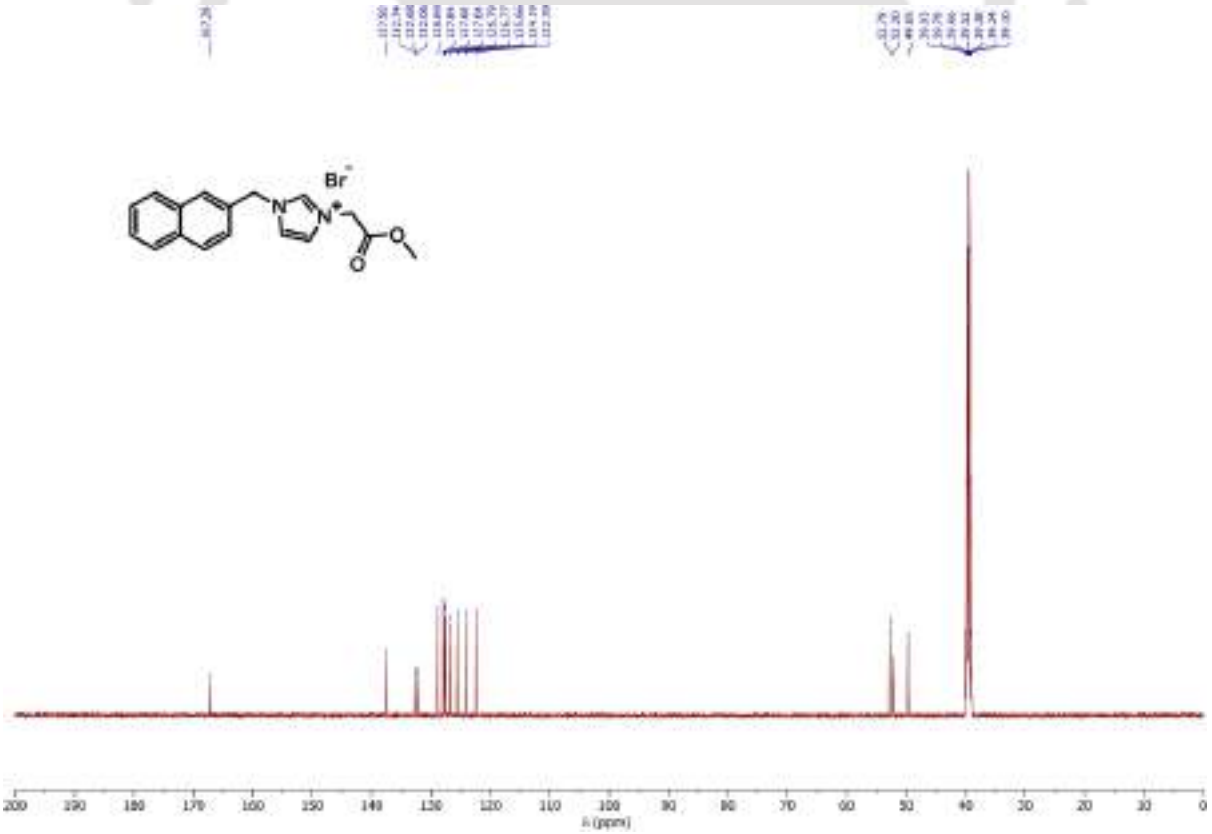

Figure 6.16. ^{13}C NMR spectrum of 3-(2-methoxy-2-oxoethyl)-1-(naphthalen-2-ylmethyl)-1H-imidazol-3-ium **(G)** in $CDCl_3$

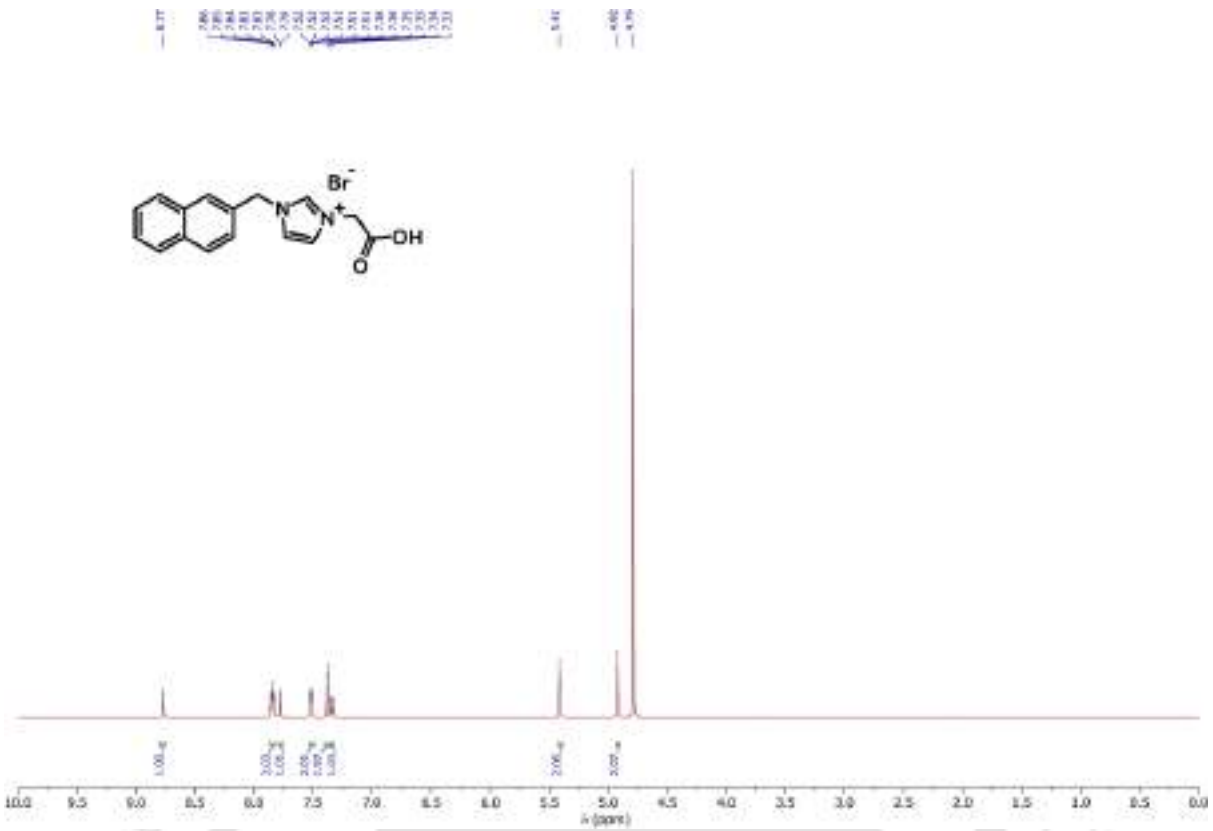

Figure 6.17. ^{1}H NMR spectrum of 3-(carboxymethyl)-1-(naphthalen-2-ylmethyl)-1H-imidazol-3-ium bromide **(H)** in D_2O

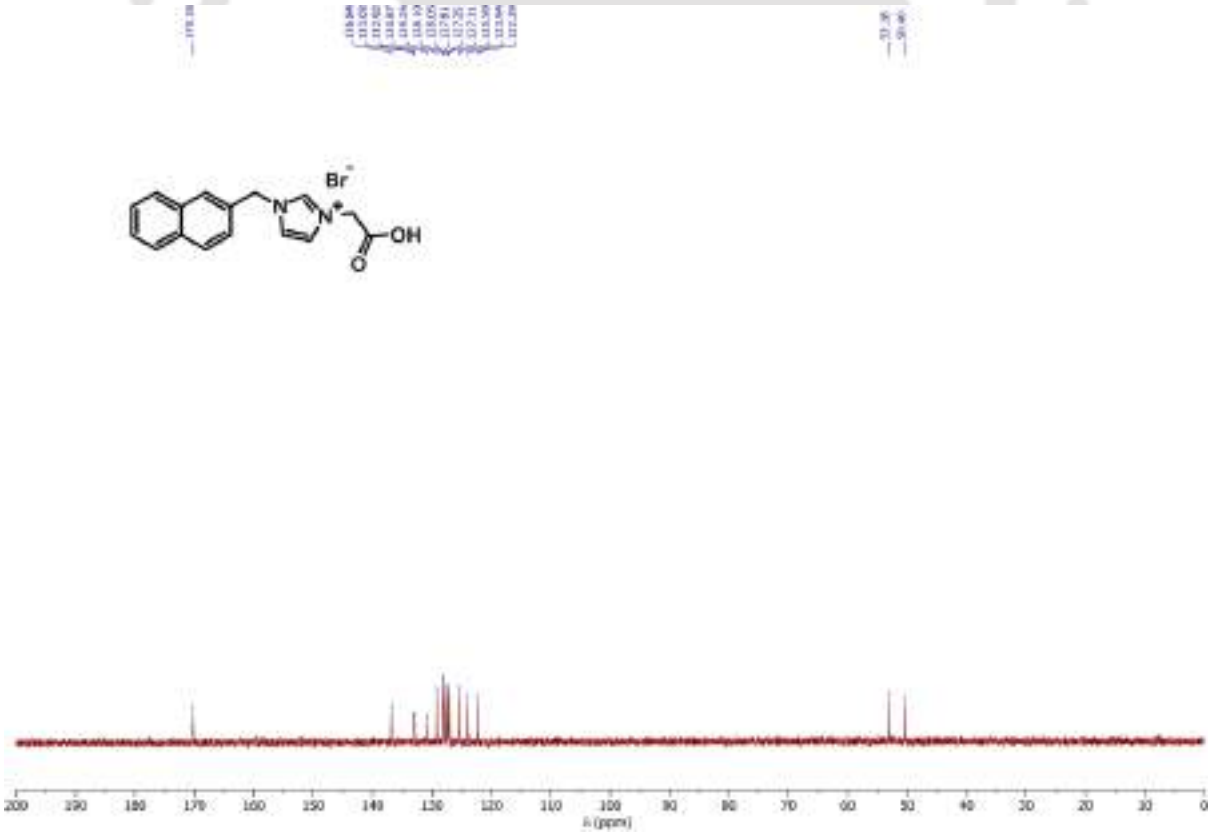

Figure 6.18. ^{13}C NMR spectrum of 3-(carboxymethyl)-1-(naphthalen-2-ylmethyl)-1H-imidazol-3-ium bromide **(H)** in D_2O

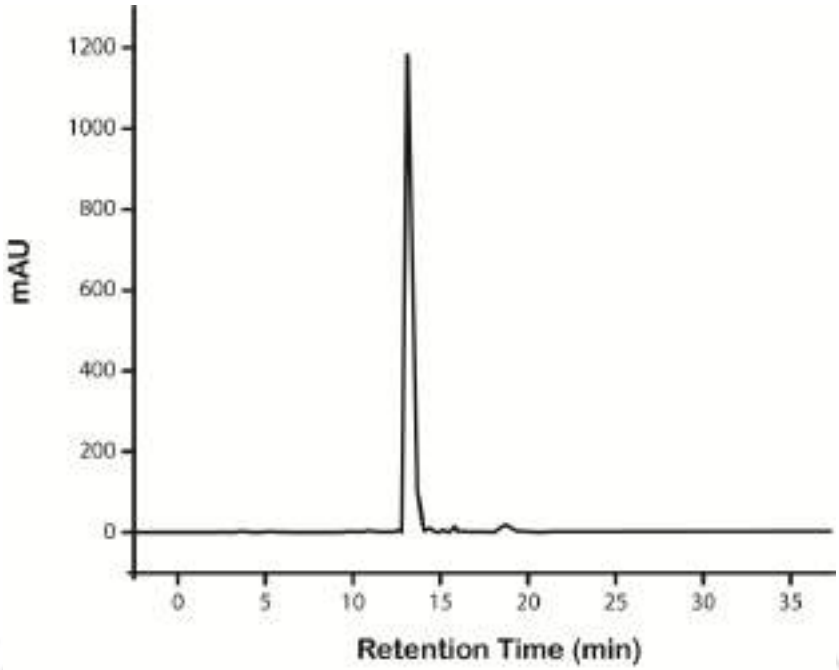

Figure 6.19. Analytical HPLC chromatogram of Nap-P

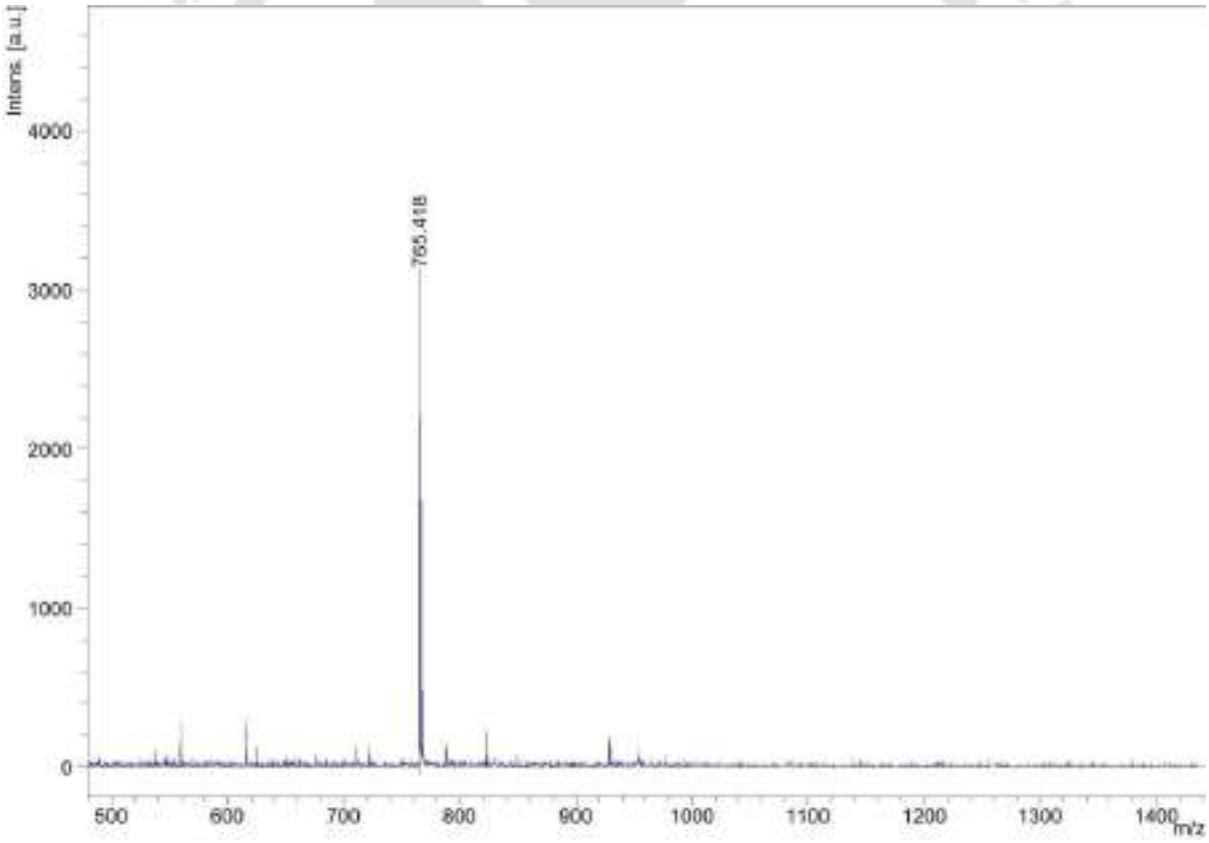

Figure 6.20. MALDI-TOF MS spectrum of Nap-P

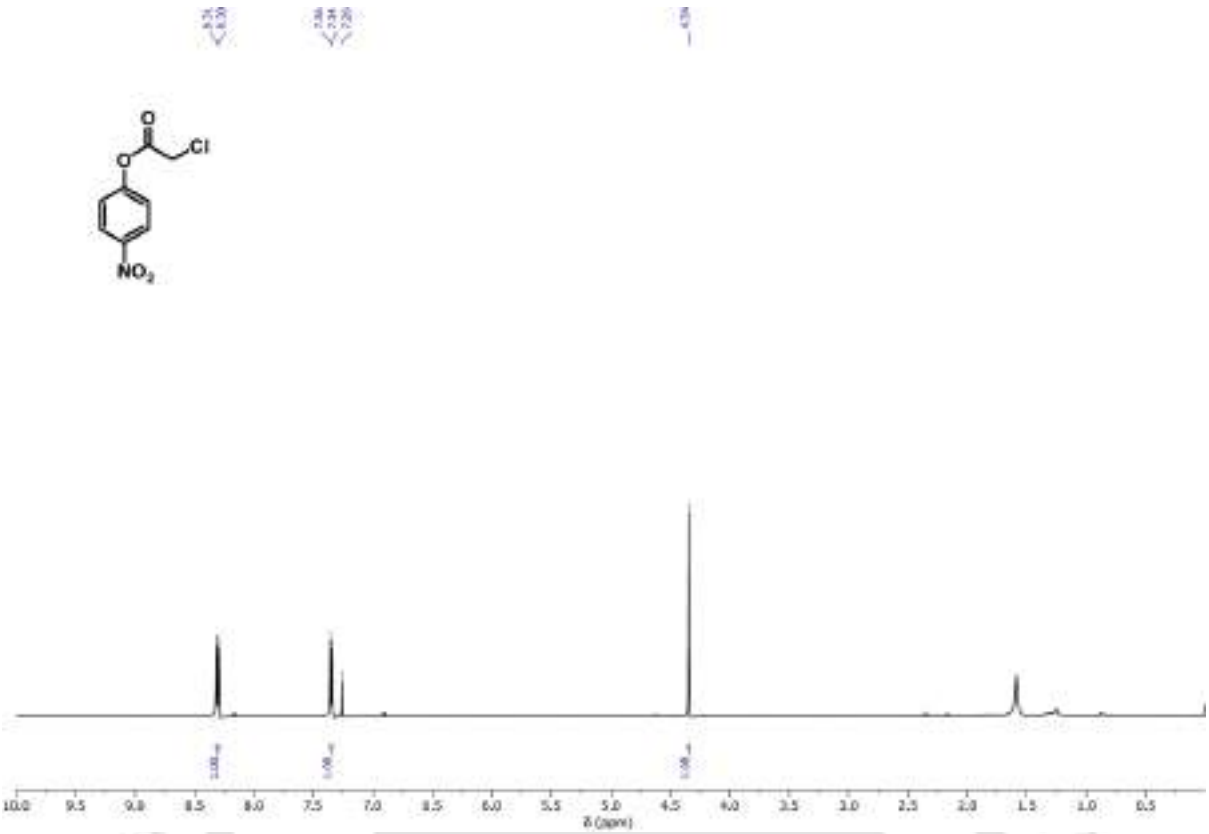

Figure 6.21. ^{1}H NMR spectrum of 4-nitrophenyl 2-chloroacetate **(pNPCAA)** in $CDCl_3$

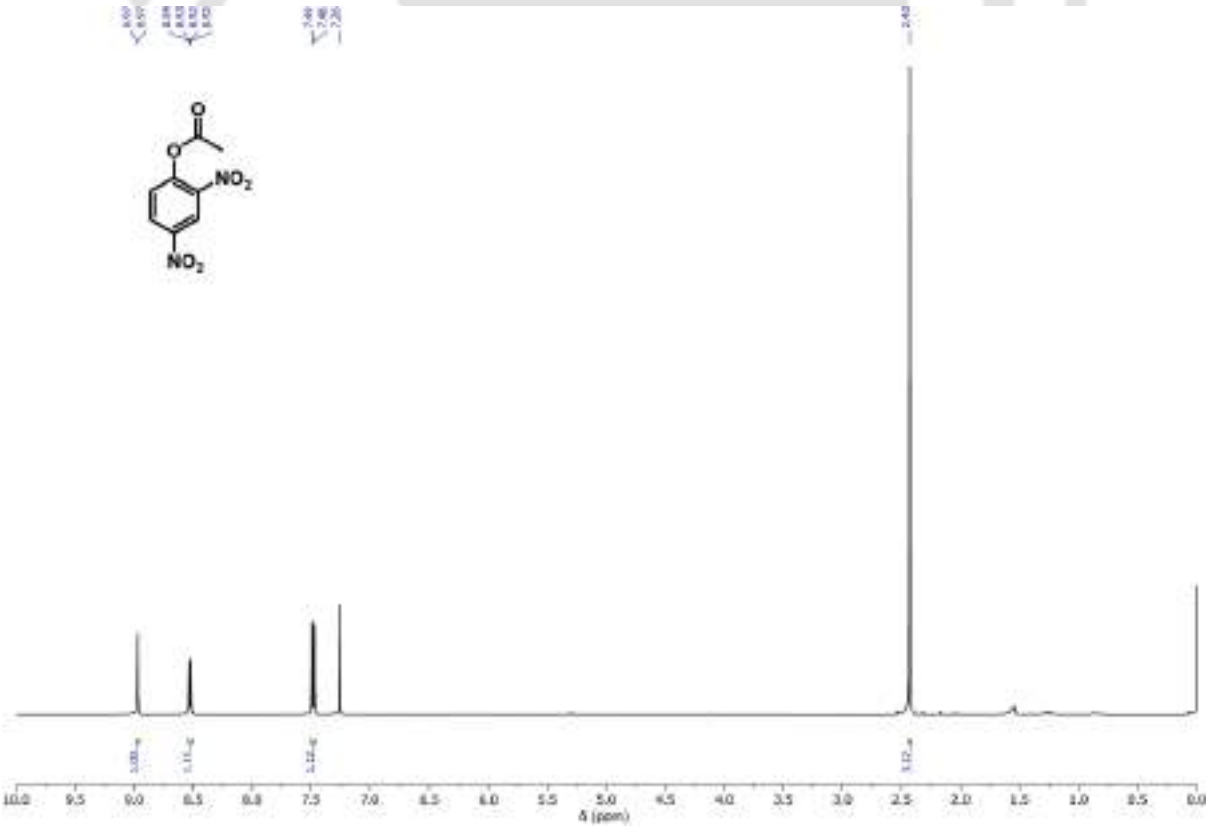

Figure 6.22. ^{1}H NMR spectrum of 2,4-dinitrophenyl acetate **(DNPA)** in $CDCl_3$

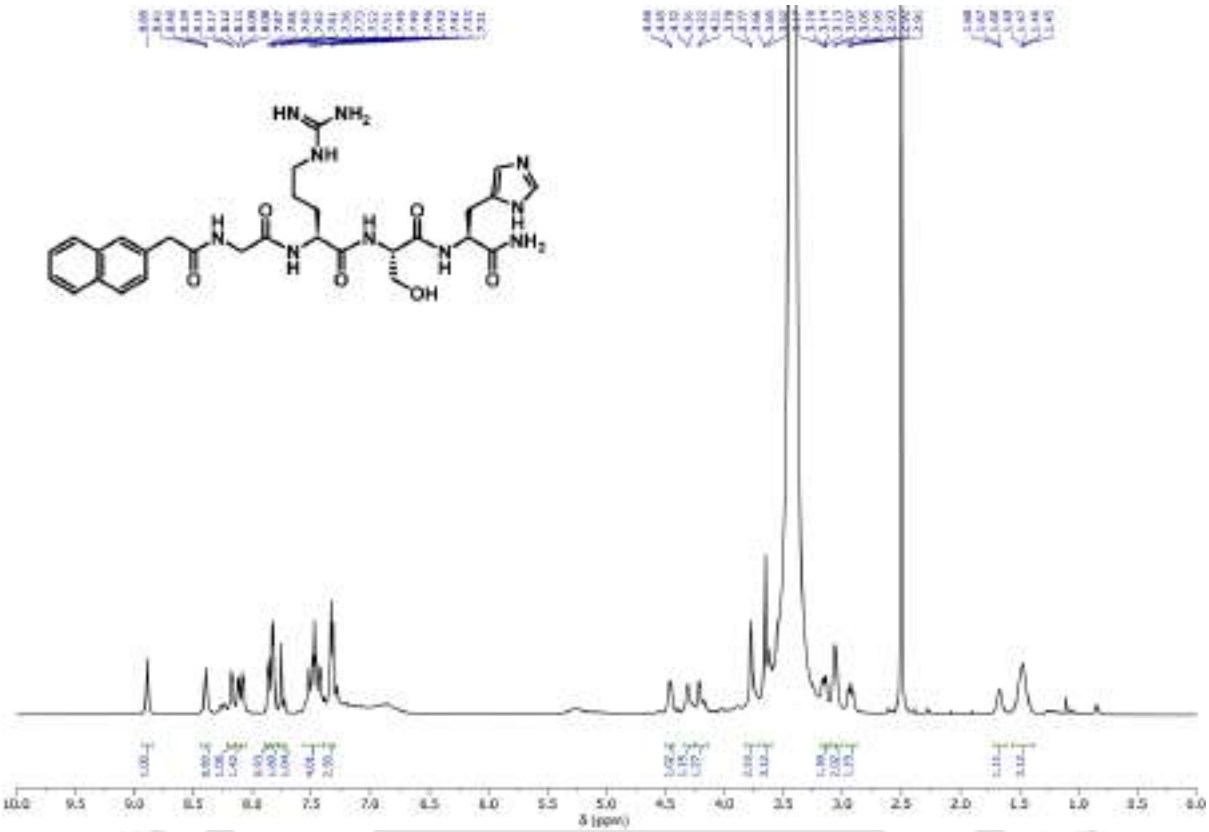

Figure 6.23. ^{1}H NMR spectrum of Nap-His peptide in DMSO-d_6

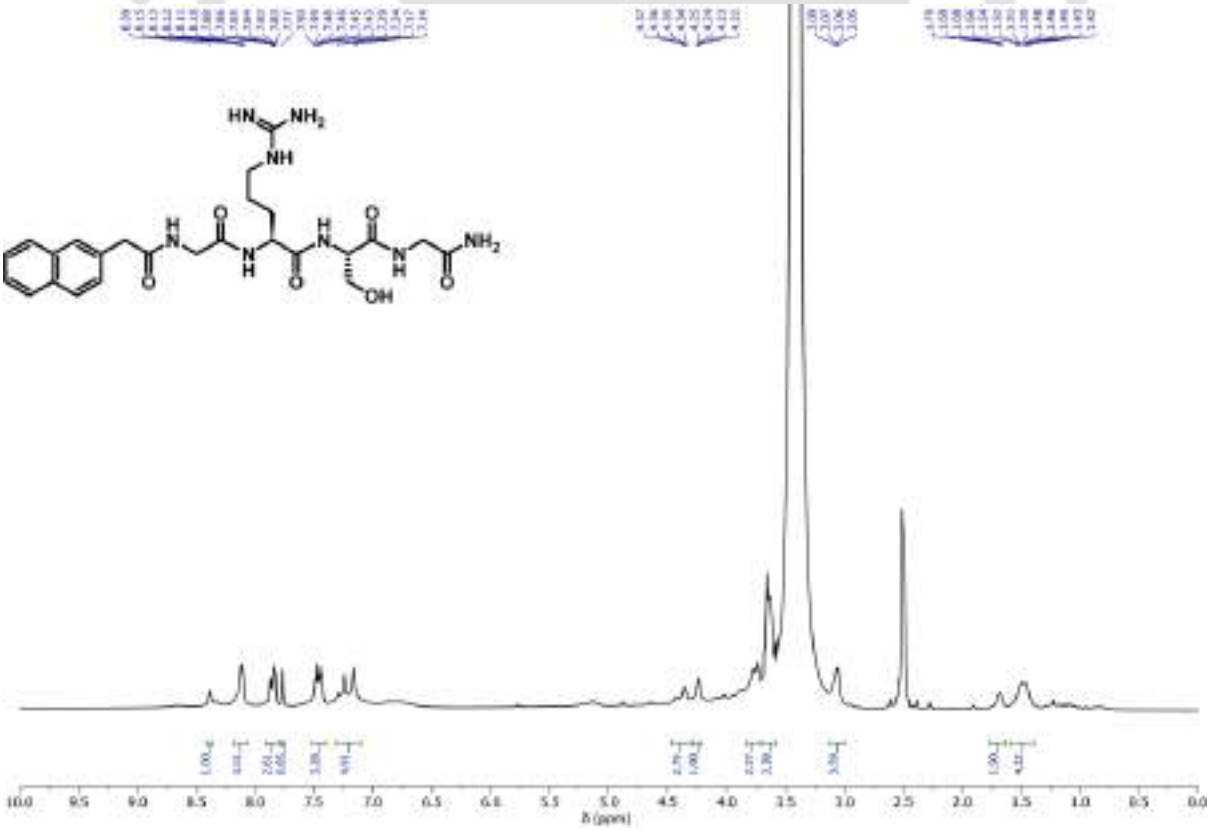

Figure 6.24. ^{1}H NMR spectrum of Nap-Gly peptide in DMSO-d_6

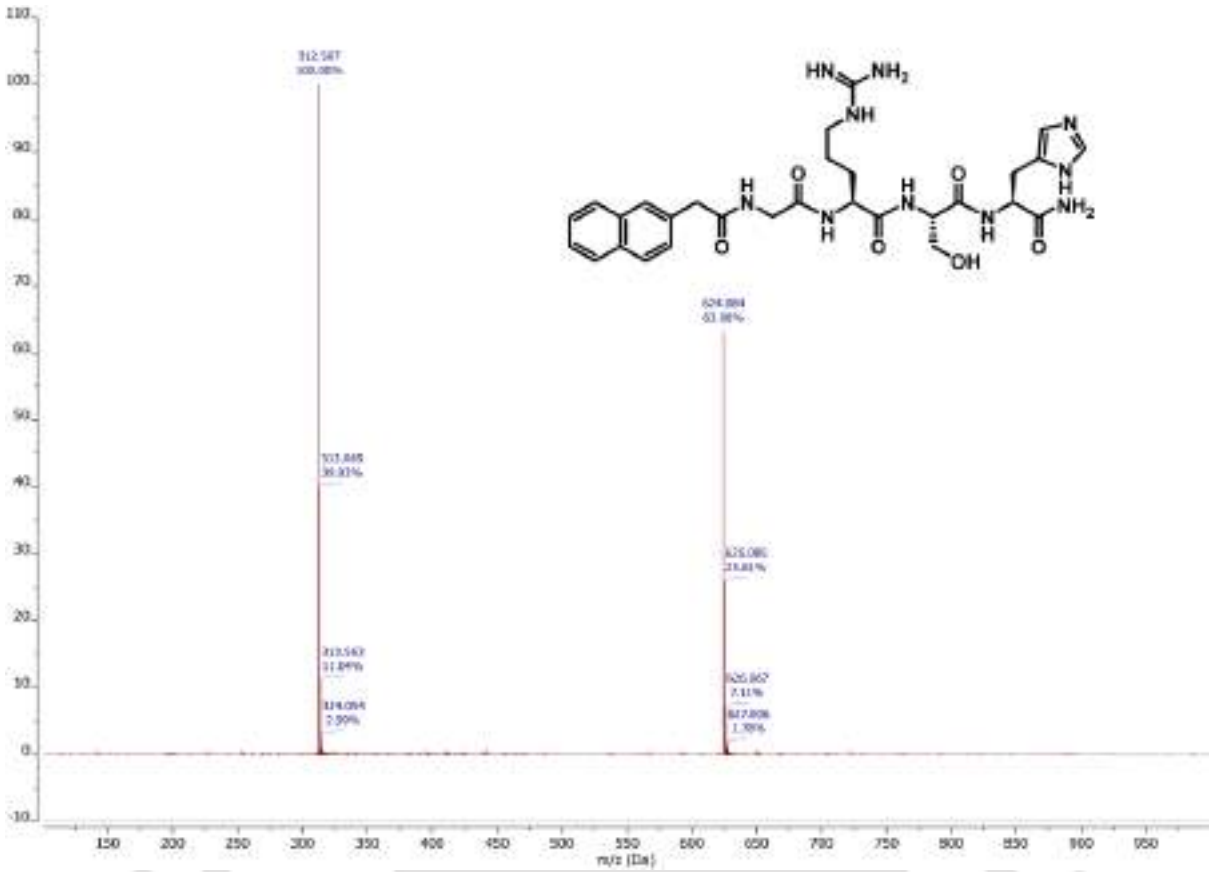

Figure 6.25. ESI-MS spectrum of Nap-His peptide

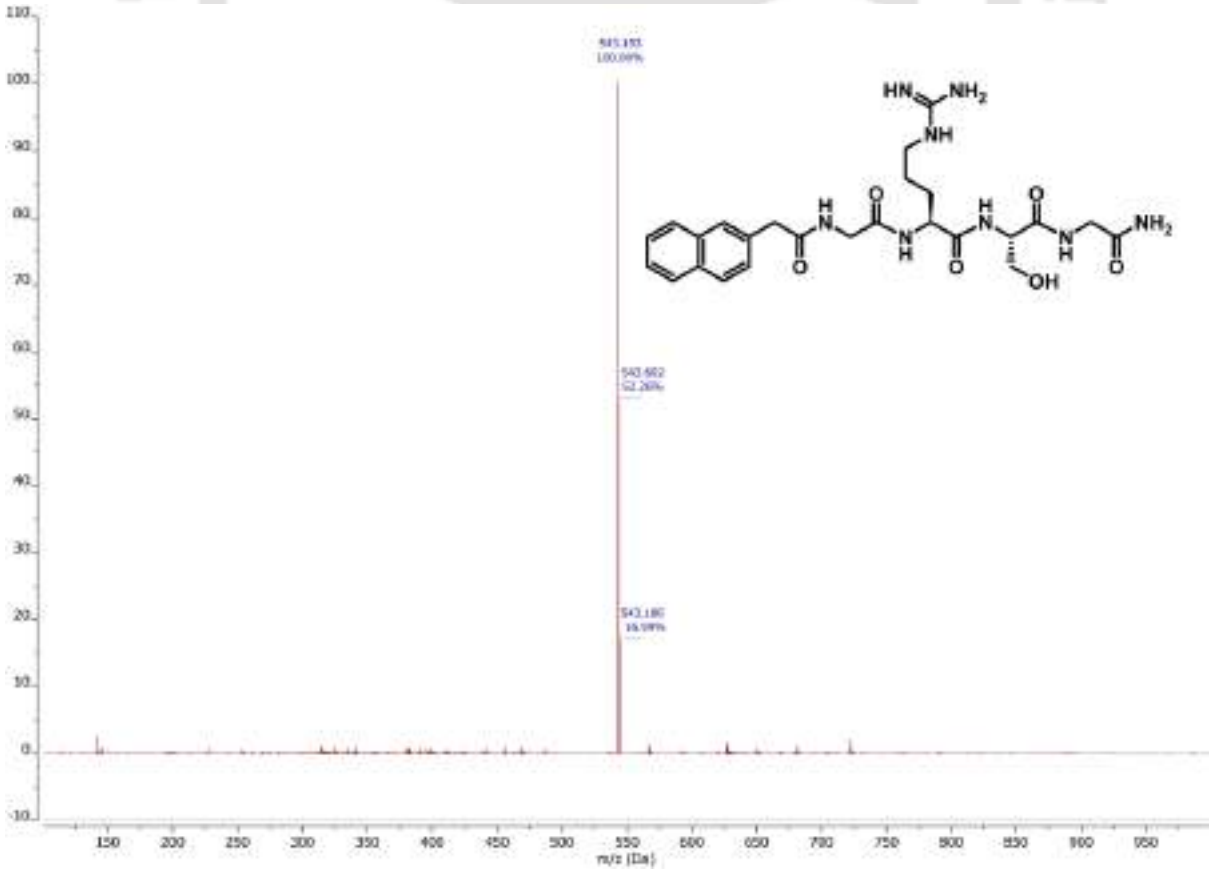

Figure 6.26. ESI-MS spectrum of Nap-Gly peptide

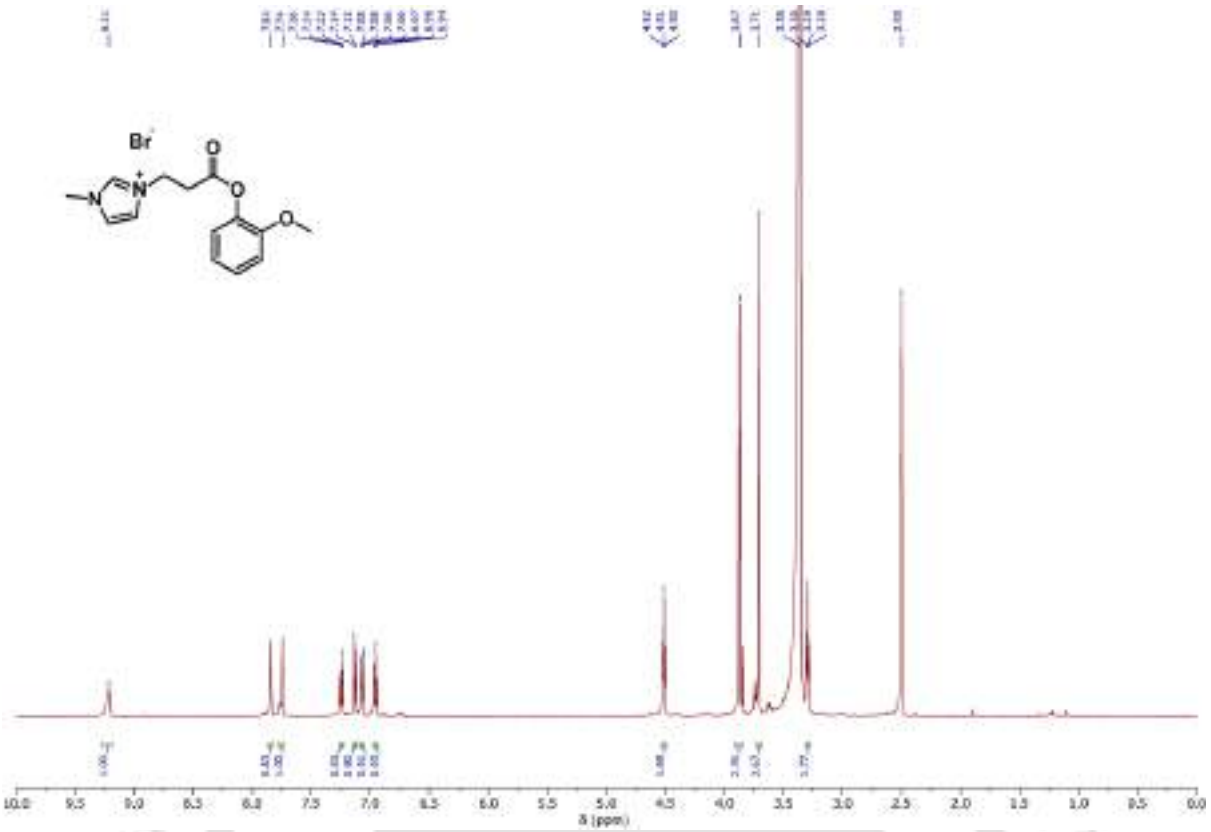

Figure 6.27. ^{1}H NMR spectrum of MP-Im in DMSO-d_6

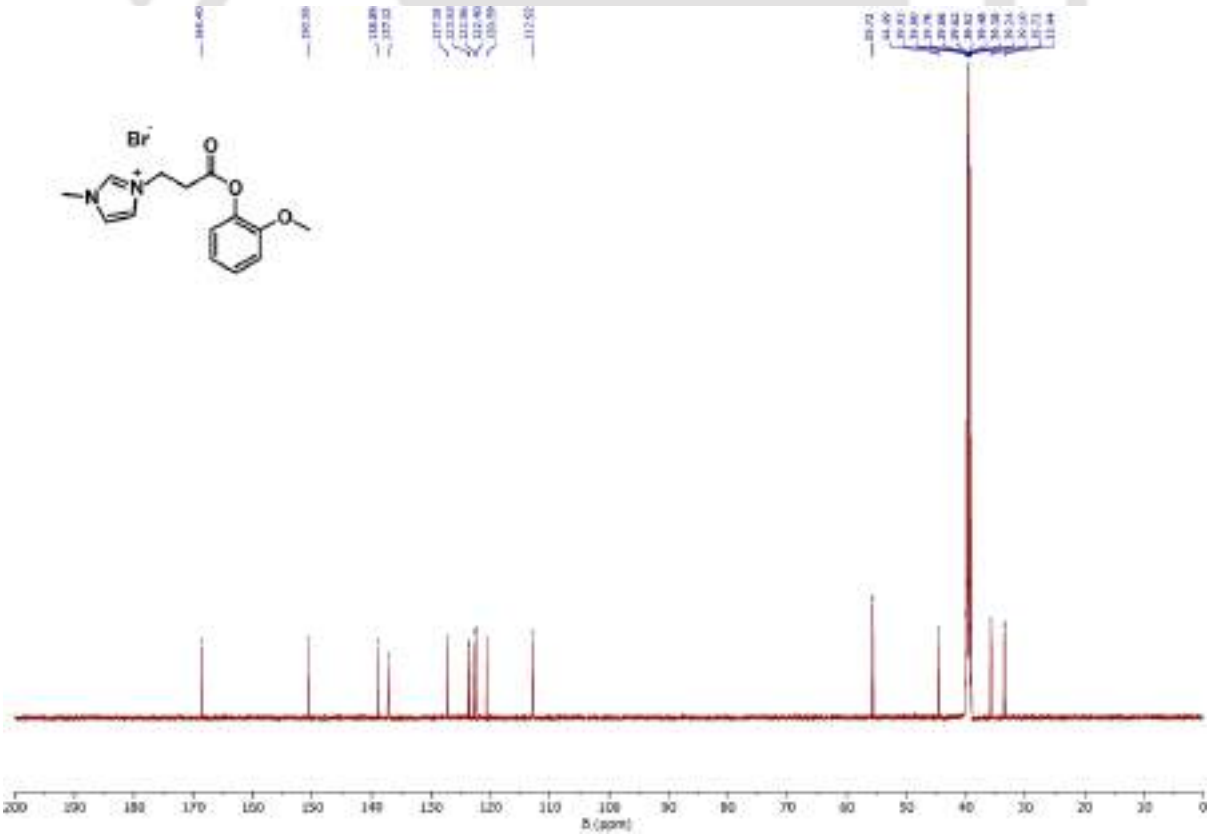

Figure 6.28. ^{13}C NMR spectrum of MP-Im in DMSO-d_6

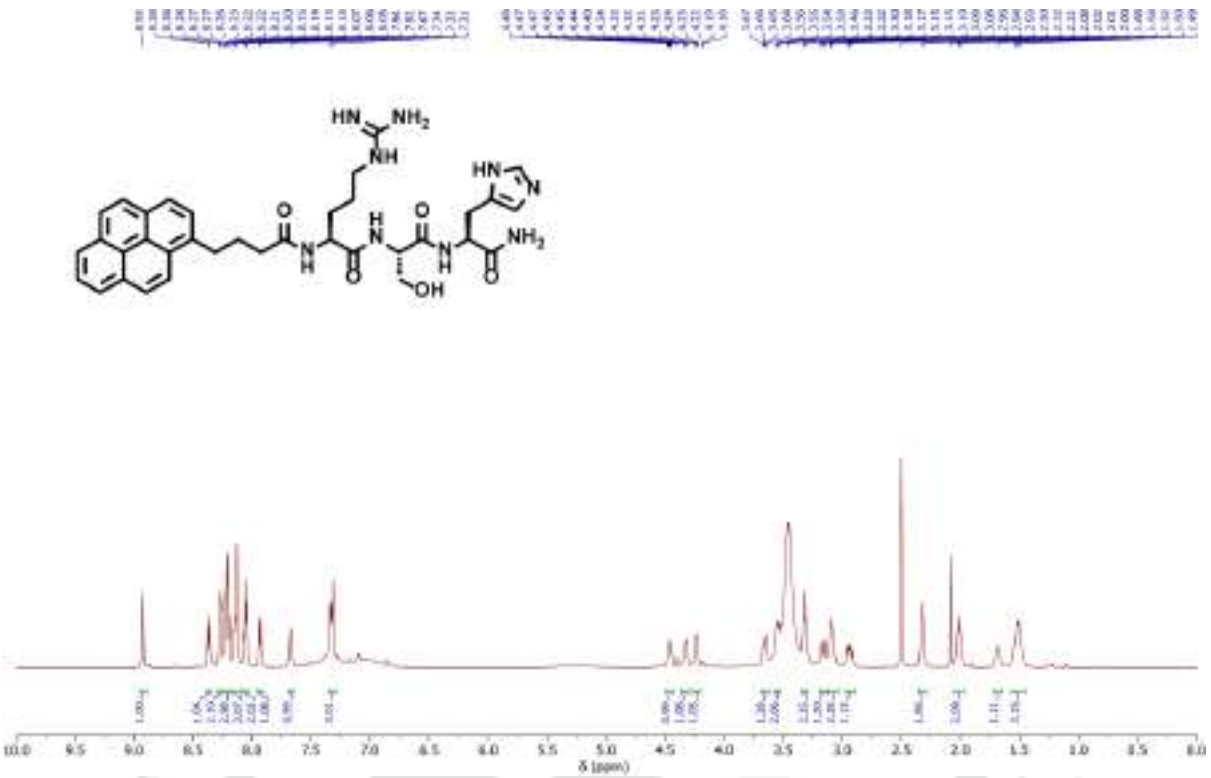

Figure 6.29. ^{1}H NMR spectrum of Py-RSH peptide in DMSO-d_6

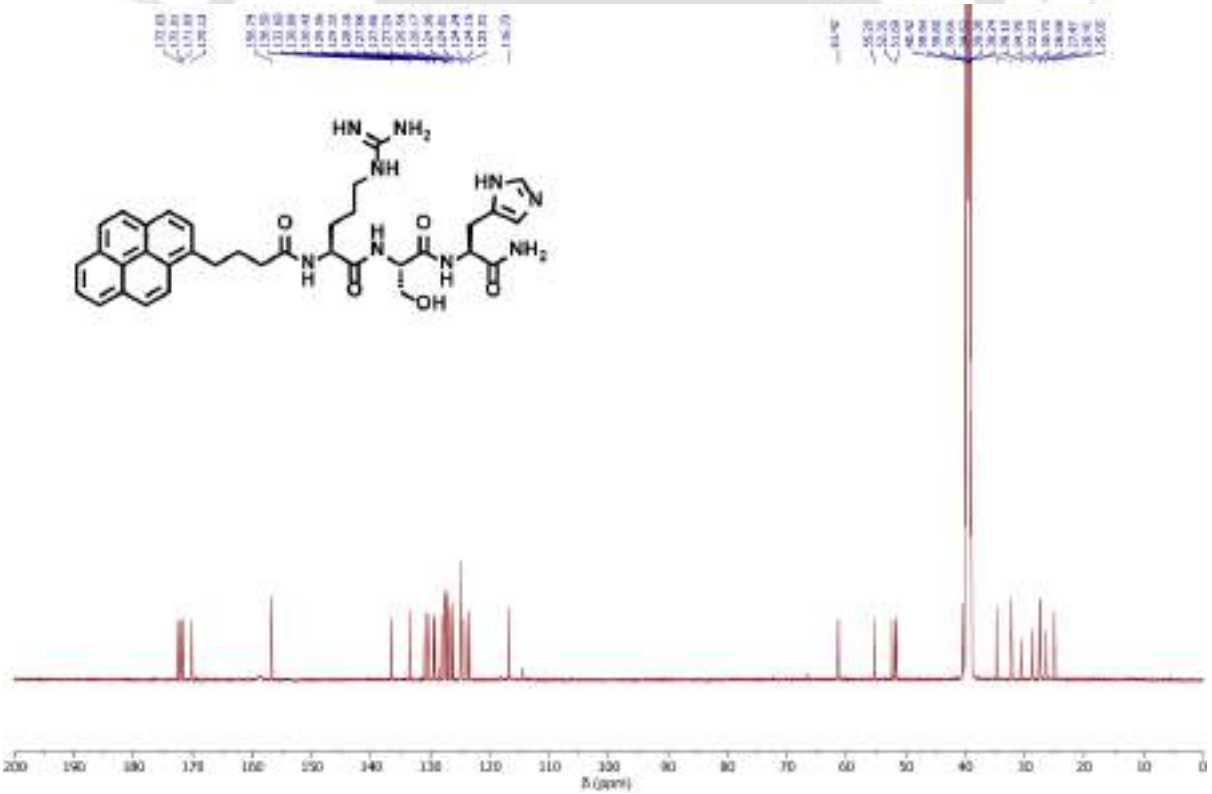

Figure 6.30. ^{13}C NMR spectrum of Py-RSH peptide in DMSO-d_6

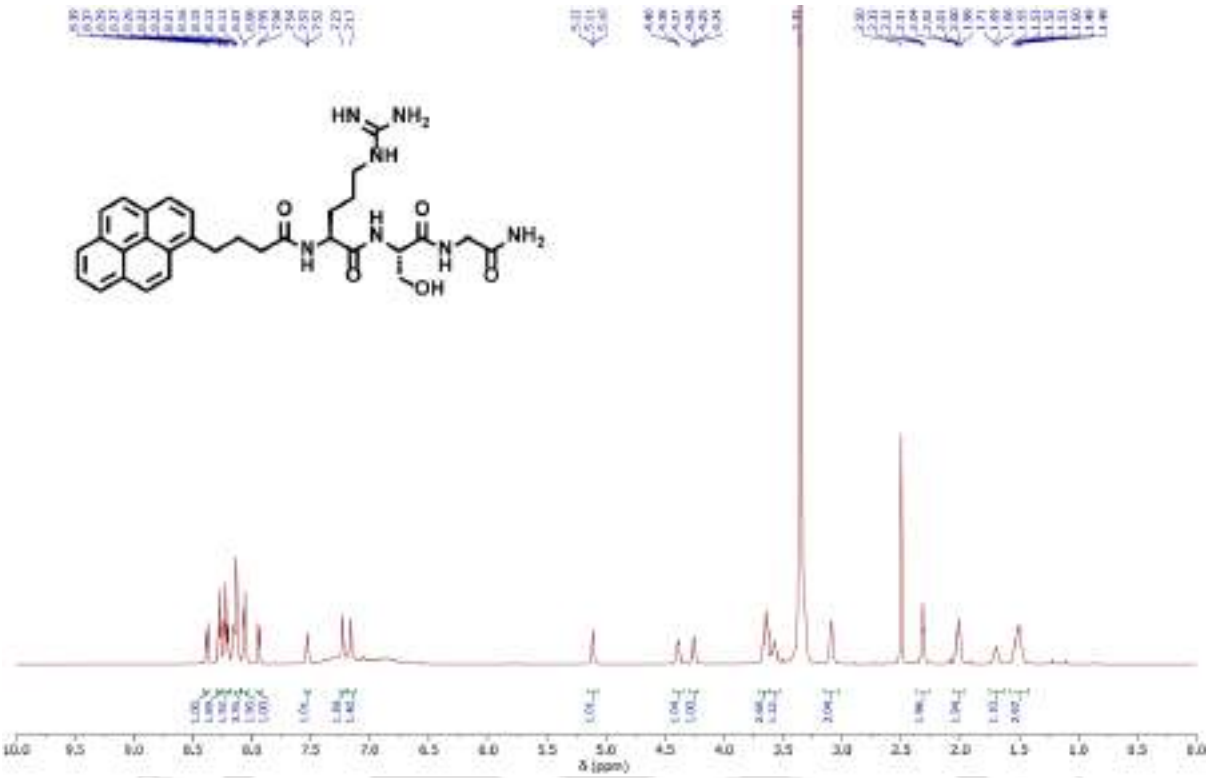

Figure 6.31. ^{1}H NMR spectrum of Py-RSG peptide in DMSO-d_6

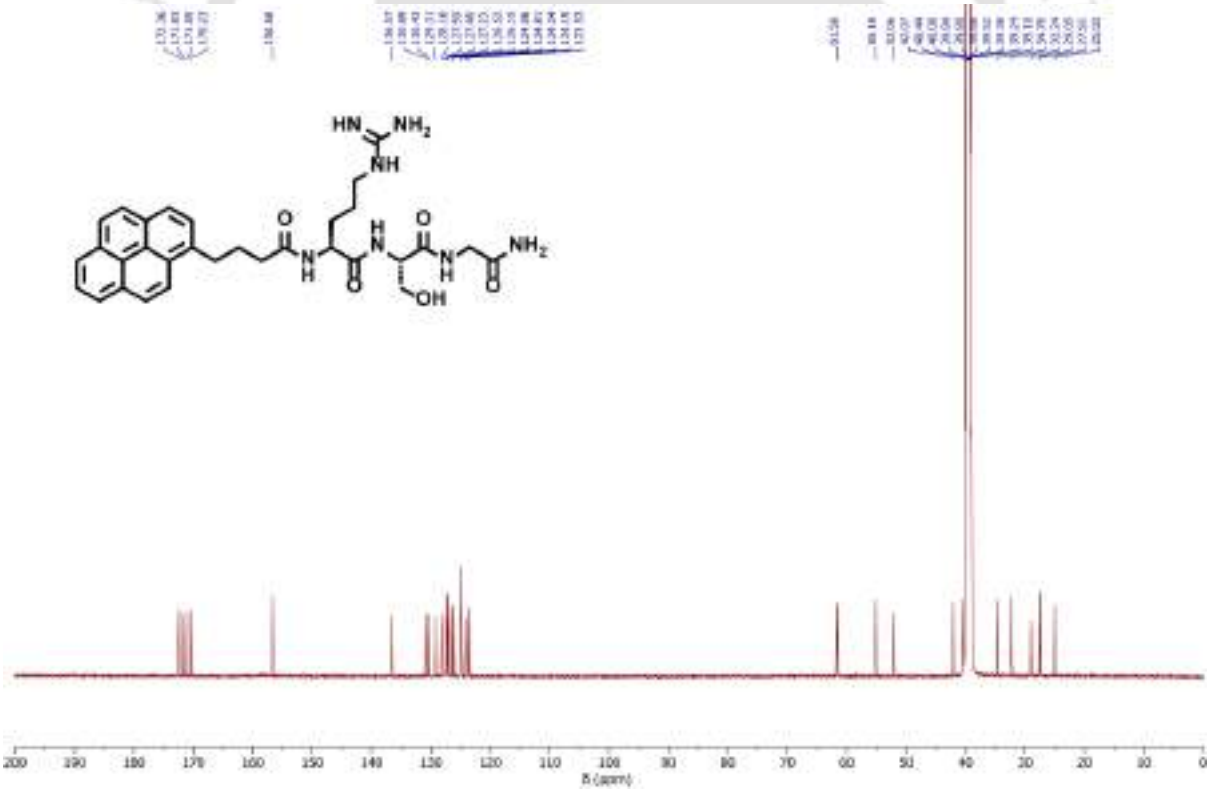

Figure 6.32. ^{13}C NMR spectrum of Py-RSG peptide in DMSO-d_6

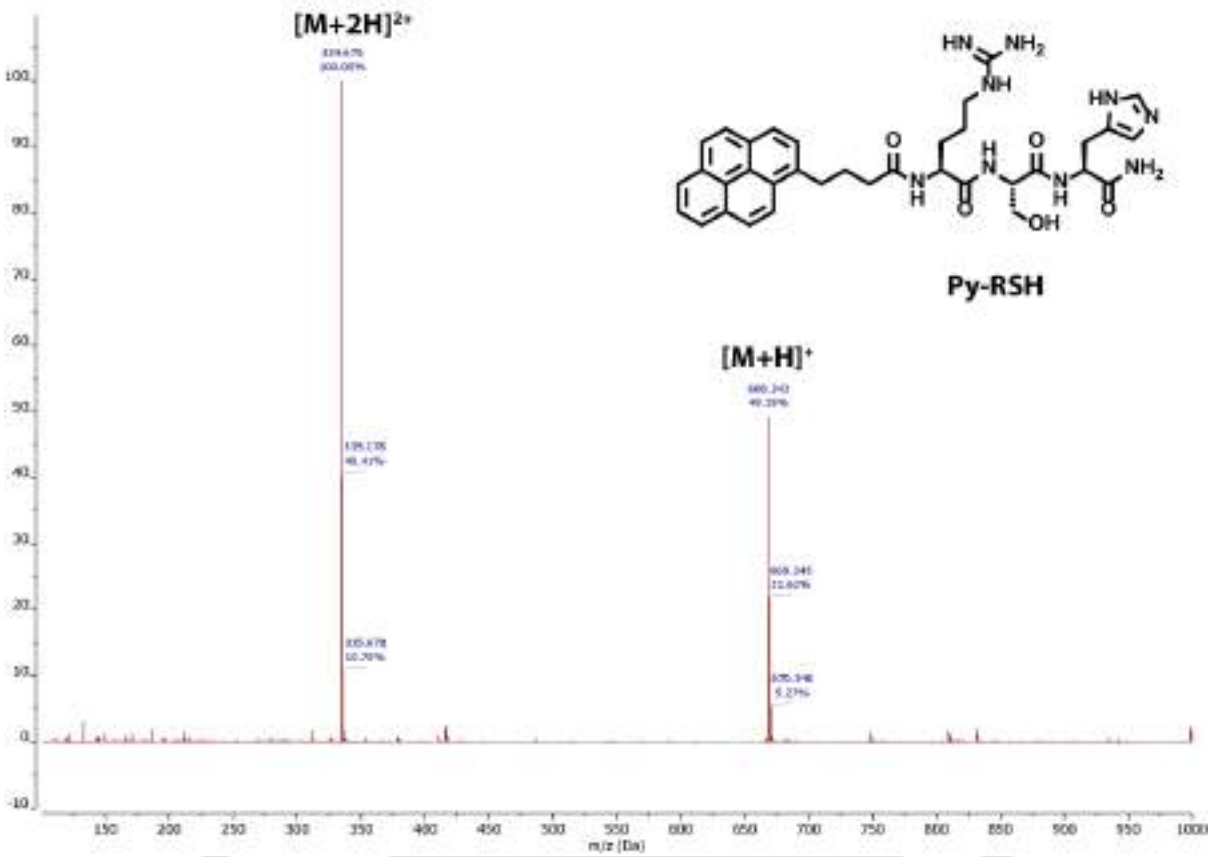

Figure 6.33. ESI-MS spectrum of Py-RSH peptide

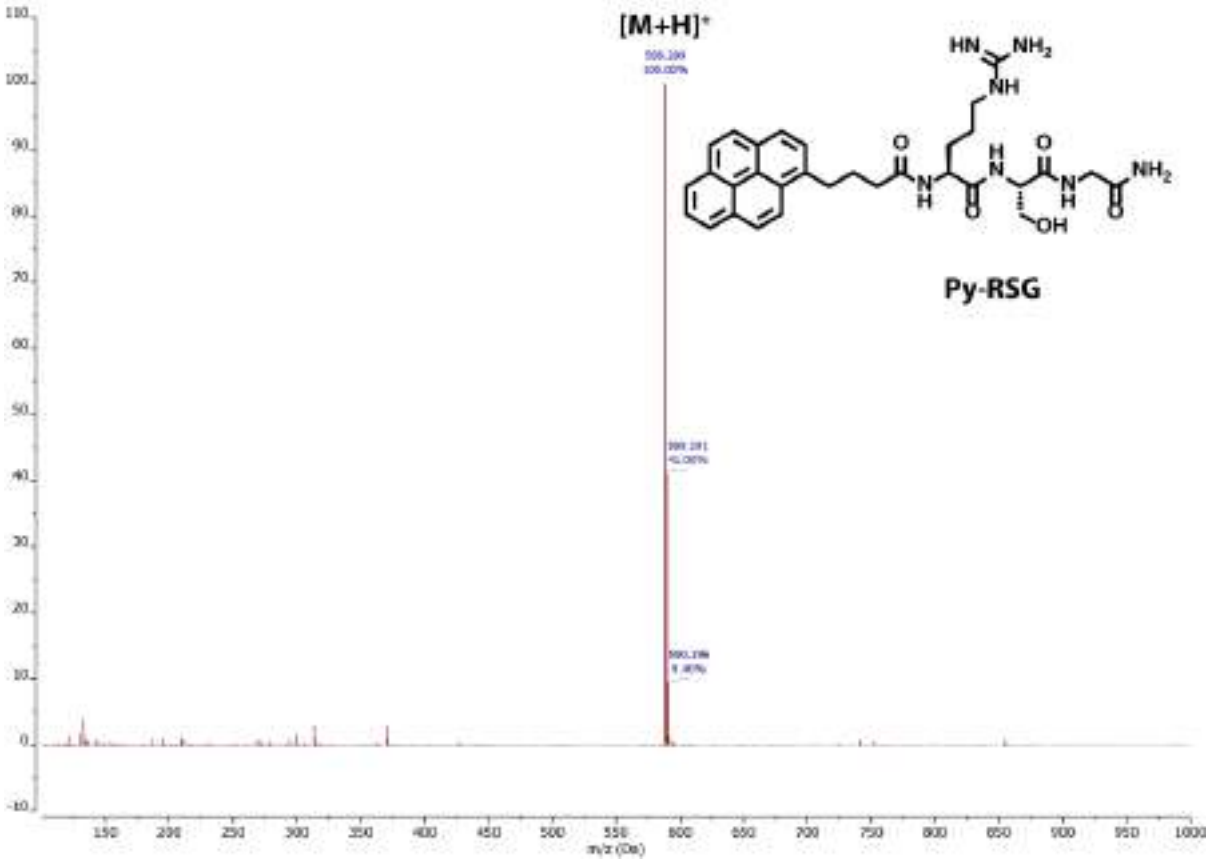

Figure 6.34. ESI-MS spectrum of Py-RSG peptide

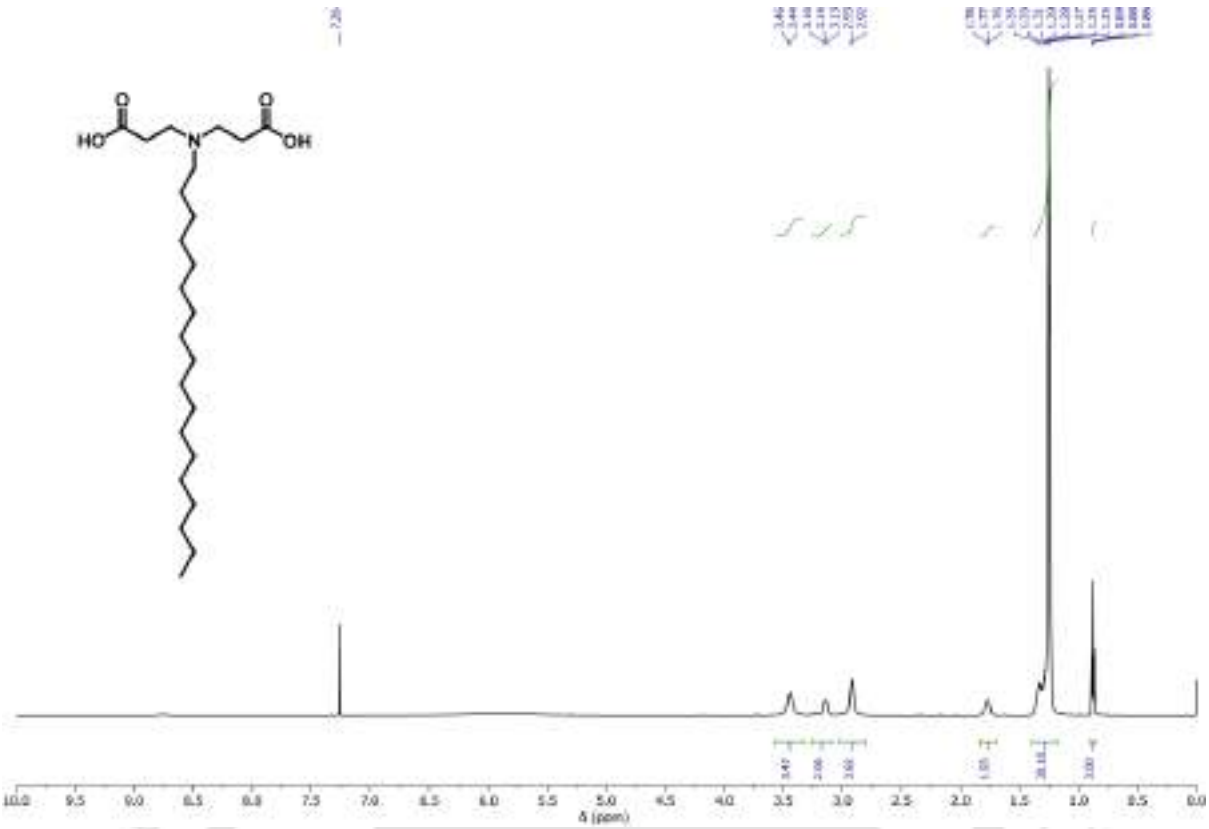

Figure 6.35. ^{1}H NMR spectrum of amphiphile **1** in $CDCl_3$

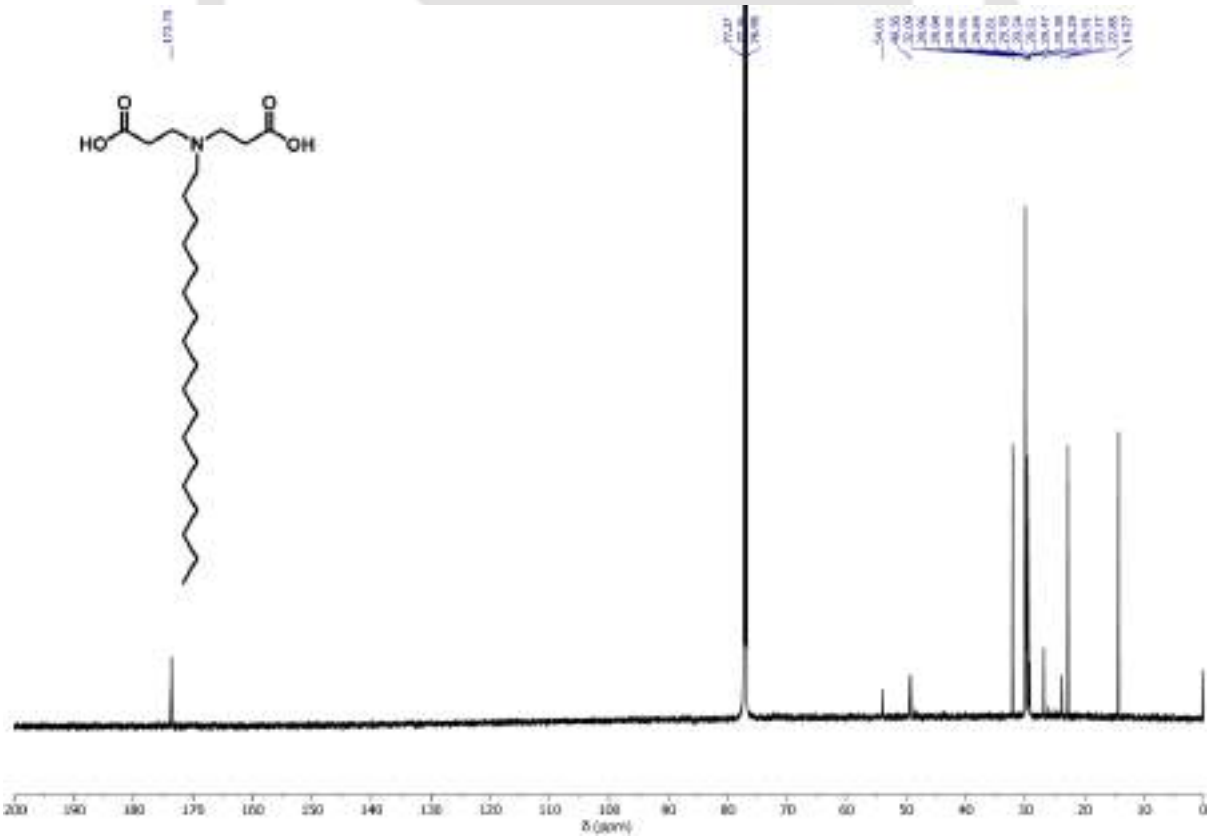

Figure 6.36. ^{13}C NMR spectrum of amphiphile **1** in $CDCl_3$

7. References

1. Reisler, E.; Egelman, E. H., Actin structure and function: what we still do not understand. *J. Biol. Chem.* **2007,** *282* (50), 36133-7.

2. Desai, A.; Mitchison, T. J., Microtubule polymerization dynamics. *Annu. Rev. Cell Dev. Biol.* **1997,** *13* (1), 83-117.

3. Howard, J.; Clark, R. L., Mechanics of Motor Proteins and the Cytoskeleton. *Appl. Mech. Reviews* **2002,** *55* (2), B39-B39.

4. Rizzoli, S. O., Synaptic vesicle recycling: steps and principles. *EMBO J.* **2014,** *33* (8), 788-822.

5. Mattia, E.; Otto, S., Supramolecular systems chemistry. *Nat. Nanotechnol.* **2015,** *10* (2), 111-9.

6. Sorrenti, A.; Leira-Iglesias, J.; Markvoort, A. J.; de Greef, T. F. A.; Hermans, T. M., Non-equilibrium supramolecular polymerization. *Chem. Soc. Rev.* **2017,** *46* (18), 5476-5490.

7. Lodish, H.; Berk, A.; Kaiser, C. A.; Krieger, M.; Bretscher, A.; Ploegh, H.; Amon, A.; Martin, K. C., *Molecular Cell Biology.* 8 ed.; W.H. Freeman and Company: New York, 2016.

8. Das, K.; Gabrielli, L.; Prins, L. J., Chemically Fueled Self-Assembly in Biology and Chemistry. *Angew. Chem. Int. Ed.* **2021,** *60* (37), 20120-20143.

9. Howard, J.; Hyman, A. A., Growth, fluctuation and switching at microtubule plus ends. *Nat. Rev. Mol. Cell Biol.* **2009,** *10* (8), 569-74.

10. Mitchison, T.; Kirschner, M., Dynamic instability of microtubule growth. *Nature* **1984,** *312* (5991), 237-42.

11. Pollard, T. D.; Blanchoin, L.; Mullins, R. D., Molecular mechanisms controlling actin filament dynamics in nonmuscle cells. *Annu. Rev. Biophys. Biomol. Struct.* **2000,** *29* (1), 545-76.

12. Pantaloni, D.; Le Clainche, C.; Carlier, M. F., Mechanism of actin-based motility. *Science* **2001,** *292* (5521), 1502-6.

13. Mateu, M. G., Assembly, stability and dynamics of virus capsids. *Arch. Biochem. Biophys.* **2013,** *531* (1-2), 65-79.

14. Perlmutter, J. D.; Hagan, M. F., Mechanisms of virus assembly. *Annu. Rev. Phys. Chem.* **2015,** *66* (1), 217-39.

15. Perlmutter, J. D.; Perkett, M. R.; Hagan, M. F., Pathways for virus assembly around nucleic acids. *J. Mol. Biol.* **2014,** *426* (18), 3148-3165.

16. Vicente-Manzanares, M.; Ma, X.; Adelstein, R. S.; Horwitz, A. R., Non-muscle myosin II takes centre stage in cell adhesion and migration. *Nat. Rev. Mol. Cell Biol.* **2009,** *10* (11), 778-90.

17. Shang, Z.; Zhou, K.; Xu, C.; Csencsits, R.; Cochran, J. C.; Sindelar, C. V., High-resolution structures of kinesin on microtubules provide a basis for nucleotide-gated force-generation. *Elife* **2014,** *3*, e04686.

18. Rosenbaum, D. M.; Rasmussen, S. G.; Kobilka, B. K., The structure and function of G-protein-coupled receptors. *Nature* **2009,** *459* (7245), 356-63.

19. Clark, E. A.; Brugge, J. S., Integrins and signal transduction pathways: the road taken. *Science* **1995,** *268* (5208), 233-9.

20. Debnath, S.; Roy, S.; Ulijn, R. V., Peptide nanofibers with dynamic instability through nonequilibrium biocatalytic assembly. *J. Am. Chem. Soc.* **2013,** *135* (45), 16789-92.

21. Maiti, S.; Fortunati, I.; Ferrante, C.; Scrimin, P.; Prins, L. J., Dissipative self-assembly of vesicular nanoreactors. *Nat. Chem.* **2016,** *8* (7), 725-31.

22. Spitzer, D.; Rodrigues, L. L.; Strassburger, D.; Mezger, M.; Besenius, P., Tuneable Transient Thermogels Mediated by a pH- and Redox-Regulated Supramolecular Polymerization. *Angew. Chem. Int. Ed.* **2017,** *56* (48), 15461-15465.

23. Heinen, L.; Heuser, T.; Steinschulte, A.; Walther, A., Antagonistic Enzymes in a Biocatalytic pH Feedback System Program Autonomous DNA Hydrogel Life Cycles. *Nano Lett.* **2017,** *17* (8), 4989-4995.

24. Mishra, A.; Korlepara, D. B.; Kumar, M.; Jain, A.; Jonnalagadda, N.; Bejagam, K. K.; Balasubramanian, S.; George, S. J., Biomimetic temporal self-assembly via fuel-driven controlled supramolecular polymerization. *Nat. Commun.* **2018,** *9* (1), 1295.

25. Angulo-Pachon, C. A.; Miravet, J. F., Sucrose-fueled, energy dissipative, transient formation of molecular hydrogels mediated by yeast activity. *Chem. Commun.* **2016,** *52* (31), 5398-401.

26. Nguyen, P. Q.; Courchesne, N. D.; Duraj-Thatte, A.; Praveschotinunt, P.; Joshi, N. S., Engineered Living Materials: Prospects and Challenges for Using Biological Systems to Direct the Assembly of Smart Materials. *Adv. Mater.* **2018,** *30* (19), e1704847.

27. Del Grosso, E.; Amodio, A.; Ragazzon, G.; Prins, L. J.; Ricci, F., Dissipative Synthetic DNA-Based Receptors for the Transient Loading and Release of Molecular Cargo. *Angew. Chem. Int. Ed.* **2018,** *57* (33), 10489-10493.

28. Green, L. N.; Subramanian, H. K. K.; Mardanlou, V.; Kim, J.; Hariadi, R. F.; Franco, E., Autonomous dynamic control of DNA nanostructure self-assembly. *Nat. Chem.* **2019,** *11* (6), 510-520.

29. Leira-Iglesias, J.; Sorrenti, A.; Sato, A.; Dunne, P. A.; Hermans, T. M., Supramolecular pathway selection of perylenediimides mediated by chemical fuels. *Chem. Commun.* **2016,** *52* (58), 9009-12.

30. Wojciechowski, J. P.; Martin, A. D.; Thordarson, P., Kinetically Controlled Lifetimes in Redox-Responsive Transient Supramolecular Hydrogels. *J. Am. Chem. Soc.* **2018,** *140* (8), 2869-2874.

31. Heuser, T.; Steppert, A. K.; Lopez, C. M.; Zhu, B.; Walther, A., Generic concept to program the time domain of self-assemblies with a self-regulation mechanism. *Nano Lett.* **2015,** *15* (4), 2213-9.

32. Jain, A.; Dhiman, S.; Dhayani, A.; Vemula, P. K.; George, S. J., Chemical fuel-driven living and transient supramolecular polymerization. *Nat. Commun.* **2019,** *10* (1), 450.

33. De, S.; Klajn, R., Dissipative Self-Assembly Driven by the Consumption of Chemical Fuels. *Adv. Mater.* **2018,** *30* (41), e1706750.

34. Kumar, M.; Ing, N. L.; Narang, V.; Wijerathne, N. K.; Hochbaum, A. I.; Ulijn, R. V., Amino-acid-encoded biocatalytic self-assembly enables the formation of transient conducting nanostructures. *Nat. Chem.* **2018,** *10* (7), 696-703.

35. Bal, S.; Das, K.; Ahmed, S.; Das, D., Chemically Fueled Dissipative Self-Assembly that Exploits Cooperative Catalysis. *Angew. Chem. Int. Ed.* **2019,** *58* (1), 244-247.

36. Wang, H.; Wang, Y.; Shen, B.; Liu, X.; Lee, M., Substrate-Driven Transient Self-Assembly and Spontaneous Disassembly Directed by Chemical Reaction with Product Release. *J. Am. Chem. Soc.* **2019,** *141* (10), 4182-4185.

37. della Sala, F.; Verbeet, W.; Silvestrini, S.; Fortunati, I.; Ferrante, C.; Prins, L. J., Stepwise Hierarchical Self-Assembly of Supramolecular Amphiphiles into Higher-Order Three-Dimensional Nanostructures. *ChemNanoMat* **2018,** *4* (8), 821-830.

38. Boekhoven, J.; Hendriksen, W. E.; Koper, G. J.; Eelkema, R.; van Esch, J. H., Transient assembly of active materials fueled by a chemical reaction. *Science* **2015,** *349* (6252), 1075-9.

39. Wang, J.; Liu, K.; Xing, R.; Yan, X., Peptide self-assembly: thermodynamics and kinetics. *Chem. Soc. Rev.* **2016,** *45* (20), 5589-5604.

40. Singh, N.; Formon, G. J. M.; De Piccoli, S.; Hermans, T. M., Devising Synthetic Reaction Cycles for Dissipative Nonequilibrium Self-Assembly. *Adv. Mater.* **2020,** *32* (20), e1906834.

41. Boekhoven, J.; Brizard, A. M.; Kowlgi, K. N.; Koper, G. J.; Eelkema, R.; van Esch, J. H., Dissipative self-assembly of a molecular gelator by using a chemical fuel. *Angew. Chem. Int. Ed.* **2010,** *49* (28), 4825-8.

42. Rieß, B.; Grötsch, R. K.; Boekhoven, J., The Design of Dissipative Molecular Assemblies Driven by Chemical Reaction Cycles. *Chem* **2020,** *6* (3), 552-578.

43. Tena-Solsona, M.; Riess, B.; Grotsch, R. K.; Lohrer, F. C.; Wanzke, C.; Kasdorf, B.; Bausch, A. R.; Muller-Buschbaum, P.; Lieleg, O.; Boekhoven, J., Non-equilibrium dissipative supramolecular materials with a tunable lifetime. *Nat. Commun.* **2017,** *8* (1), 15895.

44. Dai, K.; Fores, J. R.; Wanzke, C.; Winkeljann, B.; Bergmann, A. M.; Lieleg, O.; Boekhoven, J., Regulating Chemically Fueled Peptide Assemblies by Molecular Design. *J. Am. Chem. Soc.* **2020,** *142* (33), 14142-14149.

45. Kriebisch, B. A. K.; Jussupow, A.; Bergmann, A. M.; Kohler, F.; Dietz, H.; Kaila, V. R. I.; Boekhoven, J., Reciprocal Coupling in Chemically Fueled Assembly: A Reaction Cycle Regulates Self-Assembly and Vice Versa. *J. Am. Chem. Soc.* **2020,** *142* (49), 20837-20844.

46. Tena-Solsona, M.; Wanzke, C.; Riess, B.; Bausch, A. R.; Boekhoven, J., Self-selection of dissipative assemblies driven by primitive chemical reaction networks. *Nat. Commun.* **2018,** *9* (1), 2044.

47. Donau, C.; Spath, F.; Sosson, M.; Kriebisch, B. A. K.; Schnitter, F.; Tena-Solsona, M.; Kang, H. S.; Salibi, E.; Sattler, M.; Mutschler, H.; Boekhoven, J., Active coacervate droplets as a model for membraneless organelles and protocells. *Nat. Commun.* **2020,** *11* (1), 5167.

48. Spath, F.; Donau, C.; Bergmann, A. M.; Kranzlein, M.; Synatschke, C. V.; Rieger, B.; Boekhoven, J., Molecular Design of Chemically Fueled Peptide-Polyelectrolyte Coacervate-Based Assemblies. *J. Am. Chem. Soc.* **2021,** *143* (12), 4782-4789.

49. Kariyawasam, L. S.; Hartley, C. S., Dissipative Assembly of Aqueous Carboxylic Acid Anhydrides Fueled by Carbodiimides. *J. Am. Chem. Soc.* **2017,** *139* (34), 11949-11955.

50. Zhang, B.; Jayalath, I. M.; Ke, J.; Sparks, J. L.; Hartley, C. S.; Konkolewicz, D., Chemically fueled covalent crosslinking of polymer materials. *Chem. Commun.* **2019,** *55* (14), 2086-2089.

51. Bai, S. Y.; Niu, X. F.; Wang, H. C.; Wei, L.; Liu, L. Q.; Liu, X. Y.; Eelkema, R.; Guo, X. H.; van Esch, J. H.; Wang, Y. M., Chemical reaction powered transient polymer hydrogels for controlled formation and free release of pharmaceutical crystals. *Chem. Eng. J.* **2021,** *414*, 128877.

52. Panja, S.; Dietrich, B.; Adams, D. J., Chemically Fuelled Self-Regulating Gel-to-Gel Transition. *ChemSystemsChem* **2019,** *2* (1), e1900038.

53. Grotsch, R. K.; Wanzke, C.; Speckbacher, M.; Angi, A.; Rieger, B.; Boekhoven, J., Pathway Dependence in the Fuel-Driven Dissipative Self-Assembly of Nanoparticles. *J. Am. Chem. Soc.* **2019,** *141* (25), 9872-9878.

54. Del Giudice, D.; Frateloreto, F.; Sappino, C.; Di Stefano, S., Chemical Tools for the Temporal Control of Water Solution pH and Applications in Dissipative Systems. *Eur. J. Org. Chem.* **2022,** *n/a* (n/a), e202200407.

55. Berrocal, J. A.; Biagini, C.; Mandolini, L.; Di Stefano, S., Coupling of the Decarboxylation of 2-Cyano-2-phenylpropanoic Acid to Large-Amplitude Motions: A Convenient Fuel for an Acid-Base-Operated Molecular Switch. *Angew. Chem. Int. Ed.* **2016,** *55* (24), 6997-7001.

56. Biagini, C.; Albano, S.; Caruso, R.; Mandolini, L.; Berrocal, J. A.; Di Stefano, S., Variations in the fuel structure control the rate of the back and forth motions of a chemically fuelled molecular switch. *Chem. Sci.* **2018,** *9* (1), 181-188.

57. Franchi, P.; Poderi, C.; Mezzina, E.; Biagini, C.; Di Stefano, S.; Lucarini, M., 2-Cyano-2-phenylpropanoic Acid Triggers the Back and Forth Motions of an Acid-Base-Operated Paramagnetic Molecular Switch. *J. Org. Chem.* **2019,** *84* (14), 9364-9368.

58. Ghosh, A.; Paul, I.; Adlung, M.; Wickleder, C.; Schmittel, M., Oscillating Emission of [2]Rotaxane Driven by Chemical Fuel. *Org. Lett.* **2018,** *20* (4), 1046-1049.

59. Ghosh, A.; Paul, I.; Schmittel, M., Time-Dependent Pulses of Lithium Ions in Cascaded Signaling and Out-of-Equilibrium (Supra)molecular Logic. *J. Am. Chem. Soc.* **2019,** *141* (48), 18954-18957.

60. Erbas-Cakmak, S.; Fielden, S. D. P.; Karaca, U.; Leigh, D. A.; McTernan, C. T.; Tetlow, D. J.; Wilson, M. R., Rotary and linear molecular motors driven by pulses of a chemical fuel. *Science* **2017,** *358* (6361), 340-343.

61. Biagini, C.; Fielden, S. D. P.; Leigh, D. A.; Schaufelberger, F.; Di Stefano, S.; Thomas, D., Dissipative Catalysis with a Molecular Machine. *Angew. Chem. Int. Ed.* **2019,** *58* (29), 9876-9880.

62. Choi, S.; Mukhopadhyay, R. D.; Kim, Y.; Hwang, I. C.; Hwang, W.; Ghosh, S. K.; Baek, K.; Kim, K., Fuel-Driven Transient Crystallization of a Cucurbit[8]uril-Based Host-Guest Complex. *Angew. Chem. Int. Ed.* **2019,** *58* (47), 16850-16853.

63. Liyana Gunawardana, V. W.; Finnegan, T. J.; Ward, C. E.; Moore, C. E.; Badjic, J. D., Dissipative Formation of Covalent Basket Cages. *Angew. Chem. Int. Ed.* **2022,** *n/a* (n/a), e202207418.

64. Del Giudice, D.; Spatola, E.; Valentini, M.; Bombelli, C.; Ercolani, G.; Di Stefano, S., Time-programmable pH: decarboxylation of nitroacetic acid allows the time-controlled rising of pH to a definite value. *Chem. Sci.* **2021,** *12* (21), 7460-7466.

65. Weißenfels, M.; Gemen, J.; Klajn, R., Dissipative Self-Assembly: Fueling with Chemicals versus Light. *Chem* **2021,** *7* (1), 23-37.

66. Klajn, R., Spiropyran-based dynamic materials. *Chem. Soc. Rev.* **2014,** *43* (1), 148-84.

67. Kundu, P. K.; Samanta, D.; Leizrowice, R.; Margulis, B.; Zhao, H.; Borner, M.; Udayabhaskararao, T.; Manna, D.; Klajn, R., Light-controlled self-assembly of non-photoresponsive nanoparticles. *Nat. Chem.* **2015,** *7* (8), 646-52.

68. Samanta, D.; Klajn, R., Aqueous Light-Controlled Self-Assembly of Nanoparticles. *Adv. Opt. Mater.* **2016,** *4* (9), 1373-1377.

69. Yang, L. P.; Jia, F.; Cui, J. S.; Lu, S. B.; Jiang, W., Light-Controlled Switching of a Non-photoresponsive Molecular Shuttle. *Org. Lett.* **2017,** *19* (11), 2945-2948.

70. Cissé, N.; Kudernac, T., Light-Fuelled Self-Assembly of Cyclic Peptides into Supramolecular Tubules. *ChemSystemsChem* **2020,** *2* (6), e2000012.

71. Chen, X. M.; Feng, W. J.; Bisoyi, H. K.; Zhang, S.; Chen, X.; Yang, H.; Li, Q., Light-activated photodeformable supramolecular dissipative self-assemblies. *Nat. Commun.* **2022,** *13* (1), 3216.

72. Liu, M.; Creemer, C. N.; Reardon, T. J.; Parquette, J. R., Light-driven dissipative self-assembly of a peptide hydrogel. *Chem. Commun.* **2021,** *57* (100), 13776-13779.

73. Teders, M.; Pogodaev, A. A.; Bojanov, G.; Huck, W. T. S., Reversible Photoswitchable Inhibitors Generate Ultrasensitivity in Out-of-Equilibrium Enzymatic Reactions. *J. Am. Chem. Soc.* **2021,** *143* (15), 5709-5716.

74. Teders, M.; Murray, N. R.; Huck, W. T. S., Reversible Photoswitchable Inhibitors Enable Wavelength-Selective Regulation of Out-of-Equilibrium Bi-enzymatic Systems. *ChemSystemsChem* **2021,** *3* (6), e2100020.

75. Dhasaiyan, P.; Ghosh, T.; Lee, H. G.; Lee, Y.; Hwang, I.; Mukhopadhyay, R. D.; Park, K. M.; Shin, S.; Kang, I. S.; Kim, K., Cascade reaction networks within audible sound induced transient domains in a solution. *Nat. Commun.* **2022,** *13* (1), 2372.

76. Hwang, I.; Mukhopadhyay, R. D.; Dhasaiyan, P.; Choi, S.; Kim, S. Y.; Ko, Y. H.; Baek, K.; Kim, K., Audible sound-controlled spatiotemporal patterns in out-of-equilibrium systems. *Nat. Chem.* **2020,** *12* (9), 808-813.

77. Choi, S.; Mukhopadhyay, R. D.; Sen, S. K.; Hwang, I.; Kim, K., Out-of-equilibrium chemical logic systems: Light and sound controlled programmable spatiotemporal patterns and mechanical functions. *Chem* **2022**.

78. Vamvakaki, M.; Papoutsakis, L.; Katsamanis, V.; Afchoudia, T.; Fragouli, P. G.; Iatrou, H.; Hadjichristidis, N.; Armes, S. P.; Sidorov, S.; Zhirov, D.; Zhirov, V.; Kostylev, M.; Bronstein, L. M.; Anastasiadis, S. H., Micellization in pH-sensitive amphiphilic block copolymers in aqueous media and the formation of metal nanoparticles. *Faraday Discuss.* **2005,** *128* (0), 129-47.

79. Aggeli, A.; Bell, M.; Carrick, L. M.; Fishwick, C. W.; Harding, R.; Mawer, P. J.; Radford, S. E.; Strong, A. E.; Boden, N., pH as a trigger of peptide beta-sheet self-assembly and reversible switching between nematic and isotropic phases. *J. Am. Chem. Soc.* **2003,** *125* (32), 9619-28.

80. Lagzi, I.; Kowalczyk, B.; Wang, D.; Grzybowski, B. A., Nanoparticle oscillations and fronts. *Angew. Chem. Int. Ed.* **2010,** *49* (46), 8616-9.

81. Fan, X.; Walther, A., pH Feedback Lifecycles Programmed by Enzymatic Logic Gates Using Common Foods as Fuels. *Angew. Chem. Int. Ed.* **2021,** *60* (20), 11398-11405.

82. Heuser, T.; Weyandt, E.; Walther, A., Biocatalytic Feedback-Driven Temporal Programming of Self-Regulating Peptide Hydrogels. *Angew. Chem. Int. Ed.* **2015,** *54* (45), 13258-62.

83. Tang, C.; Ulijn, R. V.; Saiani, A., Effect of glycine substitution on Fmoc-diphenylalanine self-assembly and gelation properties. *Langmuir* **2011,** *27* (23), 14438-49.

84. Heuser, T.; Merindol, R.; Loescher, S.; Klaus, A.; Walther, A., Photonic Devices Out of Equilibrium: Transient Memory, Signal Propagation, and Sensing. *Adv. Mater.* **2017,** *29* (17), 1606842.

85. Che, H.; Buddingh, B. C.; van Hest, J. C. M., Self-Regulated and Temporal Control of a "Breathing" Microgel Mediated by Enzymatic Reaction. *Angew. Chem. Int. Ed.* **2017,** *56* (41), 12581-12585.

86. Panja, S.; Patterson, C.; Adams, D. J., Temporally-Programmed Transient Supramolecular Gels. *Macromol. Rapid Commun.* **2019,** *40* (15), e1900251.

87. Panja, S.; Adams, D. J., Gel to gel transitions by dynamic self-assembly. *Chem. Commun.* **2019,** *55* (68), 10154-10157.

88. Pramanik, B.; Mondal, J. H.; Singha, N.; Ahmed, S.; Mohanty, J.; Das, D., A Viologen-Perylenediimide Conjugate as an Efficient Base Sensor with Solvatochromic Property. *ChemPhysChem* **2017,** *18* (2), 245-252.

89. Ahmed, S.; Singha, N.; Pramanik, B.; Mondal, J. H.; Das, D., Redox controlled reversible transformation of a supramolecular alternating copolymer to a radical cation containing homo-polymer. *Polym. Chem.* **2016,** *7* (26), 4393-4401.

90. Dhiman, S.; Ghosh, R.; George, S. J., Redox-Mediated Transient Reconfiguration of a Supramolecular Assembly. *ChemSystemsChem* **2019,** *2* (3), e1900042.

91. Jalani, K.; Dhiman, S.; Jain, A.; George, S. J., Temporal switching of an amphiphilic self-assembly by a chemical fuel-driven conformational response. *Chem. Sci.* **2017,** *8* (9), 6030-6036.

92. Jain, M.; Ravoo, B. J., Fuel-Driven and Enzyme-Regulated Redox-Responsive Supramolecular Hydrogels. *Angew. Chem. Int. Ed.* **2021,** *60* (38), 21062-21068.

93. Chowdhuri, S.; Ghosh, M.; Adler-Abramovich, L.; Das, D., The Effects of a Short Self-Assembling Peptide on the Physical and Biological Properties of Biopolymer Hydrogels. *Pharmaceutics* **2021,** *13* (10).

94. Chowdhuri, S.; Saha, A.; Pramanik, B.; Das, S.; Dowari, P.; Ukil, A.; Das, D., Smart Thixotropic Hydrogels by Disulfide-Linked Short Peptides for Effective Three-Dimensional Cell Proliferation. *Langmuir* **2020,** *36* (50), 15450-15462.

95. Singha, N.; Srivastava, A.; Pramanik, B.; Ahmed, S.; Dowari, P.; Chowdhuri, S.; Das, B. K.; Debnath, A.; Das, D., Unusual confinement properties of a water insoluble small peptide hydrogel. *Chem. Sci.* **2019,** *10* (23), 5920-5928.

96. Ogden, W. A.; Guan, Z., Redox Chemical-Fueled Dissipative Self-Assembly of Active Materials. *ChemSystemsChem* **2019,** *2* (4), e1900030.

97. Pietschnig, R., Polymers with pendant ferrocenes. *Chem. Soc. Rev.* **2016,** *45* (19), 5216-31.

98. Li, L.; Zhang, J.; Yang, C.; Huang, L.; Zhang, J.; Bai, J.; Redshaw, C.; Feng, X.; Cao, C.; Huo, N.; Li, J.; Tang, B. Z., Stimuli-Responsive Materials from Ferrocene-Based Organic Small Molecule for Wearable Sensors. *Small* **2021,** *17* (46), e2103125.

99. Ahmed, S.; Chatterjee, A.; Das, K.; Das, D., Fatty acid based transient nanostructures for temporal regulation of artificial peroxidase activity. *Chem. Sci.* **2019,** *10* (32), 7574-7578.

100. Pappas, C. G.; Sasselli, I. R.; Ulijn, R. V., Biocatalytic Pathway Selection in Transient Tripeptide Nanostructures. *Angew. Chem. Int. Ed.* **2015,** *54* (28), 8119-23.

101. Kumar, M.; Sementa, D.; Narang, V.; Riedo, E.; Ulijn, R. V., Self-Assembly Propensity Dictates Lifetimes in Transient Naphthalimide-Dipeptide Nanofibers. *Chem. Eur. J.* **2020,** *26* (38), 8372-8376.

102. Mishra, A.; Dhiman, S.; George, S. J., ATP-Driven Synthetic Supramolecular Assemblies: From ATP as a Template to Fuel. *Angew. Chem. Int. Ed.* **2021,** *60* (6), 2740-2756.

103. Kumar, M.; Brocorens, P.; Tonnele, C.; Beljonne, D.; Surin, M.; George, S. J., A dynamic supramolecular polymer with stimuli-responsive handedness for in situ probing of enzymatic ATP hydrolysis. *Nat. Commun.* **2014,** *5* (1), 5793.

104. Dhiman, S.; Jain, A.; George, S. J., Transient Helicity: Fuel-Driven Temporal Control over Conformational Switching in a Supramolecular Polymer. *Angew. Chem. Int. Ed.* **2017,** *56* (5), 1329-1333.

105. Li, Z.; Zeman, C. J. t.; Valandro, S. R.; Bantang, J. P. O.; Schanze, K. S., Adenosine Triphosphate Templated Self-Assembly of Cationic Porphyrin into Chiral Double Superhelices and Enzyme-Mediated Disassembly. *J. Am. Chem. Soc.* **2019,** *141* (32), 12610-12618.

106. Saha, B.; Chatterjee, A.; Reja, A.; Das, D., Condensates of short peptides and ATP for the temporal regulation of cytochrome c activity. *Chem. Commun.* **2019,** *55* (94), 14194-14197.

107. Dhiman, S.; George, S. J., Temporally Controlled Supramolecular Polymerization. *Bull. Chem. Soc. Jpn.* **2018,** *91* (4), 687-699.

108. Larsen, D.; Beeren, S. R., Enzyme-mediated dynamic combinatorial chemistry allows out-of-equilibrium template-directed synthesis of macrocyclic oligosaccharides. *Chem. Sci.* **2019,** *10* (43), 9981-9987.

109. Wang, Q.; Zhang, Q.; Zhang, Q. W.; Li, X.; Zhao, C. X.; Xu, T. Y.; Qu, D. H.; Tian, H., Color-tunable single-fluorophore supramolecular system with assembly-encoded emission. *Nat. Commun.* **2020,** *11* (1), 158.

110. Samuelsen, L.; Larsen, D.; Schonbeck, C.; Beeren, S. R., pH-Responsive templates modulate the dynamic enzymatic synthesis of cyclodextrins. *Chem. Commun.* **2022,** *58* (33), 5152-5155.

111. Larsen, D.; Bjerre, P. M.; Beeren, S. R., Light-controlled out-of-equilibrium assembly of cyclodextrins in an enzyme-mediated dynamic system. *Chem. Commun.* **2019,** *55* (100), 15037-15040.

112. Lu, H.; Hao, J.; Wang, X., Host-Fueled Transient Supramolecular Hydrogels. *ChemSystemsChem* **2022,** *4* (3), e202100050.

113. Solis Munana, P.; Ragazzon, G.; Dupont, J.; Ren, C. Z.; Prins, L. J.; Chen, J. L., Substrate-Induced Self-Assembly of Cooperative Catalysts. *Angew. Chem. Int. Ed.* **2018,** *57* (50), 16469-16474.

114. Post, E. A. J.; Fletcher, S. P., Dissipative self-assembly, competition and inhibition in a self-reproducing protocell model. *Chem. Sci.* **2020,** *11* (35), 9434-9442.

115. Wanzke, C.; Jussupow, A.; Kohler, F.; Dietz, H.; Kaila, V. R. I.; Boekhoven, J., Dynamic Vesicles Formed By Dissipative Self-Assembly. *ChemSystemsChem* **2019,** *2* (1), e1900044.

116. Ragazzon, G.; Prins, L. J., Energy consumption in chemical fuel-driven self-assembly. *Nat. Nanotechnol.* **2018,** *13* (10), 882-889.

117. Dambenieks, A. K.; Vu, P. H. Q.; Fyles, T. M., Dissipative assembly of a membrane transport system. *Chem. Sci.* **2014,** *5* (9), 3396-3403.

118. Pezzato, C.; Prins, L. J., Transient signal generation in a self-assembled nanosystem fueled by ATP. *Nat. Commun.* **2015,** *6* (1), 7790.

119. Cardona, M. A.; Chen, R.; Maiti, S.; Fortunati, I.; Ferrante, C.; Gabrielli, L.; Das, K.; Prins, L. J., Time-gated fluorescence signalling under dissipative conditions. *Chem. Commun.* **2020,** *56* (90), 13979-13982.

120. Cardona, M. A.; Prins, L. J., ATP-fuelled self-assembly to regulate chemical reactivity in the time domain. *Chem. Sci.* **2019,** *11* (6), 1518-1522.

121. Würbser, M. A.; Schwarz, P. S.; Heckel, J.; Bergmann, A. M.; Walther, A.; Boekhoven, J., Chemically Fueled Block Copolymer Self-Assembly into Transient Nanoreactors**. *ChemSystemsChem* **2021,** *3* (5), e2100015.

122. Chen, R.; Neri, S.; Prins, L. J., Enhanced catalytic activity under non-equilibrium conditions. *Nat. Nanotechnol.* **2020,** *15* (10), 868-874.

123. Xing, P. Y.; Sun, T.; Hao, A. Y., Vesicles from supramolecular amphiphiles. *RSC Adv.* **2013,** *3* (47), 24776-24793.

124. Barrow, S. J.; Kasera, S.; Rowland, M. J.; del Barrio, J.; Scherman, O. A., Cucurbituril-Based Molecular Recognition. *Chem. Rev.* **2015,** *115* (22), 12320-406.

125. Jiao, D.; Geng, J.; Loh, X. J.; Das, D.; Lee, T. C.; Scherman, O. A., Supramolecular peptide amphiphile vesicles through host-guest complexation. *Angew. Chem. Int. Ed.* **2012,** *51* (38), 9633-7.

126. Mondal, J. H.; Ghosh, T.; Ahmed, S.; Das, D., Dual self-sorting by cucurbit[8]uril to transform a mixed micelle to vesicle. *Langmuir* **2014,** *30* (39), 11528-34.

127. Mondal, J. H.; Ahmed, S.; Ghosh, T.; Das, D., Reversible deformation-formation of a multistimuli responsive vesicle by a supramolecular peptide amphiphile. *Soft Matter* **2015,** *11* (24), 4912-20.

128. Zozulia, O.; Dolan, M. A.; Korendovych, I. V., Catalytic peptide assemblies. *Chem. Soc. Rev.* **2018,** *47* (10), 3621-3639.

129. Kushner, D. J., Self-assembly of biological structures. *Bacteriol. Rev.* **1969,** *33* (2), 302-45.

130. Assaf, K. I.; Nau, W. M., Cucurbiturils: from synthesis to high-affinity binding and catalysis. *Chem. Soc. Rev.* **2015,** *44* (2), 394-418.

131. Das, D.; Assaf, K. I.; Nau, W. M., Applications of Cucurbiturils in Medicinal Chemistry and Chemical Biology. *Front. Chem.* **2019,** *7*, 619.

132. Jeon, Y. J.; Bharadwaj, P. K.; Choi, S.; Lee, J. W.; Kim, K., Supramolecular amphiphiles: spontaneous formation of vesicles triggered by formation of a charge-transfer complex in a host. *Angew. Chem. Int. Ed.* **2002,** *41* (23), 4474-6.

133. Ko, Y. H.; Kim, E.; Hwang, I.; Kim, K., Supramolecular assemblies built with host-stabilized charge-transfer interactions. *Chem. Commun.* **2007,** (13), 1305-15.

134. Bush, M. E.; Bouley, N. D.; Urbach, A. R., Charge-mediated recognition of N-terminal tryptophan in aqueous solution by a synthetic host. *J. Am. Chem. Soc.* **2005,** *127* (41), 14511-7.

135. Zhang, Y. M.; Liu, J. H.; Yu, Q.; Wen, X.; Liu, Y., Targeted Polypeptide-Microtubule Aggregation with Cucurbit[8]uril for Enhanced Cell Apoptosis. *Angew. Chem. Int. Ed.* **2019,** *58* (31), 10553-10557.

136. Pramanik, B.; Ahmed, S.; Singha, N.; Das, B. K.; Dowari, P.; Das, D., Unorthodox Combination of Cation-pi and Charge-Transfer Interactions within a Donor-Acceptor Pair. *Langmuir* **2019,** *35* (2), 478-488.

137. Singha, N.; Das, B. K.; Pramanik, B.; Das, S.; Das, D., Freeze the dynamicity: charge transfer complexation assisted control over the reaction pathway. *Chem. Sci.* **2019,** *10* (43), 10035-10039.

138. Pramanik, B.; Das, D., Aggregation-Induced Emission or Hydrolysis by Water? The Case of Schiff Bases in Aqueous Organic Solvents. *J. Phys. Chem. C* **2018,** *122* (6), 3655-3661.

139. Cesareo, S. D.; Langton, S. R., Kinetic properties of Helicobacter pylori urease compared with jack bean urease. *FEMS Microbiol. Lett.* **1992,** *78* (1), 15-21.

140. Mondal, J. H.; Ahmed, S.; Das, D., Physicochemical analysis of mixed micelles of a viologen surfactant: extended to water-in-oil (w/o) microemulsion and cucurbit[8]uril-assisted vesicle formation. *Langmuir* **2014,** *30* (28), 8290-9.

141. Kim, J.; Jung, I.-S.; Kim, S.-Y.; Lee, E.; Kang, J.-K.; Sakamoto, S.; Yamaguchi, K.; Kim, K., New Cucurbituril Homologues: Syntheses, Isolation, Characterization, and X-ray Crystal Structures of Cucurbit[n]uril (n = 5, 7, and 8). *J. Am. Chem. Soc.* **2000,** *122* (3), 540-541.

142. Nitschke, J. R., Systems chemistry: Molecular networks come of age. *Nature* **2009,** *462* (7274), 736-8.

143. Freeman, M., Feedback control of intercellular signalling in development. *Nature* **2000,** *408* (6810), 313-9.

144. Ashkenasy, G.; Hermans, T. M.; Otto, S.; Taylor, A. F., Systems chemistry. *Chem. Soc. Rev.* **2017,** *46* (9), 2543-2554.

145. Russell, J. A.; Leng, G.; Douglas, A. J., The magnocellular oxytocin system, the fount of maternity: adaptations in pregnancy. *Front. Neuroendocrinol.* **2003,** *24* (1), 27-61.

146. Jesty, J.; Beltrami, E., Positive feedbacks of coagulation: their role in threshold regulation. *Arterioscler. Thromb. Vasc. Biol.* **2005,** *25* (12), 2463-9.

147. Modell, H.; Cliff, W.; Michael, J.; McFarland, J.; Wenderoth, M. P.; Wright, A., A physiologist's view of homeostasis. *Adv. Physiol. Educ.* **2015,** *39* (4), 259-66.

148. Afrose, S. P.; Bal, S.; Chatterjee, A.; Das, K.; Das, D., Designed Negative Feedback from Transiently Formed Catalytic Nanostructures. *Angew. Chem. Int. Ed.* **2019,** *58* (44), 15783-15787.

149. Pramanik, S.; Aprahamian, I., Hydrazone Switch-Based Negative Feedback Loop. *J. Am. Chem. Soc.* **2016,** *138* (46), 15142-15145.

150. Yurt, M. N. Z.; Cakmak, Y.; Tekin, G.; Karakurt, S.; Erbas-Cakmak, S., Autoinhibitory Feedback Control over Photodynamic Action. *ACS Omega* **2019,** *4* (7), 12293-12299.

151. Huang, W.; Zhou, Y.; Deng, Y.; He, Y., A negative feedback loop based on proton-driven in situ formation of plasmonic molybdenum oxide nanosheets. *Phys. Chem. Chem. Phys.* **2018,** *20* (6), 4347-4350.

152. van Rossum, S. A. P.; Tena-Solsona, M.; van Esch, J. H.; Eelkema, R.; Boekhoven, J., Dissipative out-of-equilibrium assembly of man-made supramolecular materials. *Chem. Soc. Rev.* **2017,** *46* (18), 5519-5535.

153. Kariyawasam, L. S.; Hossain, M. M.; Hartley, C. S., The Transient Covalent Bond in Abiotic Nonequilibrium Systems. *Angew. Chem. Int. Ed.* **2021,** *60* (23), 12648-12658.

154. Schwarz, P. S.; Tena-Solsona, M.; Dai, K.; Boekhoven, J., Carbodiimide-fueled catalytic reaction cycles to regulate supramolecular processes. *Chem. Commun.* **2022,** *58* (9), 1284-1297.

155. van der Helm, M. P.; Wang, C. L.; Fan, B.; Macchione, M.; Mendes, E.; Eelkema, R., Organocatalytic Control over a Fuel-Driven Transient-Esterification Network*. *Angew. Chem. Int. Ed.* **2020,** *59* (46), 20604-20611.

156. Panja, S.; Adams, D. J., Urea-Urease Reaction in Controlling Properties of Supramolecular Hydrogels: Pros and Cons. *Chem. Eur. J.* **2021,** *27* (35), 8928-8939.

157. Panja, S.; Bohacova, K.; Dietrich, B.; Adams, D. J., Programming properties of transient hydrogels by an enzymatic reaction. *Nanoscale* **2020,** *12* (24), 12840-12848.

158. Dowari, P.; Das, S.; Pramanik, B.; Das, D., pH clock instructed transient supramolecular peptide amphiphile and its vesicular assembly. *Chem. Commun.* **2019,** *55* (94), 14119-14122.

159. Hao, X.; Yang, K.; Wang, H.; Peng, F.; Yang, H., Biocatalytic Feedback-Controlled Non-Newtonian Fluids. *Angew. Chem. Int. Ed.* **2020,** *59* (11), 4314-4319.

160. Dasgupta, A.; Das, D., Designer Peptide Amphiphiles: Self-Assembly to Applications. *Langmuir* **2019,** *35* (33), 10704-10724.

161. Das, S.; Das, D., Rational Design of Peptide-based Smart Hydrogels for Therapeutic Applications. *Front. Chem.* **2021,** *9*, 770102.

162. Biedermann, F.; Rauwald, U.; Zayed, J. M.; Scherman, O. A., A supramolecular route for reversible protein-polymer conjugation. *Chem. Sci.* **2011,** *2* (2), 279-286.

163. Ko, Y. H.; Kim, K.; Kang, J. K.; Chun, H.; Lee, J. W.; Sakamoto, S.; Yamaguchi, K.; Fettinger, J. C.; Kim, K., Designed self-assembly of molecular necklaces using host-stabilized charge-transfer interactions. *J. Am. Chem. Soc.* **2004,** *126* (7), 1932-3.

164. Ma, N.; Li, F.; Li, S.; Chu, S.; Han, L.; Liu, S.; Yan, T.; Tian, R.; Luo, Q.; Liu, J., A remote optically controlled hydrolase model based on supramolecular assembly and disassembly of its enzyme-like active site. *Nanoscale* **2019,** *11* (8), 3521-3526.

165. Nothling, M. D.; Xiao, Z.; Hill, N. S.; Blyth, M. T.; Bhaskaran, A.; Sani, M. A.; Espinosa-Gomez, A.; Ngov, K.; White, J.; Buscher, T.; Separovic, F.; O'Mara, M. L.; Coote, M. L.; Connal, L. A., A multifunctional surfactant catalyst inspired by hydrolases. *Sci. Adv.* **2020,** *6* (14), eaaz0404.

166. Yang, L.; Yang, H.; Li, F.; Zhang, X., Supramolecular glycolipid based on host-enhanced charge transfer interaction. *Langmuir* **2013,** *29* (40), 12375-9.

167. Das, S.; Das, P.; Dowari, P.; Das, B. K.; Das, D., Bi-directional feedback controlled transience in Cucurbituril based tandem nanozyme. *J. Colloid Interface Sci.* **2022,** *614*, 172-180.

168. Chen, Y.; Yang, Y.; Orr, A. A.; Makam, P.; Redko, B.; Haimov, E.; Wang, Y.; Shimon, L. J. W.; Rencus-Lazar, S.; Ju, M.; Tamamis, P.; Dong, H.; Gazit, E., Self-Assembled Peptide Nano-Superstructure towards Enzyme Mimicking Hydrolysis. *Angew. Chem. Int. Ed.* **2021,** *60* (31), 17164-17170.

169. Grenier, M. C.; Davis, R. W.; Wilson-Henjum, K. L.; LaDow, J. E.; Black, J. W.; Caran, K. L.; Seifert, K.; Minbiole, K. P., The antibacterial activity of 4,4'-bipyridinium amphiphiles with conventional, bicephalic and gemini architectures. *Bioorg. Med. Chem. Lett.* **2012,** *22* (12), 4055-8.

170. Delort, E.; Darbre, T.; Reymond, J. L., A strong positive dendritic effect in a peptide dendrimer-catalyzed ester hydrolysis reaction. *J. Am. Chem. Soc.* **2004,** *126* (48), 15642-3.

171. Singh, N.; Conte, M. P.; Ulijn, R. V.; Miravet, J. F.; Escuder, B., Insight into the esterase like activity demonstrated by an imidazole appended self-assembling hydrogelator. *Chem. Commun.* **2015,** *51* (67), 13213-6.

172. Pasquato, L.; Rancan, F.; Scrimin, P.; Mancin, F.; Frigeri, C., N-methylimidazole-functionalized gold nanoparticles as catalysts for cleavage of a carboxylic acid ester. *Chem. Commun.* **2000,** (22), 2253-2254.

173. Appendix 1: Dissociation Constants (pKa) of Organic Acids (at 20°C). In *Applications of Ion Chromatography for Pharmaceutical and Biological Products*, 2012; pp 449-453.

174. Pearce, P. J.; Simkins, R. J. J., Acid Strengths of Some Substituted Picric Acids. *Can. J. Chem.* **1968,** *46* (2), 241-&.

175. Guarise, C.; Manea, F.; Zaupa, G.; Pasquato, L.; Prins, L. J.; Scrimin, P., Cooperative nanosystems. *J. Pept. Sci.* **2008,** *14* (2), 174-83.

176. Lopez-Gallego, F.; Schmidt-Dannert, C., Multi-enzymatic synthesis. *Curr. Opin. Chem. Biol.* **2010,** *14* (2), 174-83.

177. Joyce, G. F., Building the RNA world. Ribozymes. *Curr. Biol.* **1996,** *6* (8), 965-7.

178. Lohr, T. L.; Marks, T. J., Orthogonal tandem catalysis. *Nat. Chem.* **2015,** *7* (6), 477-82.

179. Qu, P.; Kuepfert, M.; Hashmi, M.; Weck, M., Compartmentalization and Photoregulating Pathways for Incompatible Tandem Catalysis. *J. Am. Chem. Soc.* **2021,** *143* (12), 4705-4713.

180. Lee, L. C.; Lu, J.; Weck, M.; Jones, C. W., Acid-Base Bifunctional Shell Cross-Linked Micelle Nanoreactor for One-Pot Tandem Reaction. *ACS Catal.* **2016,** *6* (2), 784-787.

181. Elani, Y.; Law, R. V.; Ces, O., Vesicle-based artificial cells as chemical microreactors with spatially segregated reaction pathways. *Nat. Commun.* **2014,** *5* (1), 5305.

182. Tan, H.; Guo, S.; Dinh, N. D.; Luo, R.; Jin, L.; Chen, C. H., Heterogeneous multi-compartmental hydrogel particles as synthetic cells for incompatible tandem reactions. *Nat. Commun.* **2017,** *8* (1), 663.

183. Singh, N.; Zhang, K.; Angulo-Pachon, C. A.; Mendes, E.; van Esch, J. H.; Escuder, B., Tandem reactions in self-sorted catalytic molecular hydrogels. *Chem. Sci.* **2016,** *7* (8), 5568-5572.

184. Chatterjee, A.; Mahato, C.; Das, D., Complex Cascade Reaction Networks via Cross beta Amyloid Nanotubes. *Angew. Chem. Int. Ed.* **2021,** *60* (1), 202-207.

185. Chatterjee, A.; Afrose, S. P.; Ahmed, S.; Venugopal, A.; Das, D., Cross-beta amyloid nanotubes for hydrolase-peroxidase cascade reactions. *Chem. Commun.* **2020,** *56* (57), 7869-7872.

186. Mann, S., Systems of creation: the emergence of life from nonliving matter. *Acc. Chem. Res.* **2012,** *45* (12), 2131-41.

187. Buddingh, B. C.; van Hest, J. C. M., Artificial Cells: Synthetic Compartments with Life-like Functionality and Adaptivity. *Acc. Chem. Res.* **2017,** *50* (4), 769-777.

188. Grzybowski, B. A.; Huck, W. T., The nanotechnology of life-inspired systems. *Nat. Nanotechnol.* **2016,** *11* (7), 585-92.

189. Jalani, K.; Das, A. D.; Sasmal, R.; Agasti, S. S.; George, S. J., Transient dormant monomer states for supramolecular polymers with low dispersity. *Nat. Commun.* **2020,** *11* (1), 3967.

190. Lee, J. W.; Kim, K.; Choi, S.; Ko, Y. H.; Sakamoto, S.; Yamaguchi, K.; Kim, K., Unprecedented host-induced intramolecular charge-transfer complex formation. *Chem. Commun.* **2002,** (22), 2692-3.

191. Pazos, E.; Novo, P.; Peinador, C.; Kaifer, A. E.; Garcia, M. D., Cucurbit[8]uril (CB[8])-Based Supramolecular Switches. *Angew. Chem. Int. Ed.* **2019,** *58* (2), 403-416.

192. Alsharabasy, A. M.; Pandit, A.; Farras, P., Recent Advances in the Design and Sensing Applications of Hemin/Coordination Polymer-Based Nanocomposites. *Adv. Mater.* **2021,** *33* (2), e2003883.

193. Wang, Q.; Yang, Z.; Zhang, X.; Xiao, X.; Chang, C. K.; Xu, B., A supramolecular-hydrogel-encapsulated hemin as an artificial enzyme to mimic peroxidase. *Angew. Chem. Int. Ed.* **2007,** *46* (23), 4285-9.

194. Biedermann, F.; Scherman, O. A., Cucurbit[8]uril mediated donor-acceptor ternary complexes: a model system for studying charge-transfer interactions. *J. Phys. Chem. B* **2012,** *116* (9), 2842-9.

195. Gharibi, H.; Moosavi-Movahedi, Z.; Javadian, S.; Nazari, K.; Moosavi-Movahedi, A. A., Vesicular mixed gemini-SDS-hemin-imidazole complex as a peroxidase-like nano artificial enzyme. *J. Phys. Chem. B* **2011,** *115* (16), 4671-9.

196. Yang, X.; Fang, C.; Mei, H.; Chang, T.; Cao, Z.; Shangguan, D., Characterization of G-quadruplex/hemin peroxidase: substrate specificity and inactivation kinetics. *Chem. Eur. J.* **2011,** *17* (51), 14475-84.

197. Uno, T.; Takeda, A.; Shimabayashi, S., Effects of Imidazoles and Ph on the Peroxidase-Activity of the Hemin Hydrogen-Peroxide System. *Inorg. Chem.* **1995,** *34* (6), 1599-1607.

198. Cardinal, S.; Paquet-Cote, P. A.; Azelmat, J.; Bouchard, C.; Grenier, D.; Voyer, N., Synthesis and anti-inflammatory activity of isoquebecol. *Bioorg. Med. Chem.* **2017,** *25* (7), 2043-2056.

199. Santimone, M. M., *C. R. Acad. Sci. Paris, Serie D: Sciences Naturelles* **1974,** *279*, 951-954.

200. Santimone, M. M.; Dou, H. J. M., *C. R. Acad. Sci. Paris, Serie C* **1974,** *278*, 1469-1471.

201. Cunningham, I. D.; Bachelor, J. L.; Pratt, J. M., Peroxidatic activity of haem octapeptide complexes with anilines, naphthols and phenols. *J. Chem. Soc., Perkin Trans. 2* **1994,** (6), 1347-1350.

202. Doerge, D. R.; Divi, R. L.; Churchwell, M. I., Identification of the colored guaiacol oxidation product produced by peroxidases. *Anal. Biochem.* **1997,** *250* (1), 10-7.

203. Deamer, D. W., The first living systems: a bioenergetic perspective. *Microbiol. Mol. Biol. Rev.* **1997,** *61* (2), 239-61.

204. Dzieciol, A. J.; Mann, S., Designs for life: protocell models in the laboratory. *Chem. Soc. Rev.* **2012,** *41* (1), 79-85.

205. Morowitz, H. J.; Heinz, B.; Deamer, D. W., The chemical logic of a minimum protocell. *Orig. Life Evol. Biosph.* **1988,** *18* (3), 281-7.

206. Menger, F. M.; Angelova, M. I., Giant Vesicles: Imitating the Cytological Processes of Cell Membranes. *Acc. Chem. Res.* **1998,** *31* (12), 789-797.

207. Menger, F. M.; Gabrielson, K. D., Cytomimetic Organic-Chemistry - Early Developments. *Angew. Chem. Int. Ed.* **1995,** *34* (19), 2091-2106.

208. Dong, R.; Zhu, B.; Zhou, Y.; Yan, D.; Zhu, X., "Breathing" vesicles with jellyfish-like on-off switchable fluorescence behavior. *Angew. Chem. Int. Ed.* **2012,** *51* (46), 11633-7.

209. Xu, L.; Ren, N.; Pang, J.; Deng, H. P.; Zhu, X. Y.; Sun, M.; Yan, D. Y., Fluorescent and "breathable" CO2 responsive vesicles inspired from green fluorescent protein. *Polym. Chem.* **2017,** *8* (40), 6283-6288.

210. Lin, S.; Shang, J.; Zhang, X.; Theato, P., "Breathing" CO2 -, O2 -, and Light-Responsive Vesicles from a Triblock Copolymer for Rate-Tunable Controlled Release. *Macromol. Rapid Commun.* **2018,** *39* (1), 1700313.

211. Yan, Q.; Zhou, R.; Fu, C.; Zhang, H.; Yin, Y.; Yuan, J., CO2-responsive polymeric vesicles that breathe. *Angew. Chem. Int. Ed.* **2011,** *50* (21), 4923-7.

212. Yan, Q.; Wang, J.; Yin, Y.; Yuan, J., Breathing polymersomes: CO2-tuning membrane permeability for size-selective release, separation, and reaction. *Angew. Chem. Int. Ed.* **2013,** *52* (19), 5070-3.

213. Moreno, S.; Sharan, P.; Engelke, J.; Gumz, H.; Boye, S.; Oertel, U.; Wang, P.; Banerjee, S.; Klajn, R.; Voit, B.; Lederer, A.; Appelhans, D., Light-Driven Proton Transfer for Cyclic and Temporal Switching of Enzymatic Nanoreactors. *Small* **2020,** *16* (37), e2002135.

214. Yu, S.; Azzam, T.; Rouiller, I.; Eisenberg, A., "Breathing" vesicles. *J. Am. Chem. Soc.* **2009,** *131* (30), 10557-66.

215. Das, S.; Das, T.; Das, P.; Das, D., Controlling the lifetime of cucurbit[8]uril based self-abolishing nanozymes. *Chem. Sci.* **2022,** *13* (14), 4050-4057.

216. Howlett, M. G.; Engwerda, A. H. J.; Scanes, R. J. H.; Fletcher, S. P., An autonomously oscillating supramolecular self-replicator. *Nat. Chem.* **2022,** *14* (7), 805-810.

217. Howlett, M. G.; Scanes, R. J. H.; Fletcher, S. P., Selection between Competing Self-Reproducing Lipids: Succession and Dynamic Activation. *JACS Au* **2021,** *1* (9), 1355-1361.

218. Engwerda, A. H. J.; Southworth, J.; Lebedeva, M. A.; Scanes, R. J. H.; Kukura, P.; Fletcher, S. P., Coupled Metabolic Cycles Allow Out-of-Equilibrium Autopoietic Vesicle Replication. *Angew. Chem. Int. Ed.* **2020,** *59* (46), 20361-20366.

219. Morrow, S. M.; Colomer, I.; Fletcher, S. P., A chemically fuelled self-replicator. *Nat. Commun.* **2019,** *10* (1), 1011.

220. Shimomura, O., A short story of aequorin. *Biol. Bull.* **1995,** *189* (1), 1-5.

221. Shimomura, O.; Johnson, F. H.; Saiga, Y., Extraction, purification and properties of aequorin, a bioluminescent protein from the luminous hydromedusan, Aequorea. *J. Cell. Comp. Physiol.* **1962,** *59* (3), 223-39.

222. Jiang, T.; Du, L.; Li, M., Lighting up bioluminescence with coelenterazine: strategies and applications. *Photochem. Photobiol. Sci.* **2016,** *15* (4), 466-80.

223. McElroy, W. D.; Seliger, H. H.; White, E. H., Mechanism of bioluminescence, chemiluminescence and enzyme function in the oxidation of firefly luciferin. *Photochem. Photobiol.* **1969,** *10* (3), 153-70.

224. Hopkins, T. A.; Seliger, H. H.; White, E. H.; Cass, M. H., The chemiluminescence of firefly luciferin. A model for the bioluminescent reaction and identification of the product excited state. *J. Am. Chem. Soc.* **1967,** *89* (26), 7148-50.

225. White, E. H.; Steinmetz, M. G.; Miano, J. D.; Wildes, P. D.; Morland, R., Chemi-and bioluminescence of firefly luciferin. *J. Am. Chem. Soc.* **1980,** *102* (9), 3199-3208.

226. Hao, M.; Sun, G.; Zuo, M.; Xu, Z.; Chen, Y.; Hu, X. Y.; Wang, L., A Supramolecular Artificial Light-Harvesting System with Two-Step Sequential Energy Transfer for Photochemical Catalysis. *Angew. Chem. Int. Ed.* **2020,** *59* (25), 10095-10100.

227. Xu, Z.; Peng, S.; Wang, Y. Y.; Zhang, J. K.; Lazar, A. I.; Guo, D. S., Broad-Spectrum Tunable Photoluminescent Nanomaterials Constructed from a Modular Light-Harvesting Platform Based on Macrocyclic Amphiphiles. *Adv. Mater.* **2016,** *28* (35), 7666-71.

228. Huang, J.; Yu, Y.; Wang, L.; Wang, X.; Gu, Z.; Zhang, S., Tetraphenylethylene-Induced Cross-Linked Vesicles with Tunable Luminescence and Controllable Stability. *ACS Appl. Mater. Interfaces* **2017,** *9* (34), 29030-29037.

229. Geng, W. C.; Liu, Y. C.; Wang, Y. Y.; Xu, Z.; Zheng, Z.; Yang, C. B.; Guo, D. S., A self-assembled white-light-emitting system in aqueous medium based on a macrocyclic amphiphile. *Chem. Commun.* **2016,** *53* (2), 392-395.

230. Guo, S.; Song, Y.; He, Y.; Hu, X. Y.; Wang, L., Highly Efficient Artificial Light-Harvesting Systems Constructed in Aqueous Solution Based on Supramolecular Self-Assembly. *Angew. Chem. Int. Ed.* **2018,** *57* (12), 3163-3167.

231. Israelachvili, J. N., *Intermolecular and Surface Forces*. 2 ed.; Academic Press: London, 1991; Vol. 17, p 370.

232. Mitra, D.; Chakraborty, I.; Bhattacharya, S. C.; Moulik, S. P.; Roy, S.; Das, D.; Das, P. K., Physicochemical studies on cetylammonium bromide and its modified (mono-, di-, and trihydroxyethylated) head group analogues. Their micellization characteristics in water and thermodynamic and structural aspects of water-in-oil microemulsions formed with them along with n-hexanol and isooctane. *J. Phys. Chem. B* **2006,** *110* (23), 11314-26.

233. Xie, H. T.; Lu, W. S.; Wang, J. D.; Wang, W., pH responsive vesicles with tunable size formed by single-tailed surfactants with a dendritic headgroup. *RSC Adv.* **2017,** *7* (36), 22079-22085.

234. Ghosh, S.; Pramanik, B.; Das, D., Self-Aggregation of a Naphthalene-Monoimide Amphiphile and Its Charge-Transfer-Complex Driven Morphogenesis in Water. *ChemNanoMat* **2018,** *4* (8), 867-873.

235. Israelachvili, J. N., *Physics of Amphiphiles: Micelles, Vesicles and Microemulsions*. North Holland Amsterdam, 1985.

236. Slavík, J., Anilinonaphthalene sulfonate as a probe of membrane composition and function. *Biochim. Biophys. Acta - Rev. Biomembr.* **1982,** *694* (1), 1-25.

237. Hawe, A.; Sutter, M.; Jiskoot, W., Extrinsic fluorescent dyes as tools for protein characterization. *Pharm. Res.* **2008,** *25* (7), 1487-99.

238. Gasymov, O. K.; Glasgow, B. J., ANS fluorescence: potential to augment the identification of the external binding sites of proteins. *Biochim. Biophys. Acta* **2007,** *1774* (3), 403-11.

239. Matulis, D.; Lovrien, R., 1-Anilino-8-naphthalene sulfonate anion-protein binding depends primarily on ion pair formation. *Biophys. J.* **1998,** *74* (1), 422-9.

240. Lesslauer, W.; Cain, J.; Blasie, J. K., On the location of 1-anilino-8-naphthalene-sulfonate in lipid model systems. *Biochim. Biophys. Acta - Biomembr.* **1971,** *241* (2), 547-566.

241. Lesslauer, W.; Cain, J. E.; Blasie, J. K., X-ray diffraction studies of lecithin bimolecular leaflets with incorporated fluorescent probes. *Proc. Natl. Acad. Sci. U.S.A.* **1972,** *69* (6), 1499-503.

242. Jendrasiak, G. L.; Estep, T. N., The interaction of 1-anilino-8-naphthalenesulfonate with lipids: A nuclear magnetic resonance study. *Chem. Phys. Lipids* **1977,** *18* (2), 181-198.

243. Podo, F.; Blasie, J. K., Nuclear magnetic resonance studies of lecithin bimolecular leaflets with incorporated fluorescent probes. *Proc. Natl. Acad. Sci. U.S.A.* **1977,** *74* (3), 1032-6.

244. Gutowicz, J.; Krawczyk, A., Effects of 1-anilinonaphthalene-8-sulphonate on phase transition temperature of dipalmitoylphosphatidylcholine liposomes. *Chem. Phys. Lipids* **1986,** *39* (4), 357-364.

245. Guan, W.; Yang, T.; Lu, C., Measurement of Solubilization Location in Micelles Using Anchored Aggregation-Induced Emission Donors. *Angew. Chem. Int. Ed.* **2020,** *59* (31), 12800-12805.

246. Mohapatra, M.; Mishra, A. K., Photophysical behavior of 8-anilino-1-naphthalenesulfonate in vesicles of pulmonary surfactant dipalmitoylphosphatidylcholine (DPPC) and its sensitivity toward the bile salt-vesicle interaction. *Langmuir* **2013,** *29* (36), 11396-404.

247. Israelachvili, J. N., *Intermolecular and Surface Forces* 3rd Edition ed.; Academic Press: San Diego, 2011.

248. Peng, H. Q.; Niu, L. Y.; Chen, Y. Z.; Wu, L. Z.; Tung, C. H.; Yang, Q. Z., Biological Applications of Supramolecular Assemblies Designed for Excitation Energy Transfer. *Chem. Rev.* **2015,** *115* (15), 7502-42.

8. List of Publications

1. **Saurav Das**; Tanushree Das; Shreya Debnath; Oren A. Scherman and Debapratim Das*; Transiently breathing multi-luminescent vesicles with broad-spectrum tunability (Submitted)
2. Sumit Chowdhuri; **Saurav Das**; Ritvika Kushwaha; Tanushree Das; Basab Kanti Das and Debapratim Das*; Cumulative Effect of pH and Redox Triggers on Highly Adaptive Transient Coacervates (Submitted)
3. Payel Dowari; Shalini Roy; **Saurav Das**; Sumit Chowdhuri; Ritvika Kushwaha; Basab Kanti Das; Anindita Ukil and Debapratim Das*; Mannose-Decorated Composite Peptide Hydrogel with Thixotropic and Syneresis Properties and its Application in Treatment of Leishmaniasis, *Chem. Asian J.,* **2022** (DOI: 10.1002/asia.202200550)
4. Subhra Kanti Roy; Anisha Purkait; Rajib Shome; **Saurav Das**; Debapratim Das; Siddhartha Sankar Ghosh and Chandan K. Jana*; Proline Selective Labeling via On-Site Construction of Naphthoxazole (NapOx), *Chem. Commun.,* **2022**, *58,* 5909-5912.
5. Payel Dowari; Malay Kumar Baroi; Tanushree Das; Basab Kanti Das; **Saurav Das**; Sumit Chowdhuri; Avinash Garg; Ananya Debnath and Debapratim Das*; Development of a hydrolase mimicking peptide amphiphile and its immobilization on silica surface for stereoselective and enhanced catalysis; *J. Colloid Interface Sci.,* **2022**, *618*, 98-110.
6. **Saurav Das**; Tanushree Das; Priyam Das and Debapratim Das*; Controlling the lifetime of cucurbit[8]uril based self-abolishing nanozymes, *Chem. Sci.,* **2022**, *13*, 4050-4057.
7. **Saurav Das***; Priyam Das; Payel Dowari;[§] Basab Kanti Das[§] and Debapratim Das*; Bi-directional feedback controlled transience in Cucurbituril based tandem nanozyme; *J. Colloid Interface Sci.,* **2022**, *614*, 172-180. (§ Authors contributed equally.)
8. **Saurav Das** and Debapratim Das*; Rational Design of Peptide-based Smart Hydrogels for Therapeutic Applications; *Front. Chem.,* **2021**, *9*, 770102.
9. Sumit Chowdhuri; Amrita Saha; Bapan Pramanik; **Saurav Das**; Payel Dowari; Anindita Ukil* and Debapratim Das*,Smart Thixotropic Hydrogels by Disulfide-Linked Short Peptides for Effective Three-Dimensional Cell Proliferation. *Langmuir,* **2020,** *36* (50), 15450-15462.
10. Bapan Pramanik*; **Saurav Das**; Debapratim Das*, Aggregation-directed High Fidelity Sensing of Picric Acid by a Perylenediimide-based Luminogen. *Chem. Asian J.,* **2020,** *15*, 4291-4296.
11. **Saurav Das**;[‡] Payel Dowari;[‡] Bapan Pramanik and Debapratim Das*, pH clock instructed transient supramolecular peptide amphiphile and its vesicular assembly. *Chem. Commun.,* **2019,** *55* (94), 14119-14122. (‡ Authors contributed equally.)
12. Nilotpal Singha;[‡] Basab Kanti Das;[‡] **Saurav Das**;[§] Bapan Pramanik[§] and Debapratim Das*, Freeze the dynamicity: charge transfer complexation assisted control over the reaction pathway. *Chem. Sci.,* **2019,** *10* (43), 10035-10039. (‡, § Authors contributed equally.)
13. Nilotpal Singha; Samya Neogi; Bapan Pramanik; **Saurav Das**; Antara Dasgupta; Ranajit Ghosh and Debapratim Das*, Ultrafast, Highly Sensitive, and Selective Detection of p-Xylene at Room Temperature by Peptide-Hydrogel-Based Composite Material. *ACS Appl. Polym. Mater.,* **2019,** *1*, 2267-2272.